FACULDADE DE CIÊNCIAS E TECNOLOGIA
UNIVERSIDADE NOVA DE LISBOA

VIBRATION CONTROL WITH SHAPE-MEMORY ALLOYS

IN CIVIL ENGINEERING STRUCTURES

Filipe Pimentel Amarante dos Santos
Mestre em Engenharia de Estruturas

Dissertação apresentada à Faculdade de Ciências e Tecnologia da Universidade Nova de Lisboa para obtenção do grau de Doutor em Engenharia Civil

Orientador: Professor Doutor Corneliu Cismaşiu

Júri:

Presidente: Professor Doutor Manuel Américo Gonçalves da Silva
Arguente: Professor Doutor Álvaro Alberto de Matos Ferreira da Cunha
Arguente: Professor Doutor Luís Manuel Coelho Guerreiro
Vogal: Professor Doutor António José Luís dos Reis
Vogal: Professor Doutor João Carlos Gomes Rocha de Almeida

Março 2011

To my wife Inês and our son Afonso

Acknowledgments

This dissertation would not have been accomplished without the support and assistance from many people in many different ways.

I would like to express my deepest and heartfelt recognition to my adviser, Prof. Corneliu Cismaşiu. I cannot thank him enough for his priceless scientific teachings, for his invaluable guidance and commitment, for his inestimable encouragement, confidence and utmost support, and last but not the least, for his enormous generosity and kind friendship, which have made this graduation experience so positive and so meaningful. To work with him was a great pleasure and a privilege.

I am truly and forever grateful to Prof. J. Pamies Teixeira for his incalculable help during the design and construction phases of the physical prototype. Without his inspired input and thoughtful dedication the interdisciplinary nature of this study could not have been achieved.

I would like to show my true appreciation to Prof. F. M. Brás Fernandes, who first brought me into the shape-memory world and with whom I had so many fruitful and delightful discussions, and to K.K. Mahesh for his precious help during the DSC tests.

I would like to thank Prof. Fernando Coito for his availability and for his insightful explanations about modern control engineering.

I am also indebted to Prof. J. C. G. Rocha de Almeida and I profoundly thank him for his unconditional support in overcoming all the bureaucratic perils that have appeared along the way.

I thank Prof. M. Gonçalves da Silva for his warm welcome to the Civil Enginnering Department and for his relentless efforts in providing me with the necessary logistic

conditions to pursuit this work.

I kindly acknowledge Prof. F. Henriques for the use of the infrared camera, during the study of the transformation fronts.

I thank Prof. António Reis for introducing me to scientific investigation, for inciting my natural curiosity in the pursuit of further knowledge and for motivating me to continue my academic studies. I am also grateful to him for the technical data regarding the S. Martinho viaduct.

To my colleagues and friends I thank for all the good disposition and support.

I specially would like to thank my good friend Mário Silva for his priceless technical support with Linux, always managing to solve the innumerable helpless situations I found myself into during the coarse of this work. I also thank him and José Varandas for all the waves I had the pleasure of sharing with them and for all the laughter.

I thank my parents for all their love and everlasting devotion.

Finally, all my love goes to Inês and Afonso as they are the bright sunshine of my life.

I acknowledge the financial support of Fundação Calouste Gulbenkian (bolsa de curta duração) and of Fundação para a Ciência e Tecnologia (FCT/MCTES grant SFRH/BD/37653/2007).

Abstract

The superelastic behavior exhibited by shape-memory alloys shows a vast potential for technological applications in the field of seismic hazard mitigation, for civil engineering structures. Due to this property, the material is able to totally recover from large cyclic deformations, while developing a hysteretic loop. This is translated into a high inherent damping, combined with repeatable re-centering capabilities, two fundamental features of vibration control devices.

An extensive experimental program provides a valuable insight into the identification of the main variables influencing superelastic damping in Nitinol while exploring the feasibility and optimal behavior of SMAs when used in seismic vibration control.

The knowledge yielded from the experimental program, together with an extensive bibliographic research, allows for the development of an efficient numerical framework for the mathematical modeling of the complex thermo-mechanical behavior of SMAs. These models couple the mechanical and kinetic transformation constitutive laws with a heat balance equation describing the convective heat problem. The seismic behavior of a superelastic restraining bridge system is successfully simulated, being one of the most promising applications regarding the use of SMAs in civil engineering structures.

A small-scale physical prototype of a novel superelastic restraining device is built. The device is able to dissipate a considerable amount of energy, while minimizing a set of adverse effects, related with cyclic loading and aging effects, that hinder the dynamic performances of vibration control devices based on passive superelastic wires.

Resumo

O comportamento superelástico desenvolvido pelas ligas com memória de forma confere-lhes um vasto potencial no que diz respeito a aplicações tecnológicas no domínio do controlo de vibrações em estruturas de engenharia civil. Devido à superelasticidade, o material é capaz de recuperar a sua forma original, após ter sido submetido a grandes deformações, desenvolvendo um comportamento histerético. Este comportamento traduz-se numa capacidade de amortecimento intrínseca que, conjuntamente com as elevadas capacidades de reposicionamento do material, constituem características fundamentais para a eficácia de um dispositivo de controlo de vibrações.

É apresentado um vasto programa experimental que contribui para a identificação das principais varáveis que influenciam o amortecimento superelástico do Nitinol, numa tentativa de explorar e optimizar a possibilidade da aplicação de ligas com memória de forma no controlo estrutural de vibrações.

É também apresentada uma ferramenta numérica para a modelação matemática do complexo comportamento termo-mecânico das ligas com memória de forma. Os modelos considerados fazem o acoplamento de leis constitutivas que traduzem o seu comportamento mecânico bem como a cinética das transformações martensíticas, com uma equação de balanço energético. O comportamento sísmico de um dispositivo de retenção superelástico para pontes é testado com sucesso, sendo que se trata de uma das mais promissoras utilizações de elementos superelásticos em estruturas de engenharia civil.

Finalmente, é apresentado um protótipo à escala reduzida de um dispositivo superelástico para o controlo de vibrações que, sendo capaz de dissipar uma quantidade apreciável de energia, permite minimizar uma série de efeitos adversos ligados à superelasticidade.

Contents

List of Figures

List of Tables

Chapter 1

Introduction

1.1 Problem Description

Shape-memory alloys (SMAs) are a unique class of metallic alloys that show two outstanding properties: the shape-memory effect and superelasticity. These properties derive from the ability of these materials to develop a diffusionless phase transformation in solids called martensitic transformation. The shape-memory effect allows the material to recover its original geometry during heating, after being deformed. Superelasticity enables the material to withstand large cyclic deformations, without residual strains, while developing a hysteretic loop. The formation of this hysteretic loop translates into the ability of the material to dissipate energy. Due to this high inherent damping, combined with repeatable re-centering capabilities and relatively high strength properties, SMAs have been progressively introduced in new technological applications related with energy dissipation in civil engineering structural design.

For the time being, most of the applications regarding the use of SMAs in civil engineering structures are linked with the seismic resistance enhancement of cultural heritage structures [35, 43, 77]. However, several studies have already proved the effectiveness of SMAs in a wide range of vibration control devices, i.e. bracing systems [27, 53, 103, 177], base isolation systems [42, 149, 174], bridge hinge restraining systems [8, 46, 82, 127] and structural connections [117, 157].

Although these studies have clearly demonstrated the vast potential of SMAs in

passive vibration control, they are affected by a set of undesirable effects that have an adverse impact on the dynamic performances of vibration mitigation devices based on superelastic (SE) kernel components. These effects comprise the high dependence of these materials towards strain-rate, strain-amplitude and temperature [51, 55, 78, 109, 124, 131, 132, 135, 137, 139, 143, 169].

When passing from quasi-static conditions to dynamic ones, significant changes occur in the shape and size of the SE hysteresis [91, 94, ?], affecting the damping capabilities of the SMA dissipating element. One of the problems hindering the application of SMAs in vibration control systems is that the total area enclosed by a SE cycle, representing the dissipated energy, tends to decrease as the frequency of the dynamic loading increases [51, 62, 135].

Strain-amplitude also plays an important role in the hysteretic damping mechanism, since the total amount of dissipated energy during a SE cycle directly depends on the extent of the martensitic transformation [62]. This is why some of the most promising applications regarding SMAs in structural vibration control comprise pre-strained SE elements [51, 177]. This enables higher martensite ratios during the dynamic solicitation and, hence, higher damping. However, time-dependent effects like stress relaxation in pre-strained SE specimens have been identified [78], and need to be conveniently controlled in order for the pre-strain to remain effective during service.

Civil engineering structures have to endure important temperature variations. Like other structural components, SE vibration control devices are highly influenced by ambient temperature. This relation is translated through a phase-plane diagram which enables the characterization of the stresses that induce the martensitic transformations in a SE specimen, for a given temperature [131]. As these critical stresses increase with temperature, there is a temperature threshold above which the SE damping effect may be compromised, for a given dynamic excitation. It is therefore necessary to clearly establish the temperature range within which a SE vibration control mechanism can still perform competitively.

Re-centering is a mandatory feature in structural vibration control devices. In order to be reliable, these devices must show limited accumulation of residual strains due to cyclic loading. However, SE elements exhibit permanent deformation due to progressive cumulative creep during cyclic loading [88, 144, 145, 165], before the full

stabilization of the SE hysteresis. This causes the net strain produced by a given structural oscillation to be reduced, decreasing the energy dissipation capabilities of the material. This effect may be controlled by an initial training procedure, or by limiting the stress levels during the dynamic loading within a narrower SE window [107, 111].

These effects may constitute an important setback to the application of SMAs in structural vibration control.

1.2 Objectives and Scope

The main objective of this dissertation is the material characterization of SE NiTi while exploring the feasibility and optimal behavior of SMAs when used in structural vibration control.

A set of parametric studies comprising experimental uniaxial tensile tests in SE NiTi wires, with various strain-rates, strain-amplitudes and ambient temperatures are performed, aiming to provide a valuable insight to the behavior of SMAs, and assess their adequacy to seismic vibration control in civil engineering structures. The cyclic behavior of NiTi wires is also investigated through an experimental approach, addressing the effects of cycling on cumulative creep, critical stress to induce martensite and hysteretic width.

A numerical framework adequately describing the complex thermo-mechanical behavior of the SMAs is developed, taking into consideration the knowledge yielded from the experimental program. This numerical framework is used to explore several constitutive models and congurations for SMAs, using bibliographic referenced models as a starting point for the research [15, 30, 60, 103, 159, 169]. The performance of these models is evaluated in order to adopt a suitable numerical model for fast dynamic SE simulations, also identifying the most significant SMA parameters affecting the dynamic response of a structural system. The numerical model is then used in a seismic simulation of SE bridge restraining devices, one of the most promising applications SMAs in civil engineering structures. The restrainers are aimed to prevent unseating during earthquakes due to excessive relative hinge opening and displacements [8, 46].

A control strategy aiming for the attenuation or suppression of the undesirable effects affecting SMAs, which have an adverse impact on their dynamic performances, is developed. This control strategy is first implemented numerically to assess its performance in structural vibration control. Once validated, the control strategy is implemented in a small-scale prototype, reproducing a SE bridge restraining system. This prototype is subjected to various dynamic actions including the ones produced by a reduced shaking table.

1.3 Dissertation Outline

The content of the dissertation is organized into the following seven chapters:

Chapter 2 General introduction to SMAs, including a detailed description of the martensitic transformation which is responsible for the superelasticity and shape-memory effect in SMAs. Analysis of the SE energy dissipation mechanism and its application in vibration control devices. Bibliographic survey regarding seismic hazard mitigation devices based in SE kernel elements.

Chapter 3 Analysis of the austenitic and martensitic crystallographic phases in Nitinol. Description of an extensive experimental program regarding the characterization of Nitinol, including temperature-controlled cyclic tensile tests, differential scanning calorimetry and infrared thermo-imaging. Discussion of the results obtained during the experimental procedures.

Chapter 4 Study of constitutive models for the mathematical modeling of SMAs and corresponding governing laws, coupling the mechanical properties and the transformation kinetics. Analysis of the convective heat transfer problem. Numerical implementation and subsequent assessment and comparison of the performance of the considered constitutive models.

Chapter 5 Numerical analysis of dynamic systems comprising SE components. Study of three SDOF mechanisms based in SE restoring elements and evaluation of their performance as passive vibration control systems. Application of one of these devices in a simplified numerical model of a railway viaduct, as a seismic restraining system and discussion of the obtained results.

Chapter 6 Numerical implementation of a semi-active control strategy aiming to attenuate or suppress the undesirable effects affecting SMAs, which have an adverse impact on their dynamic performances. Description of the proposed vibration mitigation device and analysis of the results yielded by the numerical tests.

Chapter 7 Analysis of a small-scale prototype for the simulation of a SE based bridge restraining system. Description of the proportional-plus-integral-plus-derivative (PID) algorithm used to control the mechanism. Discussion of the experimental results.

Chapter 8 Summary of the research and conclusions. Discussion of the anticipated impacts of the work and suggestions for future research.

Chapter 2

Shape-Memory Alloys in Vibration Control Devices

2.1 Introduction

The emphasis which is currently given to energy dissipation in civil engineering structural design makes materials which are able to reduce vibrations increasingly more appealing. The desired features of high strength, stiffness and tolerance to adverse environments are, for most materials, incompatible with high damping capabilities. Although viscoelastic materials are able to exhibit high damping capabilities, they often show insufficient strength. In the last couple of years, a set of high damping metallic alloys, combining high inherent damping with relatively high strength properties, have been progressively introduced in new technological applications. They are called *Shape-Memory Alloys*. Two of their most important properties are the so called shape-memory effect and superelasticity.

The shape-memory effect is a unique property of certain alloys that exhibit martensitic transformations, that enables the material to recover its original shape, after being deformed upon heating to a critical temperature. Superelasticity is associated with large nonlinear recoverable strains (up to 8%) during a mechanical cycle of loading and unloading [141]. Associated with the discovery of the superelasticity is the Swedish physicist Arne Ölander, in the year of 1932, when he first encountered the SE behavior using an AuCd alloy [124]. In 1938, Greninger and Moorandian

observed the disappearance and reappearance of a martensitic crystal structure by increasing and decreasing the temperature of a CuZn alloy [66]. The thermoelastic properties of the martensitic crystal phase of an AuCd alloy were widely reported by Kurdjumov and Khandros (1949) [86], and Chang and Read (1951) [37]. In the 1960s, Buehler and Wiley discovered the NiTi alloys, while working at the Naval Ordnance Laboratory (NOL). The NOL, now disestablished, was formerly located in White Oak, Maryland and was the site of considerable work that had practical impact upon world technology. As a tribute to their workplace, they named this family of alloys Nitinol [71]. While the potential applications for Nitinol were realized immediately, practical efforts to commercialize the alloy didn't take place until a decade later. This delay was largely due to the extraordinary difficulty in melting, processing and machining the alloy, technological processes that weren't really overcome until the 1990s, when finally these practical difficulties began to be resolved [71].

Shape-memory alloys and other types of smart materials (i.e. piezoelectric materials, magnetorheologic fluids and so on) are being progressively introduced in lectures of engineering courses. Also, in the last years, SMAs have been the object of various innovative studies and industrial applications [8, 11, 25, 27, 42, 46, 53, 70, 82, 95, 97, 103, 112, 117, 125, 127, **?**, 149, 157, 174, 177, 178].

2.2 General aspects of Shape-Memory alloys

2.2.1 Martensitic transformation

The transformation which yields superelasticity and the shape-memory effect is a diffusionless phase transformation in solids, called martensitic transformation. During this transformation, the atoms are cooperatively rearranged into a different crystalline structure with identical chemical composition, through a displacive distortion process [60]. The absence of diffusion, without the net transport of atoms, makes the martensitic phase transformation almost instantaneous [131]. In SMAs, the martensitic transformation changes the material from the parent phase, a high-temperature (high-energy) phase called austenite, to a low-temperature phase (low-energy) called martensite. Being a first-order phase transition, parent and product phases coexist

during the phase transformation [131].

An ideal crystal is constructed by the infinite repetition in space of identical structural units. The structure of all crystals is described in terms of a lattice, which is a regular periodic arrangement of points in space, with a group of atoms attached to each lattice point. One important feature of crystal structures is symmetry. Some lattices possess a large measure of symmetry, whilst others are symmetric in a much less extent. Since the martensite has lower symmetry than austenite, many variants can be formed from the same parent phase [124].

During the transformation from the high-temperature phase to the low-temperature phase, these martensitic variants are formed in a twinned pattern, in which the atoms achieve displacements with mirror symmetry. This occurs since the crystal lattice strives to achieve minimal potential energy states for a given temperature [141].

While most materials deform by slip or dislocation motion, martensite responds to stress by changing the orientation of its crystal lattice trough movement of the twin boundaries to the most accommodating variant to the applied stress [141]. By applying a certain level of unidirectional stress on a martensite specimen, one can cause most of the martensite to *tilt* in the same direction, causing the detwinning of crystal structure [71]; see Figure 2.1.

Stress and temperature have large influence on martensitic transformations. Such transformations can be either induced by heating (or cooling) or by stressing. The stress-temperature phase diagram is of the utmost importance in order to comprehend the process of martensite transformation in SMA materials. As illustrated in Figure 2.2, the transformation develops across the strips [A],[M],[d] and [t], when a given point (T, σ), representing the local state of the system moves across a strip in the direction of the transformation, i.e., from the starting boundary to the finishing boundary, as indicated by the *director vectors* n^i (i = A, M, d, t) [23].

The phase diagram is divided into four major regions:

- M^d region: only detwinned martensite can exist;
- A region: only austenite can exist;
- $M^{t,d}$ region: both twinned and detwinned martensite can co-exist;
- $M^{t,d}A$ region: all phases can coexist.

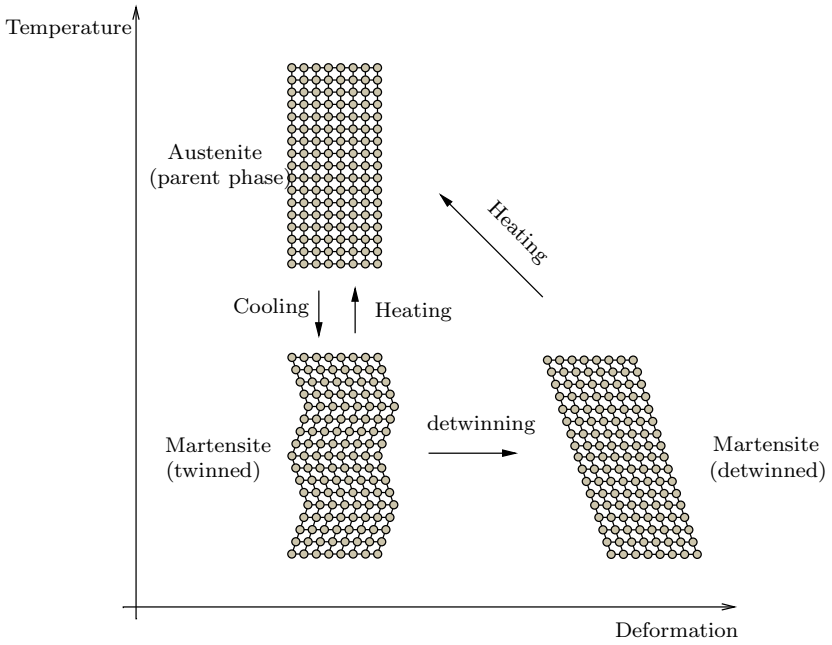

Figure 2.1: Schematic diagram of martensitic transformations (after Otsuka and Wayman [124]).

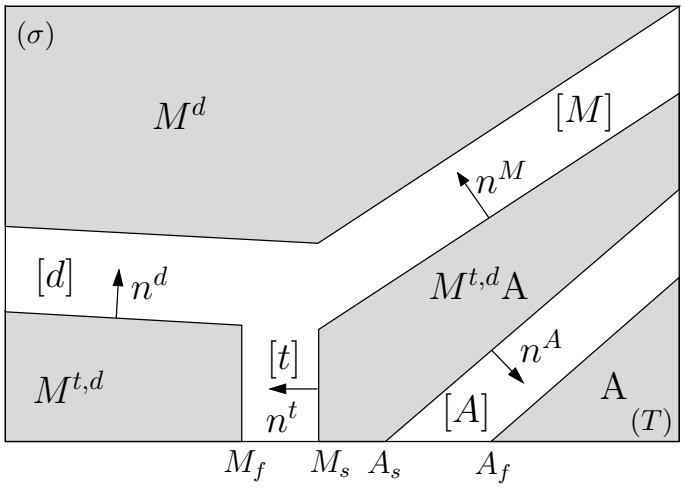

Figure 2.2: Typical uniaxial stress-temperature phase diagram of SMA material. Transformation strips are the unshaded regions (after Bekker and Brinson [23]).

In the stress-free state, a SMA is characterized by four transformation temperatures: M_s and M_f during cooling and A_s and A_f during heating. The first two (with $M_s > M_f$) indicate the temperatures at which the forward transformation starts and finishes, respectively. The last two (with $A_s < A_f$) are the temperatures at which the inverse transformation starts and finishes, A_f being the temperature above which the martensite becomes completely unstable [124]. Another important temperature value is M_d, which is an upper temperature limit above which martensite cannot be stress-induced [55], because of the stability attained by austenite [109]. These transformation temperatures depend mainly on the alloy's composition and processing [131].

2.2.2 Superelasticity

A generic stress-strain response of a SE wire is shown in Figure 2.3. When an unidirectional stress is applied to an austenitic specimen, within a temperature range between A_f and M_d ($M_d > A_f$), an elastic distortion of the austenitic lattice starts to occur (o-a). There is a critical value (a) whereupon austenite becomes unstable and a transformation from austenite to *stress-induced martensite* (SIM) takes place; see Figure 2.4. As the deformation proceeds the stress remains almost constant until the material is fully transformed (a-b). During this part of the response the two phases coexist. Upon stress removal, the elastic unloading of the detwinned martensite (b-c') takes place. Since martensite becomes unstable below a critical stress (c') a reverse transformation occurs as the unloading process continues. Detwinned martensite reverts back to austenite, at a lower stress plateau than during loading (c'-d'). When the material is fully transformed to the parent phase (d') further unloading will follow the initial loading path, with full recovery of the deformation. A hysteretic effect is hence produced. If the temperature is greater than A_f, the strain attained during loading is completely recovered at the end of the unloading. This process is translated by an energy-absorption capacity with zero residual strain, called superelasticity. If the temperature is less than A_f, only a part of stress induced martensite re-transforms into austenite. A residual strain is then found at the end of the unloading, which can be recovered by heating above A_f. This phenomenon is generally referred to as partial superelasticity [60].

As already mentioned, at the end of the stress plateau (a-b), most of the material

has transformed into martensite. Further straining requires the elastic loading of the detwinned martensite (*b*-*c*). At point (*c*) the stress is high enough to cause the slipping of the martensite lattices, as permanent deformation starts and the tangent modulus of the material begins to decay (*c*-*d*). At an even higher stress level, a second region of relatively low modulus starts (*d*-*e'*) which, under persistent deformation, would cause the failure of the specimen.

If the material is unloaded above point (*c*), some sockets of the material transform back into austenite, but an important residual deformation would be present.

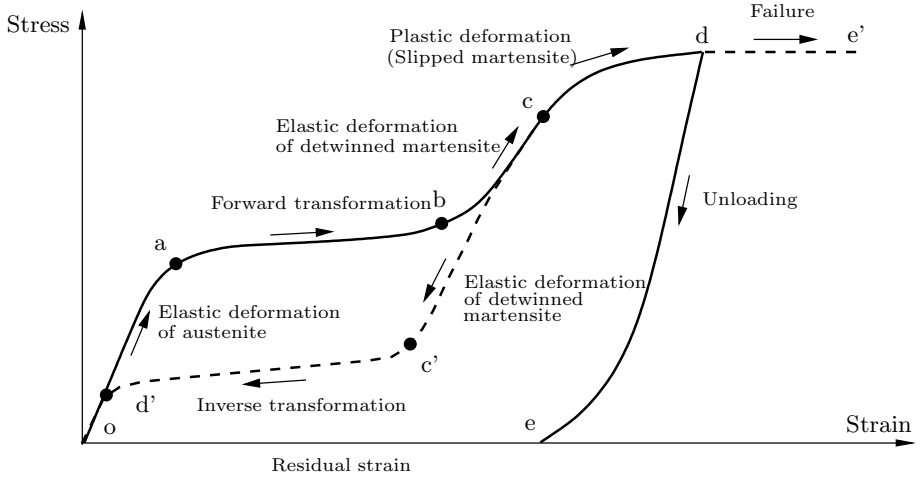

Figure 2.3: Generic stress-strain response of a SMA above A_f (adapted from Shaw and Kyriakides [**?**]).

Since the martensitic transformation involves latent heat (enthalpy of transformation), energy is absorbed into the material, or released to the surrounding environment, depending on the direction of the transformation. The forward, austenite-to-martensite (A→M) transformation is exothermic and the reverse martensite-to-austenite (M→A) transformation is endothermic [61, 131].

In the superelastic domain, the stress-temperature phase diagram shown in Figure 2.2 can be simplified by considering a temperature range between A_f and M_d. In Figure 2.5, a pseudo-static, isothermal superelastic cycle, together with the associated transformation path in the corresponding stress-temperature phase diagram is represented. Considering that the cycle is performed with a constant temperature, the forward transformation path, between points (*a*) and (*b*), and the inverse transformation path, between points (*c*) and (*d*), lie over the same vertical line,

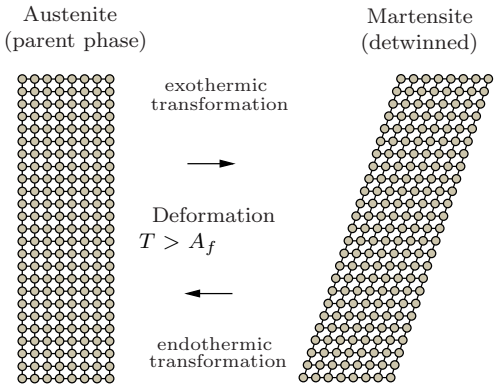

Figure 2.4: Mechanism of superelasticity (after Otsuka and Wayman [124]).

associated with T = T_0.

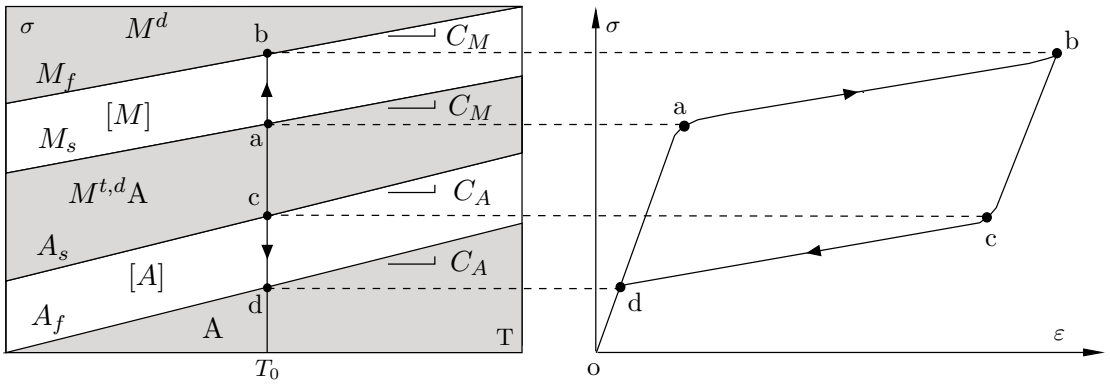

Figure 2.5: Isothermal path on phase diagram and correspondent hysteresis.

To characterize the stress effect on the martensitic transformation, the Clausius-Clapeyron relation is often used [124]. The Clausius-Clapeyron equation relates temperature and stress along the transformation strips of the SMA stress-temperature phase diagram. This relation, for uniaxial stress, may be written as follows,

$$\frac{\mathrm{d}\sigma}{\mathrm{d}T} = -\frac{\Delta H}{\varepsilon T_0} \tag{2.1}$$

where σ is the uniaxial stress, ε is the transformation strain and ΔH is the enthalpy of the transformation per unit volume for temperature T_0 [29].

During the forward transformation, which is exothermic, an overall decrease in enthalpy occurs, achieved by the generation of heat. In this case, ΔH is negative. On

the other hand, during the reverse transformation, which is endothermic, heat is absorbed by the system and ΔH is positive.

The relation between temperature and the critical stress to induce the martensitic transformation can be described by the material properties C_M and C_A. These values represent the slope ($\mathrm{d}\sigma/\mathrm{d}T$) of the lines defining the boundaries of the SMA transformation strips, represented in Figure 2.5. Although experimental results for the determination of critical stress values associated with the beginning and the end of the forward and inverse transformations do rarely yield precisely linear results, it is usual to admit that the relation between critical stress and temperature tends to be approximately linear. It is generally assumed that both C_M and C_A have the same value, constant over all temperature ranges [29]. This value is also referred to as the Clausius-Clapeyron coefficient (CCC or α_{CC}) [78].

2.2.3 Shape-Memory effect

The other manifestation of the thermoelastic martensitic transformation in SMAs is the so called shape-memory effect. Whereas stressed induced martensite consists of a single preferential variant according to the applied stress, martensite produced by cooling consists of a random mixture of several variants (including twins). Twin boundaries can be relatively easily moved by the application of stress. Movement of twin boundaries by stressing, called detwinning, results in change of orientation from one variant to another which is more favorably oriented to the direction of the applied stress. During the detwinning process of the martensitic crystal structure, when facing an unidirectional loading, the stress remains almost constant until the martensite is completely detwinned. Crystals favorably aligned to the load direction deform first, at a lower stress level, (o-a-b) in Figure 2.6. Less favorably aligned crystals deform later, at higher stresses (b-c). Further straining causes the elastic loading of the detwinned martensite (c-d). Unloading from any point in (o-d) initially results in elastic unloading of the detwinned material. The deformation recovered is much smaller than the one supplied by detwinning, giving the apparent impression of permanent deformation. This deformation can be recovered by raising the temperature above A_f, transforming the detwinned martensite back to austenite; see Figure 2.7. This shape is maintained during cooling below M_f, when the material re-transforms to twinned martensite. Straining further than point (d) will

first cause the slipping of the martensite lattices and eventually lead the specimen to failure, corresponding to point (*e'*). The force exerted by a specimen when it trans-

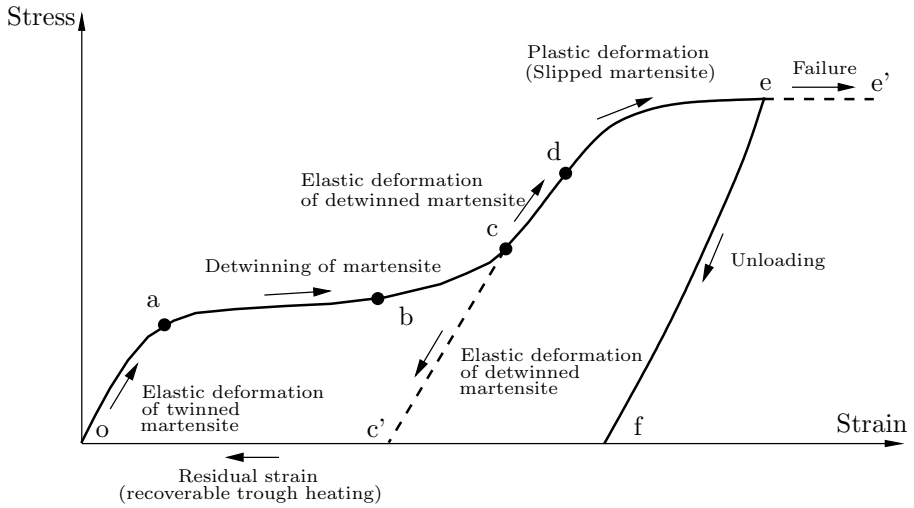

Figure 2.6: Generic stress-strain response of a SMA below M_f (adapted from Shaw and Kyriakides [**?**]).

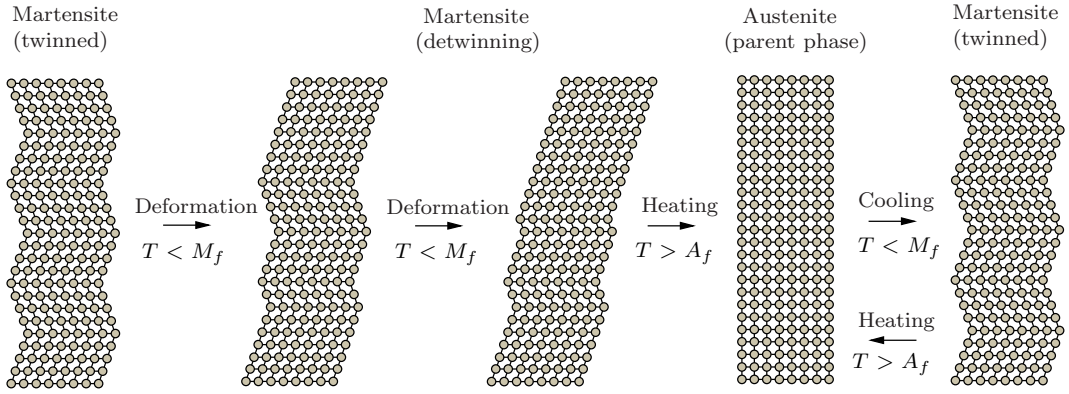

Figure 2.7: Mechanism of shape-memory effect (after Otsuka and Wayman [124]).

forms from martensite to austenite is associated with a first-order phase transition, involving enthalpy of transformation. During this transition, the system absorbs an amount of energy, through heating. This force may be much higher than the force needed to deform the martensite specimen, causing it to detwin. This last transformation is a second-order phase transition, a continuous phase transition with no associated latent heat [71].

Finally, a sequence of martensitic transformations is shown in Figure 2.8, combining both a superelastic cycle and a shape-memory recovery.

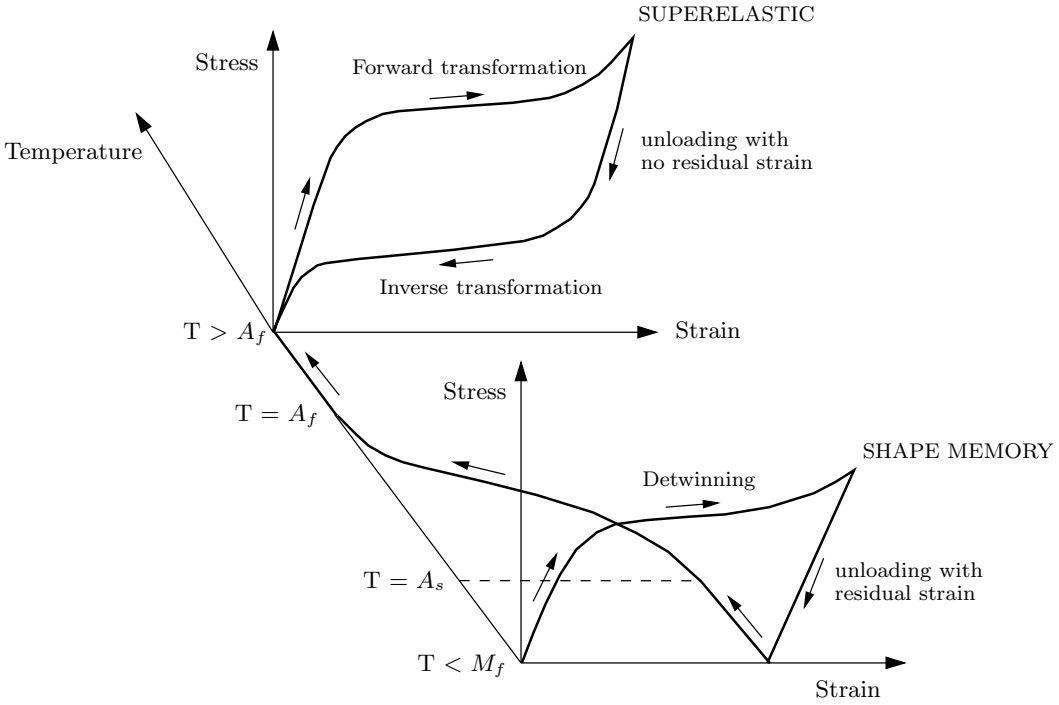

Figure 2.8: Shape-memory and superelastic sequence. Three dimensional stress, strain and temperature diagram.

2.2.4 Internal friction

The martensitic transformation involves latent heat, i.e. energy is absorbed into the material or released to the surrounding environment, depending on the direction of the transformation. The energy generated during one tensile cycle is proportional to the volume fraction of formed martensite, reaching its maximum at the middle of the solicitation.

The other source of energy generation during martensitic transformation is the internal friction. The amount of energy dissipated due to internal friction is always small compared to the latent heat of transformation [122]. It is generally accepted that internal friction, or damping capacity of SMAs, derives from the movement between martensite-martensite and parent-martensite transforming interfaces [124, **?**].

This energy loss due to interfacial motion enables a high degree of strain reversibility while providing material damping, in contrast to dislocation based plasticity, in which damping is associated with irreversible inelastic deformations [**?**]. Internal friction is usually related to the dissipative response of a material when subjected to a cyclic deformation [90].

The energy dissipated in a cycle of harmonic vibrations corresponds to the area enclosed by the hysteresis loop and is usually referred as E_D. It is usually defined for a full cyclic deformation, comprising tension and compression. If such a deformation is applied on a SMA, the stress-strain curve in compression can be considered similar to the one in tension [135]. E_{S0}, in Figure 2.9, is the maximum strain energy [38].

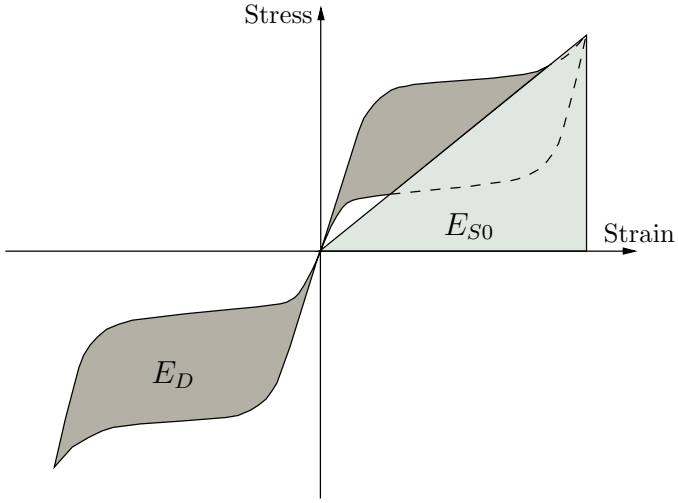

Figure 2.9: Definition of energy dissipated E_D in a superelastic loading cycle and maximum strain energy E_{S0}.

For one complete cycle, the total dissipated energy is then equal to twice the energy dissipated in tension. In Nitinol, depending on temperature and strain-rate, the maximum energy dissipated in tension can reach values as high as 40 to 50 J/cm^3 [55].

To mathematically describe damping, the viscous damping element is most commonly used. The damping force f_D is related to the velocity $\dot{u}$ of the linear viscous damper by $f_D = c\dot{u}$, where the constant c is called the viscous damping coefficient. In usual structures, damping derives from several different energy-dissipating mechanisms, making it difficult to clearly identify and to mathematically describe each

one of these mechanisms. Therefore, the damping coefficient of a given structure is chosen in such a way that the vibrational energy it dissipates equals the energy dissipated in all of the combined damping mechanisms present in the structure. This idealization is called equivalent viscous damping [38].

The most common method for defining the equivalent viscous damping is to equate the energy dissipated in a vibration cycle of the actual structure and an equivalent viscous system. The equivalent viscous damping as a measure of damping or internal friction in a structure is very advantageous since it is clearly defined in terms of observable quantities. For a given dynamic system, the stress-strain relation can be easily obtained through a cyclic loading experiment. The subsequent evaluation of the area enclosed by the hysteresis, corresponding to the dissipated energy (E_D), is very simple to compute.

The energy dissipated by a viscous system is given by

$$E_D = \int f_D \, du \tag{2.2}$$

where f_D is the damping force. The steady-state vibrations of a single-degree-of-freedom (SDOF) system due to an harmonic force can be described as $u(t) = u_0 sin(\omega t - \phi)$. The dissipated energy in one cycle of harmonic vibration equals

$$E_D = \int_0^{2\pi/\omega} (c\dot{u})\dot{u} \, dt \; = \; \pi c \omega {u_0}^2 \tag{2.3}$$

As the damping ratio, ζ is defined by

$$\zeta = \frac{c}{2m\omega_n} \tag{2.4}$$

and the natural undamped frequency of the system is defined by $\omega_n = \sqrt{k/m}$, expression (2.3) may be rewritten as

$$E_D = 2\pi\zeta \frac{\omega}{\omega_n} k {u_0}^2 \tag{2.5}$$

Taking into account that the maximum strain energy is $E_{S0} = k{u_0}^2/2$, equation (2.5)

can be rewritten as

$$E_D = 4\pi\zeta\frac{\omega}{\omega_n}E_{S0} \tag{2.6}$$

or

$$\zeta = \frac{1}{4\pi}\frac{\omega_n}{\omega}\frac{E_D}{E_{S0}} \tag{2.7}$$

If the stress-strain hysteresis, and the correspondent E_D, is determined at $\omega = \omega_n$, equation (2.7) specializes to

$$\zeta_{eq} = \frac{1}{4\pi}\frac{E_D}{E_{S0}} \tag{2.8}$$

The damping ratio ζ_{eq} determined with $\omega = \omega_n$ would not be correct at any other exciting frequency, but it would be a satisfactory approximation [38].

2.3 Vibration control devices

Technological applications built up of shape-memory components are designed to take advantage of the shape-memory effect and/or superelasticity. Regarding the shape-memory effect, three different categories are usually considered for the aforementioned applications, i.e., free recovery, constrained recovery and actuators [55]. Free recovery is when a shape-memory component is allowed to freely recover its original shape during heating, generating a recovery strain. If this recovery is prevented, constraining the material in its martensitic form while recovering, large stresses are developed, although no strain is recovered. These applications, based on a constrained recovery, include fasteners and pipe couplings and are the oldest and most widespread type of practical use [55]. In applications where there is both a recovered strain and stress during heating, such as in the case of a Nitinol spring being warmed to lift a ball, work is being done. Such applications are often further categorized according to their actuation mode, i.e. electrical or thermal.

Technological applications based on SE components are mainly built for passive energy dissipation. Like all passive control systems, these applications do not require external power sources. Contrary to active control devices, which apply forces to the structure in a prescribed manner, by means of an external power source, they impart forces that are developed in response to the motion of the structure itself. When a system combines the use o both active and passive control it is called a hybrid

control system. In a semi-active control system, mechanical energy is not added into the structural system nor to the control actuators. These devices are mostly passive control devices with controllable properties, and therefore have external energy requirements which are orders of magnitude smaller than ordinary active control systems [73].

Passive energy dissipation in a vibrating structure mainly occurs due to internal stressing, rubbing, cracking, and plastic deformations [73]. When facing a dynamic event, the amplitude of the structural vibrations varies inversely with the capacity of the structure to dissipate energy. As some structures show very low damping, they may experience large amplitudes of vibration even for moderately strong earthquakes. Increasing the energy dissipation capacity of a structure is a very effective method to reduce the amplitudes of vibration. A great variety of different devices providing supplemental damping exist and have been already installed in structures all over the world, enhancing their energy dissipation capacity by converting kinetic energy into heat. These devices operate on principles such as frictional sliding, deformation of viscoelastic solids or fluids, yielding of metals and phase transformations in metals or alloys. The latter method includes SE, which allows the material to dissipate a considerable amount of energy through hysteresis, while recovering from large nonlinear strains [73].

2.4 Seismic mitigation devices based on SMAs

Recent earthquakes in urban areas such as the Loma Prieta (1989) and the Northridge (1994) earthquakes, in the U.S.A., the Kobe (1995) earthquake, in Japan, the Kocaeli (1999) earthquake, in Turkey, and the Nisqually (2001) earthquake, in the U.S.A, resulted in significant damage to the civil engineering infrastructure [104].

Structural components suffered large permanent deformations as a result of conventional design techniques, which rely on their inelastic response to dissipate energy during a seismic event. As a result of these shortcomings, the structural engineering community has concentrated on a performance-based design approach, to earthquake mitigation in structures. The performance guidelines for such a design approach mostly rely on the characterization of acceptable structural inter-story drift values, for a given seismic hazard, where an increased maximum inter-story

drift can be associated with increased damage levels [68].

Meanwhile, several devices aimed to limit the inelastic behavior of critical structural members are being developed, in order to comply with these performance guidelines. These devices are based on three primary concepts: energy dissipation (damping), decoupling of the structure from the foundation (base isolation) and limiting the force transmission to critical load bearing members [168].

The current development of both passive and active vibration control devices based on these concepts has led to a recent interest in the use of *smart materials*. A relatively consensual definition of a *smart material* is proposed in [106]: a structural material that inherently contains actuating, sensing and controlling capabilities built into its microstructure. These materials undergo changes in one or more of their properties (chemical, mechanical, electrical, magnetic or thermal) in a direct response to an external stimuli associated with the environment surrounding the material. These changes are direct and reversible, with no need for an external control system [1]. SMAs are one class of *smart materials* that have shown significant potential for exploitation as a cost-effective mean to control the response of civil engineering structures in both new and retrofit applications [49, 104].

2.4.1 Bracing systems

Most of the structural damages occurring in building structures during an earthquake event, result from large inter-story drifts. The addition of passive energy dissipation bracing systems, connecting two consecutive storeys of the building, have been proved effective in limiting such inter-story drifts, preventing significant inelastic deformations in structural members [53].

Currently used bracing systems dissipate energy through yielding of metals, sliding friction between suitable surfaces, motion of a piston or plate within viscous fluid, extrusion of fluid through orifices or, finally, viscoelastic action of polymers. Recently, SMAs are being increasingly considered for bracing systems in structures, in order to limit inter-story and residual drifts, by providing additional energy dissipation capacities and re-centering capabilities [53].

The use of SMAs in structural bracing systems has been addressed by several researchers [2, 3, 14, 27, 34, 69, 99, 103, 110, 142, 158]. Some of these papers report

on shake-table tests in small-scale steel framed prototypes, used to study Nitinol and copper-based cross-bracing systems; see Figure 2.10. These systems showed a significant decrease in the maximum inter-story drift values, with the use of SMA braces. Almost no residual displacements were experienced by the structural prototypes, due to the re-centering capability of the SMA material. Furthermore, in the study conducted by McCormick *et al.* [103] an additional conventional steel braced structure was analyzed, as a benchmark, that underwent yielding and buckling. This resulted in permanent story drifts and less effective seismic vibration control.

Figure 2.10: Small-scale steel framed prototype with SMA braces (adapted from Boroscheck *et al.* [27]).

One of the most important initiatives regarding the exploitation of SMAs for applications in structural systems is the "MANSIDE" (Memory Alloys for New Seismic Isolation and Energy Dissipation Devices) project, conducted by the European Union. This project, which thoroughly studied the mechanical behavior of martensite bars and SE austenite wires, carried out an extensive experimental program of shaking table tests on reduced-scale structural models. SMA-based braces; see Figure 2.11, configured to provide re-centering and/or energy dissipation, were studied

by Dolce *et al.* [53] in a reinforced concrete structure. The aim of the experimental program was to compare the behavior of structures endowed with innovative SMA-based devices to the behavior of conventional structures and of structures endowed with currently used passive control systems.

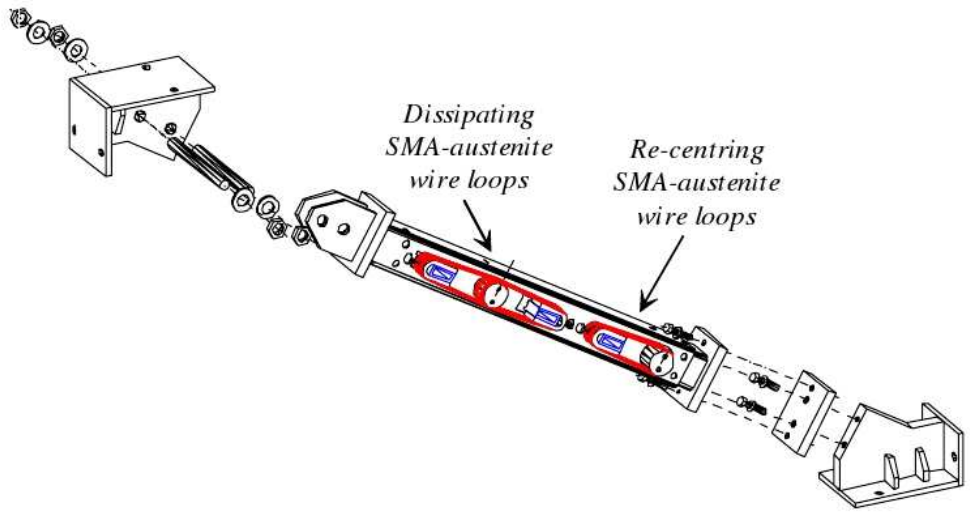

Figure 2.11: SMA-based energy dissipating and re-centering brace (adapted from Dolce *et al.* [53]).

The addition of passive control braces in the reinforced concrete frame proved to convey great benefits to the overall seismic behavior of the structure. The seismic intensity producing structural collapse was considerably raised and the inter-story drifts and shear forces in columns were drastically reduced. The experimental outcomes have also shown that the new SMA braces can provide performances at least comparable to those provided by currently used devices.

Adaptive vibration control devices for bracing systems, based on SE austenitic wires, were proposed by Zhang and Zu [176, 177]; see Figure 2.12. These devices present two distinctive features: its tunable hysteretic behavior and the ability to withstand several design level earthquakes. The hysteretic behavior of the dampers could be modified to best fit passive structural control applications, by adjusting the dampers design parameters such as the inclination angle of the SE wires, pre-tension level and the friction coefficient.

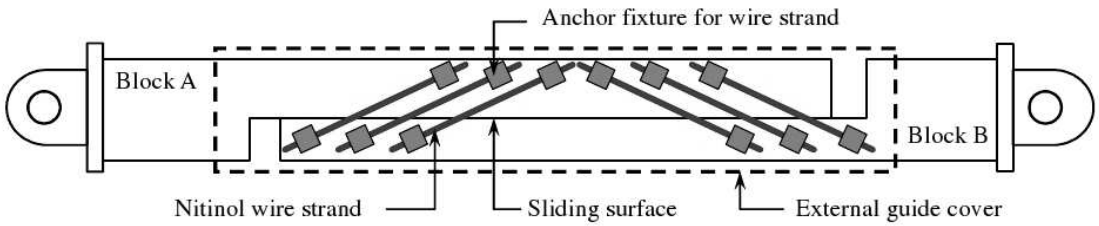

Figure 2.12: Adaptive vibration control device for bracing systems (adapted from Zhang and Zu [177]).

2.4.2 Base isolation system

Although dampers are probably the most popular application for SMAs in structures, their use has also been addressed in applications for base isolation systems. These systems are meant to decouple the superstructure from its foundation while also providing additional energy dissipation and re-centering capabilities. They filter the seismic energy transferred from the ground motion to the superstructure so that the damage of the superstructure is attenuated [150]. Corbi [42] has implemented such an isolation device in a multi-degree-of-freedom (MDOF) elastic-plastic structural model of a building and demonstrated its efficacy in suppressing plastic deformations in the super-structure. A hybrid base isolation system, composed of linear elastomeric bearings, friction-pendulum bearings, SE austenitic wires and magnetorheological (MR) dampers was proposed by Shook *et al.* [149], for mitigation of seismic motions. To manage the superstructure response to ground motions, each sub-component of the isolation system was designed for a specific task. The SE austenitic wires were used to supply recoverable hysteretic behavior and to serve as an additional restoring force. The isolation system comprehends a set of low-friction wheels in order to reduce the total length of the SMA installation while guaranteeing the effective length of the SMA wires.

Results showed that the proposed SE base isolation system could significantly reduce base drifts, maintaining a favorable response from the superstructure. Dolce *et al.* [54] also proposed a hybrid isolation system, based on both SMA and steel components.

Base isolation also provides a very effective passive method of protecting bridges

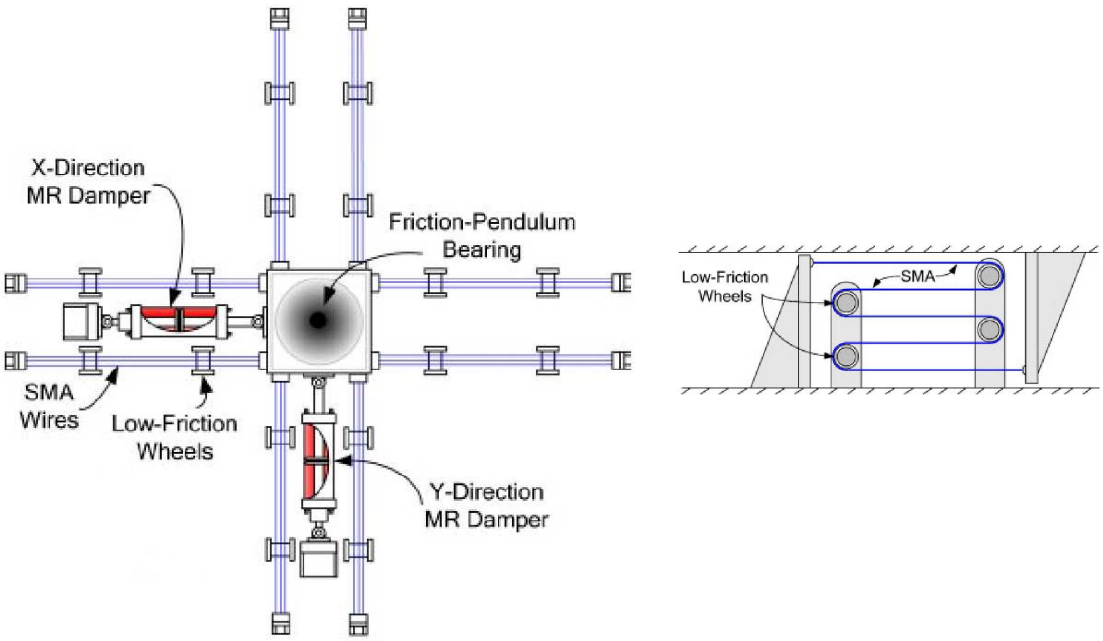

Figure 2.13: Configuration of elastomeric bearings, friction-pendulum bearings, SE austenitic wires and magnetorheological dampers. Low-friction wheels for SMA wire installation (adapted from Shook *et al.* [149]).

from the hazard of earthquakes. Wilde *et al.* [174] proposed an isolation system combining a laminated rubber bearing with a SMA device. The isolation system uses the different responses of the SMA, at different levels of strain, to control the displacements of the rubber bearing for different excitation levels. It provides a stiff connection between the pier and the deck for small external loading. For a medium size earthquake, the SMA bars increase the damping capacity of the isolation system due to stress-induced martensitic transformation of the alloy. Finally, for the largest considered earthquake, the SMA bars provides both hysteretic damping and displacement control due to the hardening of the alloys after completeness of the phase transformation. The SMA based isolation system also has an inherent re-centering ability due to the SE response of the alloy.

2.4.3 Bridge hinge restrainers

During earthquake events, bridges are susceptible to unseating and collapse due to excessive longitudinal motion at in-span hinges or supports. Such damage can cause

significant disruptions to the transportation network, posing a threat to emergency response and recovery as well as resulting in severe direct and indirect economic losses for a region. The unseating mechanism of a bridge during an earthquake, associated with an in-span hinge, is presented in Figure 2.14. The unseating at in-span hinge, during the 1994 Northridge earthquake, for an existing bridge and a bridge retrofit with traditional steel restrainer cables, taken from the NISEE (National Information Service for Earthquake Engineering) collection [82] is illustrated in Figure 2.15.

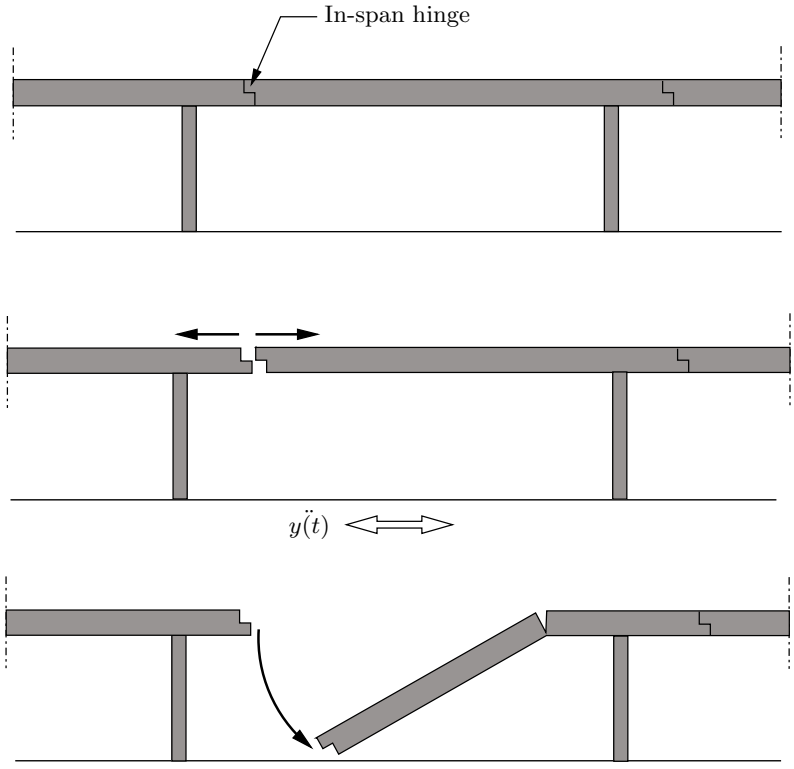

Figure 2.14: Unseating of bridge at in-span hinge during an earthquake.

Several authors have studied the retrofit and rehabilitation of bridges, in order to overcome their seismic vulnerabilities [8, 46, 48]. Andrawes *et al.* [8] and DesRoches *et al.* [46] have studied the efficacy of using SMA restrainers to reduce the response of decks in a multi-span simply supported bridge. These SMAs based seismic damping devices are aimed to concentrate energy dissipation in controlled locations, reducing the demand on individual frames in a multiple-frame bridge. In Figure 2.16 is depicted a restraining solution with SMA elements in a multi-span simply supported bridge. Analytical models showed that the SMA restrainers reduce relative hinge

Figure 2.15: Unseating of bridge at in-span hinge during the 1994 Northridge earthquake for an existing bridge and a bridge retrofit with traditional steel restrainer cables (adapted from Johnson *et al.* [82]).

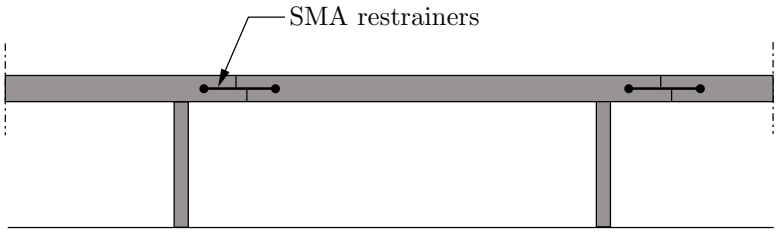

Figure 2.16: Restraining solution with SMA elements in a multi-span simply supported bridge.

displacements at the abutment much more effectively than conventional steel cable restrainers. The large elastic strain range exhibited by SMA restrainers allows them to undergo large deformations while remaining elastic. In addition, the SE properties of the SMA restrainers result in energy dissipation at the hinges. Finally, evaluation of the multi-span simply supported bridge subjected to near-field ground motion showed that the SMA restrainer bars are extremely effective for limiting the response of bridge decks to near field ground motion. The increased stiffness of the SMA restrainers at large strains provides additional restraint to limit the relative openings in a bridge.

A large scale testing program was conducted by Johnson *et al.* [82], to determine the effects of SMA restrainer cables on the seismic performance of in-span hinges, in bridges. Their performance was compared to that of traditional steel restrainers for reducing hinge displacement and the likelihood of collapse during earthquakes. Figures 2.17 and 2.18 show a schematic of the test setup and the actual SMA

restrainer test setup, respectively, which comprise a representative multiple-frame concrete box girder bridge and the SMA restrainer cable.

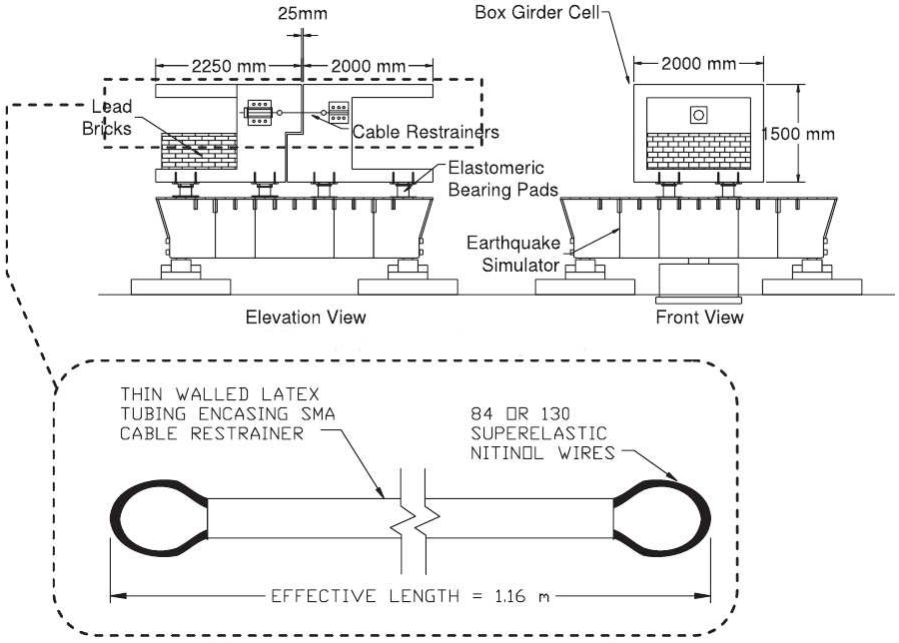

Figure 2.17: Schematic of the test setup and SMA restrainer cable (adapted from Johnson *et al.* [82]).

Figure 2.18: SMA restrainer test setup (adapted from Johnson *et al.* [82]).

The results of the tests showed that SMA restrainers performed very well as restraining devices. They showed minimal residual strain after repeated loading and

little strength and stiffness degradation after undergoing many cycles. In addition, the hysteretic damping that was observed in the larger ground accelerations demonstrated the ability of the materials to dissipate energy.

Another large scale testing program, also regarding the use of SMA restrainer cables in bridges, was undertaken by Padgett *et al.* [127]; see Figures 2.19 and 2.20. It concerned the evaluation of the effectiveness of SMA restrainers in limiting the hinge opening at the deck-abutment interfaces. The SMA restrainers were tested on a four-span, one-quarter scale, concrete slab bridge. The bridge was subjected to a suite of ground motions to assess the performance of the SMAs under different magnitudes of loading.

The results of the experimental tests show that the SMA cables were effective in reducing the potential for unseating by reducing the as-built openings. In addition, the hinge displacements were also accompanied by reductions in column drift.

2.4.4 Structural connections

Another innovative uses for SMA applications in structures are materialized by column base anchors in buildings [157] and isolation applications in beam-column connections [5, 117]. Ocel *et al.* [117] showed the feasibility of a new class of partially restrained SMA based connections, in the martensitic form. In this crystallographic phase it is possible to recover large residual deformations by heating the alloy above its transformation temperature. The proposed connection consisted of four large diameter NiTi SMA bars connecting the beam flange to the column flange, and serving as primary moment transfer mechanism. The schematic test setup is shown in Figure 2.21. The tested full-scale connection is illustrated in Figure 2.22.

The connections exhibited a high level of energy dissipation, large ductility capacity and no strength degradation after being subjected to cycles up to 4% drift. Following the initial testing series, the tendons were heated to recover the residual beam tip displacement. After initiating the shape-memory effect within the tendons, the connections were retested, displaying repeatable and stable hysteretic behavior. An additional test was performed under dynamic loading to examine the strain-rate effects on the performance of the connection. The dynamic tests showed similar behavior, except for a decrease in energy dissipation capacity when compared to the

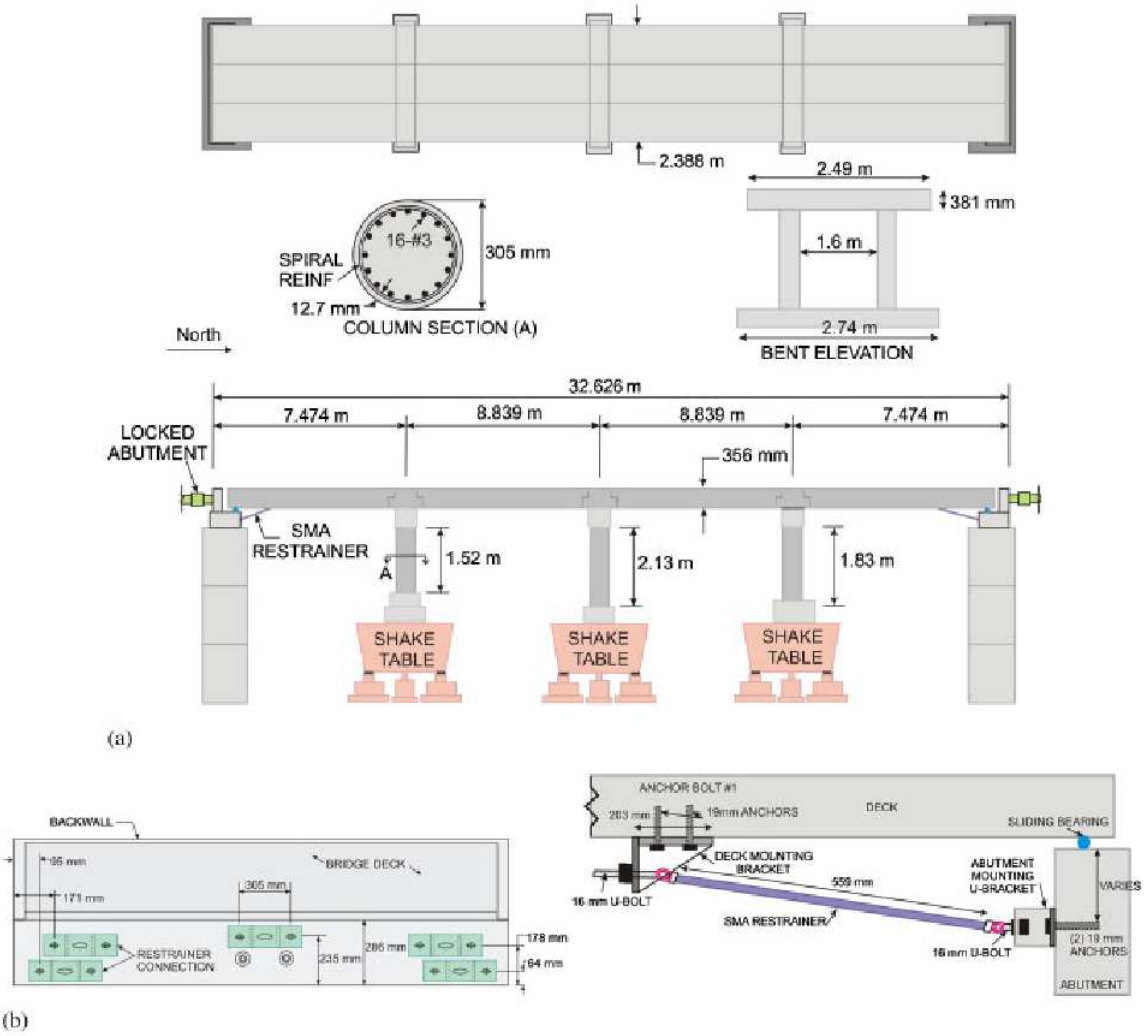

Figure 2.19: Schematic of the test setup and SMA restrainer cable. Adapted from Padgett *et al.* [127].

quasi-static tests.

Alam *et al.* [5] successfully tested the use of SMAs in plastic hinge regions of beam-column elements in reinforced concrete structures, for mitigating the problem of permanent deformation during strong earthquakes. In Figure 2.23 is shown a schematic detail of the beam-column element including a single barrel screw-lock coupler for connecting SMA rebar with regular steel rebar.

Figure 2.20: SMA restrainer test setup (adapted from Padgett *et al.* [127]).

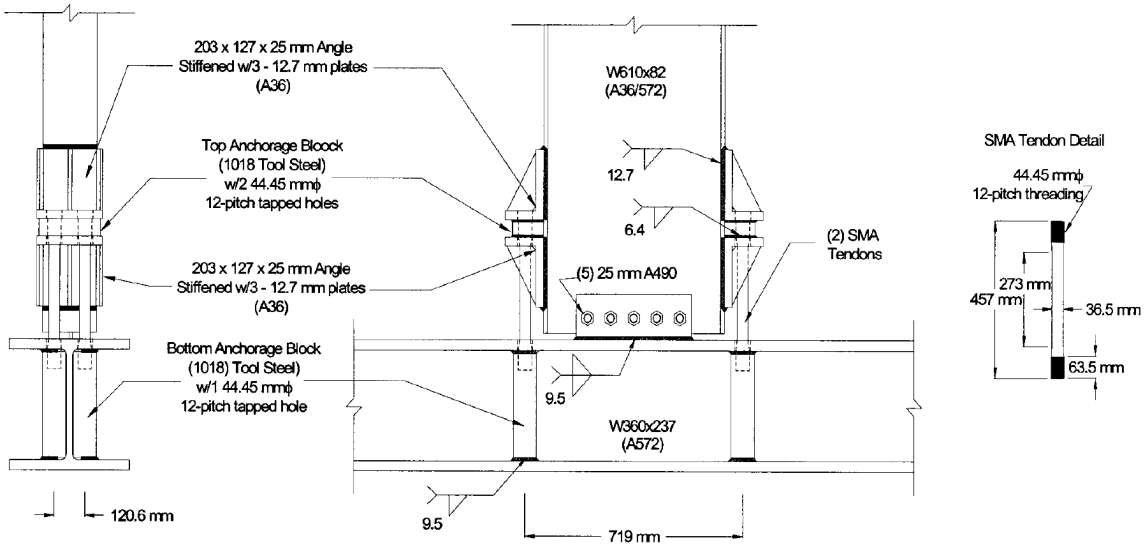

Figure 2.21: Schematic of the SMA-based connection test setup (adapted from Ocel *et al.* [117]).

2.4.5 Applications in existing civil engineering structures

Even though a considerable amount of progress has been achieved in developing industrial applications for civil engineering structures based on shape-memory alloys, only few devices have been implemented in existing structures. Among the cases where such devices have been implemented are the Basilica of St. Francis of Assisi [43], the St. Feliciano Cathedral [35], the St. Giorgio Church bell-tower [77], in Italy, and the Bridge carrying Sherman Road over US-31 in the USA [152].

Figure 2.22: SMA-based full-scale connection test setup (adapted from Ocel *et al.* [117]).

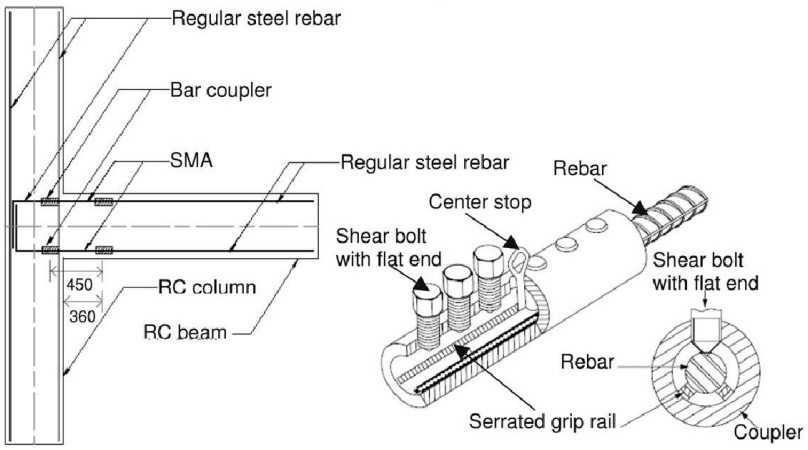

Figure 2.23: Reinforcement details of beam-column element with coupler (dimensions in mm) (adapted from Alam *et al.* [5]).

The first time SMAs were used in the field of cultural-heritage structural engineering was on the Basilica of St. Francis in Assisi, shown in Figure 2.24(a). A series of five earthquakes, occurred in September of 1997, had inflicted severe damage to the basilica and it became necessary to implement a retrofit program that would

prevent future damage to this historic building. The most common solution traditionally used to enhance the seismic resistance of cultural heritage structures is the introduction of localized reinforcements, usually steel ties, increasing structural stability and ductility [77], but often too invasive. The EU's Fourth Framework Program for Research & Technical Development funded a project that enabled the development of an innovative technique based in custom-made shape-memory alloy devices (SMAD). These devices were used to connect the tympanum wall to the roof structure, as shown in Figures 2.24(b), (c) and (d).

(a) General view.

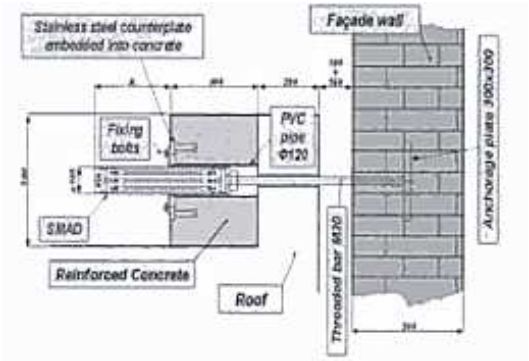

(b) Anchorage detail of SMAD.

(c) SMAD application.

(d) SMADs arrangement.

Figure 2.24: Basilica of St. Francis of Assisi in Italy (adapted from [43, 108]).

Another successful intervention with SMADs on walls subjected to horizontal seismic forces was in the S. Feliciano Cathedral façade, in Foligno, as an effective connection between orthogonal walls was needed. In fact, a typical collapse mechanism in masonry buildings is the out-of-plane collapse of peripheral walls due to inertia forces generated by an earthquake acting orthogonally to the walls [35]. Figure 2.25 depicts some aspects of the intervention.

(a) General view.

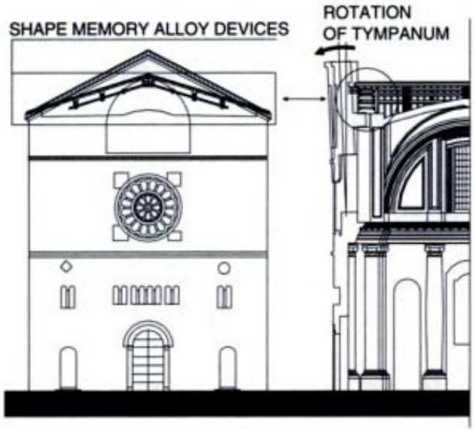

(b) SMADs arrangement.

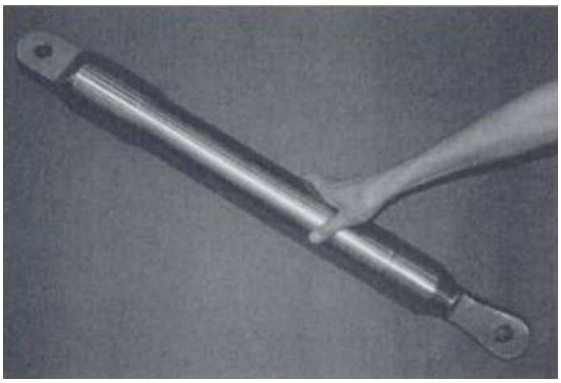

(c) SMAD (F = 27 kN, $\Delta u = \pm 20$ mm).

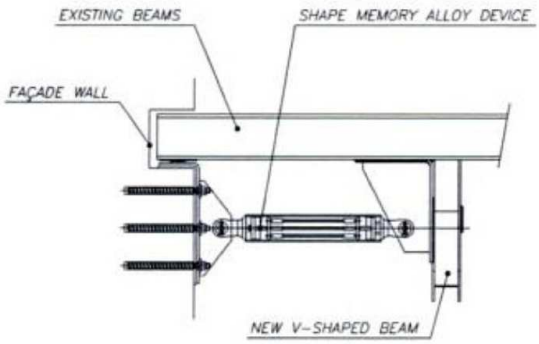

(d) Anchorage detail of SMAD.

Figure 2.25: St. Feliciano Cathedral in Italy (adapted from [35, 108]).

Experimental tests have demonstrated that the seismic protection of monuments with SMAD yields structures with higher earthquake resistance than structures reinforced with traditional steel bars [43]. SMADs were considered a powerful alternative to the traditional rehabilitation methods, providing acceleration reduction, force limitation and energy dissipation [77].

The rehabilitation of the S. Giorgio Church Bell-Tower, in Trignano, was completed in September 1999; see Figure 2.26(a). This masonry building suffered considerable damage due to the earthquake of October 15th, 1996, which struck the Reggio Emilia and Modena Districts in Italy (4.8 Richter magnitude). To increase the flexural resistance of the tower, four vertical pre-stressing steel tie bars with four post-tensioned SMAD connected in series were anchored at the roof and foundation in the internal corners of the structure [77]. Each SMA device included 60 SE wires

with 1 mm in diameter and 300 mm in length; see Figure 2.26(b).

(a) General view. (b) SMAD application.

Figure 2.26: S. Giorgio Church Bell-Tower in Italy (adapted from [77]).

The good performance of the innovative rehabilitation scheme was confirmed after the tower was, once again, submitted to another 4.5 Richter magnitude earthquake with no damage, in June 18th, 2000 [77].

Soroushian *et al.* [152] engaged in an innovative rehabilitation program using iron-based SMA bars for the retrofit of deficient bridge girders. The practical demonstration of this repairing approach was applied in a bridge in Michigan, shown in Figure 2.27(a), which was lacking in shear strength and suffered some cracks initiating in the T-beams and extending into the deck [152]; see Figure 2.27(b). Martensite SMA bars were pre-elongated and anchored to the deficient structural element, as displayed in the design detail presented in Figure 2.27(c). Upon electrical resistance heating and transforming to austenite, the constraint shape recovery caused transfer of corrective forces to the structure [152]; see Figure 2.27(d).

This repair approach was previously tested in an experimental setup comprising a RC beam with shear deficiency. The beam presented several shear cracks, which appeared during the load introduction. The RC beam was subsequently repaired through post-tensioning with SMA rods and tested to failure. The results showed that the initial ductility and load-carrying capacity of the rehabilitated beam were almost fully regained [152]. Regarding the bridge retrofit, the local post-tensioning of the cracked region with SMA rods successfully reduced the average crack width by about 40%.

(a) General view (variable depth T-beam bridge).

(b) Shear cracks on beam stem.

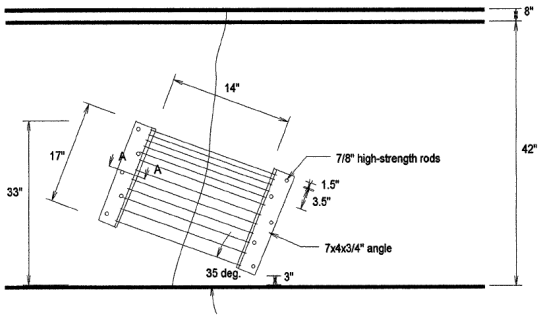

(c) Configuration of the Shape-Memory rods.

(d) Electrical resitance heating of SM rods.

Figure 2.27: Bridge carrying Sherman Road over US-31, Michigan, USA (adapted from [84, 123]).

2.5 Constraints of using shape-memory alloys

One of the major constraints regarding the use of SMAs in the civil engineering industry is associated with their high price, in comparison to conventional construction materials [4]. Even though the use SMAs in structural applications has been shown effective and feasible [32], the substantial amount of material required by these type of applications still constitutes an important restrainer to a wider implementation of SMAs. Over the last decade, however, a significant reduction in the price of Nitinol has occurred (below €150/kg), as well as the development of alternative low-cost iron based SMAs. Another difficulty regarding the application of Nitinol is the machining of large diameter bars using conventional equipment, due to its hardness [4]. The lack of effective knowledge transfer across materials

science and structural engineering has also contributed to hinder the widespread use of Nitinol in civil engineering structures [**?**].

2.6 Closure

A description of the martensitic transformation in SMAs provides insight into the superelasticity and shape-memory effect properties. In SMAs, this solid-solid diffusionless phase transformation changes the material from the parent phase, a high-temperature phase called austenite to a low-temperature phase called martensite. The shape-memory effect allows the material, after been deformed, to recover its original geometry during heating. Superelasticity enables the material to withstand large cyclic deformations, without residual strains, while developing a hysteretic loop. The formation of this hysteretic loop translates into the ability of the material to dissipate energy. This dissipative response of the material, when subjected to a cyclic deformation, is usually called internal friction.

Based on the SE effect, several technological applications have been built for passive energy dissipation, in vibration control devices. A review of the current state-of-the-art, regarding these applications, demonstrates the potential shown by shape-memory alloys in seismic hazard mitigation. Several vibration control devices are analyzed, including bracing systems, base isolation systems, bridge hinge restrainers and structural connections.

Some built applications making use of SMAs are presented, mainly used to enhance the seismic resistance of cultural heritage structures. An innovative rehabilitation program using iron-based SMA bars for the retrofit of shear deficient bridge girders is also presented. The constraints of using SMAs in the civil engineering industry are analyzed.

Chapter 3

NiTi Shape-Memory Alloys

3.1 Introduction

Shape-Memory Alloys in practical use are almost limited to three types: NiTi alloys, Cu-based alloys and Ferrous alloys. For applications regarding the use of SMAs in dampers, under the direct action of external weather (i.e., wet weather, direct rain), NiTi shows an excellent corrosion behavior, in comparison with the moisture sensitive Cu-based alloys [12]. Nitinol also shows good fatigue properties, high corrosion resistance, similar to stainless steel, and ductility [177]. For this reason, Nitinol is used in most of the SE based technological applications, and is given particular emphasis in this work. The main objective of the next sections is to outline the thermomechanical behavior of Nitinol, both on microscopic and macroscopic levels, stressing out the properties which are of particular interest for civil engineering and seismic applications.

Reference values for some important mechanical properties, regarding applications in civil engineering, are presented in Table 3.1, where a comparison between structural steel and Nitinol in its martensitic and austenitic phases is made. One can see that structural steel is much stiffer than Nitinol and that the martensitic yield strength of Nitinol is lower than its austenitic counterpart. The most important characteristic of Nitinol is its outstanding ability to recover from strains up to about 8%, without residual deformations, while describing a mechanical hysteresis. This provides the material with unique energy dissipation and re-centering capabilities.

Property	Structural Steel	Martensitic NiTi	Austenitic NiTi
Density (g/cm^3)	7.85	6.45	6.45
Elastic Modulus (GPa)	200	$21 - 41$	$30 - 83$
Poisson's Ratio	$0.27 - 0.30$	0.33	0.33
Yield Strength (MPa)	$248 - 517$	$70 - 140$	$195 - 690$
Ultimate Tensile Strength (MPa)	$448 - 827$	$895 - 1900$	$895 - 1900$
Elongation at Failure (%)	20	$5 - 50$	$5 - 50$
Recoverable Elongation (%)	0.20	up to 8	up to 8

Table 3.1: Properties of structural steel and Nitinol (reference values from [102]).

Other mechanical properties, like the ultimate tensile strength and elongation at failure, show favorable values when compared with steel.

3.2 Characterization of Nitinol

3.2.1 Microstructure

In Nitinol, the shape-memory effect and the superelasticity occur associated with the transformation between two different crystalline structures, with identical chemical composition, called austenite and martensite.

The classification of a given crystal is based on the identification of all its inherent symmetry. The lattice systems are a grouping of crystal structures according to the axial system used to describe their lattice. Each lattice system consists of a set of three axes in a particular geometrical arrangement. By connecting the lattice points, the space is divided into parallelepipeds, the unit cells. The size and shape of a unit cell is specified by means of the lengths a, b and c of the three independent edges, known as the lattice parameters, and the angles α, β and γ between these edges. In Nitinol, each Ni atom has eight next neighboring Ti atoms, and vice versa. The position of Ni and Ti atoms in the unit cell is maintained over considerable distances. The general opinion is that this is an important condition for alloys to show the shape-memory effect. The austenitic high-temperature phase is a body centered cubic (bcc) lattice, which has a so called B2 structure, with $a = 0.3015$ nm [136, 167], as shown in Figure 3.1. The martensitic low-temperature phase has a so called monoclinic B19' structure, with lattice parameters $a = 0.2889$ nm,

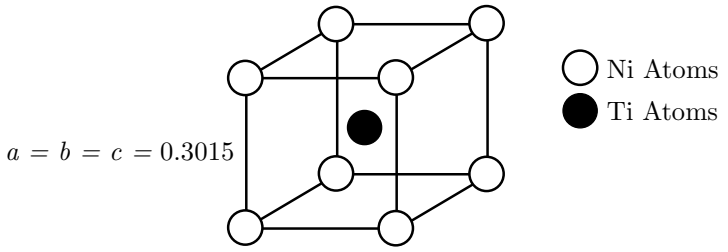

Figure 3.1: Austenite unit cell with B2 structure (adapted from[167]).

$b = 0.4210$ nm, $c = 0.4622$ nm and $\beta = 96.8°$ [74]. Most often, this transformation is associated with the two-step transformation from the B2 to a trigonal phase (so called R-phase) and then to the B19' phase [124]. Refer to Figure 3.2 for a schematic view of the B2 $\rightarrow$ B19' transformation. Nitinol greatly depends on its

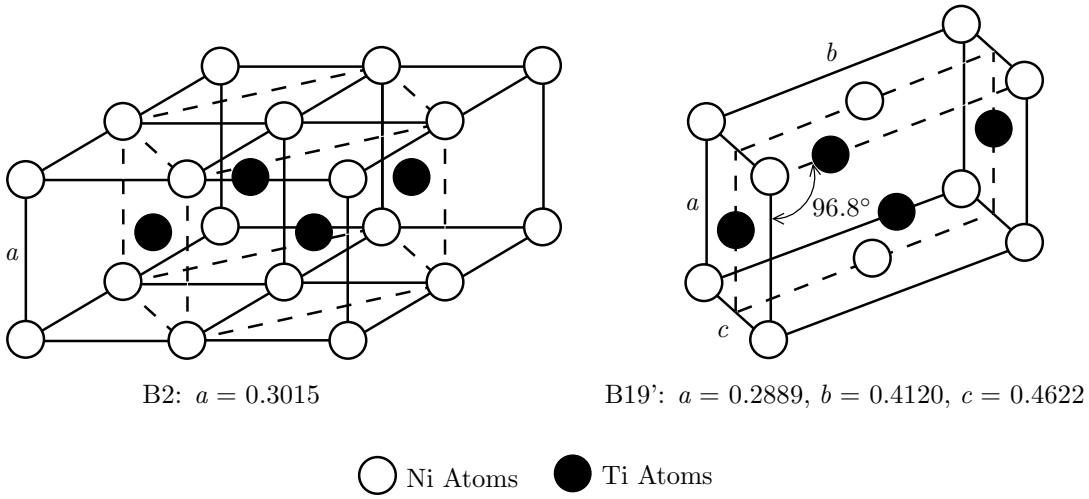

Figure 3.2: Schematic view of the B2 $\rightarrow$ B19' transformation (adapted from[167]).

exact compositional make-up, processing history, and small ternary additions, being extremely sensitive to the precise Titanium/Nickel ratio [175]. Alloys with 49.0 to 50.7 at.% Ti are generally commercially common, with SE alloys in the range of 49.0 to 49.4 at.% Ti and shape-memory alloys in the range of 49.7 to 50.7 at% Ti. Ductility drops rapidly as Ni is increased [55], at the same time increasing the yield strength of the austenitic phase and depressing the transformation temperatures [60].

3.2.2 Tensile properties

While some other commercial forms are also available, namely as tubing, strip and sheet, Nitinol is most commonly used in form of wire or bar. In order to characterize the tensile behavior of Nitinol in its wire form, experimental, strain-driven, uniaxial tensile tests are performed on two Nitinol wire specimens. A Zwick/Roell Z050 testing machine is used to test a Nitinol SE508 wire, provided by *Euroflex GmbH*, with a strain-rate of $0.067\%/s$. A Shimadzu Autograph testing machine is used to test a Nitinol S wire, provided by *Memory Metalle-GmbH* with a strain-rate of $0.020\%/s$. In Figure 3.3, is shown the SE wire placed in the gripping apparatus of the testing machine. Both Nitinol wires have the same chemical composition, 49

Figure 3.3: Zwick/Roell Z050 testing machine. Gripping apparatus for tensile test.

at.% Ni-51 at.% Ti and a circular cross section of 2.40 mm diameter. The samples were tested as-received. The maximum strain of the tensile tests is 6.0% and the tests are conducted at an ambient temperature of 24°C. The stress-strain diagrams obtained for the tensile tests are plotted in Figure 3.4.

As it can be seen, two different hysteretic cycles are obtained. Since the chemical composition of the alloys is the same, these differences may derive from the processing history of each wire, and of small ternary additions. As it will be shown later, the strain-rate of the tensile testing may also have a major influence on the shape

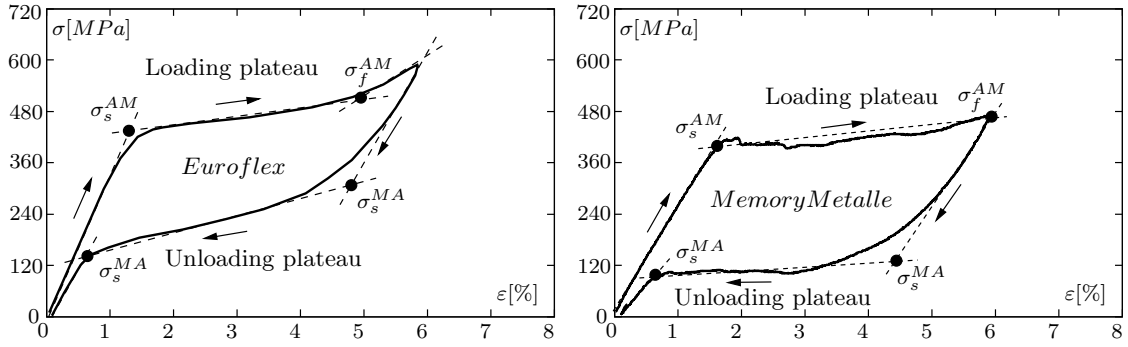

(a) Nitinol SE 508 wire, provided by *Euroflex GmbH* (b) Nitinol S wire, provided by *Memory Metalle-GmbH*

Figure 3.4: Stress-strain response of Nitinol wires during uniaxial tensile tests.

and size of the SE hysteresis. In polycrystalline Nitinol, the free-recoverable strain can reach about 8%, but is limited to 6% if complete recovery is expected [55].

The usual shape of a SE hysteretic cycle is characterized by two regions of almost constant stress. The loading plateau, during the forward transformation, which is delimited by σ_s^{AM} and σ_f^{AM} and the unloading plateau, delimited by σ_s^{MA} and σ_f^{MA}, during the inverse transformation. Once identified the limiting stresses for the SE plateaus, one can say that the loading plateau of the Nitinol wires ranges from 400 to 600 MPa, and the unloading plateau from 120 to 140 MPa. These values are consistent with the values reported in the literature [55], ranging from 190 to 700 MPa, for the loading plateau, and from 70 to 250 MPa, for the unloading plateau. The austenitic modulus of elasticity (E_A) is approximately 35 and 22.5 GPa, for the SE508 and the S wires, respectively. As for the lower martensitic modulus of elasticity (E_M), the tests yield approximate values of 20 and 19 GPa. A reference value for the Poisson's coefficient (ν) is 0.33 [55]. The ultimate tensile strength (σ_u) and elongation at failure of the SE508 wire are also investigated, resulting in the stress-strain diagram presented in Figure 3.5. The ultimate tensile strength (σ_u) of the of the SE508 Nitinol wire yields $\simeq$ 1400 MPa, with an elongation at failure of 22%. According to the literature [55], in a fully annealed[1] Nitinol specimen, the ultimate tensile strength is $\simeq$ 900 MPa and the elongation at failure about 25 to

[1]Annealing, in metallurgy and materials science, is a heat treatment wherein a material is altered, causing changes in its properties such as strength and hardness. These changes are produced by heating above the re-crystallization temperature and maintaining a suitable temperature, and then cooling. Annealing is used to induce ductility, soften the material, relieve internal stresses, refine the structure by making it homogeneous, and improve cold working properties [45].

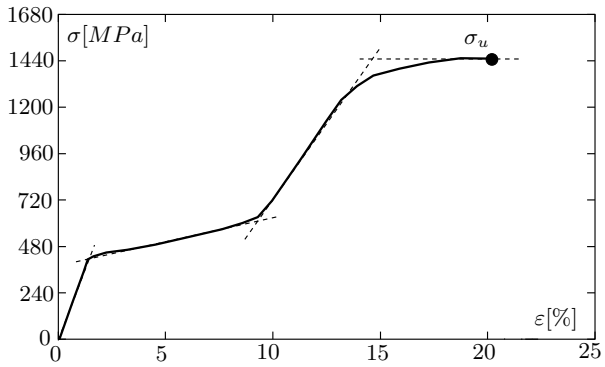

Figure 3.5: Stress-strain response during ultimate strength test.

50%. If the material is strain hardened[2], the ultimate tensile strength may reach up to 1900 MPa and the elongation at failure reduces to 5 to 10%.

3.2.3 Transformation temperatures

To characterize the transformation temperatures in an alloy, one of the most used methods is the Differential Scanning Calorimetry (DSC) [36, 141, **?**]. DSC is a thermoanalytical technique in which the difference in the amount of heat required to increase the temperature of a sample and reference are measured as a function of temperature [138]. Both the sample and reference are maintained at nearly the same temperature throughout the experiment. Generally, the temperature program for a DSC analysis is designed such that the sample holder temperature increases linearly as a function of time. The reference sample should have a well-defined heat capacity over the range of temperatures to be scanned. The basic principle underlying this technique is that, when the sample undergoes a physical transformation such as phase transitions, more (or less) heat will need to flow to it than the reference, to maintain both at the same temperature. Whether more or less heat must flow to the sample depends on whether the process is exothermic, as the forward martensitic transformation, or endothermic, as the inverse martensitic transformation. Care must be taken because the presence of an eventual R-phase prior to thermal cycling,

[2]Strain hardening is the strengthening of a material by plastic deformation, increasing the material's dislocation density. As the material becomes increasingly saturated with new dislocations, more dislocations are prevented from nucleating, developing a resistance to dislocation-formation. This resistance to the formation of new dislocations manifests itself as a resistance to plastic deformation with the consequent strengthening [45].

and/or residual stresses from sample cutting, tend to complicate the curves and to introduce spurious peaks [55, 138].

Other physical properties like the electrical resistivity, elastic modulus, yield strength and strain of the alloy, also change significantly at the transformation temperatures. The electrical resistivities of the austenite and martensite phases are 84 $\times 10^{-6}\Omega$cm and 96 $\times 10^{-6}\Omega$cm, respectively [57]. Tracking these discontinuities also enables the characterization of the transformation temperatures of a given alloy.

In Figure 3.6, a schematic illustration of a DSC diagram is shown, together with a generic plot resulting from a strain variation test, during heating and cooling, under constant stress. Transformation temperatures of Nitinol strongly depend on

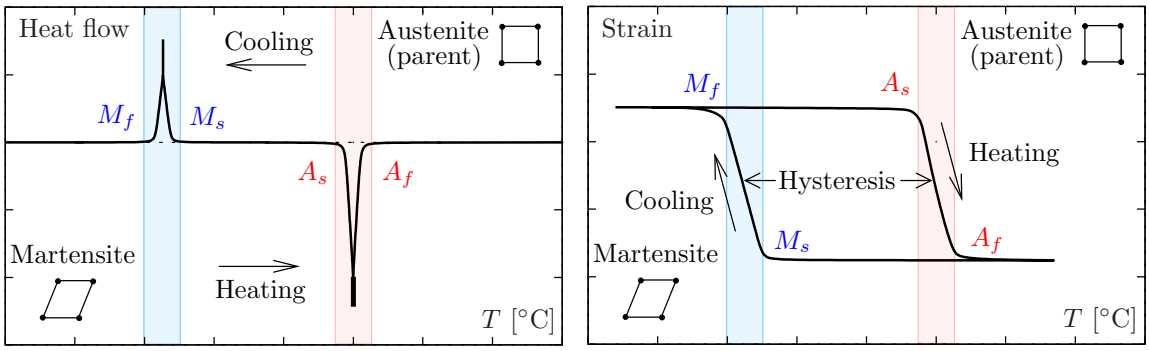

Figure 3.6: Schematic illustration of a DSC. Variation in strain during heating and cooling under constant stress.

its composition. Typical hysteresis widths for a binary alloy range from about 40 to 60°C; see Figure 3.6.

In order to characterize the transformation temperatures of a Nitinol wire specimen, a DSC test is performed in a SETARAM-DSC92 thermal analyzer. A general view of the thermal analyzer is shown in Figure 3.7. The sample is extracted from a Nitinol SE 508 wire, with a 2.40 mm diameter circular cross section. The chemical composition of the Nitinol sample is 49 at.% Ni-51 at.% Ti. The sample is tested as-received, and the temperature program comprises a thermal cycle where the sample is heated up to 80°C, held at this temperature for 6 min, and then cooled to -80°C, with heating and cooling rates of 7.5°C/min. Prior to the DSC experiment, the sample is submitted to a chemical etching (10 vol.% HF + 45 vol.% HNO_3 + 45 vol.% H_2O) in order to remove the oxide and the layer formed by the cutting

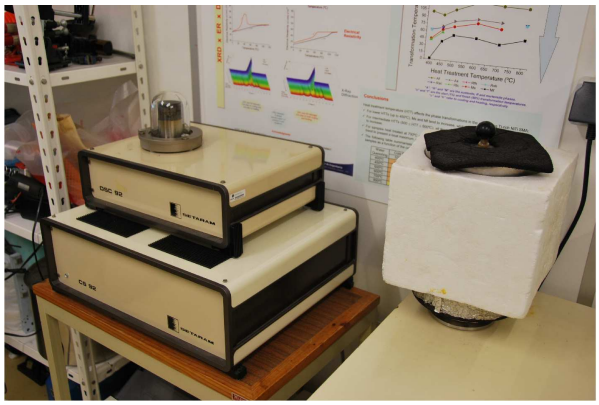

Figure 3.7: SETARAM-DSC92 thermal analyzer. General view.

operation. A baseline analysis of the resulting curves easily allows to identify the four transformation temperatures of the alloy, which are: M_f = -45°C, M_s = -35°C, A_s = -15°C and A_f = -5°C.

3.2.4 Clausius-Clapeyron coefficient

The most straightforward experimental procedure to compute the Clausius-Clapeyron coefficient (CCC) of a previously stabilized SMA specimen is to determine its critical transformation stresses for a set of different ambient temperatures. An experimental procedure based on this testing principle is implemented, using a temperature increment of 3°C. The experiment is conducted with a Zwick temperature controlled chamber, W91255, using a 2.40 mm diameter circular cross section Nitinol SE 508 wire specimen. The wire is subjected to a series of sequential loading-unloading cycles using a Zwick/Roell Z050 testing machine, up to a maximum strain of $\simeq 7.5\%$ and with a strain-rate of $0.068\%/s$. Two views of the temperature controlled chamber are presented in Figure 3.8. Figure 3.8(a) depicts the tensile testing apparatus inside the temperature controlled chamber, prior to the experimental procedure. In Figure 3.8(b) one can see the thermal chamber during the temperature controlled tensile testing.

The tests range from an ambient temperature of 30°C to an ambient temperature of 75°C. At the end of each cycle, the temperature within the thermal chamber is increased by 3°C while the wire's temperature is constantly monitored. The temperature in the wire is measured with a thermocouple, placed at its mid-section.

(a) Opened temperature chamber. (b) Closed temperature chamber.

Figure 3.8: Temperature controled chamber during the tensile tests. General views.

After the chamber's temperature is increased, and the thermal stabilization of the Nitinol wire specimen is complete, a new loading-unloading cycle begins. The stress-strain diagrams obtained from these experimental, temperature controlled, cyclic tensile tests, are displayed in Figure 3.9.

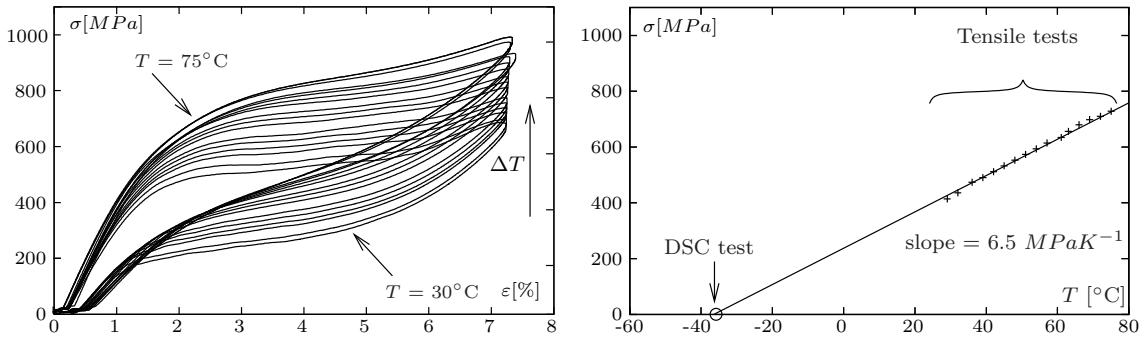

(a) Progressive stress induced transformation cycles (b) Stress-temperature diagram

Figure 3.9: Temperature dependence of the stress induced martensitic transformation in a NiTi wire.

Observing the graph on Figure 3.9(a), it is clear that the SE hysteresis shifts upwards as ambient temperature rises. The Clausius-Clapeyron coefficient represents the slope ($d\sigma/dT$) of the lines defining the boundaries of the SMA transformation strips. To evaluate the variation of stress with temperature it is easier to use, as

reference, the loading stress plateau, rather than a specific point on the hysteresis. Particular hysteretic points, like the one associated with the beginning of the forward transformation, for instance, may be quite difficult to identify. The average variation of the loading stress plateau, for the prescribed temperature increment (3°C), yields approximately 19.5 MPa. This leads to a Clausius-Clapeyron coefficient of 6.5 MPaK^{-1}. Once determined the CCC, one can use it together with the M_s value obtained during the DSC experiment (-35°C), to plot the linear relation between temperature and the stress associated with the beginning of the forward transformation; see Figure 3.9(b).

3.2.5 Influence of ambient temperature on damping

In this section one addresses the influence of ambient temperature on damping, in strain-controlled conditions. The SE hysteresis exhibited by Nitinol wires during mechanical cycling, shows a clear dependence regarding ambient temperature. As ambient temperature rises, the stress associated with the beginning of the forward transformation also increases, as the whole hysteretic loop shifts upwards; see Figure 3.9(a). The stress-temperature phase diagram path associated with a variation in the ambient temperature, together with the variation in the corresponding isothermal hysteresis, is represented in Figure 3.10. As the original cycle is performed with

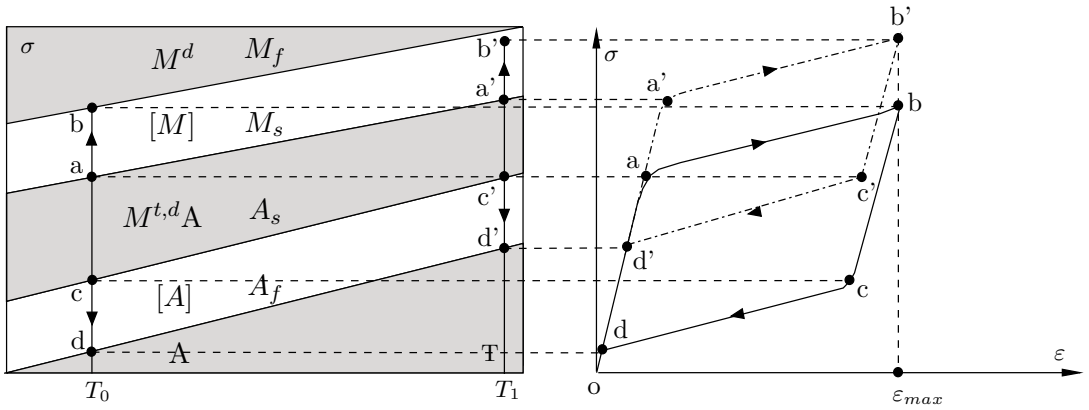

Figure 3.10: Variation of ambient temperature. Phase diagram path and correspondent isothermal hysteresis.

a constant temperature, the forward transformation path, between points (a) and (b), and the inverse transformation path, between points (c) and (d), lie over the

same vertical line, associated with $T = T_0$. When the ambient temperature rises from T_0 to T_1 the transformation path moves right, in the phase diagram, to the vertical line associated with $T = T_1$, as the process continues to be isothermic. The forward transformation begins in point (a'), which is associated with a higher stress level than point (a). This stress variation is directly proportional to the CCC value, which, in Nitinol, is about 6.5 MPaK^{-1}, as previously determined. An annual variation of 20°C, on the average ambient temperature, yields a variation on the stress to induce the martensitic transformation of about 130 MPa. This may compromise the behavior of a vibration mitigation device based on SE SMAs, as the transformation may cease to exist. For instance, in the presented example, a stress level associated with point (b), that when $T = T_0$ brings about the full range of the martensitic transformation in the SMA wire, is insufficient to even induce that transformation when $T = T_1$.

In a CuAlBe alloy, a Cu-based alloy which begins to appear in some technological applications related to damping, the CCC value is 2.2±0.4 MPaK^{-1} [78]. This means that the transformation stresses in Nitinol will change by a factor of three when compared with the changes exhibited by CuAlBe alloys, for the same temperature variation. For these reasons, an adequate temperature isolation system, that would limit the temperature variation of the SE kernel during the year, would highly benefit a vibration mitigation device based on SE SMAs. In the case of Nitinol, this seems to be particularly important, as it has a high CCC value.

Another important difference between the two hysteresis shown on Figure 3.10 is that for the higher temperature case T_1, the transformation is not complete. One can see in the stress-temperature phase diagram that, in the forward transformation path, point (b') does not reach the finishing boundary of the corresponding transformation strip (M_f). Since the total strain of the transformation is a constant of the material, and, as temperature rises, higher strains are needed to induce the transformation, if the maximum strain is limited, the hysteresis loop becomes necessarily truncated.

The results on Figure 3.9(a), illustrate the response shown by a vibration mitigation system based on SE Nitinol, calibrated for a given displacement amplitude and temperature, when subjected to an ambient temperature variation. Between A_f and M_d, as temperature rises, the dissipated energy, E_D, decreases while the maximum strain energy, E_{s0}, increases. Consequently, as temperature rises, the equivalent viscous damping (ζ_{eq}) of the aforementioned system has to decrease. On Figure 3.11

are represented the values calculated for ζ_{eq}, function of the tested ambient temperatures. One can see that an increase on the ambient temperature causes the

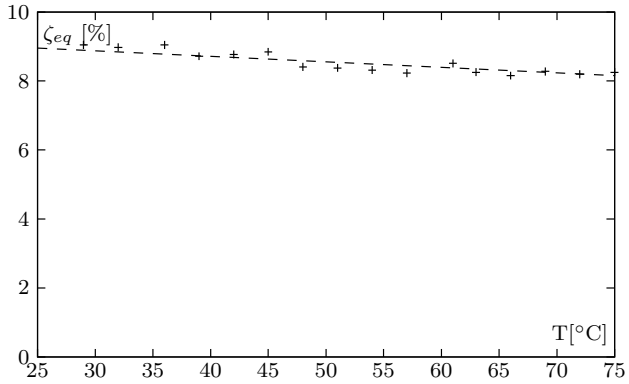

Figure 3.11: Influence of ambient temperature on damping.

system's equivalent viscous damping to decrease in a proportional way. Nevertheless, an annual variation of 20°C, on the average ambient temperature, only yields a variation of ζ_{eq} of approximately 1%, which is relatively small. To conclude this section, one might say that even though ambient temperature does influence the damping capacity of a SE Nitinol based vibration mitigation system, this influence in only marginal.

3.2.6 Internal loops

The mechanical cycling of a SE specimen produces a hysteretic effect due to a solid-solid phase transformation called martensitic transformation. During the forward transformation, the martensite fraction increases with strain, as austenite is progressively transformed into martensite. When the forward transformation is complete, austenite is fully transformed into martensite. Conversely, during the inverse transformation, the martensite fraction decreases with strain, as martensite is progressively re-transformed into austenite. When the inverse transformation is complete, martensite is fully re-transformed into austenite.

The objective of this section is to evaluate the behavior of a SE Nitinol sample subjected to internal loops, i.e. to cycling situations where the full extent of the forward and inverse transformations are not attained.

A commercial SE Nitinol alloy S wire is tested, with a 2.40 mm diameter circular cross section. Tests are conducted at room temperature (T≃22°C) with a strain-rate of $\dot{\varepsilon} = 0.02\%/s$, which is consistent with quasi-static conditions. Two different tests are performed in the wire, the first comprising three complete cycles of decreasing amplitude, with maximum strains of 6.3, 4.2 and 2.1%, respectively. The second test consists of a complete cycle, with a maximum strain of 6.3%, followed by two smaller inner cycles, with maximum strains of 5.8%; see Figure 3.12.

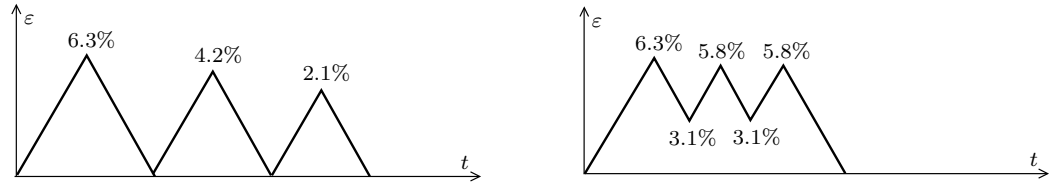

(a) Three complete cycles of decreasing amplitude. (b) Complete cycle followed by two smaller inner cycles.

Figure 3.12: Strain time-histories for internal loop testing in a SE Nitinol wire sample.

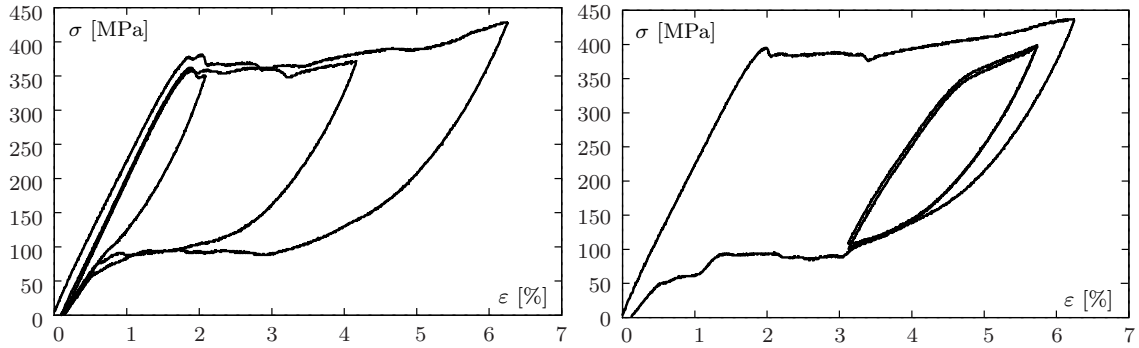

(a) Three complete cycles of decreasing amplitude. (b) Complete cycle followed by two smaller inner cycles.

Figure 3.13: Stress-strain diagrams ($\dot{\varepsilon} = 0.02\%/s$).

When an unidirectional stress is applied to an austenitic SE specimen, an elastic distortion of the austenitic lattice starts to occur. The transformation from austenite to stress induced martensite takes place above a critical stress value and, as deformation proceeds, stress remains almost constant. During this part of the response the two phases coexist. Unloading, if the material is fully transformed, will cause an elastic response of the detwinned martensite. If the forward transformation is not complete, the elastic unloading of the material will account for the coexistence of the two crystallographic phases, and corresponding martensite fraction.

Analyzing Figure 3.13(a) it can be seen that, as the extent of the forward transformation decreases, the modulus of elasticity associated with the elastic response during unloading increases. According to this plot, as the extent of the forward transformation decreases, the response shown by the material during unloading is closer to the response exhibited by a pure austenitic specimen than the one exhibited by a fully detwinned martensitic specimen.

Since martensite becomes unstable below a critical stress, an inverse transformation occurs as the unloading process continues and detwinned martensite reverts back to austenite. When the material is fully transformed to the parent phase, further unloading will follow the initial loading path, with total recovery of the deformation. If, however, an unidirectional stress is once again applied to the material, before a complete inverse transformation, the elastic response during loading will also account for the coexistence of the two crystallographic phases.

Looking at Figure 3.13(b) one can see that when an unidirectional stress is applied to the material, before the inverse transformation is complete ($\simeq$3.0% strain), the modulus of elasticity associated with the elastic response during loading is between the austenitic and the martensitic one.

The SE tangent elastic modulus associated with a given hysteretic point is usually computed through a rule of mixtures using both the austenitic and martensitic elastic modulus.

3.2.7 Influence of strain-amplitude on damping

In this section, the influence of strain-amplitude on damping is addressed. The stress-temperature phase diagram path associated with a variation in the strain-amplitude, together with the variation in the corresponding isothermal hysteresis, is represented in Figure 3.14.

As both cycles are performed with constant temperature, all the corresponding paths within the phase diagram lie over the same vertical line, $T = T_0$. The outer, wider loop is associated with the full extent of the forward and inverse transformations, corresponding, in the phase diagram, to lines (a-b) and (c-d), respectively. The inner, smaller loop is associated with half the transformation length, for both the forward and inverse transformations. Upon unloading, after reaching points (b) and

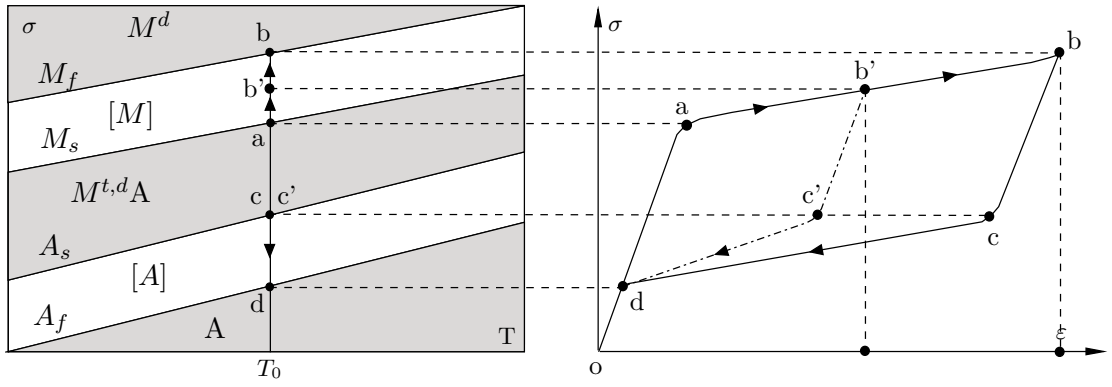

Figure 3.14: Variation of strain-amplitude. Phase diagram path and correspondent isothermal hysteresis.

(b'), the elastic response of the material is similar because the elastic modulus of austenite and martensite are considered to be the same, for the sake of simplicity. Points (c) and (c') correspond to the critical stress that enables the beginning of the inverse transformation, which only depends on the temperature of the material (T_0). Hence, although differing in terms of strain-amplitude, points (c) and (c') are located in the same position on the phase diagram. Point (d) represents the end of the inverse transformation, for both the outer and inner cycles.

In order to assess the influence of strain-amplitude on the damping capacity of the SE wire, the values of ζ_{eq} are calculated, for the whole range of the martensitic transformation. As it can be seen on Figure 3.15, after the beginning of the martensitic transformation in the SE wire ζ_{eq} increases rapidly with strain. As the strain-amplitude further increases the equivalent viscous damping of the wire continues to increase linearly, until the full extent of the transformation is reached.

Further tensile tests are performed, using a SE Nitinol SE 508 wire specimen, with a 2.40 mm diameter circular cross section. These tests comprise seven complete cycles of increasing amplitude, with maximum strains ranging up to 8.0%. They are also conducted at room temperature (T±22°C) with a strain-rate of $\dot{\varepsilon} = 0.067\%/s$. The results obtained from these additional tensile tests are also presented on Figure 3.15 and show coherent results with the first tests.

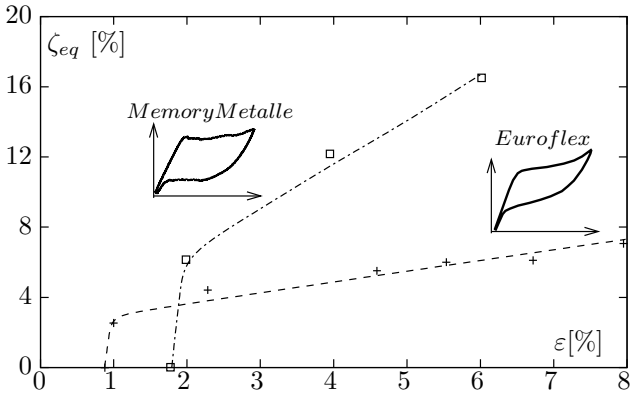

Figure 3.15: Influence of strain-amplitude on damping.

3.2.8 Self-heating on mechanical cycling

When a fluid/solid body is at a different temperature than its surroundings, transfer of thermal energy, also known as heat transfer, or heat exchange, occurs in such a way that the body and the surroundings reach a thermal equilibrium. Heat transfer always occurs from a higher-temperature object to a cooler temperature one. Energy transfer by heat can occur between objects by radiation, conduction and convection. Convection is usually the dominant form of heat transfer in liquids and gases. This is a term used to characterize the combined effects of conduction and fluid flow. Two types of convection are commonly distinguished: free convection, in which gravity and buoyancy forces drive the fluid movement, and forced convection, where a fan, stirrer, or other means are used to move the fluid. In natural convection, fluid surrounding a heat source receives heat, becomes less dense and rises. The surrounding, cooler fluid then moves to replace it. This cooler fluid is then heated and the process continues, forming a convection current. The driving force for natural convection is buoyancy, a result of differences in fluid density [76].

During the cyclic deformation of a SMA specimen, self-heating depends on the balance between the total generated energy (enthalpy of transformation and internal friction) and the dissipated energy by heat transfer.

To illustrate how the strain-rate of the dynamic loading may influence the temperature variation of a SE specimen during a cyclic test, as well as the shape of its corresponding hysteretic loop, a series of experimental tensile tests are conducted. These experimental tests comprise four different strain-rates, 0.008, 0.067, 0.250

and 0.333%/s. They are performed at room temperature ($\simeq$ 20°C), on the same Nitinol SE 508 wire specimen, with a 2.40 mm diameter circular cross section. The temperature of the SE wire is continuously monitored, with a T type thermocouple (Copper-Constantan), with a temperature reading range of -40°C to 100°C, during the whole loading-unloading process. The thermocouple is placed at the mid-section of the wire, as shown in Figure 3.16. The thermocouple is connected to a National

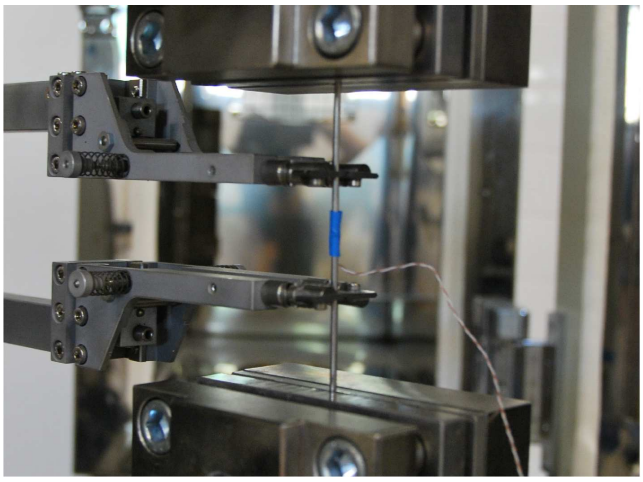

Figure 3.16: Detail of the thermocouple placed in the SE wire.

Instruments (NI) SCXI-1112 8-Channel Thermocouple Input Module. A Virtual Instrument (VI) is created, using the LabView 9.1 framework and the NI-DAQmx Software to monitor the temperature. The results obtained during this experimental procedure, regarding temperature time-histories and corresponding stress-strain diagrams are represented in Figure 3.17, for all tested strain-rates. According to these results, when passing from quasi-static conditions to dynamic ones, important changes do occur in the temperature time-history of the SE wire. Changes are also present in the shape of the corresponding hysteretic loops. For $\dot{\varepsilon} = 0.008\%/s$, the temperature variation during the whole procedure is almost negligible, only amounting to approximately 2°C. At the end of the tensile test, the wire's temperature equals the ambient temperature. As the strain-rate increases to 0.067%/s, important changes occur in the wire's temperature during the tensile test. Starting with a temperature of 20°C, the wire's temperature rapidly rises to 35°C during loading. During unloading, it decreases below ambient temperature, reaching 15°C at the end of the mechanical cycle. Regarding the shape of the hysteresis, one notices that both the loading and unloading plateaus become steeper than in the

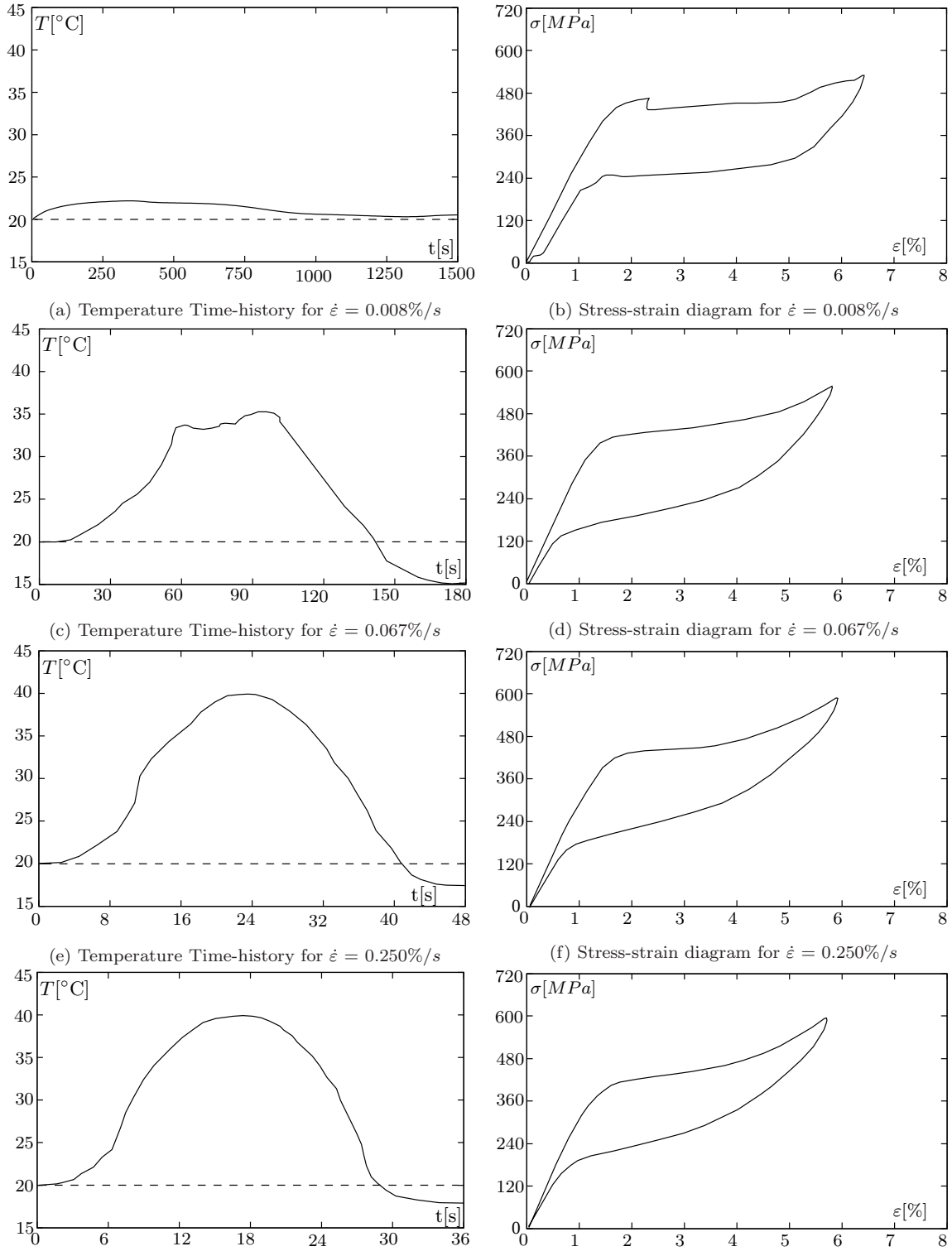

(a) Temperature Time-history for $\dot{\varepsilon} = 0.008\%/s$

(b) Stress-strain diagram for $\dot{\varepsilon} = 0.008\%/s$

(c) Temperature Time-history for $\dot{\varepsilon} = 0.067\%/s$

(d) Stress-strain diagram for $\dot{\varepsilon} = 0.067\%/s$

(e) Temperature Time-history for $\dot{\varepsilon} = 0.250\%/s$

(f) Stress-strain diagram for $\dot{\varepsilon} = 0.250\%/s$

(g) Temperature Time-history for $\dot{\varepsilon} = 0.333\%/s$

(h) Stress-strain diagram for $\dot{\varepsilon} = 0.333\%/s$

Figure 3.17: Self heating on mechanical cycling for different strain-rates ($T_0 = 20°C$). Temperature time-histories and stress-strain diagrams.

quasi-static situation, as the maximum stress level rises. When the strain-rate further increases to 0.25%/s the same general temperature variation trend is observed during the test. The maximum wire's temperature at the end of the loading process, 40°C being, nevertheless slightly higher. At the end of the unloading process, the wire's temperature is 17°C. The maximum stress level of the hysteresis continues to rise, as the loading and unloading plateaus continue to grow steeper. When using a strain-rate of 0.333%/s, which corresponds to the maximum loading rate of the testing machine, the wire's response during loading, is approximately the same as in the previous test, reaching the same maximum temperature of 40°C. During unloading, however, the temperature at the end of the test continues to rise, to about 19°C.

3.2.9 Influence of strain-rate on damping

The rate of the dynamic loading influences the temperature variation of a SE specimen during a dynamic loading [56]. For quasi-static loading conditions, the heat exchanges between the material and its surrounding environment generates almost isothermic processes. When the rate of the dynamic loading increases, the total amount of generated energy per unit time increases accordingly. As the dissipation capacity of the thermomechanical system is limited by the heat convection mechanism, for fast dynamic cycling, the generated and the dissipated energy become unbalanced, causing the specimen's temperature to change as well as the shape of the hysteretic loop. As the rate of the dynamic loading increases, the system behavior becomes closer to adiabatic [169].

The simplified stress-temperature phase diagram path associated with a temperature variation during mechanical cycling, together with the changes occurring in the corresponding hysteresis, is represented in Figure 3.18. One admits that the overall temperature variation during the SE cycle amounts to $\Delta \mathrm{T} = T_1 - T_0$.

In the beginning of the cycle, the temperature in the material equals T_0. As the dynamic loading proceeds, during the forward transformation, temperature rises until it reaches T_1, when the maximum strain is attained. The corresponding stress level, point (b'), is higher than its isothermal counterpart, point (b). This causes the loading plateau to be steeper than the isothermal one, since they share the same original point (a). If the temperature of the material is considered to be constant

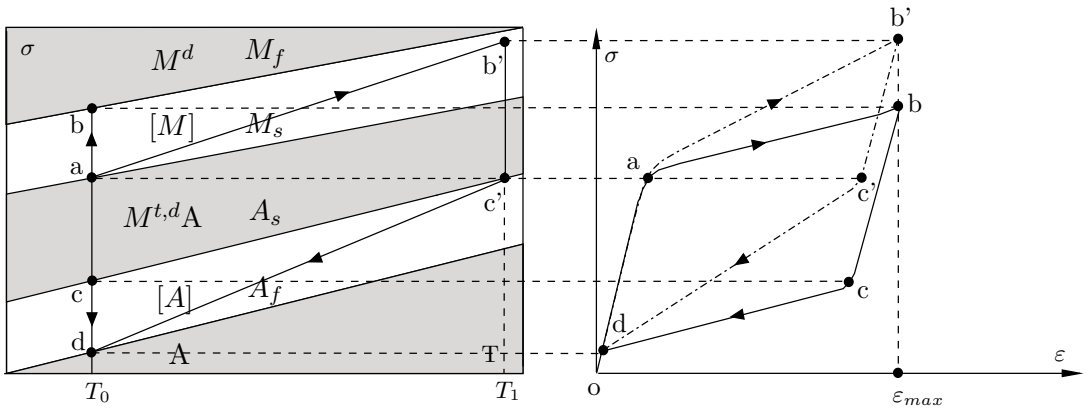

Figure 3.18: Temperature variation during a SE mechanical cycle. Phase diagram path and correspondent isothermal hysteresis.

during the elastic unloading, between points (*b'*) and (*c'*), the beginning of the inverse transformation also occurs at a higher stress level, point (*c'*), remaining above the isothermal unloading plateau until it meets its end, at point (*d*). Although representing a particular case of a dynamic response, this simplified example is able to show how the temperature variation during a SE cycle is coupled with the corresponding strain-rate. Experimental evidence presented by Leo *et al.* [93] shows that the heat transfer characteristics of the surrounding media and the geometry of the alloy control the extent of the strain-rate effect on SE behavior. If the temperature of the alloy remains constant during the loading process, the effect of strain-rate on the alloy's SE behavior becomes negligible.

Analyzing the stress-strain diagrams presented in Figure 3.17, one can observe important differences in the hysteretic loops when passing from quasi-static conditions to dynamic ones. The equivalent viscous damping is calculated for the four tested strain-rates, and the results are plotted in Figure 3.19.

The graph plotted in Figure 3.19 confirms that the dissipation capability of the SMA wire changes when passing from quasi-static conditions to dynamic ones. Moreover, it illustrates that the maximum of the equivalent viscous damping occurs around $\dot{\varepsilon} = 0.067\%/s$, and not in the actual quasi-static situation. This is explained by the fact that, as the strain-rate increases, the SMA temperature increases in loading and decreases during unloading, producing an increase of the hysteretic loop. However, for higher frequencies, the temperature during unloading increases over the ambient temperature, causing a decrease in the dissipated energy [135].

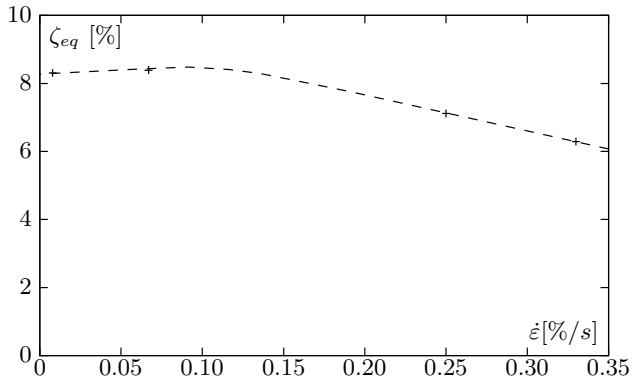

Figure 3.19: Influence of strain-rate on the equivalent viscous damping.

3.2.10 Transformation fronts

Under uniaxial loading of SMAs, the phase transitions are often accompanied by unstable mechanical behavior and localized transformation, resulting in propagating transformation fronts [89, 105]. An experimental setup is built in order to observe the propagation of these transformation fronts. The experimental setup mainly consists of a classical tensile test where a SE wire is subjected to a loading-unloading cycle, with a maximum strain of 6.0% and a strain-rate of 0.250%/s. The test is conduced at ambient temperature ($\simeq$ 24°C), being the temperature in the wire monitored by a thermocouple, placed at its mid-section. A FLIR ThermaCAM B4 infrared camera, see Figure 3.20, is used to monitor the temperature patterns within the wire specimen, through the whole duration of the tensile test.

Figure 3.20: FLIR ThermaCAM B4.

Figure 3.21 shows six images retrieved with the infrared camera during the exper-

iment, displayed in chronological order. Both the stress-strain diagram obtained during the complete tensile test and the temperature time-history, measured by the thermocouple, are displayed on the top left hand corner of the images. The small dots shown in these graphs represent the time instant associated with the corresponding thermo-image.

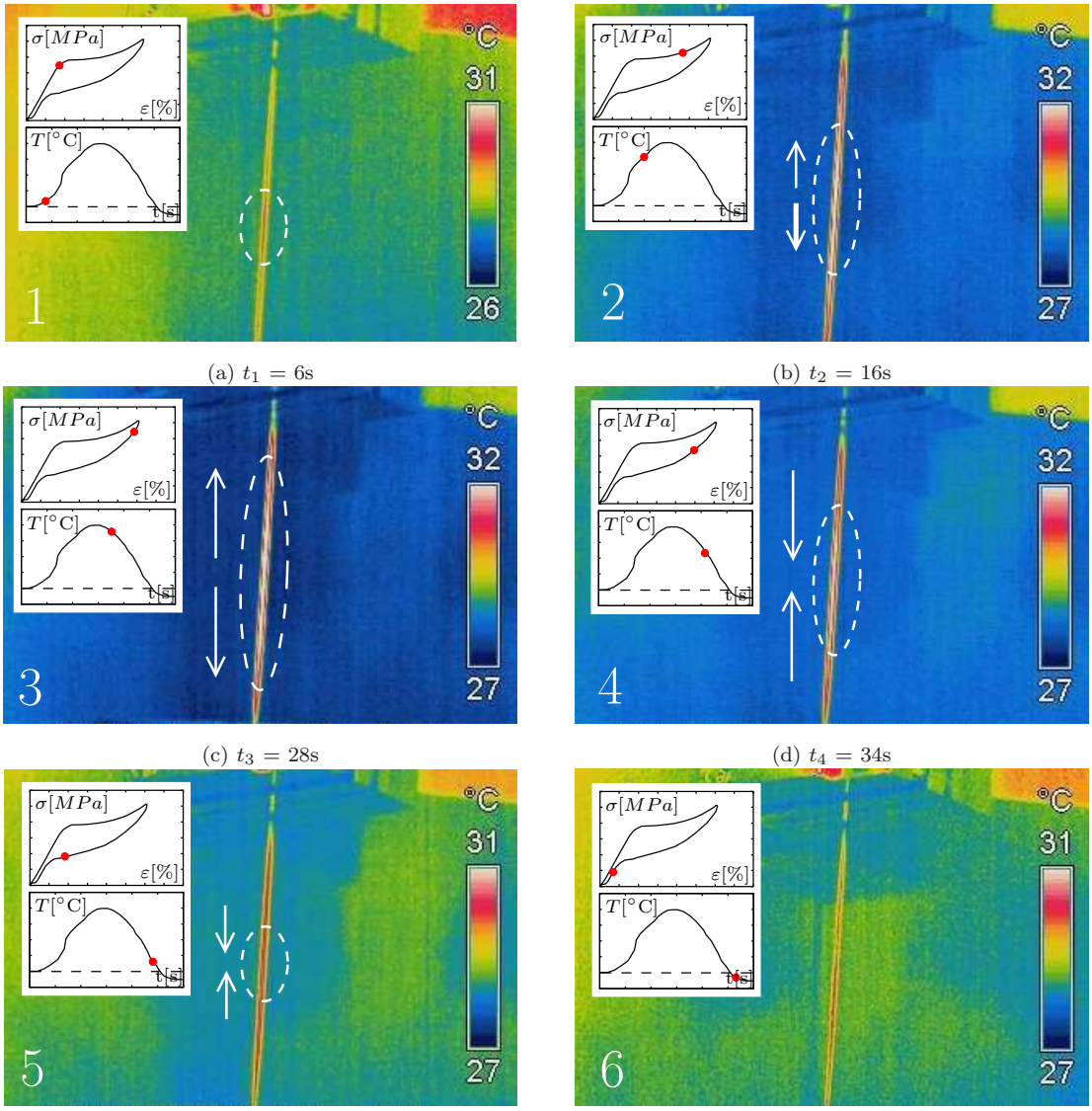

(a) $t_1 = 6$s (b) $t_2 = 16$s

(c) $t_3 = 28$s (d) $t_4 = 34$s

(e) $t_5 = 39$s (f) $t_6 = 44$s

Figure 3.21: Temperature patterns within the SE wire specimen, during the loading-unloading tensile test ($\dot{\varepsilon} = 0.250\%/s$).

Through the observation of the thermo-images obtained during the experimental procedure, one can see that, during the loading process, the propagating transfor-

mation fronts start from the central part of the specimen and develop towards the specimen grips. During the unloading process, they move the opposite way, from the grips and towards the central part of the specimen. The enthalpy of the martensitic transformation leads to a local temperature variation near the moving front [105]. In quasi-static situations, isothermal conditions within the material are present, but with growing strain-rates this moving heat source problem becomes more important, leading to significant non-uniform deformation and temperature fields [133].

3.2.11 Cyclic properties

Cyclic loading is known to influence the SE behavior of SMAs in general, and Nitinol in particular. According to experimental observations made by Tobushi*et al.* [145, 162, 163] under isothermal conditions, the SE loop is shifted to the larger strain side and to the lower stress side, with increasing number of cycles. Miyazaki*et al.* [107] has been able to further clarify some of the implications of cyclic loading on the SE stress-strain diagram, based on the study of the evolution of the stress-strain diagram of a Nitinol wire specimen during a cyclic quasi-static loading comprising 150 cycles, at different ambient temperatures. In the present work, a set of additional experimental cyclic tests are performed, under four different strain-rates, ranging from quasi-static conditions up to $\dot{\varepsilon} = 0.333\%/s$. These tests comprise 60 loading cycles and are conducted at ambient temperature ($\simeq 20°C$). Four Nitinol SE 508 wire specimens are used, one for each experiment, with a 2.40 mm diameter circular cross section. The experimental stress-strain diagrams obtained for the four tested strain-rates are represented in Figure 3.22.

It can be seen that during cyclic loading, the starting point of the stress-strain diagram tends to deviate, in a process of cumulative creep deformation. This deviation can be explained by the accumulation of slip deformations during stress induced transformation, resulting in residual strains, which increase during the first cycles and tend to stabilize with saturation [111].

The slip deformations induce internal stresses that can assist the formation of stress induced martensite, and, as a consequence, decrease the critical stress needed to induce martensite [111]. Conversely, the level of the reverse transformation stresses changes very little. As a consequence, the width of the hysteretic loop is significantly reduced upon cycling [78].

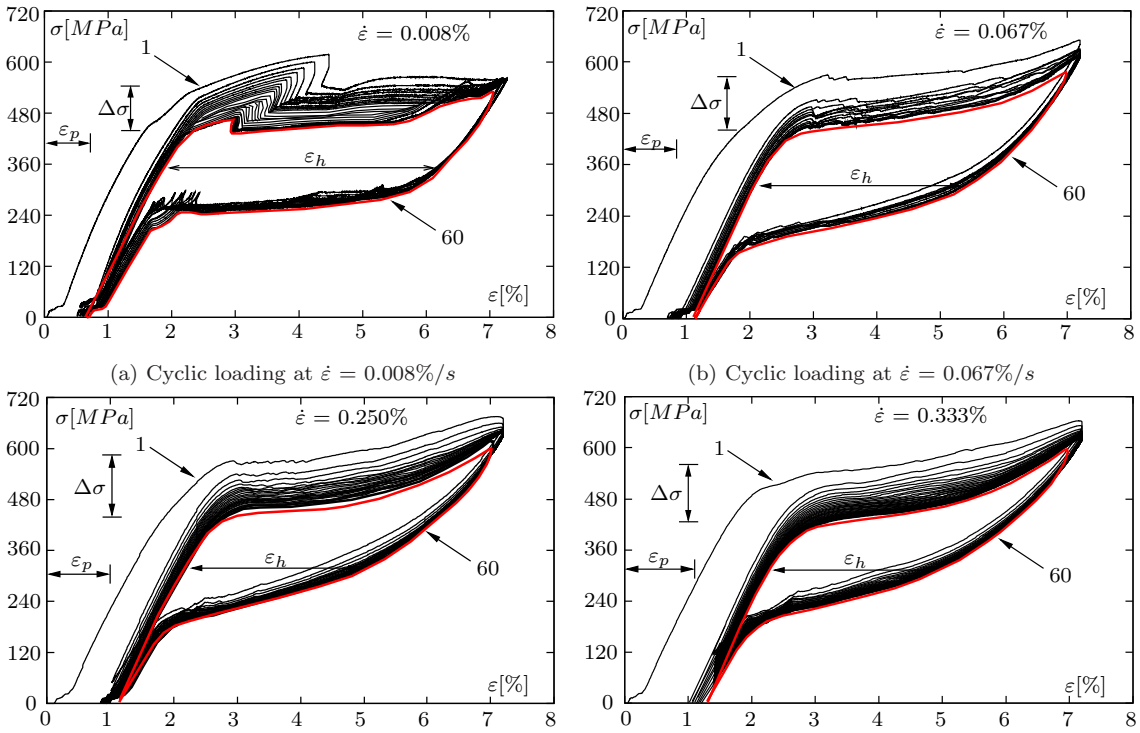

(a) Cyclic loading at $\dot{\varepsilon} = 0.008\%/s$

(b) Cyclic loading at $\dot{\varepsilon} = 0.067\%/s$

(c) Cyclic loading at $\dot{\varepsilon} = 0.250\%/s$

(d) Cyclic loading at $\dot{\varepsilon} = 0.333\%/s$

Figure 3.22: Experimental cyclic tensile tests. Stress-strain diagrams.

As the number of cycles continue to grow, the slip deformations increase the density of dislocations within the crystal structure. These dislocations obstruct the formation of martensite in a way similar to strain hardening in plasticity. As a consequence, the slope of the stress-strain diagram increases during loading [111].

These parameters, namely the cumulative creep deformation (ε_p), the critical stress needed to induce martensite and the width of the hysteretic loop (ε_h), are quantified, during the cyclic loading, and plotted in Figure 3.23, side by side with the experimental results obtained by Miyazaki [107].

It can be seen that the effects under consideration are rather important, but tend to gradually disappear with cycling. For a constant rate of the mechanical cycling, one obtains an asymptotic hysteretic loop in about fifty cycles. However, the decrease of the critical stress to induce martensite continues until about one hundred cycles.

It can also be seen that, for a given number of cycles, degradation increases with temperature, since higher stresses are needed to induce the transformation [78]. A similar trend is found in strain-rate variations, with an increase in the hysteresis

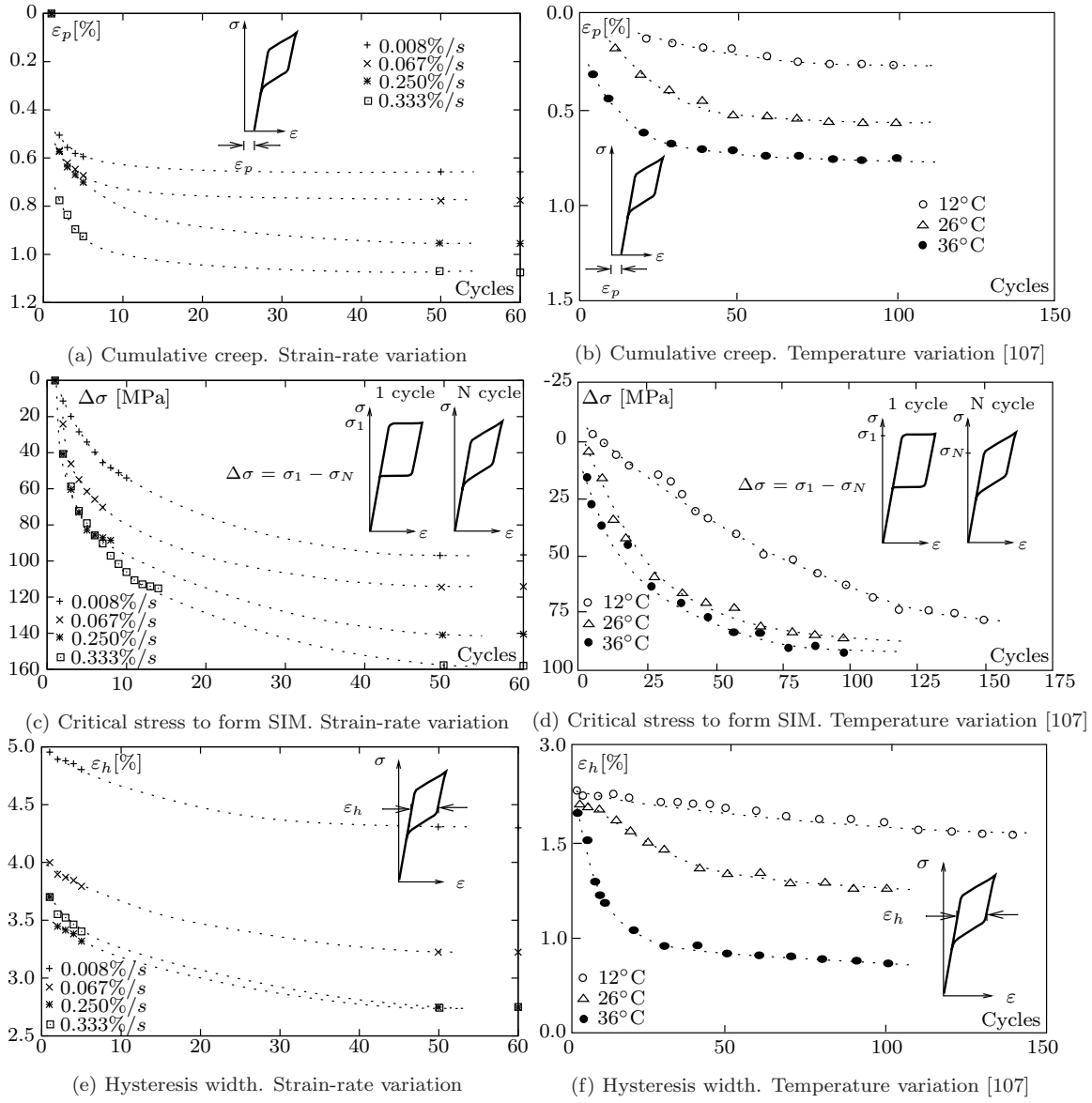

(a) Cumulative creep. Strain-rate variation

(b) Cumulative creep. Temperature variation [107]

(c) Critical stress to form SIM. Strain-rate variation

(d) Critical stress to form SIM. Temperature variation [107]

(e) Hysteresis width. Strain-rate variation

(f) Hysteresis width. Temperature variation [107]

Figure 3.23: Effects of SE cycling.

degradation as the strain-rate increases.

During the experimental cyclic tensile tests, together with strain and stress, the temperature of the Nitinol wire specimens is monitored by a thermocouple placed at the mid-section of the wires. In Figure 3.24 are represented the temperature time-history graphs, during the first 20 cycles, except for the quasi-static case, where isothermal conditions are present.

Analyzing the plots in Figure 3.24, one can observe that during mechanical cycling,

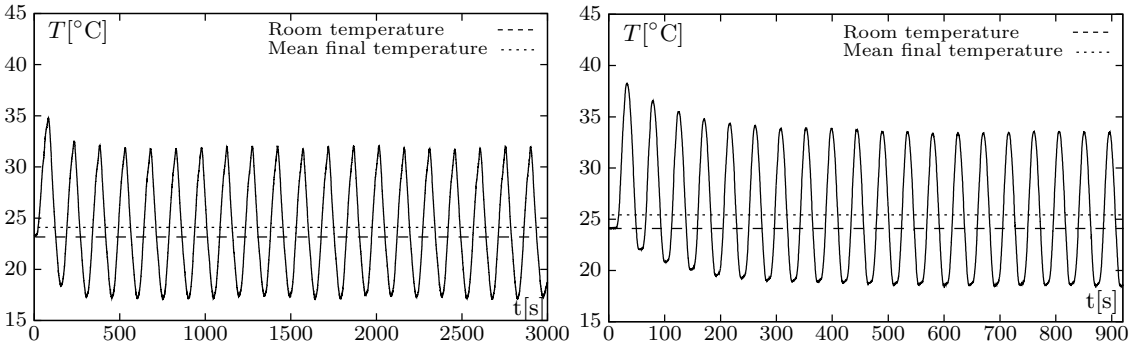

(a) Cyclic loading at $\dot{\varepsilon} = 0.067\%/s$

(b) Cyclic loading at $\dot{\varepsilon} = 0.250\%/s$

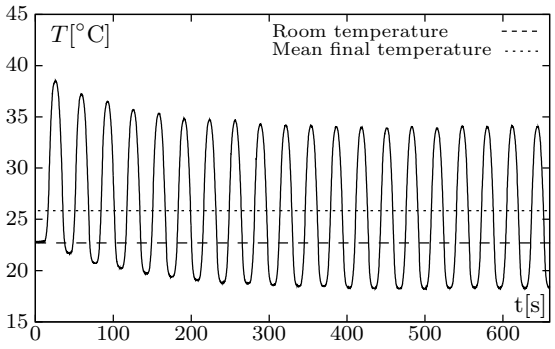

(c) Cyclic loading at $\dot{\varepsilon} = 0.333\%/s$

Figure 3.24: Experimental cyclic tensile tests. Temperature time-history.

higher strain-rates cause both higher temperature variations and higher maximum temperatures in the SE specimen. For the tested strain-rates, the temperature of the wires follow the same general pattern, eventually stabilizing around a given value, which grows with the strain-rate.

3.2.12 Influence of cycling on damping

The use of Nitinol kernel elements in vibrations mitigation devices in structures requires that progressive permanent deformation during cyclic loading (cumulative creep) is kept to a minimum. If the material progressively increases its length, the net strain produced by a given structural oscillation is reduced. For sufficiently large permanent deformations the martensitic transformation may not even be induced, hindering the energy dissipation capabilities of the material.

Cumulative creep in Nitinol is related to dislocations and other lattice defects, gen-

erated at high stress during the preceding loading cycle [111, 107], and due to the repeated motion of the parent-martensite interface [124]. Wang *et al.* have shown that with the same number of cycles, the residual strain increases with strain amplitude [172]. To mitigate this effect, stress levels during a dynamic loading should be limited within a narrower SE window.

The stability of the deformation behavior may be improved by raising the critical stress for slip. Thermomechanical heat treatments aimed to stabilize the SE behavior of Nitinol have been found effective [107], minimizing cumulative creep and avoiding the modification of the hysteretic cycle. A thermal heat treatment promoting grain growth in CuAlBe wires has allowed to develop near 4.5% of deformation without progressive permanent deformation on cycling [**?**]. It has also been suggested that training by deformation prior to actual service is effective for stabilizing superelasticity [124].

3.2.13 Fatigue properties

Fatigue behavior in Nitinol is of extreme complexity and encompasses two main different subjects:

1. Classical mechanical fatigue due to SE cycling;
2. Thermal fatigue or *amnesia* of the material, due to the degradation of the material characteristics responsible for the shape-memory effect, like the transformation temperatures [111, 130].

As SE Nitinol can accommodate high strains without excessive stresses it excels in low-cycle, strain controlled environments [55]. Charkaluk *et al.* [111] showed that a low-cycle fatigue criterion relating the dissipated energy at the stabilized cycle and the number of cycles to failure allows a good correlation between prediction and experimental results. Figure 3.25 shows experimental tests conducted by Moumni [111], which allowed to represent this relation in the following form:

$$E_D = \alpha N_f^{\beta} \tag{3.1}$$

where E_D is the dissipated energy in the stabilized cycle and N_f the number of cycles at failure. The material parameters α and β have values of 11 and -0.377

respectively.

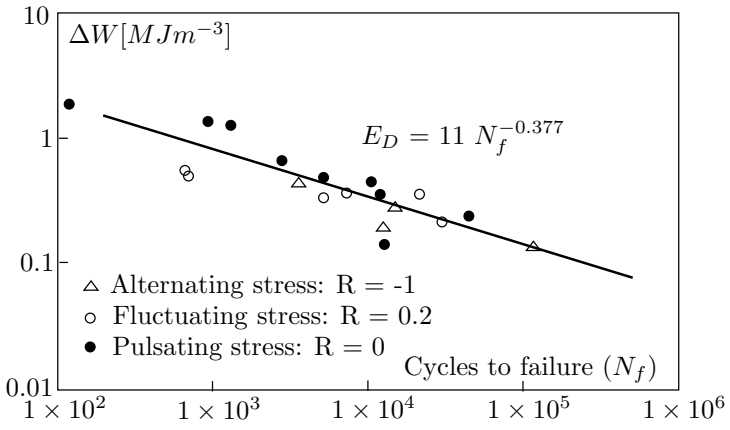

Figure 3.25: Dissipated energy versus the number of cycles at failure [111].

Carreras *et al.* experimentally studied the fatigue-life at constant amplitude in SE Nitinol, for damping applications of structures under wind or rain. The results showed that the fracture level overcomes 130000 cycles when the moving air is used for cooling. When the number of working cycles overcomes 30000, the frictional energy decreases by 40%, roughly with an exponential behavior [**?**].

3.2.14 Strain-creep and stress-relaxation

Martensitic transformation can be induced either by stress or temperature. The relation between strain and temperature during heating and cooling, under constant stress is shown in Figure 3.6. It can be seen that strain decreases during the inverse transformation, between A_s and A_f, in the heating process, and increases during the forward transformation, between M_s and M_f, in the cooling process. Thermal expansion and contraction may be considered negligibly small [101]. During the forward transformation temperature rises and during the inverse transformation temperature decreases. If a SE cycle is interrupted, keeping stress at a constant level, transformation-induced strain-creep or strain-recovery occur. In Figure 3.26, during the loading process, from point (a) to (b), temperature increases with stress. This is reflected in the stress-temperature phase diagram by the correspondent transformation path. Reaching point (b), the loading process is interrupted, and the stress is kept constant. Temperature tends to decrease back to the ambient temperature T_0.

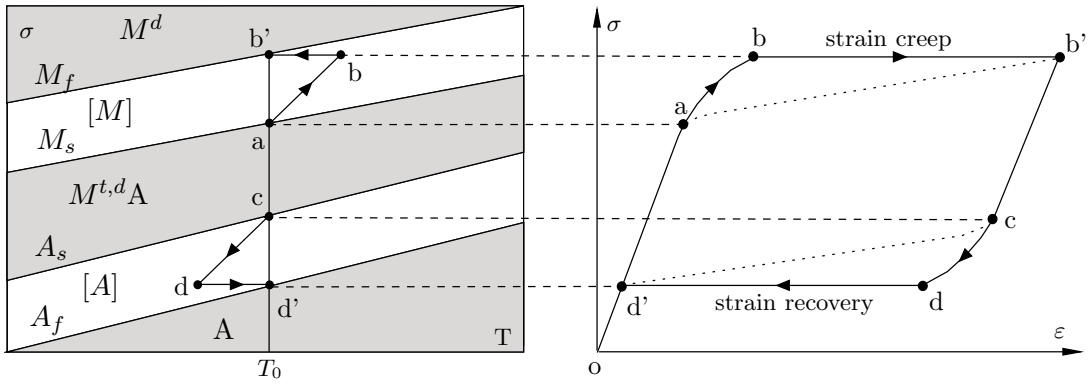

Figure 3.26: Strain-creep and strain-recovery. Phase diagram path and correspondent hysteresis.

This cooling process between M_s and M_f causes the strain to increase, from point (b) to point (b'), due to the martensitic transformation. During the unloading process, from point (c) to (d), temperature decreases with stress. The cycle is interrupted by the time it reaches point (d), keeping the stress constant. If, by that time, the specimen's temperature is below ambient temperature, it will gradually rise until thermal balance with the surroundings is achieved. This heating process between A_s and A_f causes the strain to decrease, from point (d) to point (d'), also due to the martensitic transformation. These dual processes are usually called strain-creep and strain-recovery due to martensitic transformation [21, 22].

In Figure 3.27, during the loading process, from point (a) to (b), temperature also increases with stress. This is reflected in the stress-temperature phase diagram by the correspondent transformation path. Reaching point (b), the loading process is interrupted, and the strain is kept constant. As temperature decreases back to the ambient temperature T_0, between M_s and M_f, strain tends to increase. Since the strain is blocked, a set of auto balanced compressive forces develops within the SE specimen, causing the stress to decrease. The opposite effect occurs when, reaching point (e), during the process of unloading, temperature rises to the ambient temperature, between A_s and A_f, and strain tends to decrease. Since the strain is blocked, a set of auto balanced compressive forces develops within the SE specimen, causing the stress to increase [134]. These dual processes are usually called stress relaxation and stress recovery due to martensitic transformation [21, 22].

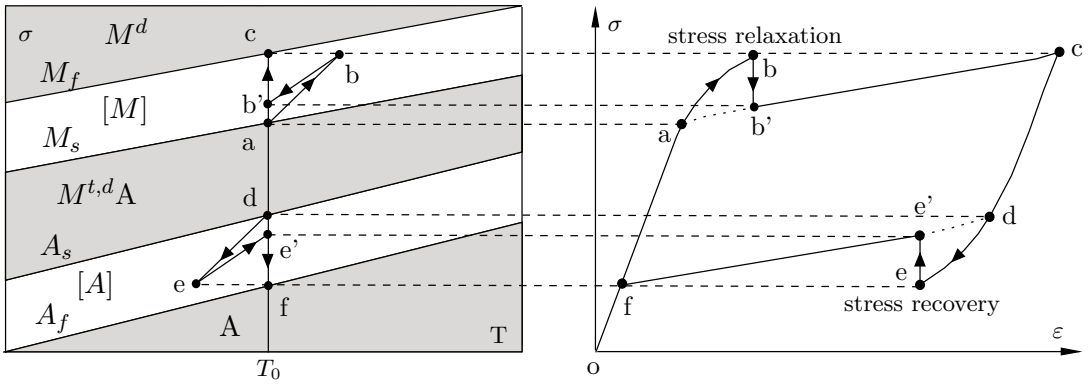

Figure 3.27: Stress-relaxation and stress-recovery. Phase diagram path and correspondent hysteresis.

3.2.15 Aging effects

Vibration mitigation devices based on SE SMAs, like all technological applications, must be totally reliable during operation. In order to be dependable, the design of such devices must clearly specify the working conditions of the SE material, namely its working temperature range, maximum admissible strain and stress values, maximum strain-rate, the number of working cycles and expected lifetime behavior [166].

The extensive life cycles exhibited by civil engineering structures demand the full characterization of time effects on SE properties, for both austenitic and martensitic phases, and also for the coexistence zones of the hysteretic cycle. This section addresses the effects of long term static loadings, like pre-stress, on the SE behavior of SMAs, in the different zones of the hysteretic cycle.

Various types of aging phenomena have been known to occur in SMAs. Among these alloys, Cu-based alloys are, in general, more prone to aging effects than other alloys, even at ambient temperature [124].

It is known that when a SE alloy, in the parent phase, is submitted to a given constraint (stress or strain) the critical stress to induce martensite decreases by an certain amount ($\Delta\sigma$). This decrease is due to residual stresses that promote the formation of martensite, remaining in the material once the applied constraint is removed. These residual stresses are a function of the intensity of the constraint and of its duration [81, 166].

The aging effects in Nitinol, in the austenitic phase, are very slow. The order of magnitude of the time constants involved may reach several months, in comparison to the ones observed in CuAlBe and CuZnAl, which amount to only two days and one hour respectively [13].

Using the Clausius-Clapeyron coefficient, which translates the slope ($d\sigma/dT$) of the lines defining the boundaries of the SMA transformation strips, the variation of the transformation temperature M_s (ΔM_s) can be expressed as a function of $\Delta\sigma$, yielding $\Delta M_s = -1/\mathrm{CCC}\Delta\sigma$. Hence, the transformation temperature increases when a SE alloy ages under loading, in the parent phase.

The simplified stress-temperature phase diagram path associated with a variation in the critical stress to induce martensite ($\Delta\sigma$), together with the variation in the corresponding isothermal hysteresis, is represented in Figure 3.28.

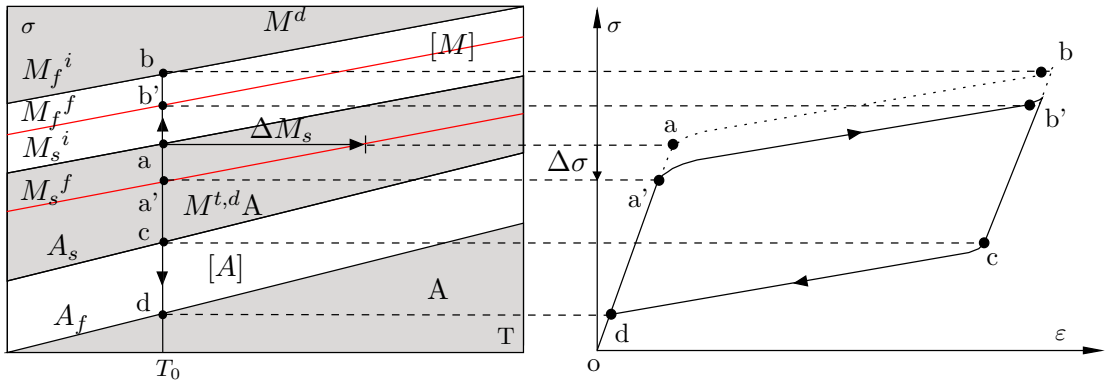

Figure 3.28: Aging under load in the parent phase. Phase diagram path and correspondent hysteresis.

Due to aging under loading in the parent phase (o-a), the critical stress to induce martensite decreases from point (a) to point (a'), in the phase diagram represented in Figure 3.28. The line corresponding to the beginning of the forward transformation shifts leftwards, as the M_s transformation temperature increases. This step in the critical stress to induce martensite is reflected in the whole upper plateau of the SE hysteresis [13]. Hence, the line corresponding to the finishing of the forward transformation also shifts leftwards, as the M_f transformation temperature increases, and point (b) moves to point (b'). The lower hysteretic plateau remains unchanged [13].

In the coexistence zone, both the crystallographic phases, i.e. austenite and martensite, are present. When a SE specimen ages under constant stress in the coexistence zone, the residual stresses that arise in the material continue to assist the formation of martensite. Torra *et al.* [166] reports that in the phase coexistence domain, a spontaneous increase of the available martensite is noticed, at constant stress, with increasing deformation, in a process similar to strain-creep. So, as the material ages under constant stress in the coexistence domain, an increase of the M_s transformation temperature also occurs, depending on time and necessarily on the austenite fraction of the aging material. If the material is in its pure austenitic form, the reduction of the critical stress to induce martensite is maximum. As the austenite fraction of the aging material decreases, this reduction becomes less important. Figure 3.29 represents the simplified stress-temperature phase diagram path associated with aging at constant stress in the coexistence domain, together with the variation in the corresponding isothermal hysteresis.

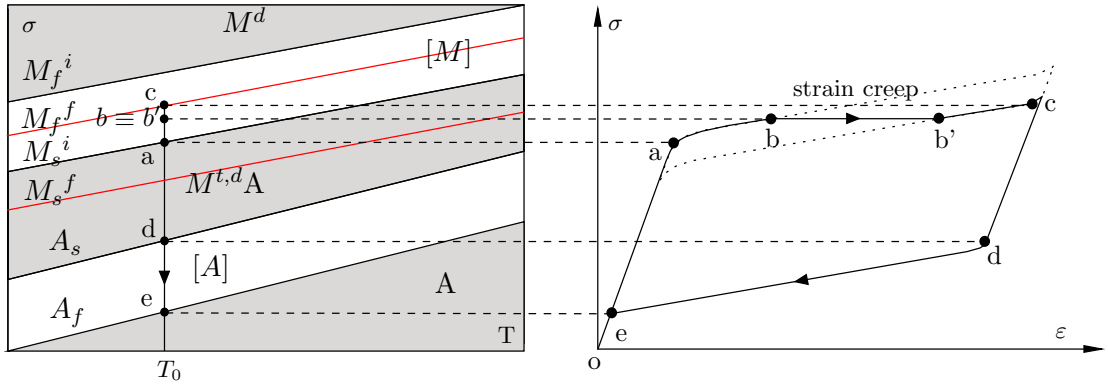

Figure 3.29: Aging under constant stress in the coexistence zone. Phase diagram path and correspondent hysteresis.

When the SE cycle is interrupted, after describing the first initial path (*o*-*a*-*b*), the martensitic transformation slowly continues to develop, with increasing deformation (*b*-*b'*). If, after a certain period of time, the mechanical tensile cycle continues, the SE hysteresis deviates from the standard hysteresis. The stress step reduction being a function of time and of the austenitic fraction of the material during aging. Unfortunately, there is still very little experimental evidence of this phenomena.

If the material ages at constant strain in the coexistence domain, a stress step occurs, leading to the stress relaxation of the material [13]. This stress step is also a function

of time and of the austenitic fraction present in the aging material. Figure 3.30 represents the simplified stress-temperature phase diagram path associated with aging at constant strain in the coexistence domain, together with the variation in the corresponding isothermal hysteresis.

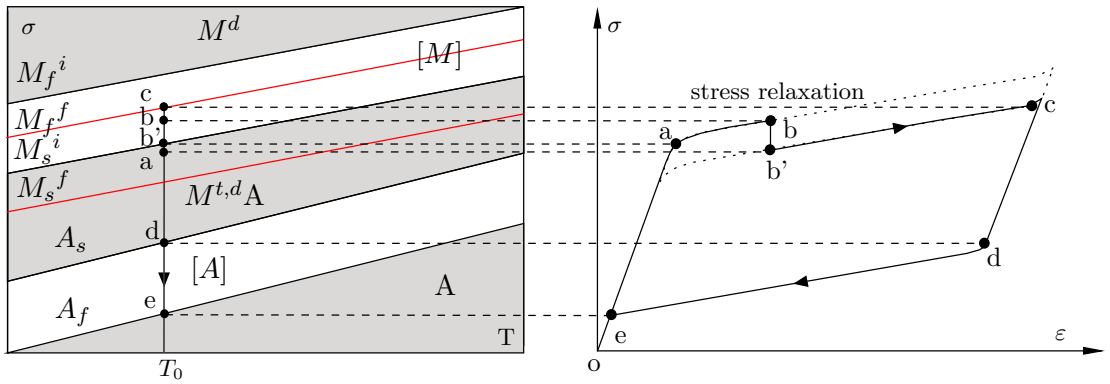

Figure 3.30: Aging under constant strain in the coexistence zone. Phase diagram path and correspondent hysteresis.

When the SE cycle is interrupted, after describing the first initial path *(o-a-b)*, the martensitic transformation slowly continues to develop, and strain tends to increase. Since the strain is blocked, a set of auto balanced compressive forces develops within the SE specimen, causing the stress to decrease. If, after a certain period of time, the mechanical tensile cycle continues, the SE hysteresis deviates from the standard hysteresis. The stress step reduction being a function of time and also of the austenitic fraction of the material during aging. Unfortunately, there is also still very little experimental evidence to fully clarify this phenomena.

The estimations of the time constants and amplitudes of changes in the transformation temperatures for NiTi SE alloys are very difficult to obtain, due to the large time scales involved in the aging process. In Cu-based alloys, given the smaller time scales involved, variations of M_s are easier to obtain, and have been reported to reach about 15% [13].

The evaluation of the asymptotic variation of the NiTi transformation temperatures with time shows that these temperatures can increase more than 15 K. This represents, via the CCC, a change of stress over 90 MPa [12].

Another example of aging in Cu-based alloys is a phenomena usually called as

martensite stabilization. It consists in the gradual increase of the A_s temperature with time, when aging in the martensite phase. The increase in A_s becomes more important as temperature rises and may even cause the inhibition of the inverse transformation [124].

3.3 Closure

Due to its outstanding fatigue properties, high corrosion resistance and ductility, the majority of the SMA based industrial applications are mostly built up of Nitinol.

A microstructural survey of Nitinol allowed for the lattice characterization of its bcc austenitic (B2) and monoclinic martensitic (B19') crystal structures, as well as to introduce the so-called R-phase, a trigonal phase associated with a two step transformation from B2 to B19'.

In order to assess the tensile properties of Nitinol, uniaxial tensile tests are performed on two wire specimens. These tensile tests enable the characterization of the loading and unloading plateaus of the SE hysteretic cycles, associated with the forward and inverse transformations, respectively. The austenitic and martensitic modulus of elasticity (E_A and E_M) are also characterized, as well as the ultimate tensile strength (σ_u) and elongation at failure.

Differential Scanning Calorimetry (DSC) is used to characterize the transformation temperatures of a Nitinol wire specimen (M_f, M_s, A_s and A_f). This thermoanalytical technique is based on the evaluation of the enthalpy of the martensitic transformation during phase transition.

An experimental procedure to determine Clausius-Clapeyron coefficient (CCC) of a previously stabilized Nitinol specimen is implemented, evaluating its critical transformation stresses for a set of different ambient temperatures. The analysis of the resulting SE hysteresis shows a clear temperature dependence, as the hysteretic loop is shifted upwards with the rising of the ambient temperature. The stress-temperature phase diagram associated with a temperature variation helps to clarify this aspect. The equivalent viscous damping is computed for the obtained SE hysteresis, allowing to establish that an increase on the ambient temperature causes the damping capacity of the Nitinol wire to decrease in a marginal way.

The behavior of a SE Nitinol sample subjected to internal loops, i.e. to cycling situations where the full extent of the forward and inverse transformations are not attained is evaluated. A study regarding the influence of strain-amplitude on the damping capacities of Nitinol is performed, based on the analysis of the stress-temperature phase diagram path associated with a variation in the strain-amplitude, and on tensile tests of increasing amplitude. The results show that as the martensitic transformation begins, the damping capacity of the wire rapidly increases with strain. After this first transitional phase, during the remaining extent of the martensitic transformation, the damping capacity of the wire linearly increases with the strain-amplitude.

To illustrate how the strain-rate of the dynamic loading may influence the temperature variation of a SE specimen during a cyclic test, as well as the shape of its corresponding hysteretic loop, a series of experimental tensile tests are conducted. According to the results, for the range of tested strain-rates, when passing from quasi-static conditions to dynamic ones, important changes occur, affecting the dissipation capability of the SMA wire. The computation of the equivalent viscous damping demonstrates that, as the strain-rate increased, the dissipation capacity of the Nitinol wire initially increased and then started to decrease.

An experimental setup is built in order to observe the propagation of the transformation fronts that accompany the phase transitions during the uniaxial loading of SMAs. The results show that during the loading process the propagating transformation fronts start from the central part of the specimen and develop towards the specimen grips. During the unloading process, they move the opposite way, from the grips and towards the central part of the specimen.

An experimental study to clarify some of the implications of cyclic loading on the SE stress-strain diagram is performed. This study is based on the analysis of the evolution of the stress-strain diagram of a Nitinol wire specimen during cyclic loading. The cumulative creep deformation, the critical stress needed to induce martensite and the width of the hysteretic loop are quantified, under different cyclic loading conditions regarding ambient temperature and strain-rate, and although the effects under consideration are proved rather important, they gradually disappear with cycling. It is also shown that degradation increases with both temperature and strain-rate. Since cumulative creep in Nitinol is mainly due to lattice defects generated at high stress, one way to limit this effect is to keep the stress levels during

dynamic loading within a narrower SE window, also reducing the influence of cycling on damping.

It is shown that due to temperature variation during a non-isothermal SE cycle, if a SE cycle is interrupted, keeping stress at a constant level, transformation-induced strain-creep or strain-recovery occur in Nitinol. Stress-relaxation and stress-recovery due to martensitic transformation are also addressed. Regarding the Nitinol aging effects it is shown that if the material ages at constant strain in the coexistence domain, a stress step occurs, leading to the stress relaxation of the material.

Chapter 4

Constitutive Models for Shape-Memory Alloys

4.1 Introduction

The behavior of SMAs shows a high level of complexity, since it depends on stress and temperature, and is closely connected with the crystallographic phase of the material and the thermodynamics underlying the transformation processes. For this reason, any simulation regarding the design of a particular system that makes use of the interesting features exhibited by these materials, has to be based on an adequate constitutive model. The model must be able to conveniently cope with the relevant set of SMA's properties regarding the type of application at stake. While rate-independent models, insensitive to the velocity of the applied strain or stress, may be well suited for quasi-static analysis, when isothermal conditions are present, for most dynamic applications, rate-dependent models are usually required, due to self-heating.

Several constitutive mathematical models for SMAs are currently available in the literature [16, 17, 18, 20, 26, 30, 31, 60, 63, 64, 65, 103, 128, 129, 155], most of them being aimed at the one-dimensional description of the material behavior. One of the common features present in most of them, is that they can be separated into a mechanical law, governing the stress-strain behavior, and kinetic laws, governing the transformation behavior. These two relations are often coupled [30]. Rate-

dependent models require an additional thermal balance equation, coupled with the mechanical and kinetic laws.

In this work, two different constitutive models are considered, a rate-independent constitutive model, based on the model proposed by Auricchio [15, 60, 103], and a rate-dependent constitutive model, based on the model proposed by Tanaka [159].

4.2 Mechanical laws

In a typical SMA constitutive model, the mechanical law relates stress (σ), strain (ε), temperature (T) and martensite fraction (ξ). Martensite fraction is an internal state variable that represents the extent of the transformation in the material and can be regarded as the fraction of the produced phase. The original phase occupies, therefore, the rest, 1 - ξ.

The transformed phase fraction is considered to be in series with the elastic fraction of the response. There are several approaches for mathematical modeling of this elastic component. If the elastic fraction of the response is considered to be limited to the austenite phase, the model represented in Figure 4.1(a) is obtained. The models represented in Figure 4.1(b) and (c) contemplate two different crystallographic phases, austenite and martensite, not distinguishing between the twinned and the detwinned martensite. Considering a parallel distribution of austenite and martensite within the material, equivalent to the Voight scheme, yields the model represented in Figure 4.1(b). If, in alternative, the mechanical model is based in a periodical distribution of austenite and martensite within the material, orthogonal to the direction of the applied stress, the model represented in Figure 4.1(c), which is equivalent to the Reuss scheme, is obtained.

4.2.1 Simple serial model

For the mechanical model expressed in Figure 4.1(a), as the principle of superposition applies, the total strain results from the sum of the elastic strain ($\varepsilon_{elast.}$) with the transformation strain ($\varepsilon_{transf.}$),

$$\varepsilon = \varepsilon_{elast.} + \varepsilon_{transf.} \tag{4.1}$$

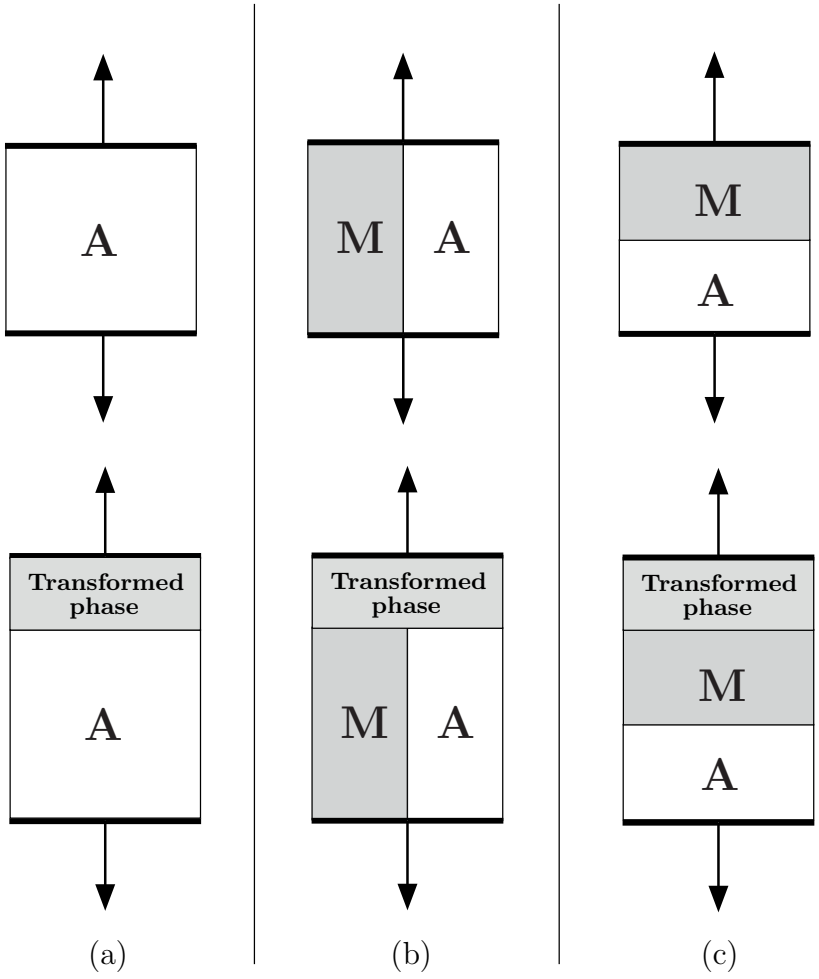

Figure 4.1: Mechanical models for SMAs: (a) Simple serial model; (b) Voight scheme; (c) Reuss scheme.

The transformation strain can be written as

$$\varepsilon_{transf.} = \varepsilon_L \xi \quad \text{with} \quad 0 \leq \xi \leq 1 \tag{4.2}$$

and

$$\varepsilon_{elast.} = \varepsilon - \varepsilon_L \xi \tag{4.3}$$

where ε_L is the maximum residual strain in the material. As the elastic strain equals the austenitic strain ($\varepsilon_{elast.} = \varepsilon_A$), the total strain reads

$$\varepsilon = \varepsilon_A + \varepsilon_L \xi \tag{4.4}$$

and the mechanical law governing the stress-strain behavior yields

$$\sigma = \sigma_A = E_A \varepsilon_A = E_A(\varepsilon - \varepsilon_L \xi) \tag{4.5}$$

where E_A is the austenitic elastic modulus. This model neglects the additional thermal strain component, which is several orders of magnitude smaller than the transformation strain [30].

4.2.2 Voight scheme

For the mechanical model equivalent to the the Voight scheme, in Figure 4.1(b), as the elastic strain equals the austenitic and martensitic strains ($\varepsilon_{elast.} = \varepsilon_A = \varepsilon_M$), the mechanical law governing the behavior of the material can be written as

$$\sigma = \xi \sigma_M + (1 - \xi)\sigma_A \tag{4.6}$$

Taking into account that $\sigma_A = E_A \varepsilon_A$ and $\sigma_M = E_M \varepsilon_M$, it yields

$$\sigma = [\xi E_M + (1 - \xi)E_A]\varepsilon_{elast.} = [\xi E_M + (1 - \xi)E_A](\varepsilon - \varepsilon_L \xi) \tag{4.7}$$

where ε_M is the martensitic strain, and E_M the martensitic elastic modulus. Adding the thermal strain component to equation(4.7) results in the mechanical law proposed by Tanaka [159]

$$\sigma = [\xi E_M + (1 - \xi)E_A](\varepsilon - \varepsilon_L \xi) + \theta(T - T_0) \tag{4.8}$$

where θ is related to the thermal coefficient of expansion and T_0 is the temperature at which the thermal strain is defined to be zero [44].

4.2.3 Reuss scheme

For the mechanical model equivalent to the Reuss scheme, in Figure 4.1(c), the total strain can be expressed as

$$\varepsilon = \xi\varepsilon_M + (1-\xi)\varepsilon_A \tag{4.9}$$

The stress in each phase is equal to the overall applied stress and the individual phase strains are given by $\varepsilon_A = \sigma/E_A$ and $\varepsilon_M = \sigma/E_M + \varepsilon_L$. Substituting the austenite and martensite phase strains in (4.9) results that

$$\sigma = \frac{E_A E_M}{\xi E_A + (1-\xi)E_M}(\varepsilon - \varepsilon_L\xi) \tag{4.10}$$

The Ishvin-Pence mechanical law [30] is obtained by adding the thermal strain component to equation(4.10), yielding

$$\sigma = \frac{E_A E_M}{\xi E_A + (1-\xi)E_M}(\varepsilon - \varepsilon_L\xi) + \theta(T - T_0) \tag{4.11}$$

4.3 Kinetic laws

In order to complete the constitutive model, the mechanical law must be coupled with the transformation kinetic equations. These expressions describe mathematically the evolution of the martensite fraction with stress and temperature, based on the material's stress-temperature phase diagram. There are several kinetic laws available in the literature. They range from the linear kinetic laws proposed by Aurichio [15], the exponential laws proposed by Tanaka [159, 160], to the cosine based kinetic laws proposed by Liang and Rogers [96] and to thermodynamically derived relations, proposed by Ishvin and Pence [79]. In the present work only the linear and the exponential kinetic relations were used.

4.3.1 Linear transformation kinetic laws

The linear transformation kinetic relations are based on the assumption that the relation between strains and stresses are represented by a series of linear segments. The material constants, M_f, M_s, A_s, A_f, C_M and C_A, are illustrated in the stress-temperature phase diagram in Figure 4.2, where a isothermal, stress-induced, martensitic transformation path is drawn. The starting and final stresses during the forward (σ_s^{AM}, σ_f^{AM}) and inverse (σ_s^{MA}, σ_f^{MA}) transformations are represented in the corresponding stress-strain diagram.

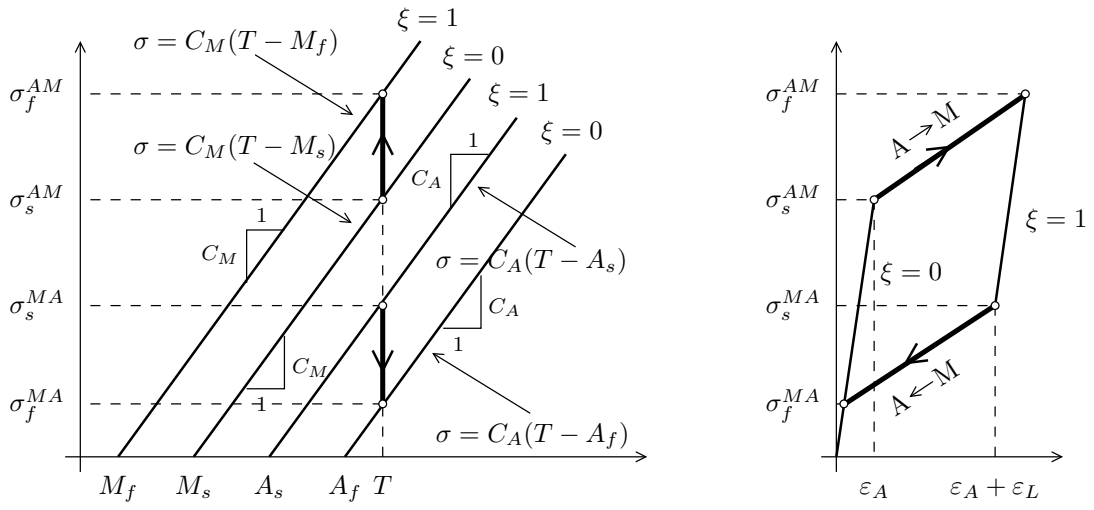

Figure 4.2: Superelastic stress-temperature phase plane diagram. Forward ($A \to M$) and inverse ($M \to A$) transformations.

The martensite fraction during the phase transformation is defined by a scalar internal variable ξ. Its variation occurs during the conversion of austenite into martensite ($A \to M$) or of martensite into austenite ($M \to A$), the forward and inverse transformations, respectively. In the case of a linear kinetic transformation law, the function $\xi(\sigma)$ is a linear function. The martensite fraction assumes values between zero and one, corresponding to the pure austenite and martensite phases. Therefore,

$$\xi(\sigma_s^{AM}) = 0 \quad \text{and} \quad \xi(\sigma_f^{AM}) = 1 \quad (A \to M) \tag{4.12}$$

$$\xi(\sigma_s^{MA}) = 1 \quad \text{and} \quad \xi(\sigma_f^{MA}) = 0 \quad (M \to A) \tag{4.13}$$

Hence, the kinetic laws describing the forward and inverse transformations, for a

specific temperature (T), may be written as,

$$\xi^{AM} = \frac{\sigma - \sigma_s^{AM}}{\sigma_f^{AM} - \sigma_s^{AM}} \tag{4.14}$$

$$\xi^{MA} = \frac{\sigma - \sigma_f^{MA}}{\sigma_s^{MA} - \sigma_f^{MA}} \tag{4.15}$$

Using the equations that define the boundary lines of the transformation strips, represented in the left hand graph of Figure 4.2,

$$\sigma_s^{AM} = C_M(T - M_s) \quad \text{and} \quad \sigma_f^{AM} = C_M(T - M_f) \tag{4.16}$$

$$\sigma_s^{MA} = C_A(T - A_s) \quad \text{and} \quad \sigma_f^{AM} = C_A(T - A_f) \tag{4.17}$$

the kinetic laws describing the transformations may be generalized for any given temperature, yielding, for the forward and inverse transformations,

$$\xi^{AM} = \frac{\sigma - C_M(T - M_s)}{C_M(M_s - M_f)} \tag{4.18}$$

$$\xi^{MA} = \frac{\sigma - C_A(T - A_f)}{C_A(A_f - A_s)} \tag{4.19}$$

4.3.2 Exponential transformation kinetic laws

The Tanaka's exponential laws are based in the Magee's transformation kinetics equations, originally proposed for steels [**?**, 100]. For the forward and inverse transformations, they yield,

$$\frac{\dot{\xi}}{1 - \xi} = a_M \dot{T} - b_M \dot{\sigma} \qquad (A \to M) \tag{4.20}$$

and

$$-\frac{\dot{\xi}}{\xi} = a_A \dot{T} - b_A \dot{\sigma} \qquad (M \to A) \tag{4.21}$$

Let one consider a forward transformation process starting from the initial values (σ_0, T_0, ξ_0), where ξ_0 stands for the fraction of martensite at the start of the forward transformation. If the transformation kinetics (4.20) is integrated from the initial values to the current values (σ, T, ξ), for constant material parameters a_M and b_M,

one finally obtains an explicit form of the forward transformation kinetics,

$$1 - \xi = (1 - \xi_0) \exp\left[-a_M(T - T_0) + b_M(\sigma - \sigma_0)\right]$$

since $\xi_0 = 0$ and $\sigma_0 = C_M(T_0 - M_s)$,

$$\xi = 1 - \exp\{-a_M(T - T_0) + b_M[\sigma - C_M(T_0 - M_s)]\}$$

and taking into account that $b_M C_M = a_M$,

$$\xi^{AM} = 1 - \exp\left[a_M(M_s - T) + b_M\sigma\right] \tag{4.22}$$

where M_s is the temperature at which the forward transformation starts, in the stress-free state. This equation is valid if $\sigma > C_M(T - M_s)$.

Now, consider a inverse transformation process, starting from the initial values (σ_0, T_0, ξ_0), where ξ_0 stands for the fraction of martensite at the start of the inverse transformation. If the transformation kinetics (4.21) is integrated from the initial values to the current values (σ, T, ξ), for constant material parameters a_M and b_M, one finally obtains an explicit form of the inverse transformation kinetics,

$$\xi = \xi_0 \exp[-a_A(T - T_0) + b_A(\sigma - \sigma_0)]$$

since $\xi_0 = 1$ and $\sigma_0 = C_A(T_0 - A_s)$,

$$\xi = \exp\left\{-a_A(T - T_0) + b_A[\sigma - C_A(T_0 - A_s)]\right\}$$

and taking into account that $b_A C_A = a_A$,

$$\xi^{MA} = \exp[a_A(A_s - T) + b_A\sigma] \tag{4.23}$$

where A_s is the temperature at which the inverse transformation starts, in the stress-free state. This equation is valid if $\sigma \leq C_A(T - A_s)$.

The exponential law equations (4.22) and (4.23) are well known in the literature and widely used [169].

To determine the material constants a_M, b_M, one follows the usual understanding in metallurgy [10], assuming that the forward transformation is complete when

$\xi = 0.99$. This results in,

$$\begin{aligned}
\xi^{AM} &= 1 - \exp\left[a_M(M_s - T) + b_M\sigma\right] \\
0.99 &= 1 - \exp\left[a_M(M_s - T) + b_M C_M(T - M_f)\right] \\
a_M &= -\frac{2\ln 10}{M_s - M_f}, \quad b_M = \frac{a_M}{C_M} \qquad (A \to M)
\end{aligned} \tag{4.24}$$

The material constants a_A and b_A are calculated similarly, assuming that the completion of the inverse transformation occurs when $\xi = 0.01$

$$\begin{aligned}
\xi^{MA} &= \exp[a_A(A_s - T) + b_A\sigma] \\
0.01 &= \exp[a_A(A_s - T) + b_A C_A(T - A_f)] \\
a_A &= \frac{2\ln 10}{A_f - A_s}, \quad b_A = \frac{a_A}{C_A} \qquad (M \to A)
\end{aligned} \tag{4.25}$$

4.4 Thermal effects

Although the heat exchanges between the SE material and its surrounding environment generates almost isothermic processes, when quasi-static loading conditions are present, as the rate of the dynamic loading increases, the total amount of generated energy per unit time increases accordingly. For fast dynamic cycling, since the dissipation capacity of the thermo-mechanical system is limited by the heat convection mechanism, the generated and the dissipated energy become unbalanced, causing the specimen's temperature to change, as well as the shape of the hysteretic loop. For a SMA constitutive model to conveniently apprehend this phenomena, it is necessary to couple, together with the mechanical and kinetic transformation laws, an adequate heat balance equation. In this section, the heat transfer problem is addressed.

The heat transfer system, as illustrated in Figure 4.3, consists of a cylindrical Nitinol wire with a circular cross section, fixed at both extremities and surrounded by air, at temperature T_f. There are internal energy sources, within the wire, deriving from the enthalpy of the martensitic transformations and internal friction, both occurring during a hysteretic SE cycle. It is assumed that the heat conduction through the wire's extremities is negligible. The differential formulation for the problem of temperature distribution in a cylinder with uniform heat generation is

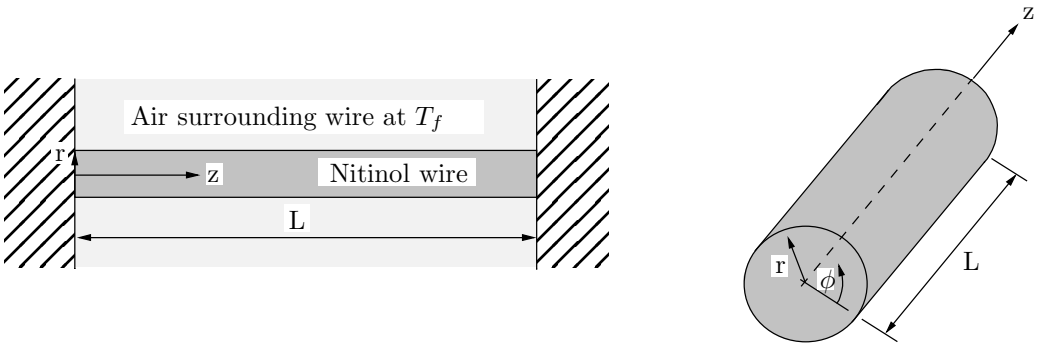

Figure 4.3: Cylindrical Nitinol wire surrounded by air.

first addressed.

In the presence of a temperature gradient inside a given body, heat flows from the regions with higher temperatures to the regions with lower temperatures. This phenomenon, known as conduction heat transfer, is described by Fourier's Law of conduction [161]. In Cartesian coordinates, the Fourier Law takes the following form,

$$\mathbf{q} = -k \left(\frac{\partial T}{\partial x}\mathbf{i} + \frac{\partial T}{\partial y}\mathbf{j} + \frac{\partial T}{\partial z}\mathbf{k} \right) = -k \, \nabla T \tag{4.26}$$

where the heat flux vector $\mathbf{q}$ is the heat transfer rate ($\dot{Q}$) per unit area, k is the thermal conductivity and $\mathbf{i}$, $\mathbf{j}$ and $\mathbf{k}$ represent the unit vectors. This is a property that describes the rate at which heat flows within a body for a given temperature gradient. The minus sign ensures that heat flows down the temperature gradient, in compliance with the second law of thermodynamics.

Applying the first law of thermodynamics (conservation of energy) to a small element within the body, one obtains

$$\nabla \mathbf{q} = q_{gen} - \frac{\mathrm{d}e}{\mathrm{d}t} \tag{4.27}$$

The power generated per unit volume is expressed by q_{gen} describes the rate of heat generation within a body. Typically, this new heat must be conducted to the body boundaries and removed via convection and/or radiation heat transfer [161]. The change in the internal energy e, which is a measure of the internal energy stored within a material per unit volume, is related to the body's ability to store heat by raising its temperature [161]

$$\frac{\mathrm{d}e}{\mathrm{d}t} = \rho c \frac{\mathrm{d}T}{\mathrm{d}t} \tag{4.28}$$

In the above relation, ρ is the density of the material and c its specific heat, a material property that indicates the amount of energy a body stores for each degree increase in temperature, on a per unit mass basis.

The energy equation may be obtained substituting the Fourier's Law of heat conduction in equation (4.27) and using definition (4.28) for the change in the internal energy,

$$\nabla^2 T - \frac{\rho c}{k}\frac{\mathrm{d}T}{\mathrm{d}t} = -\frac{q_{gen}}{k} \tag{4.29}$$

It can be concluded that the temperature profile within a body depends upon the rate of its internally-generated heat, its capacity to store some of this heat, and its rate of thermal conduction to its boundaries [161].

The energy equation (4.29) can be rewritten using cylindrical coordinates; see Figure 4.3, as:

$$\frac{1}{r}\frac{\partial}{\partial r}\left(r\frac{\partial T}{\partial r}\right) + \frac{1}{r^2}\frac{\partial^2 T}{\partial \phi^2} + \frac{\partial^2 T}{\partial z^2} - \frac{\rho c}{k}\frac{\partial T}{\partial t} = -\frac{q_{gen}}{k},\ T = T(r,\phi,z,t) \tag{4.30}$$

Since the cylindrical Nitinol wire is surrounded by air, the heat transfer mechanism is called convection. In convection, the conduction heat transfer mechanism always plays a primary role. Regarding the mechanisms in which fluid motion is produced, convection systems are characterized in forced convection and natural convection. While natural convection is caused by temperature-induced density gradients within the fluid, forced convection involves fluid motion caused by mechanical means, such as pumps and fans [76].

A practical approach to the analysis of convection heat transfer from surfaces has been developed in [161], which employs an equation of the form,

$$q_c = \overline{h} A_s (T_s - T_f) \tag{4.31}$$

where q_c is the heat flux transferred from a surface at uniform temperature T_s to a fluid with reference temperature T_f, A_s is the surface area and $\overline{h}$ is the mean coefficient of heat transfer. Equation (4.31) is usually referred to as the Newton law of cooling [161].

In convection, the mean coefficient of heat transfer replaces the role of the thermal conductivity that appears in conduction heat transfer, present in the Fourier's

Law (4.26). The mean coefficient of heat transfer depends upon the hydrodynamic conditions as well as on the thermodynamic and thermophysical properties of the fluid.

In some cases, for particular values of the Biot number, the energy equation (4.30) can be further simplified. The Biot number (Bi) is defined as

$$Bi = \frac{\overline{h} L_c}{k} \tag{4.32}$$

where L_c is the characteristic length, commonly defined as the volume of the body divided by the surface area of the body, such that $L_c = V_b/A_s$. The Biot number is a dimensionless number that gives a simple index of the ratio of the heat transfer resistances inside and at the surface of a body. This ratio determines whether or not the temperatures inside a body will vary significantly in space, while the body heats or cools over time [76]. For small values of the Biot number, the variation of temperature within the cylindrical Nitinol wire is essentially independent of r. Values of the Biot number less than 0.1 imply that the heat conduction inside the body is much faster than the heat convection away from its surface, and temperature gradients are negligible inside of it. In these cases, the use of an one-dimensional analysis leads to an error less than about 10% [161]. According to [76], the energy equation expressed in (4.30), can be thus simplified to the following form,

$$-\rho c V \frac{\mathrm{d}T}{\mathrm{d}t} = \overline{h} A \left[T - T_f\right] - q_{gen} V \qquad \text{with } T(0) = T_f \tag{4.33}$$

The power generated per unit volume, is described by,

$$q_{gen} = c_L \rho \frac{\mathrm{d}\xi}{\mathrm{d}t} + \frac{\mathrm{d}W}{\mathrm{d}t} \tag{4.34}$$

The first term is related to the martensite fraction, assuming constant latent heat of transformation, c_L, and the second term to internal friction. In a complete tensile loading-unloading cycle, the dissipated energy by internal friction corresponds to the total area enclosed by the hysteretic cycle. The total generated power during this cycle may, therefore, be computed by dividing the dissipated energy by the duration of the cycle.

4.5 Adopted constitutive models for SMAs

Three mathematical models for describing the mechanical behavior of SMAs, in terms of the stress-strain diagram, have been presented. These models assume that the transformed phase fraction is in series with the elastic fraction of the response. While one of the models only accounts for austenite, to describe this fraction, the other models already contemplate two different crystallographic phases, austenite and martensite. The difference between these last models, which do not distinguish between the twinned and the detwinned martensite, is in the phase distribution within the material. One of the models considers a parallel phase distribution while the other assumes an orthogonal one. Regarding the kinetic transformation laws, the discussed examples were a linear kinetic model and an exponential one. Based on these relations, two different constitutive models, describing the one-dimensional behavior of SMAs are build, as shown in Figure 4.4. They both couple a mechanical law with a set of kinetic laws, governing the forward and inverse transformations behavior. One of the constitutive models also takes into account an additional thermal balance equation. The first model uses the mechanical law which only considers

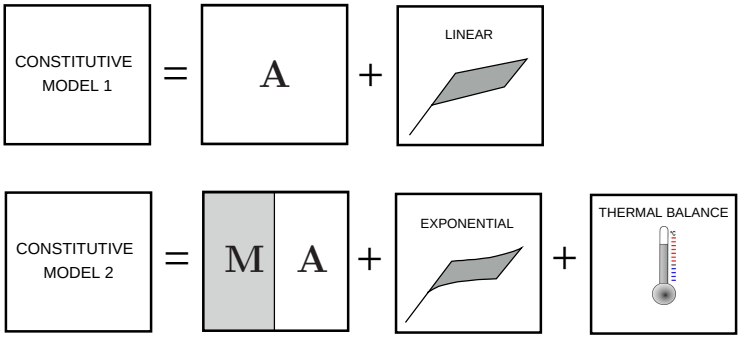

Figure 4.4: Description of the constitutive models.

austenite for the elastic fraction of the response, coupled with a set of linear kinetic laws, making it very simple and straightforward to implement. However, since it is not able to cope with temperature variations within a SMA specimen it is only well suited for quasi-static loadings, with almost isothermal processes. Therefore, this is a rate-independent constitutive model. The second constitutive model uses the mechanical law with the parallel phase distribution together with exponential kinetic laws and a thermal balance equation. This enables it to apprehend the convective heat transfer problem taking place during faster dynamic cycling, making it

a rate-dependent constitutive model.

4.6 Numerical implementation of the models

Having discussed the theoretical background concerning the two SMA constitutive models, the numerical implementation of these models is now addressed. These numerical implementations are based on strain-driven, time-discrete models, and are aimed to simulate the SE behavior of SMA's under uniaxial loadings. The numerical algorithms are implemented in a Matlab R2007a environment.

4.6.1 Numerical implementation of the rate-independent constitutive model

The rate-independent constitutive model is based on the assumption that the relation between strains and stresses is represented by a series of linear segments. The material parameters characterizing the model are the austenitic elastic modulus E_A, the strain associated with the transformation process ε_L, the starting and final stresses during the forward transformation, σ_s^{AM} and σ_f^{AM} and the corresponding stresses during the inverse transformation, σ_s^{MA} and σ_f^{MA}. The linear kinetic laws describing the forward and inverse transformations are defined as,

$$\xi^{AM} = \frac{\sigma - C_M(T - M_s)}{C_M(M_s - M_f)} \quad \text{with} \quad \sigma_s^{AM} < \sigma < \sigma_f^{AM} \quad \text{and} \quad \dot{\sigma} > 0$$
$$\xi^{MA} = \frac{\sigma - C_A(T - A_f)}{C_A(A_f - A_s)} \quad \text{with} \quad \sigma_f^{MA} < \sigma < \sigma_s^{MA} \quad \text{and} \quad \dot{\sigma} < 0$$

where ξ is a scalar internal variable representing the martensite fraction during the phase transformation.

For a given temperature T, the starting and final stresses during the forward transformation (σ_s^{AM}, σ_f^{AM}) may be computed using the equations that define the boundary lines of the corresponding transformation strips. Assuming a time-continuous model, the time evolution of the martensite fraction, is expressed using a stress-driven linear kinetic rule to yield its corresponding evolution equation. For the

forward transformation one has,

$$\xi^{AM} = \frac{\sigma - \sigma_s^{AM}}{\sigma_f^{AM} - \sigma_s^{AM}}$$
$$\dot{\xi}^{AM} = \frac{\dot{\sigma}}{\sigma_f^{AM} - \sigma_s^{AM}} = -(1 - \xi^{AM}) \frac{\dot{\sigma}}{\sigma - \sigma_f^{AM}} \tag{4.35}$$

In the case of the inverse transformation, the martensite fraction and its evolution equation reads,

$$\xi^{MA} = \frac{\sigma - \sigma_f^{MA}}{\sigma_s^{MA} - \sigma_f^{MA}}$$
$$\dot{\xi}^{MA} = \frac{\dot{\sigma}}{\sigma_s^{MA} - \sigma_f^{MA}} = \xi^{MA} \frac{\dot{\sigma}}{\sigma - \sigma_f^{MA}} \tag{4.36}$$

On the other hand, stress and its evolution equation, for the mechanical law which only considers austenite for the elastic fraction of the response (4.5), are defined as,

$$\sigma = E_A(\varepsilon - \varepsilon_L \xi) \quad \text{and} \quad \dot{\sigma} = E_A(\dot{\varepsilon} - \varepsilon_L \dot{\xi}) \tag{4.37}$$

Replacing $\dot{\sigma}$, in the transformation kinetic relations expressed by equations (4.35) and (4.36), it yields

$$\dot{\xi}^{AM} = \frac{(1 - \xi^{AM}) E_A \dot{\varepsilon}}{(1 - \xi^{AM}) E_A \varepsilon_L + \sigma_f^{AM} - \sigma} \tag{4.38}$$

and

$$\dot{\xi}^{MA} = \frac{\xi^{MA} E_A \dot{\varepsilon}}{\xi^{MA} E_A \varepsilon_L - \sigma_f^{MA} + \sigma} \tag{4.39}$$

for the forward and inverse transformations, respectively.

One wants to approximate the solution of the initial value problem

$$\dot{y} = f(t, y), \quad \text{with} \quad y(t_0) = y_0 \tag{4.40}$$

by using the first two terms of the Taylor expansion of y, representing the linear approximation around the point $(t_0, y(t_0))$. Defining the incremental quantity

$\Delta t_n = t_{n+1} - t_n$, one may write

$$y_{n+1} = y_n + \Delta t_n f(t_n, y_n) \tag{4.41}$$

This first-order numerical procedure for solving ordinary differential equations, with a given initial value, is called the Euler method [9]. The Euler method is an example of an explicit method, where y_{n+1} is defined by terms that are already known, like y_n. Let one define the additional incremental quantities,

$$\begin{aligned} &\xi_n = \xi_{n+1} - \xi_n, \quad \Delta\varepsilon_n = \varepsilon_{n+1} - \varepsilon_n \\ &\Delta T_n = T_{n+1} - T_n \quad \text{and} \quad \Delta W_n = W_{n+1} - W_n \end{aligned} \tag{4.42}$$

The use of the Euler method enables the transformation of the time-continuous evolutionary equations (4.38) and (4.39), into time-discrete evolutionary equations,

$$\Delta\xi_n^{AM} = \frac{(1-\xi^{AM})E_A\Delta\varepsilon_n}{(1-\xi^{AM})E_A\varepsilon_L + \sigma_f^{AM} - \sigma} \tag{4.43}$$

for the forward transformation time-discrete evolutionary equation, and

$$\Delta\xi_n^{MA} = \frac{\xi^{MA}E_A\Delta\varepsilon_n}{\xi^{MA}E_A\varepsilon_L - \sigma_f^{MA} + \sigma} \tag{4.44}$$

for the inverse transformation time-discrete evolutionary equation.

Finally, it is possible to obtain the equations describing the evolution of the martensite fraction according to the strain history. In particular, for the conversion of austenite into martensite one has,

$$\xi_{n+1}^{AM} = \xi_n^{AM} + \frac{(1-\xi_n^{AM})E_A(\varepsilon_{n+1} - \varepsilon_n)}{(1-\xi_n^{AM})E_A\varepsilon_L + \sigma_f^{AM} - \sigma_n} \tag{4.45}$$

while for the conversion of martensite into austenite one has,

$$\xi_{n+1}^{MA} = \xi_n^{MA} + \frac{\xi_n^{MA}E_A(\varepsilon_{n+1} - \varepsilon_n)}{\xi_n^{MA}E_A\varepsilon_L - \sigma_f^{MA} + \sigma_n} \tag{4.46}$$

Note that, in the above equations, the subscripts n and $n+1$ indicates quantities

evaluated at times t_n and t_{n+1}, respectively. Although the time-continuous model is stress-driven, the time-discrete model assumes strain as the control variable. The choice is consistent with the fact that, from the point of view of the integration scheme, the time-discrete problem is considered strain-driven.

4.6.2 Algorithm for the rate-independent constitutive model

The implemented algorithm for the rate-independent (R-I) constitutive model is presented next:

1. Initial calculations
   (a) Define T_f (ambient temperature), $\dot{\varepsilon}$ (strain-rate) and Δt
   (b) For $i = 0$, initialize T_0, ε_0, σ_0 and ξ_0
2. Calculations for every time step, i
   (a) Evaluate the strain increment by multiplying the strain-rate by the discrete time parameter and update the strain,

$$\varepsilon_{i+1} = \varepsilon_i + \dot{\varepsilon}\Delta t$$

   (b) Solve the system of equations formed by the constitutive and one of the kinetic laws to obtain the martensite fraction and stress,

$$\begin{cases} \xi_{i+1}^{AM} = \xi_i^{AM} + \dfrac{(1-\xi_i^{AM})E_A(\varepsilon_{i+1}-\varepsilon_i)}{(1-\xi_i^{AM})E_A\varepsilon_L + \sigma_f^{AM} - \sigma_i} \\ \sigma_{i+1} = E_A(\varepsilon_{i+1} - \varepsilon_L\xi_{i+1}^{AM}) \end{cases}$$

   for the forward transformation, and

$$\begin{cases} \xi_{i+1}^{MA} = \xi_i^{MA} + \dfrac{\xi_i^{MA}E_A(\varepsilon_{i+1}-\varepsilon_i)}{\xi_i^{MA}E_A\varepsilon_L - \sigma_f^{MA} + \sigma_i} \\ \sigma_{i+1} = E_A(\varepsilon_{i+1} - \varepsilon_L\xi_{i+1}^{MA}) \end{cases}$$

   for the inverse transformation

3. Repetition for the next time step. Replace i by $i+1$ and goto step 2, for the next time step. Stop when reached the final time.

4.6.3 Numerical implementation of the rate-dependent constitutive model

The exponential kinetic laws describing the forward and inverse transformations, for the rate-dependent model, are defined by,

$$\dot{\xi}^{AM} = (1-\xi)(a_M\dot{T} - b_M\dot{\sigma}) \tag{4.47}$$

and

$$\dot{\xi}^{MA} = \xi(-a_A\dot{T} + b_A\dot{\sigma}) \tag{4.48}$$

Stress and its time-derivative, according to the mechanical law proposed by Tanaka, expressed by equation (4.8), in which, without loss of generality, T_0 is assumed to be zero, read,

$$\begin{aligned} \sigma &= [\xi(E_M - E_A) + E_A](\varepsilon - \varepsilon_L\xi) + \theta T \\ \dot{\sigma} &= E(\xi)\dot{\varepsilon} + H(\xi)\dot{\xi} + \theta\dot{T} \end{aligned} \tag{4.49}$$

where

$$E(\xi) = \xi(E_M - E_A) + E_A \tag{4.50}$$

and

$$H(\xi) = (E_M - E_A)(\varepsilon - \varepsilon_L\xi) - \varepsilon_L E(\xi) \tag{4.51}$$

Replacing $\dot{\sigma}$, in the transformation kinetic relations expressed in equations (4.47) and (4.48), yields,

$$\dot{\xi}^{AM} = \frac{(1-\xi^{AM})[(a_M - b_M\theta)\dot{T} - b_M E(\xi)\dot{\varepsilon}]}{1 + (1-\xi^{AM})b_M H(\xi)} \tag{4.52}$$

for the forward transformation, and

$$\dot{\xi}^{MA} = \frac{\xi^{MA}[(-a_A + b_A\theta)\dot{T} + b_A E(\xi)\dot{\varepsilon}]}{1 - \xi^{MA}b_A H(\xi)} \tag{4.53}$$

for the inverse transformation. Reformulating equations (4.52) and (4.53), using the definitions for the incremental quantities in (4.42), yields the increment of the martensite fraction for the forward transformation,

$$\Delta\xi_n^{AM} = \frac{(1-\xi^{AM})[(a_M - b_M\theta)\Delta T - b_M E(\xi)\Delta\varepsilon]}{1+(1-\xi^{AM})b_M H(\xi)} \tag{4.54}$$

and the correspondent martensite fraction increment for the inverse transformation,

$$\Delta\xi_n^{MA} = \frac{\xi^{MA}[(-a_A + b_A\theta)\Delta T + b_A E(\xi)\Delta\varepsilon]}{1-\xi^{MA}b_A H(\xi)} \tag{4.55}$$

Hence, one can obtain the equations describing the evolution of the martensite fraction according to the strain and temperature histories. In particular, for the conversion of austenite into martensite one has,

$$\begin{aligned}\xi_{n+1}^{AM} &= \xi_n^{AM} + (1-\xi_n^{AM})\left[\frac{(a_M - b_M\theta)(T_{n+1}-T_n)}{1+(1-\xi_n^{AM})b_M H(\xi_n)} - \right. \\ &\left. - \frac{b_M E(\xi_n)(\varepsilon_{n+1}-\varepsilon_n)}{1+(1-\xi_n^{AM})b_M H(\xi_n)}\right]\end{aligned} \tag{4.56}$$

while for the conversion of martensite into austenite one has,

$$\begin{aligned}\xi_{n+1}^{MA} &= \xi_n^{MA} + \xi_n^{MA}\left[\frac{(-a_A + b_A\theta)(T_{n+1}-T_n)}{1-\xi_n^{MA}b_A H(\xi_n)} + \right. \\ &\left. + \frac{b_A E(\xi_n)(\varepsilon_{n+1}-\varepsilon_n)}{1-\xi_n^{MA}b_A H(\xi_n)}\right]\end{aligned} \tag{4.57}$$

Having implemented the mechanical and kinetic laws of the rate-dependent constitutive model, one still has to couple these relations with a heat balance equation, like the one described in (4.33). According to (4.33) and (4.34), this equation may be written in the following way,

$$-\rho c V\dot{T} = \overline{h}A\,(T - T_f) - V\left(c_L\rho\dot{\xi} + \dot{W}\right) \tag{4.58}$$

which, expressed in function of $\dot{T}$, reads,

$$\dot{T} = -\frac{\overline{h}A(T-T_f)}{\rho c V} + \frac{c_L\dot{\xi}}{c} + \frac{\dot{W}}{\rho c} \tag{4.59}$$

Reformulating the time-continuous heat balance equation (4.59), using the incremental quantities defined in (4.42), enables one to define its time-discrete incremental form, which is expressed in the following way,

$$\Delta T_n = -\frac{\overline{h}A(T - T_f)\Delta t_n}{\rho c V} + \frac{c_L \Delta \xi_n}{c} + \frac{\Delta W_n}{\rho c} \tag{4.60}$$

This allows one to compute the evolutionary heat balance equation,

$$\begin{aligned} T_{n+1} &= T_n - \frac{\overline{h}A(T_n - T_f)(t_{n+1} - t_n)}{\rho c V} + \frac{c_L(\xi_{n+1} - \xi_n)}{c} + \\ &+ \frac{W_{n+1} - W_n}{\rho c} \end{aligned} \tag{4.61}$$

The evolution of the dissipated energy as the transformation proceeds can be derived from the area enclosed by partial cycles [122]. In Figure 4.5, the numeric approach used for the computation of ΔW_n, for a given time step, is explained. Four different time steps are displayed, representing four particular situations during the development of the hysteretic process. *Time step 1*, represented in Figure 4.5(a),

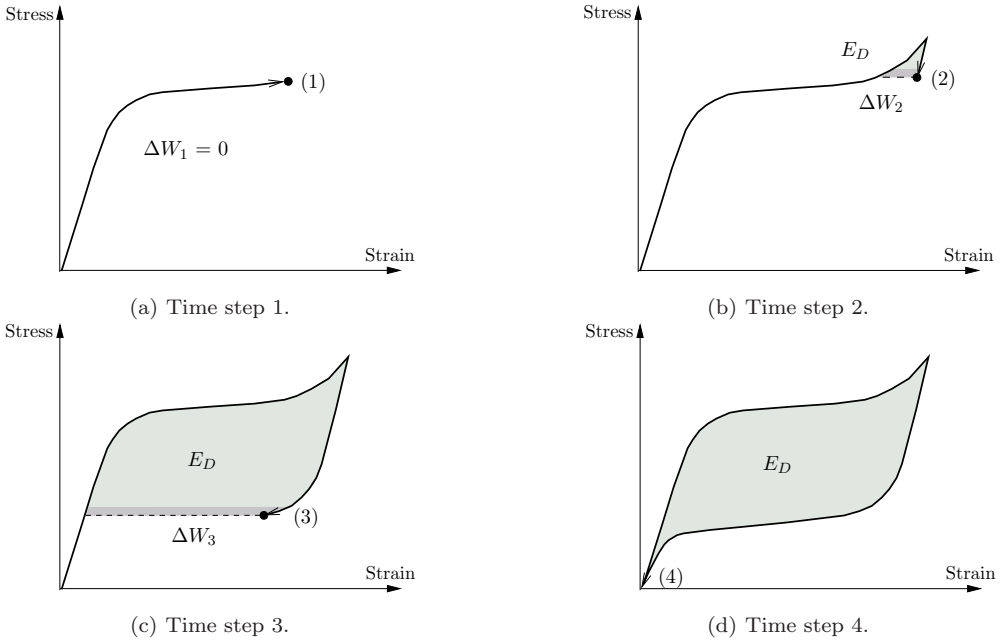

(a) Time step 1. (b) Time step 2.

(c) Time step 3. (d) Time step 4.

Figure 4.5: Computation of ΔW_n.

corresponds to a time step occurring during the forward transformation. During the forward transformation, as well as in the pure austenitic elastic phase, the numeric

model considers no energy dissipation, since the area enclosed by the hysteresis is null. As the strain reaches is maximum value and subsequently starts to decrease, the dissipated energy E_D starts to grow. *Time step 2*, in Figure 4.5(b), corresponds to a time step in this situation. During the reverse transformation, *Time step 3* in Figure 4.5(c), E_D continues to grow, as the hysteretic cycles approaches the pure austenitic phase again. At the end of the hysteretic cycle, *Time step 4* in Figure 4.5(d), the total amount of dissipated energy due to internal friction is attained.

4.6.4 Algorithm for the rate-dependent constitutive model

The implemented algorithm for the rate-dependent (R-D) constitutive model is presented next:

1. Initial calculations
   (a) Define T_f (ambient temperature), $\dot{\varepsilon}$ (strain-rate) and Δt
   (b) For $i = 0$, initialize T_0, ε_0, σ_0 and ξ_0
2. Calculations for every time step, i
   (a) Evaluate the strain increment by multiplying the strain-rate by the discrete time parameter and update the strain,

$$\varepsilon_{i+1} = \varepsilon_i + \dot{\varepsilon}\Delta t$$

   (b) Solve the system of equations formed by the balance thermal equation, constitutive law, and one of the kinetic laws to obtain the temperature, martensite fraction and stress,

$$\begin{cases} T_{i+1} = T_i - \dfrac{\overline{h}A(T_i - T_f)(t_{i+1} - t_i)}{\rho c V} + \dfrac{c_L(\xi_{i+1}^{AM} - \xi_i^{AM})}{c} \\ \xi_{i+1}^{AM} = \xi_i^{AM} + (1 - \xi_i^{AM}) \left[\dfrac{(a_M - b_M\theta)(T_{i+1} - T_i)}{1 + (1 - \xi_i^{AM}) b_M H(\xi_i)} - \right. \\ \qquad \left. - \dfrac{b_M E(\xi_i)(\varepsilon_{i+1} - \varepsilon_i)}{1 + (1 - \xi_i^{AM}) b_M H(\xi_i)} \right] \\ \sigma_{i+1} = E(\xi_{i+1})(\varepsilon_{i+1} - \varepsilon_L \xi_{i+1}^{AM}) + \theta T_{i+1} \end{cases}$$

$$\begin{cases} T_{i+1} = T_i - \dfrac{\overline{h}A(T_i - T_f)(t_{i+1} - t_i)}{\rho c V} + \dfrac{c_L(\xi_{i+1}^{MA} - \xi_i^{MA})}{c} + \\ \quad + \dfrac{W_{i+1} - W_i}{\rho c} \\ \xi_{i+1}^{MA} = \xi_i^{MA} \left[\dfrac{(-a_A + b_A\theta)(T_{i+1} - T_i)}{1 - \xi_i^{MA} b_A H(\xi_i)} + \right. \\ \quad \left. + \dfrac{b_A E(\xi_i)(\varepsilon_{i+1} - \varepsilon_i)}{1 - \xi_i^{MA} b_A H(\xi_i)} \right] \\ \sigma_{i+1} = E(\xi_{i+1})(\varepsilon_{i+1} - \varepsilon_L \xi_{i+1}^{MA}) + \theta T_{i+1} \end{cases}$$

3. Repetition for the next time step. Replace i by $i+1$ and goto step 2 for the next time step. Stop when reached the final time.

To solve the system of equations associated with the forward transformation, ξ_{i+1}^{AM} may be written in the following form

$$\xi_{i+1}^{AM} = \xi_i^{AM} + \psi_1^{AM}(\xi_i)(T_{i+1} - T_i) - \psi_2^{AM}(\xi_i, \varepsilon_i) \tag{4.62}$$

where

$$\psi_1^{AM}(\xi_i) = \frac{(1 - \xi_i^{AM})(a_M - b_M\theta)}{1 + (1 - \xi_i^{AM}) b_M H(\xi_i)} \tag{4.63}$$

and

$$\psi_2^{AM}(\xi_i, \varepsilon_i) = \frac{(1 - \xi_i^{AM}) b_M E(\xi_i)(\varepsilon_{i+1} - \varepsilon_i)}{1 + (1 - \xi_i^{AM}) b_M H(\xi_i)} \tag{4.64}$$

Replacing equation (4.62) in the time-discrete heat balance equation (4.59), one obtains

$$\begin{aligned} T_{i+1} &= T_i - \frac{\overline{h}A(T_i - T_f)(t_{i+1} - t_i)}{\rho c V} + \\ &\quad + \frac{c_L[\psi_1^{AM}(\xi_i)(T_{i+1} - T_i) - \psi_2^{AM}(\xi_i, \varepsilon_i)]}{c} \end{aligned}$$

which simplifies to the following expression, the explicit form of the temperature associated with time step t_{i+1}, for the forward transformation,

$$\begin{aligned} T_{i+1} &= \frac{c}{c - c_L \psi_1^{AM}(\xi_i)} \left\{ T_i - \frac{\overline{h} A (T_i - T_f)(t_{i+1} - t_i)}{\rho c V} - \right. \\ &\left. - \frac{c_L [\psi_1^{AM}(\xi_i) T_i + \psi_2^{AM}(\xi_i, \varepsilon_i)]}{c} \right\} \end{aligned} \tag{4.65}$$

Substituting equation (4.65) on equation (4.62) one can calculate the corresponding martensite fraction. To solve the system of equations associated with the inverse transformation, ξ_{i+1}^{MA} may be written in the following form

$$\xi_{i+1}^{MA} = \psi_1^{MA}(\xi_i)(T_{i+1} - T_i) + \psi_2^{MA}(\xi_i, \varepsilon_i) \tag{4.66}$$

where

$$\psi_1^{MA}(\xi_i) = \frac{\xi_i^{MA}(-a_A + b_A \theta)}{1 - \xi_i^{MA} b_A H(\xi_i)} \tag{4.67}$$

and

$$\psi_2^{MA}(\xi_i, \varepsilon_i) = \frac{\xi_i^{MA} b_A E(\xi_i)(\varepsilon_{i+1} - \varepsilon_i)}{1 - \xi_i^{MA} b_A H(\xi_i)} \tag{4.68}$$

Replacing equation (4.68) in the time-discrete heat balance equation (4.59), one obtains

$$\begin{aligned} T_{i+1} &= T_i - \frac{\overline{h} A (T_i - T_f)(t_{i+1} - t_i)}{\rho c V} + \\ &+ \frac{c_L [\psi_1^{MA}(\xi_i)(T_{i+1} - T_i) + \psi_2^{MA}(\xi_i, \varepsilon_i) - \xi_i^{MA}]}{c} + \\ &+ \frac{W_{i+1} - W_i}{\rho c} \end{aligned}$$

which simplifies to the following expression, the explicit form of the temperature associated with time step t_{i+1}, for the forward transformation,

$$\begin{aligned} T_{i+1} &= \frac{c}{c - c_L \psi_1^{MA}(\xi_i)} \left\{ T_i - \frac{\overline{h} A (T_i - T_f)(t_{i+1} - t_i)}{\rho c V} + \right. \\ &+ \frac{c_L[-\psi_1^{MA}(\xi_i) T_i + \psi_2^{MA}(\xi_i, \varepsilon_i) - \xi_i^{MA}]}{c} + \\ &+ \left. \frac{W_{i+1} - W_i}{\rho c} \right\} \end{aligned} \tag{4.69}$$

The main difficulty in solving this equation is related to the computation of its last term, ΔW_i. In Figure 4.6, ΔW_n is graphically represented, defining a planar, non-self-intersecting polygon, with vertices $P_1(x_1, y_1)$ to $P_4(x_4, y_4)$.

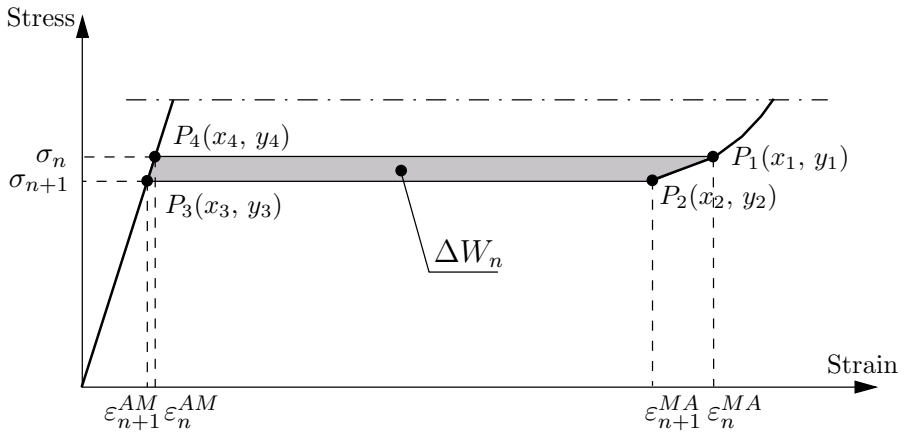

Figure 4.6: Computation of the poligonal area.

The area of a polygon with vertices (x_1,y_1), ..., (x_n,y_n) is given [173] by

$$A = \frac{1}{2} \left| \sum_{i=1}^{n} (x_i y_{i+1} - x_{i+1} y_i) \right| \tag{4.70}$$

To close the polygon, the first and last vertices are the same, i.e., x_{n+1},$y_{n+1} = x_1$,y_1. Replacing the vertices coordinates x_i and y_i with the corresponding strains and

stresses represented in Figure 4.6, it yields,

$$\begin{aligned}\Delta W_n &= \frac{1}{2}(\varepsilon_n^{MA}\sigma_{n+1} - \varepsilon_{n+1}^{MA}\sigma_n + \varepsilon_{n+1}^{MA}\sigma_{n+1} - \varepsilon_{n+1}^{AM}\sigma_{n+1} + \\ &\quad + \varepsilon_{n+1}^{AM}\sigma_n - \varepsilon_n^{AM}\sigma_{n+1} + \varepsilon_n^{AM}\sigma_n - \varepsilon_n^{MA}\sigma_n)\end{aligned}$$

which simplifies to

$$\Delta W_n = \frac{1}{2}(\varepsilon_{n+1}^{MA} + \varepsilon_n^{MA} - \varepsilon_{n+1}^{AM} - \varepsilon_n^{AM})(\sigma_{n+1} - \sigma_n) \tag{4.71}$$

where $\varepsilon_n^{AM}(\sigma_n)$ and $\varepsilon_{n+1}^{AM}(\sigma_{n+1})$ represent the strains corresponding to σ_n and σ_{n+1} during the forward transformation. This means that ΔW_i may be computed by

$$\frac{W_{i+1} - W_i}{\rho c} = \frac{1}{2\ \rho c}(\varepsilon_{i+1}^{MA} + \varepsilon_i^{MA} - \varepsilon_{i+1}^{AM} - \varepsilon_i^{AM})(\sigma_{i+1} - \sigma_i) \tag{4.72}$$

Since it is difficult to write the strain value $\varepsilon_{i+1}^{AM}(\sigma_{i+1})$ as an algebraic expression, it is assumed that $\Delta W_i \approx \Delta W_{i-1}$ and hence, equation (4.72) may be approximated by

$$\frac{W_{i+1} - W_i}{\rho c} \approx \frac{1}{2\ \rho c}(\varepsilon_i^{MA} + \varepsilon_{i-1}^{MA} - \varepsilon_i^{AM} - \varepsilon_{i-1}^{AM})(\sigma_i - \sigma_{i-1}) \tag{4.73}$$

In order to solve equation (4.73), a simple iterative searching algorithm is implemented, to extract the values ε_i^{AM} and ε_{i-1}^{AM} from the strain vector, knowing σ_i and σ_{i-1}. Substituting equation (4.73) in equation (4.69), and finally in equation (4.66) one can calculate the corresponding martensite fraction at step i+1.

4.7 Numerical assessment of the models

The objective of this section is the calibration of the implemented numerical models and the assessment of their performance in the simulation of the SE stress-strain response of SMA wires.

4.7.1 Quasi-static tests

The experimental stress-strain responses, previously presented in Figure 3.12 for a 2.40 mm diameter Nitinol S wire are compared with the numerical responses obtained with the rate-independent and rate-dependent models. These quasi-static experimental tensile tests were carried out at a strain-rate of 0.020%/s, at an ambient temperature of 24°C.

The thermophysical properties used to characterize the numerical models, such as the latent heat, c_L, the specific heat, c_p, the density, ρ, the mean convection coefficient, $\overline{h}$, the coefficient of thermal expansion, θ, and the conduction coefficient, k, are the ones reported in [169], which are presented in Table 4.1.

$E_A = 22500$ MPa	$E_M = 19000$ MPa	$M_f = -52^\circ$ C
$M_s = -37^\circ$ C	$A_s = 2^\circ$ C	$A_f = 12^\circ$ C
$C_M = 6.5$ MPaK^{-1}	$C_A = 6.5$ MPaK^{-1}	$e_L = 4.15\%$
$\rho = 6500$ kg m^{-3}	$c_L = 12914$ J kg^{-1}	$c = 500$ J kg^{-1}K^{-1}
$\overline{h} = 35$ W m^{-2} K^{-1}	$\theta = 0.55$ MPaK^{-1}	$k = 18$ W m^{-1} K^{-1}

Table 4.1: Parameters for the quasi-static tensile tests.

According to definition (4.32) the Biot number for a cylindrical wire of radius r is given by,

$$Bi = \frac{\overline{h} r}{2\ k} \tag{4.74}$$

The values considered for the mean convection coefficient $\overline{h}$ and the conduction coefficient k, yield for the Biot number a value of $Bi = 0.0012$. As this value is less than 0.1, according to [76], one may consider uniform temperature within the Nitinol wire.

Both models are able to describe a wide variety of loading histories, with numerical predictions that fit well the experimental data. This is illustrated by the graphs in Figures 4.7 and 4.8, depicting the stress-strain diagrams obtained with the two numerical models together with the corresponding experimental ones, for three complete cycles of decreasing amplitude and a complete cycle followed by a smaller inner cycle.

Particularly good estimates are obtained during the forward transformation, when

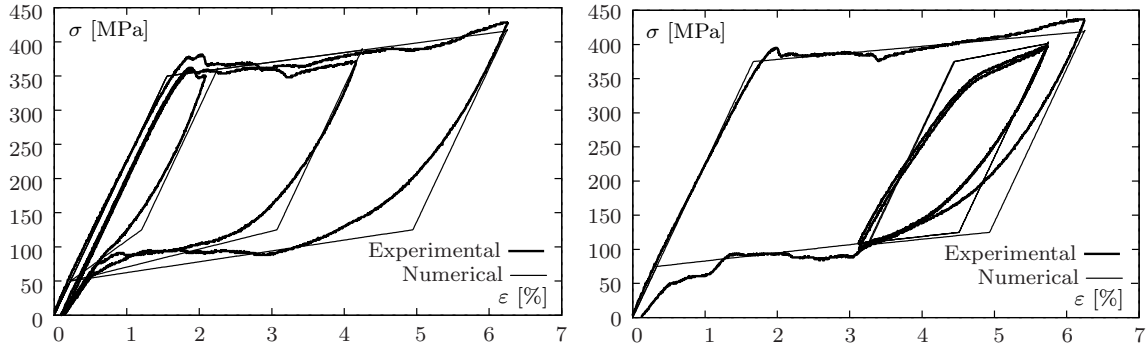

(a) Three complete cycles of decreasing amplitude (b) Complete cycle followed by small inner cycle

Figure 4.7: Rate-independent numerical model vs. experimental data: quasi-static loading.

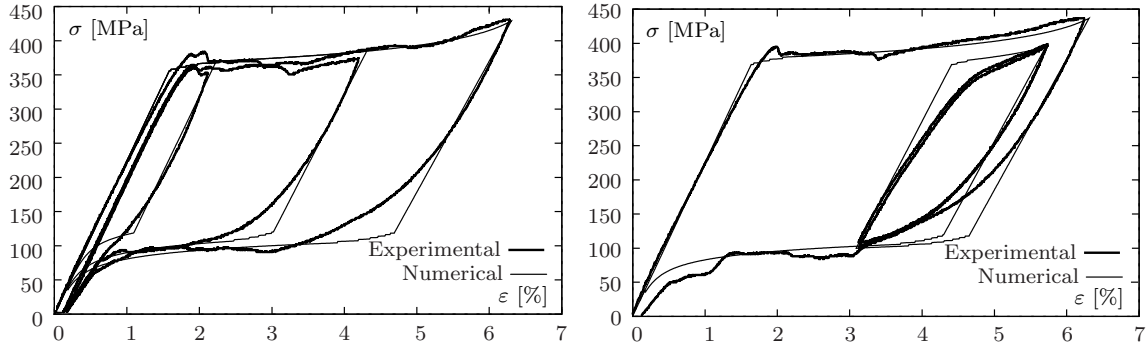

(a) Three complete cycles of decreasing amplitude (b) Complete cycle followed by small inner cycle

Figure 4.8: Rate-dependent numerical model vs. experimental data: quasi-static loading.

the relative errors between the experimental data and the simulations are practically negligible, especially for the rate-dependent model. However, upon unloading, apart from the initial segment, where the stiffness is accurately captured, both models seem to overestimate the SMAs stiffness. This is due to the fact that they do not capture the gradual transition to the inverse transformation plateau.

Apart from the pure austenitic elastic response, the rate-independent model overestimates the system's stiffness. This is because its constitutive law uses the austenitic Young's modulus instead of a combination of the austenitic and the lower martensitic elastic modulus, like the rate-dependent model does. This effect is particularly important during the elastic unloading of the fully transformed stress induced martensite, where the error associated with the Young's modulus is higher, but also in the elastic response during the inner cycles, in the coexistence zone. The kinetic

law used in the rate-dependent model enables it to provide much smother responses during the forward and inverse transformations, especially when approaching the final segment of both the transformations, due to its exponential nature.

Being a model of straightforward numerical implementation, the rate-independent constitutive model is, nonetheless, able to describe the response of the material to complex uniaxial loading histories. It yields a very accurate set of results for quasi-static tests, when isothermal conditions can be assumed.

4.7.2 Dynamic tests

Isothermal conditions may no longer be assumed as the strain-rate increases. Due to self heating, the temperature within a Nitinol wire may change significantly during mechanical cycling. For this reason, since the rate-independent model is not able to cope with temperature variations within the SMA wire, its use in simulating faster, dynamic loadings may not be totally adequate. The complex thermo-mechanical behavior of SE Nitinol wires during dynamic loading is only conveniently apprehended by the rate-dependent constitutive model.

In order to assess the behavior of the rate-dependent numerical model, the experimental tests previously shown in Figure 3.17 are used. These tests comprise four different strain rates, $\dot{\varepsilon} = 0.008$, 0.067, 0.250 and 0.333%/s, and were performed at room temperature to $\simeq 20$°C, on a Nitinol SE 508 wire specimen, with a 2.40 mm diameter circular cross section.

All the material properties used for the numerical simulations are presented in Table 4.2.

$E_A = 35000$ MPa	$E_M = 20000$ MPa	$M_f = -45°$ C
$M_s = -35°$ C	$A_s = -15°$ C	$A_f = -5°$ C
$C_M = 6.5$ MPaK^{-1}	$C_A = 6.5$ MPaK^{-1}	$e_L = 3.0\%$
$\rho = 6500$ kg m^{-3}	$c_L = 12914$ J kg^{-1}	$c = 500$ J kg^{-1}K^{-1}
$\overline{h} = 35$ W m^{-2} K^{-1}	$\theta = 0.55$ MPaK^{-1}	$k = 18$ W m^{-1} K^{-1}

Table 4.2: Parameters for the dynamic tensile tests.

The graphs in Figure 4.9 show the simulated temperature time-history and the cor-

responding stress-strain diagrams, for various strain-rates, against the experimental values.

It is quite clear from the observation of the graphs on Figure 4.9 that the implemented rate-dependent numerical model yields a set of very satisfying results, both for the temperature time-histories as well as for the corresponding stress-strain diagrams. As the strain-rate of the dynamic loading increases from 0.008 to 0.333%/s, the amplitude of the temperature variation during the SE cycle increases, in accordance with the experimental results. In what concerns the stress-strain diagrams, for increasing strain-rates, the general shape of the hysteretic loops tends to be steeper and narrower, in conformity with the trend observed in the experimental results.

The numerical assessment of the rate-dependent constitutive model, is being based on the comparison between the results taken from a series of experimental tensile tests and the corresponding numerical results. However, due to physical limitations of the tensile test machine, and in order to complement these experimental results for higher strain-rates, further results from a large set of experimental cyclic tensile tests, on SE Nitinol wires, reported by Dolce and Cardone [51], are used. These experimental tests cover two different strain-rates, 0.28 and 1.40%/s at four different ambient temperatures, 10, 20, 30 and 40°C. Even though a strain-rate of 0.28%/s is of the same order of magnitude as the maximum strain-rate obtainable with the Zwick/Roell Z050 testing machine, which is about 0.333%/s, a strain-rate of 1.4%/s is four times this value, which is significantly higher.

The graphs in Figure 4.10 show the simulated stress-strain diagrams for the two analyzed strain-rates against the bibliographic experimental values.

The material properties used for the numerical simulations presented in Figure 4.10 are the ones from Table 4.3.

$E_A = 37300$ MPa	$E_M = 21400$ MPa	$M_f = -78°$ C
$M_s = -63°$ C	$A_s = -26°$ C	$A_f = -20°$ C
$C_M = 4.7$ MPaK^{-1}	$C_A = 4.7$ MPaK^{-1}	$e_L = 4\%$
$\rho = 6500$ kg m^{-3}	$c_L = 12914$ J kg^{-1}	$c = 500$ J kg^{-1}K^{-1}
$\overline{h} = 35$ W m^{-2} K^{-1}	$\theta = 0.55$ MPaK^{-1}	$k = 18$ W m^{-1} K^{-1}

Table 4.3: Parameters for the dynamic tensile tests at higher strain-rates.

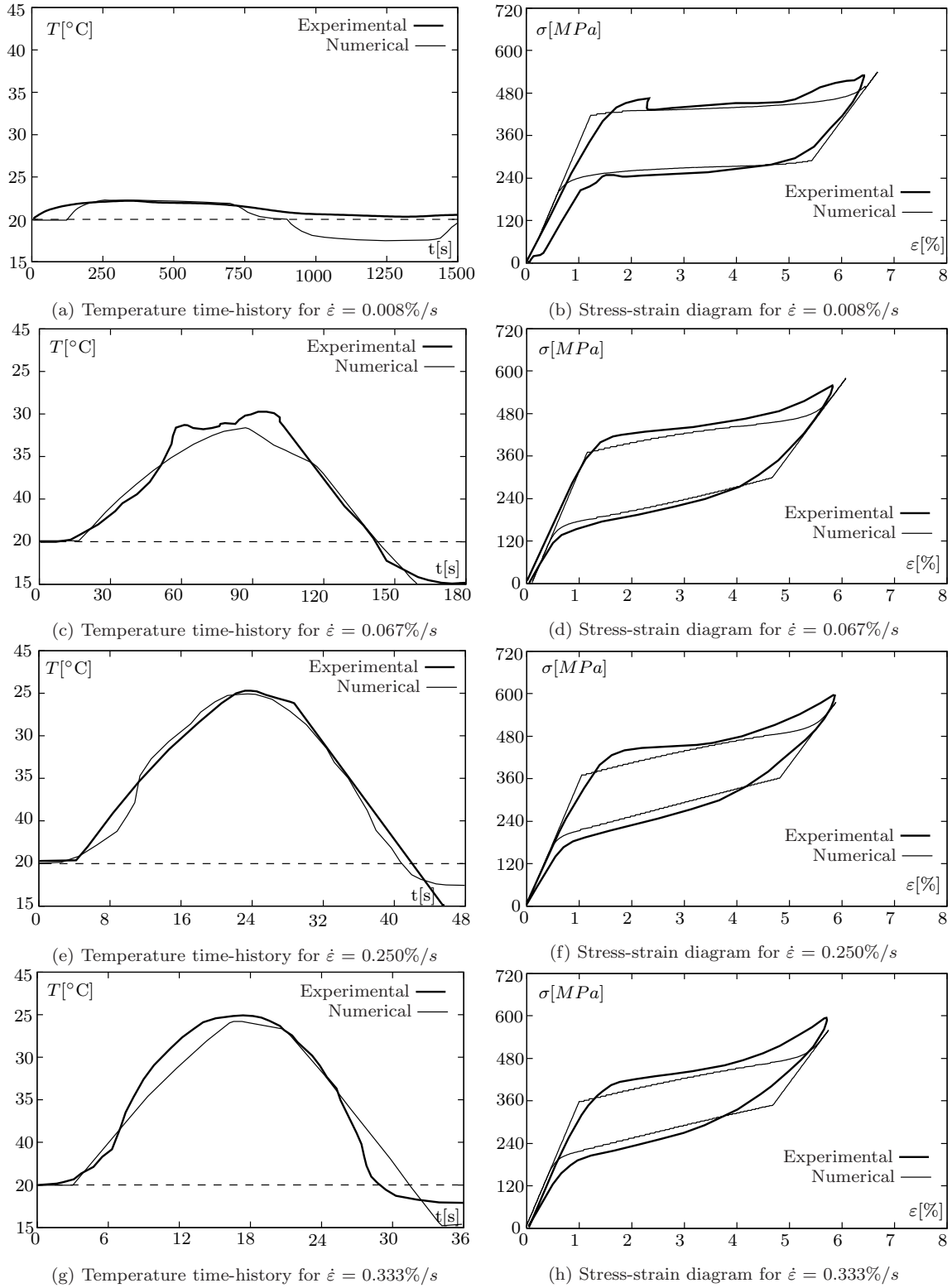

(a) Temperature time-history for $\dot{\varepsilon} = 0.008\%/s$

(b) Stress-strain diagram for $\dot{\varepsilon} = 0.008\%/s$

(c) Temperature time-history for $\dot{\varepsilon} = 0.067\%/s$

(d) Stress-strain diagram for $\dot{\varepsilon} = 0.067\%/s$

(e) Temperature time-history for $\dot{\varepsilon} = 0.250\%/s$

(f) Stress-strain diagram for $\dot{\varepsilon} = 0.250\%/s$

(g) Temperature time-history for $\dot{\varepsilon} = 0.333\%/s$

(h) Stress-strain diagram for $\dot{\varepsilon} = 0.333\%/s$

Figure 4.9: Rate-dependent numerical model vs. experimental data at temperature $T_0 = 20°C$, for increasing strain-rate ($\dot{\varepsilon}$).

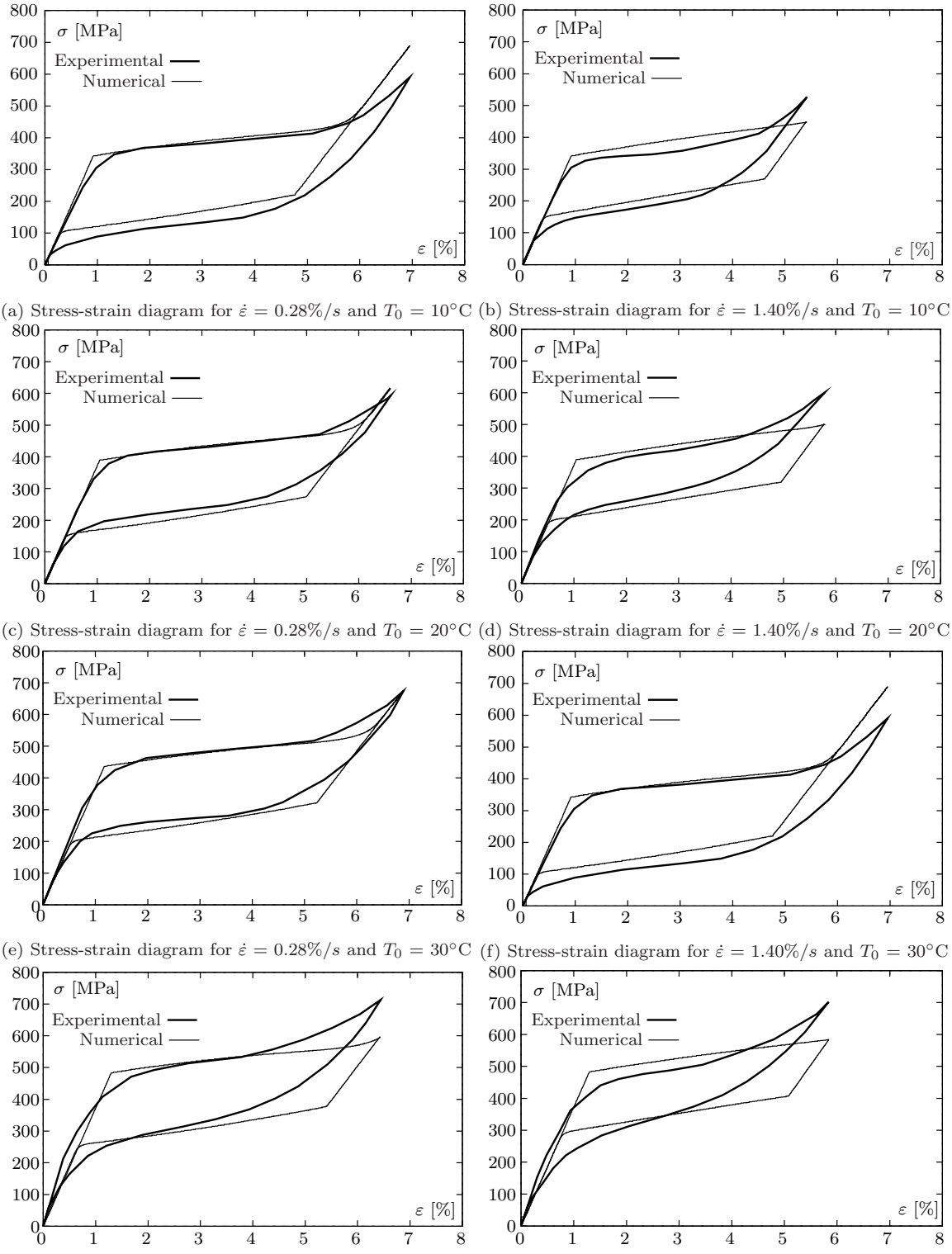

(a) Stress-strain diagram for $\dot{\varepsilon} = 0.28\%/s$ and $T_0 = 10°\text{C}$ (b) Stress-strain diagram for $\dot{\varepsilon} = 1.40\%/s$ and $T_0 = 10°\text{C}$

(c) Stress-strain diagram for $\dot{\varepsilon} = 0.28\%/s$ and $T_0 = 20°\text{C}$ (d) Stress-strain diagram for $\dot{\varepsilon} = 1.40\%/s$ and $T_0 = 20°\text{C}$

(e) Stress-strain diagram for $\dot{\varepsilon} = 0.28\%/s$ and $T_0 = 30°\text{C}$ (f) Stress-strain diagram for $\dot{\varepsilon} = 1.40\%/s$ and $T_0 = 30°\text{C}$

(g) Stress-strain diagram for $\dot{\varepsilon} = 0.28\%/s$ and $T_0 = 40°\text{C}$ (h) Stress-strain diagram for $\dot{\varepsilon} = 1.40\%/s$ and $T_0 = 0°\text{C}$

Figure 4.10: Rate-dependent numerical model vs. bibliographic experimental data [51] for two strain-rates (0.28%/s and 1.40%/s) and four temperatures (10, 20, 30 and 40°C).

The vibrations mitigation capacity of damping devices is usually evaluated through the equivalent viscous damping (ζ_{eq}). This parameter is now used to evaluate the ability of the numerical model to estimate the experimental data. Comparisons between the numerical values and the literature experimental data are presented in Figures 4.11, for the two reported strain-rates and corresponding ambient temperatures.

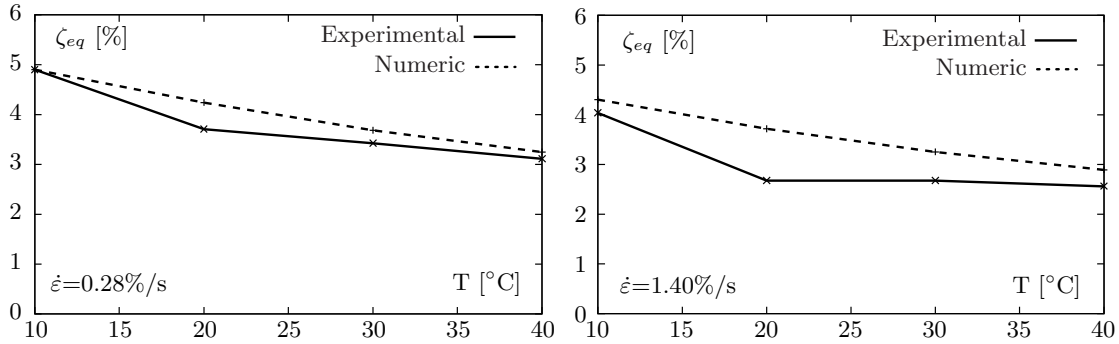

Figure 4.11: Rate-dependent numerical model vs. bibliographic experimental data [51]: equivalent viscous damping.

The plots in Figures 4.11 illustrate that the damping properties of the material decrease as the ambient temperature and/or strain-rate increases, which is in accordance with the experimental tests. Globally, one can say that the numerical predictions fit well the experimental data. However, the experimental damping is somehow overestimated by the numerical model, and this difference tends to increase for higher strain-rate values. It is a fact that the behavior of all numerical models is hampered by their simplifying hypotheses. In this particular case, for instance, the model assumes homogeneous phase transformations within the material, as well as uniform deformation. It has already been referred that propagating transformation fronts develop in the material and that for higher strain rates this moving heat source problem becomes more important, leading to significant non-uniform deformation and temperature fields [133]. A second aspect is related to the adopted convection coefficient. The complex heat convective problem depends on several factors like the temperature difference between the specimen and the environment, the air convective properties, the convection mechanism, which may be forced or not, and the specimen position in the flow [169]. Further more, for a given material, the convection coefficient is strongly dependent on whether the wire is being heated or cooled [24]. However, an average value for the convection coefficient is adopted

in the numerical model. Higher strain rates are associated with a faster variation of the material's instantaneous temperature per unit time. Hence, for higher strains, the accumulated error resulting from the heat transfer uncertainties increases more rapidly and leads to higher deviations from experimental results.

4.8 Strain-rate analysis using the rate-dependent model

The mechanical behavior of SMAs changes significantly when passing from pseudo-static to dynamic conditions. Since the rate-dependent model, calibrated with the parameters presented in Table 4.3, has yielded satisfying results in both regimes, this model is used to apprehend the overall strain-rate influence on the SE behavior of a SMA wire. For this, a set of 16 numerical tensile tests, ranging from quasi-static conditions (0.013 %/s) up to 130 %/s and four different ambient temperatures (T = 10, 20, 30 and 40°C), are simulated for a 2.4 mm diameter SMA wire. The strain-rates were chosen in order to convey a net set of frequency values for the dynamic loading, taking into account that the maximum tensile strain in the SMA wire is 6.5%. Hence, the values for the frequencies of the numerical tensile tests are, f = 0.001, 0.01, 0.1 and 10 Hz. In Figure 4.12 are represented the results obtained for the tests performed at T = 20°C, for the four tested frequencies. Analyzing the stress-strain curves presented in Figure 4.12, one can observe important differences in the hysteretic loops when passing from quasi-static conditions to dynamic ones (0.013 to 1.3 %/s). However, this is no longer the case when the strain-rate further increases (1.3 %/s to 130 %/s). The temperature time-histories are also represented, together with the stress-strain curves, showing a similar stabilization pattern as in the stress-strain diagrams. The equivalent viscous damping corresponding to the SE hysteresis obtained in the tensile numerical tests is computed, and plotted in Figure 4.13. This curves translate the evolution of the equivalent viscous damping for increasing strain-rates and various ambient temperatures. The literature experimental results represented in Figure 4.10 are also included in the graphic. One can observe that the rate-dependent model is able to conveniently adapt the response of the material, regarding its energy dissipation capability, to variations in the dynamic loading rate and ambient temperature. The plots in this graph show that the dissipation capability of the SMA wire changes significantly when passing from quasi-static

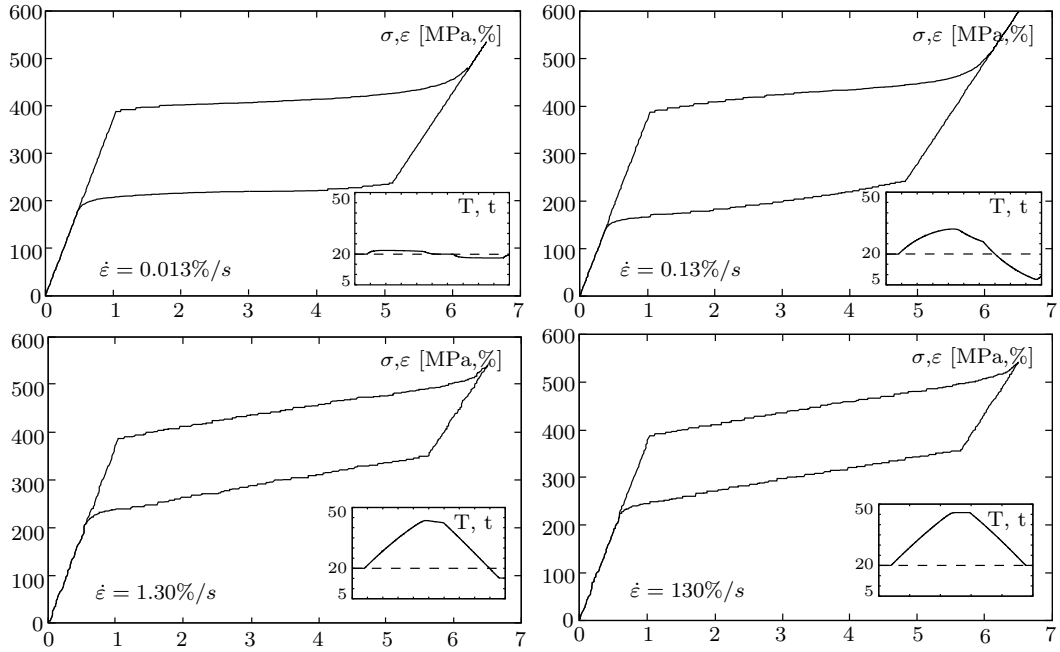

Figure 4.12: Analysis of strain-rate variation at 20°C ambient temperature.

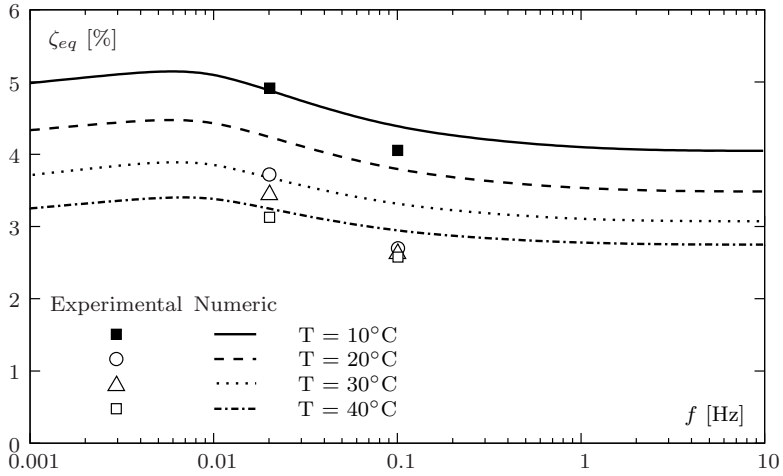

Figure 4.13: Strain-rate influence on the equivalent viscous damping.

conditions to dynamic ones, but it is only marginally affected when the strain-rate further increases. This confirms the insensitivity of the equivalent damping towards strain-rate above a certain threshold, results already reported in literature by others authors [51, 135, 164].

One can conclude that, for seismic applications, with frequencies in the range of 0.2

to 4 Hz, the behavior of SMA wires is mainly insensitive to strain-rate. Accordingly, for this type of applications, SMA models that are insensitive to strain-rate can still be adequate for simulating the response of structures including SMA elements, once calibrated with dynamic experimental tests [6].

4.9 Closure

Two constitutive models for the mathematical modeling of SMAs are described. Both rate-independent and a rate-dependent constitutive models are analyzed, regarding their mechanical and kinetic laws. The heat transfer problem due to the thermodynamics underlying the transformation processes is also addressed, for the rate-dependent constitutive model.

Several mechanical laws are addressed, relating stress (σ), strain (ε), temperature (T) and martensite fraction (ξ), which can be regarded as the fraction of the produced phase. This transformed phase fraction is considered to be in series with the elastic fraction of the response. Three approaches for the mathematical modeling of this elastic component are presented, namely the Voight scheme, the Reuss scheme and the simple linear model.

Regarding the transformation kinetic laws, describing the evolution of the martensite fraction with stress and temperature based in the material's stress-temperature phase diagram, linear and exponential laws are analyzed.

The heat transfer problem is also studied, and a practical approach to the analysis of the convective heat transfer from surfaces is presented.

Having discussed the theoretical background concerning constitutive models for SMAs, a rate-independent model and a rate-dependent model are implemented. These numerical implementations consist of strain-driven, time-discrete models, making use of the Euler method to enable the transformation of the time-continuous evolutionary equations into time-discrete evolutionary equations. The algorithms for both constitutive models, which are presented in detail, are implemented in a Matlab R2007a environment.

The performance of the implemented numerical models in quasi-static and dynamic

simulations of the SE stress-strain and temperature responses of SMA wires is analyzed. The results yielded by the simulations are successfully compared with experimental and bibliographic data. A strain-rate analysis is performed using the rate-dependent model which allowed to conclude that for seismic applications, with frequencies in the range of 0.2 to 4 Hz, the behavior of SMA wires is mainly insensitive to strain-rate. This shows that rate-independent constitutive models can still be rather efficient in simulating SMA's behavior, in this frequency range.

Chapter 5

Modeling of Superelastic Vibration Control Devices

5.1 Introduction

This chapter focuses on a series of numerical simulations of dynamic systems comprising SE components. The main purpose of these simulations is to assess the potential of SE SMAs in the vibration control of structures, namely in seismic control devices. A comparison between the rate-independent and the rate-dependent constitutive models is made.

The calibrated numerical models are used to investigate the dynamic response of several vibration control devices built up of austenitic SE wires. Their energy dissipation and re-centering capabilities, important features of these devices, are addressed in the numerical tests. The sensitivity of these devices to ambient temperature, strain-rate and strain-amplitude is also analyzed. One of these devices is tested as a seismic passive vibration control system in a numerical model of a railway viaduct, subjected to different ground accelerations.

5.2 Mathematical modeling of dynamical systems

A mathematical model for a dynamic system is defined as a set of equations that represents, in a fairly accurate way, the dynamics of that system, which is an idealization of a given structure. In the case of a simple structure, the dynamic system can be represented by a concentrated or lumped mass, m, supported by a massless frame, that provides stiffness, k, to the system, and a viscous damper, which dissipates energy. As only one independent displacement is required to define the displacement of the mass, relative to its original position, for dynamic analysis, the structure is said to have only one degree-of-freedom (DOF). This system is called a single-degree-of-freedom (SDOF) system [38].

Regarding the force-displacement relation associated with deformations in a structure, systems are characterized as linear-elastic systems, if the relationship between the external force, f_s, and resulting deformation, u, is linear ($f_s = ku$), with identical loading and unloading curves.

The stress-strain relation for a SMA component during cyclic loading has already been widely discussed. Although the initial loading branch is linear, for higher strain amplitudes the curve denotes a highly nonlinear behavior. Moreover, as loading and unloading curves do not coincide, the system is an inelastic system. This means that the relation between f_s and u cannot be translated by a single value, depending on the deformation history and if the strain is increasing (positive velocity) or decreasing (negative velocity). In this case, the resisting force can be expressed by $f_s = f_s(u, \dot{u})$.

The damping process in SMAs arises due to internal friction under cyclic deformation, with the formation of a hysteretic loop. The damping energy dissipated during one cycle is given by the area enclosed by the hysteretic loop. This energy dissipation through inelastic behavior is not usually modeled with a viscous damping, but rather by the recognition of the inelastic force-displacement relation, when solving the equation of motion [38].

For the mechanism presented in Figure 5.1, which consists in a SDOF oscillator, with a SMA wire acting as restoring element, the nonlinear equation of motion reads

$$m\,\ddot{u} + f_s(u, \dot{u}) = p(t) \tag{5.1}$$

where m is the mass of the system, f_s the restoring force provided by the SE element and $p(t)$ the applied load.

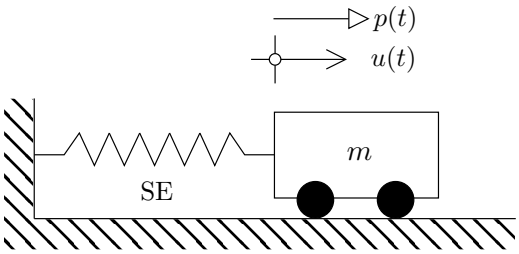

Figure 5.1: SDOF oscillator, with a SE SMA wire acting as restoring element.

The time-domain response of a dynamic system is usually specified in terms of the transient response and the steady-state response. The steady-state response of the dynamic system is the response of the system as time approaches infinity and the transient response is defined as the part of the response that tends to zero as time becomes larger [85].

5.3 Pre-strain in superelastic wires

The damping capability of a SE system can be enhanced by introducing an initial pre-strain in the SE wire [52]. This initial strain in the SE wire enables the dynamic system to work at higher martensite transformation ratios and hence, to show higher damping capabilities [177]. In Figure 5.2 is represented the difference between the behavior of a pre-strained SE wire and a non-pre-strained SE wire. Assuming the same strain amplitude for the two cases, one can easily see that for the non-pre-strained SE wire, the prescribed strain amplitude does not even allow for the beginning of the martensitic transformation. In the pre-strained SE wire however, the same strain amplitude enables the development of a SE hysteretic effect, associated with the dissipation of energy.

The numeric implementation of the pre-strain (ε_p) can be accomplished by using one of the proposed R-I or R-D algorithms. When using the rate-dependent model, one can define the strain-rate associated with the pre-strain implementation, and obtain the corresponding values for σ_p, ξ_p and T_p.

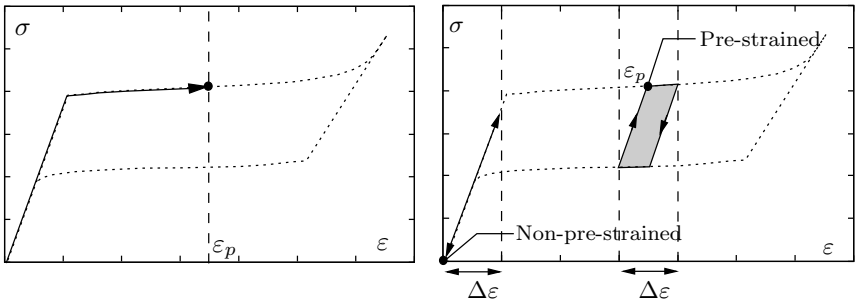

Figure 5.2: Difference between a pre-strained SE wire and a non-pre-strained SE wire subjected to the same strain amplitude: stress-strain relations.

5.4 Numerical implementation

The resulting nonlinear equation of motion is solved using the Newmark implicit algorithm [38]. The average acceleration approach is used, which assumes the variation of acceleration within a time step to be constant, equal to the average acceleration, as represented in Figure 5.3, yielding

$$\ddot{u}(\tau) = (\ddot{u}_{i+1} + \ddot{u}_i)/2 \tag{5.2}$$

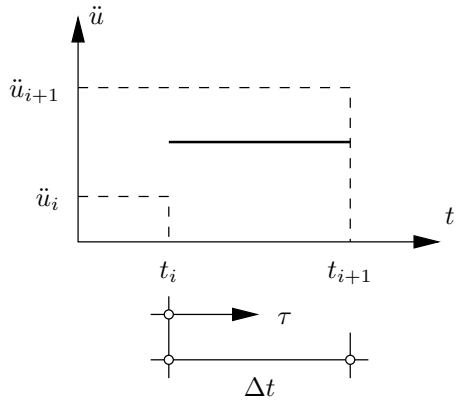

Figure 5.3: Average acceleration method, ($\gamma = 1/2$, $\beta = 1/4$).

The integration of $\ddot{u}(\tau)$ and $\dot{u}(\tau)$ gives

$$\dot{u}(\tau) = \dot{u}_i + (\ddot{u}_{i+1} + \ddot{u}_i)\,\tau/2 \tag{5.3}$$

and

$$u(\tau) = u_i + \dot{u}_i \tau + (\ddot{u}_{i+1} + \ddot{u}_i)\, \tau^2/4 \tag{5.4}$$

To evaluate the velocity $\dot{u}_{i+1}$ and the displacement u_{i+1}, at time $i+1$, one has to replace τ by $\Delta\, t$, in equations (5.3) and (5.4) to yield

$$\dot{u}_{i+1} = \dot{u}_i + (\ddot{u}_{i+1} + \ddot{u}_i)\, \Delta t/2 \qquad \text{and} \tag{5.5}$$

and

$$u_{i+1} = u_i + \dot{u}_i \Delta t + (\ddot{u}_{i+1} + \ddot{u}_i)\, (\Delta t)^2/4 \tag{5.6}$$

5.4.1 Algorithm to solve the equation of motion

The implemented algorithm is presented next, for the R-D approach:

1. Initial calculations

   (a) Define T_f (ambient temperature), ε_p (pre-strain), u_0 (initial displacement) and Δt

   (b) Introduce pre-strain (ε_p): compute σ_p, ξ_p, T_p, and k_p using R-D algorithm

   (c) Introduce initial displacement (u_0) : compute ε_0, σ_0, ξ_0, T_0 and k_0 using R-D algorithm

   (d) For $i = 0$, initialize ε_0, σ_0, ξ_0, T_0 and k_0

   (e) Compute initial acceleration:

   $$\ddot{u}_0 = \frac{p_0 - c\dot{u}_0 - (f_s)_0}{m}$$

   (f) Compute Newmark's constants:

   $$a = \frac{1}{\beta \Delta t}\, m + \frac{\gamma}{\beta}\, c \qquad \text{and} \qquad b = \frac{1}{2\beta}\, m + \Delta t \left(\frac{\gamma}{2\beta} - 1\right) c$$

2. Calculations for each time step, i

(a) Compute initial acceleration:

$$\Delta\hat{p}_i = \Delta p_i + a\dot{u}_i + b\ddot{u}_i$$

(b) Determine the tangent stiffness k_i

(c)

$$\hat{k}_i = k_i + \frac{\gamma}{\beta\Delta t}\,c + \frac{1}{\beta(\Delta t)^2}\,m$$

(d) Solve for Δu_i from $\hat{k}_i$ and $\Delta\hat{p}_i$ using the modified Newton-Raphson iterative procedure

i. Initialize data

$$u_{i+1}^{(0)} = u_i \qquad f_s^{(0)} = (f_s)_i \qquad \Delta R^{(1)} = \Delta\hat{p}_i \qquad \hat{k}_T = \hat{k}_i$$

ii. Calculation for each iteration

- $\Delta u^{(j)} = \Delta R^{(j)}/\hat{k}_T$
- $u_{i+1}^{(j)} = u_{i+1}^{(j-1)} + \Delta u^{(j)}$
- Compute $f_s^{(j)}$ using R-D algorithm
- $\Delta f^{(j)} = f_s^{(j)} - f_s^{(j-1)} + (\hat{k}_T - k_T)\Delta u^{(j)}$
- $\Delta R^{(j+1)} = \Delta R^{(j)} - \Delta f^{(j)}$

iii. Repetition for next iteration. Replace j by $j+1$ and repeat calculation steps 2(d)ii until $\Delta u^{(j)} < \varepsilon$

(e)

$$\Delta\dot{u}_i = \frac{\gamma}{\beta\Delta t}\,\Delta u_i - \frac{\gamma}{\beta}\,\dot{u}_i + \Delta t\left(1 - \frac{\gamma}{2\beta}\right)\,\ddot{u}_i$$

If a change of sign in velocity occurs, compute a new time step and recompute step 2a

(f)

$$\Delta\ddot{u}_i = \frac{1}{\beta(\Delta t)^2}\,\Delta u_i - \frac{1}{\beta\Delta t}\,\dot{u}_i - \frac{1}{2\beta}\,\ddot{u}_i$$

(g)

$$\dot{u}_{i+1} = \dot{u}_i + \Delta\dot{u}_i \quad \text{and} \quad \ddot{u}_{i+1} = \ddot{u}_i + \Delta\ddot{u}_i$$

3. Repetition for the next time step. Replace i by $i+1$ and repeat step 2a for the next time step. Stop when reached the final time.

5.5 Numerical tests

The numerical tests are performed in a SDOF dynamic system comprising a 100 kg mass, with SE restoring elements consisting of 1000 mm length and 2.4 mm diameter wires. Even though the stress-strain curves of NiTi SMAs are generally different for loading under tension and compression [**?**, 171], one assumes the same constitutive law for both situations, also disregarding problems involving buckling [87, 147]. The material parameters of the SE wires used in the numerical tests are the ones already defined in Table 4.3.

5.5.1 Vibration control device with SE wire

The first SE vibration control device to be analyzed corresponds to the SDOF system represented in Figure 5.1. The system, with zero initial conditions, is excited for 8 seconds by an harmonic load, time needed to get a clear picture of the steady-state forced vibrations, followed by a phase of free oscillations. The ambient temperature is set to 20°C. The excitation force has an amplitude of 1.95 kN, and yields in the SMA wire a strain corresponding to the complete forward transformation ($\varepsilon_{max} = 6\%$), therefore maximizing the size of the hysteretic loops. As the dominant frequencies for seismic applications are in the range of 0.2 to 4 Hz [40], a loading frequency of 2 Hz is used, leading to a strain-rate of 24%/s.

The displacement and stress time-history, the phase plane and the force-displacement response curves are presented in Figure 5.4.

After a first transient phase, the amplitude of the displacements reaches the value corresponding to the complete forward transformation. A considerable amount of energy is dissipated in this steady-state forced vibration phase, as clearly indicated in Figure 5.4(d), where the force-displacement curve shows a large hysteretic loop. However, the value of the equivalent viscous damping, $\zeta_{eq} \simeq 5\%$, is quite low when compared to the commonly required values for seismic damping devices, 10% to 20% [75].

In the following free vibration phase, the displacement of the system decreases due to the presence of the SE hysteretic loops, until the solid to solid phase transformation ceases to exist and the SMA wire stays in its austenitic form. From now on, as

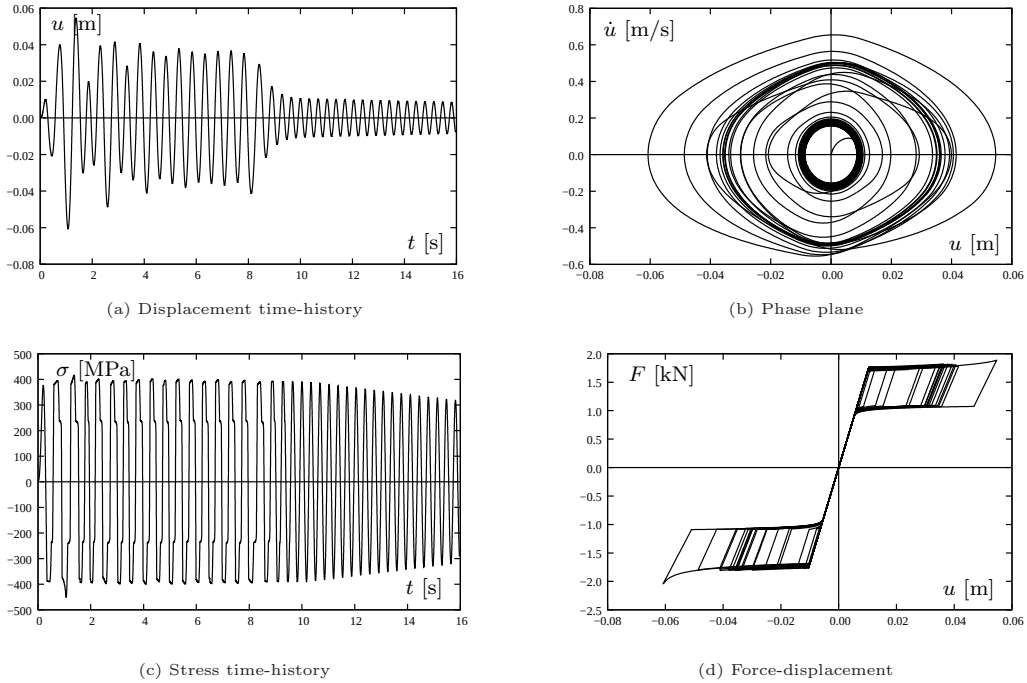

(a) Displacement time-history

(b) Phase plane

(c) Stress time-history

(d) Force-displacement

Figure 5.4: Single SE wire ($T = 20°\text{C}$, $f = 2$ Hz).

no viscous damping is present, the system exhibits a pure elastic response. In the phase plane, Figure 5.4(b), the elastic response is identified as the inner closed loop, centered in the origin. When viscous damping is present in the system, the harmonic oscillations die out and the system recovers its original equilibrium position, meaning that the system has re-centering capability.

One can conclude that the above oscillator, used as a seismic control device, exhibits self-centering but relatively low energy dissipation capability.

5.5.2 Vibration control device with two pre-strained SE wires working in phase opposition

A way to increase the size of the hysteretic loops, and, consequently, the energy dissipation capability of the system, making it more suitable for seismic control devices, is to use a set of pre-tensioned SMA wires working in phase opposition [51], like the one featured in Figure 5.5.

To increase the SE damping capability of the device, the wires are pre-strained up

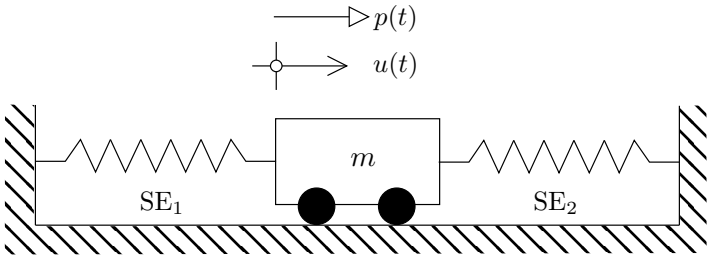

Figure 5.5: SDOF oscillator, with two pre-tensioned wires working in phase opposition.

to ε_0, in the equilibrium position. During the loading cycles, while SE_1 is loaded SE_2 is unloaded and conversely, oscillating in phase opposition around the equilibrium position, ε_0. The response of SE_1 and SE_2 during generic harmonic cycles is illustrated in Figure 5.6. Although they present symmetric strain time-history, as shown in Figure 5.6(a), their stress time-history exhibits a more complex pattern, as illustrated in Figures 5.6(b) and (c). For a given time instant, due to the fact that the martensitic transformations occurring in each of the wires are shifted in time, their thermo-mechanical characteristics are different.

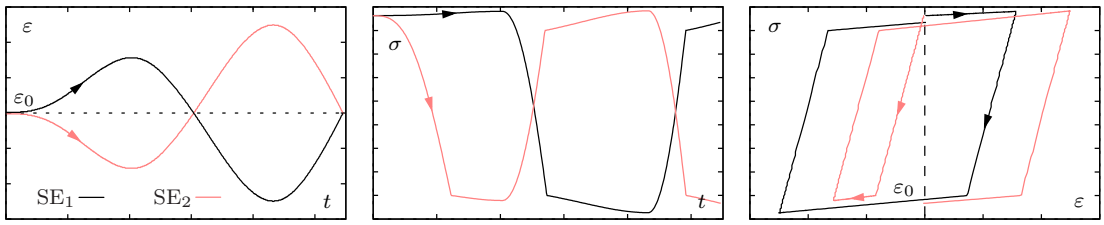

(a) strain time history (b) stress time history (c) stress-strain

Figure 5.6: Behavior of SE_1 and SE_2 during generic harmonic cycles.

In the mechanism presented in Figure 5.5, the SE wires 1 and 2 are pre-strained up to 3.5%, which corresponds to half the strain of the full transformation range. The amplitude of the applied load, 1.4 kN, yields a maximum displacement corresponding to the end of the forward transformation in one of the wires. The ambient temperature is set to 20°C and a loading frequency of 2 Hz is used. The displacement and stress time-history, the phase plane and the force-displacement response curves are presented in Figure 5.7.

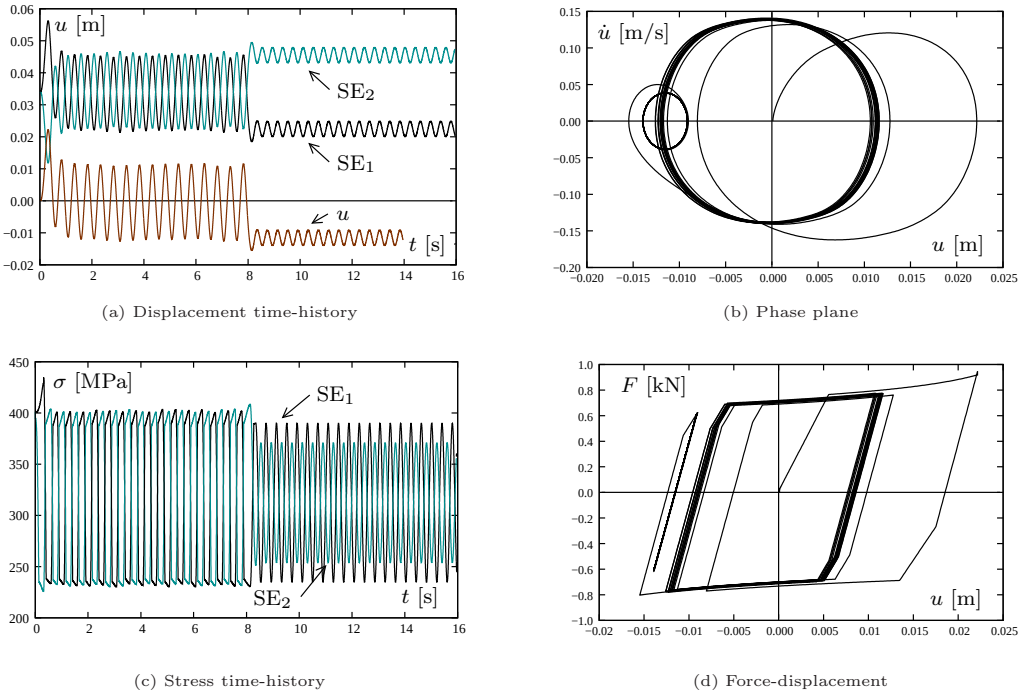

(a) Displacement time-history

(b) Phase plane

(c) Stress time-history

(d) Force-displacement

Figure 5.7: Two pre-strained wires working in phase opposition ($T = 20°\text{C}$, $f = 2$ Hz).

Plots in Figure 5.7(a) show that the positive motion u of the mass is resisted by SE_1 while assisted by SE_2. The role of the wires is inverse for the symmetric negative motion. For the steady-state forced vibration phase, the outer closed curve in Figure 5.7(b), a wide hysteretic loop is obtained, as clearly indicated in Figure 5.7(d). The equivalent viscous damping is $\zeta_{eq} = 20\%$, a much more appealing value for seismic damping devices.

In the following free vibration phase, the SE wires remain in their austenitic form and the system exhibits a pure elastic response, identified as the inner closed loop in Figure 5.7(b). It can be seen that this loop is not centered in the origin, meaning that the system has no re-centering capability. If viscous damping is added to the system, the harmonic oscillations would die out, but the system would not recover its initial position. If the above mechanism is to be used as seismic control device, it exhibits a relatively large energy dissipation capability but no self-centering.

5.5.3 Vibration control device with two pre-strained SE wires and a re-centering element

To recover the self-centering capability of the system an additional SE wire is introduced, as shown in Figure 5.8.

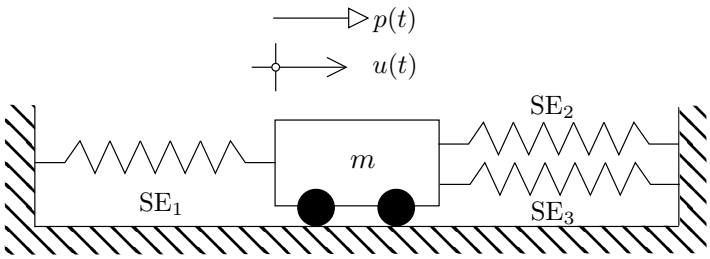

Figure 5.8: SDOF oscillator, with two pre-tensioned wires and a re-centering element.

While in the equilibrium position, SE wires 1 and 2 are pre-tensioned up to 3.5%. The third SE wire is strain/stress free in this position. As the stiffness of the system is larger, the amplitude of the applied load increases to 2.2 kN in order to yield the complete transformation in one of the first two wires. The behavior of the third SMA wire in this test is purely elastic as it is added only to recover the re-centering capacity of the system. However, its damping capacity can be exploited as well if designed to allow SE strains. The ambient temperature is set to 20°C and a loading frequency of 2 Hz is used. The displacement and stress time-history, the phase plane and the force-displacement response curves are presented in Figure 5.9.

Plots in Figure 5.9(a) show that while SE_1 and SE_2 are working in opposition to one another, SE_3 follows the displacement of the mass. The steady-state forced vibration phase is identified as the outer closed curve in Figure 5.9(b). Although the corresponding hysteretic loop in Figure 5.9(d), is much narrow and rotated when compared with the one represented in Figure 5.7(d), it leads to a similar equivalent viscous damping, $\zeta_{eq} \simeq 20\%$. Note that, designing SE_3 as to exhibit its superelasticity, one can increase the global energy dissipation capability of the mechanism.

In the following free vibration phase, all SE wires remain in their austenitic form and the system exhibits a pure elastic behavior, identified as the inner closed loop

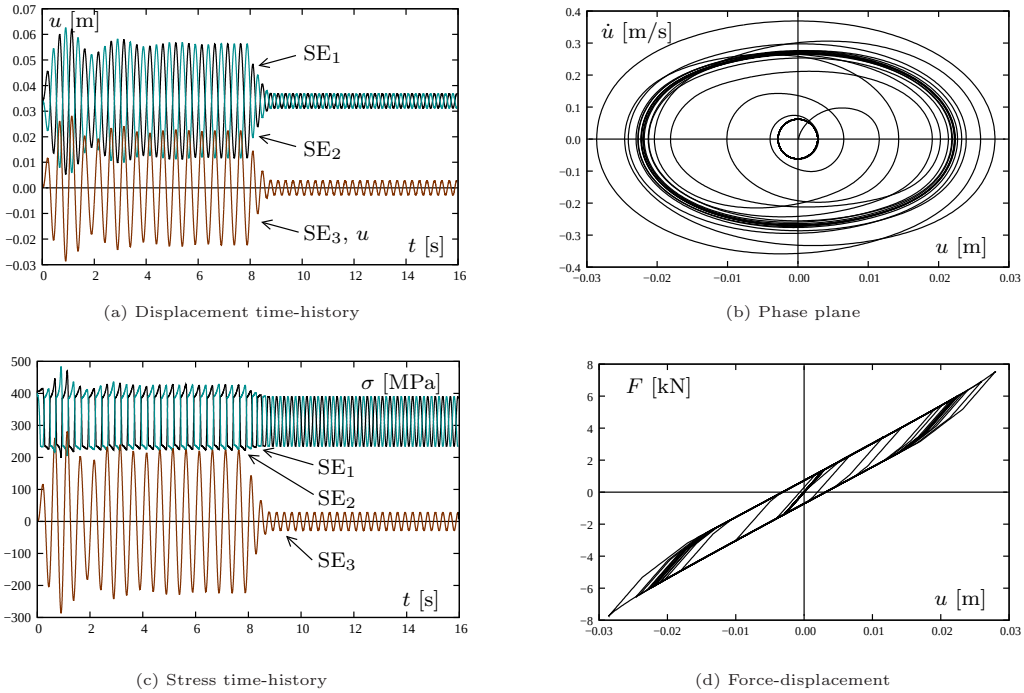

(a) Displacement time-history

(b) Phase plane

(c) Stress time-history

(d) Force-displacement

Figure 5.9: Two pre-tensioned wires with re-centering element ($T = 20°C$, $f = 2$ Hz).

in Figure 5.9(b). It can be seen that the loop is once again origin centered, meaning that the system has recovered its re-centering capability.

Combining the performances exhibited by the first two systems, yields a mechanism presenting good energy dissipation and self-centering capability, appealing properties for seismic control devices.

The graphs presented in Figures 5.4(c), 5.7(c) and 5.9(c) also illustrate the ability of these devices to limit the maximum force transmitted to the structure. This upper bound force limitation is also a very important feature in the design process of a civil engineering structure.

5.5.4 Influence of the ambient temperature on SE vibration control devices

The previous numerical tests were all performed at the same ambient temperature, as the main objective of these tests was to compare the performance of the different

dynamic systems in terms of damping and re-centering capabilities. In this section, dynamic simulations regarding the study of the influence of ambient temperature on the damping capacity of SE based vibration control systems is addressed.

As civil engineering structures are subjected to relatively large temperature gradients, the following tests are designed to analyze the influence of ambient temperature, for a given dynamic action, on the response of the two SE based devices presented in Figures 5.1 and 5.5. The systems, with zero initial conditions, are exited for 8 seconds by an harmonic load of 2 Hz, followed by a phase of free oscillations. The force amplitude is computed as to yield in the SE wires strains corresponding to the complete forward transformation, at an ambient temperature of 20°C. The tests are carried out for three ambient temperatures, 10, 20 and 30°C.

The force-displacements curves are presented in Figure 5.10. Analyzing the response of the systems, one can observe that, for the single SE wire, the behavior of the dynamic system is similar to the one already shown before, during the calibration tests. A slight decrease from 6 to 4% in the equivalent viscous damping is observed, when the temperature rises from 10 to 30°C. The double SE wire system is pratically insensitive to ambient temperature variations, with the equivalent viscous damping remaining approximatelly constant, around 20%.

5.5.5 Influence of strain-rate on SE vibration control devices

The strain-rate also has an important influence on the behavior of SE systems. A parametric study is made in order to assess the importance of this effect on the dynamic behavior of the two SE systems under analysis. The loading scheme is similar to the one used before, for an ambient temperature of 20°C and two loading rates, 2 and 3 Hz, consistent with the frequency content of seismic actions. In order to isolate the strain-rate effect, the amplitude of the dynamic loading is computed as to yield the same maximum strain in the SE wires, during the steady-state forced vibration phase.

Analyzing the force-displacements curves presented in Figure 5.11, one can observe that, in this range of frequency, both dynamic systems are practically insensitive to strain-rate, exhibiting equivalent damping ratios of 4 and 20%, respectively.

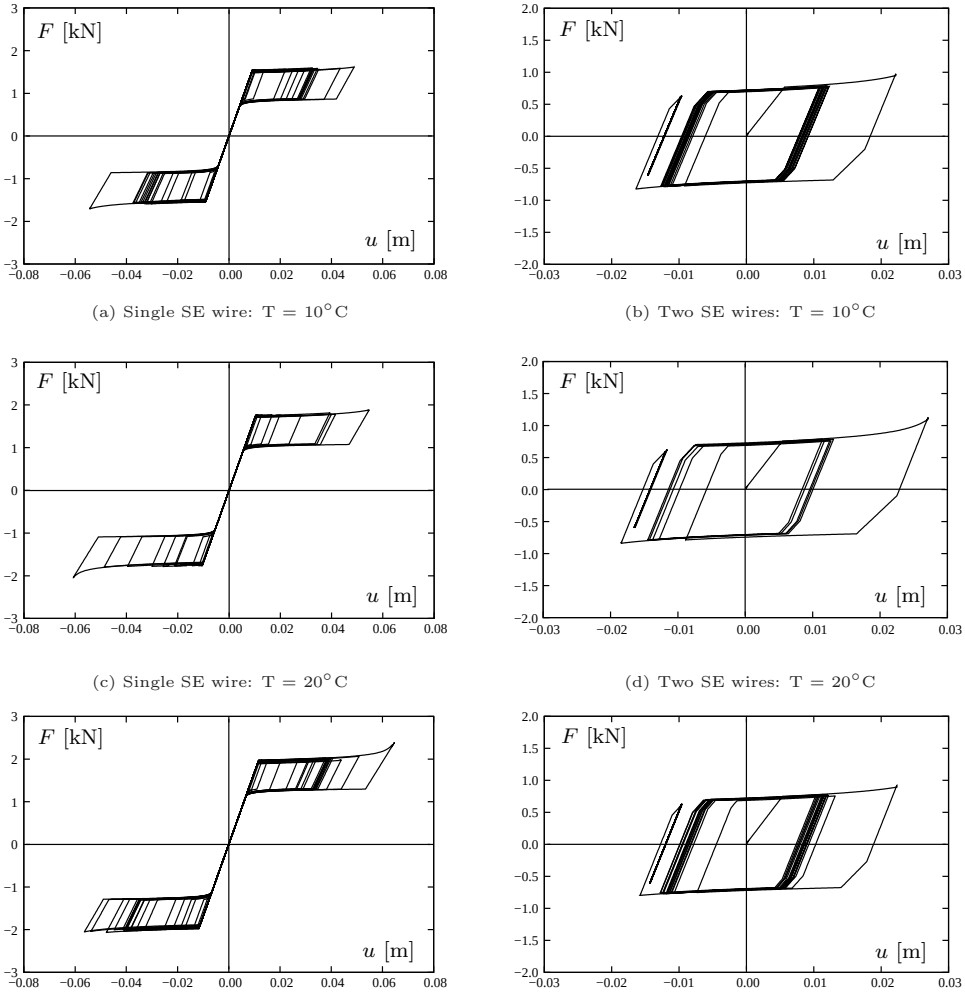

(a) Single SE wire: T = 10°C

(b) Two SE wires: T = 10°C

(c) Single SE wire: T = 20°C

(d) Two SE wires: T = 20°C

(e) Single SE wire: T = 30°C

(f) Two SE wires: T = 30°C

Figure 5.10: Influence of the ambient temperature on hysteretic cycles.

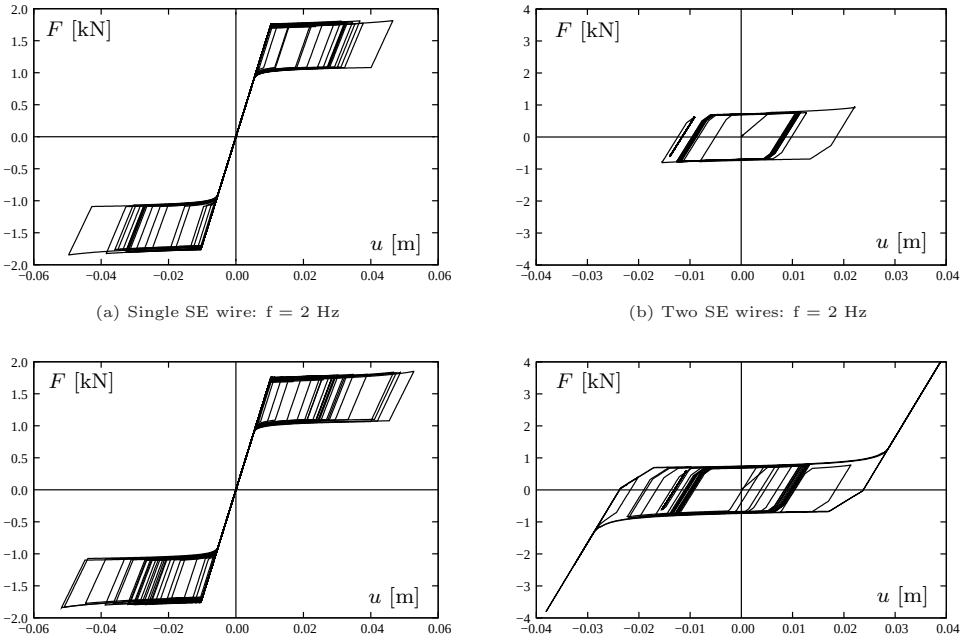

(a) Single SE wire: f = 2 Hz

(b) Two SE wires: f = 2 Hz

(c) Single SE wire: f = 3 Hz

(d) Two SE wires: f = 3 Hz

Figure 5.11: Influence of the strain-rate on hysteretic cycles.

5.5.6 Influence of strain-amplitude on SE vibration control devices

The following tests are used to analyze the variation of the damping properties of the two SE vibration control devices, due to variations in the amplitude of the induced strains. Both systems, with zero initial conditions, are excited for 8 seconds by an harmonic load of 2 Hz, followed by a phase of free oscillations. The force amplitude is changed in order to yield, at an ambient temperature of 20°C and during the steady-state forced vibration phase, strains of 1.3 and 3.5% for the single SE wire, and 0.6 and 1.5% for the SE wires in the double SE system.

As expected, the damping capability of both dynamic systems is dependent on the strain-amplitude. As the amplitude of the vibrations of the SE wires increase, the equivalent viscous damping changes from 1.5% to 4.5% for the single SE wire and from 15 to 20% for the double SE wire system.

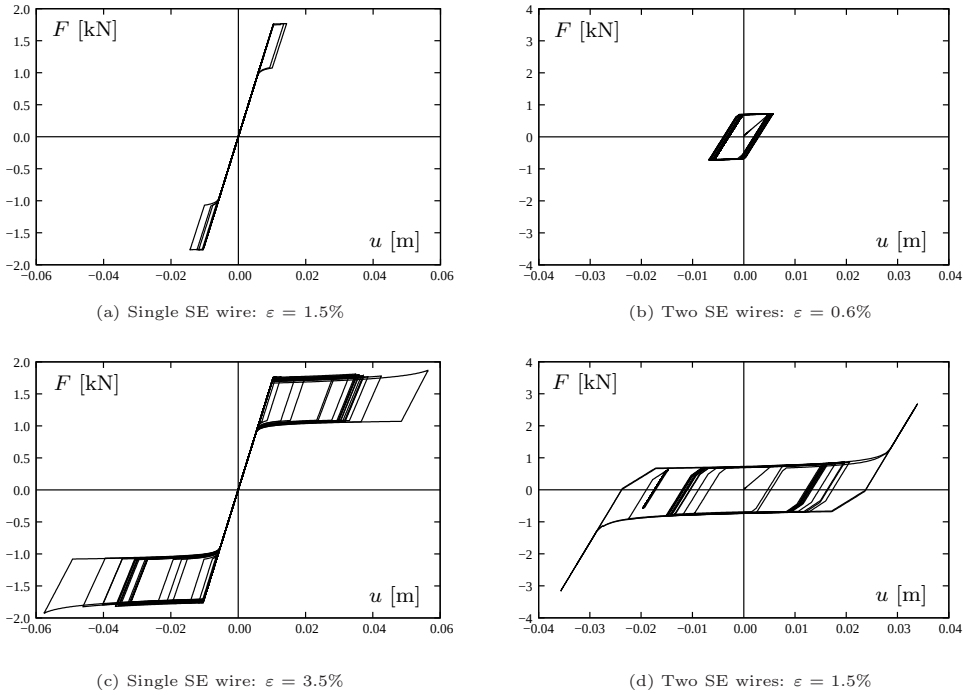

(a) Single SE wire: $\varepsilon = 1.5\%$

(b) Two SE wires: $\varepsilon = 0.6\%$

(c) Single SE wire: $\varepsilon = 3.5\%$

(d) Two SE wires: $\varepsilon = 1.5\%$

Figure 5.12: Influence of the strain-amplitude on hysteretic cycles.

5.5.7 Influence of the constitutive model on the modeling of SE vibration control devices

In this section, the behavior of a passive control device is simulated using both the rate-dependent and the rate-independent constitutive models and the results are then compared. The material parameters characterizing the constitutive models are the ones given in Table 5.1. The material parameters for the rate-independent model are obtained through the inspection of a stabilized stress-strain response of a SE wire subjected to an harmonic loading with an amplitude of 6.5% and a frequency of 1 Hz, at 20°C ambient temperature.

The dynamic system used for the comparison of the constitutive models is the one presented in Figure 5.8, representing a SDOF oscillator, with two SE wires acting as restoring elements. The behavior of the third spring is purely elastic, having a stiffness of 226 kN/m and it is only added to provide the system's re-centering capacity. The mass of the system is set to 100 kg. The system, with zero initial conditions, pre-tensioned up to 3.5%, is excited for 8 seconds by an harmonic load, followed by a phase of free oscillations. The force amplitude is 1.6 kN with a loading

Rate-dependent model		
$E_A = 37300$ MPa	$E_M = 21400$ MPa	$M_f = -78°$ C
$M_s = -63°$ C	$A_s = -26°$ C	$A_f = -20°$ C
$C_M = 4.7$ MPaK^{-1}	$C_A = 4.7$ MPaK^{-1}	$e_L = 4\%$
$\rho = 6500$ kg m^{-3}	$c_L = 12914$ J kg^{-1}	$c = 500$ J kg^{-1}K^{-1}
$h = 35$ W m^{-2} K^{-1}	$\theta = 6 \times 10^{-6}$ K^{-1}	
Rate-independent model		
$E_A = 37300$ MPa	$\sigma_s^{AM} = 380$ MPa	$\sigma_f^{AM} = 400$ MPa
$\sigma_s^{MA} = 240$ MPa	$\sigma_f^{MA} = 210$ MPa	$\varepsilon_L = 4\%$

Table 5.1: Parameters for the constitutive models.

frequency of 2 Hz, yielding a maximum martensite transformation ratio of 80%. The displacement and stress time-histories, the phase-plane diagrams and the force-displacement response curves obtained using both the rate-independent and the rate-dependent models are presented side by side in Figure 5.13.

A comparative analysis of the results obtained using the two constitutive models shows that both the displacement time-histories and phase-plane diagrams exhibit the same general pattern. The displacement and velocity during the steady-state forced vibration phase are practically the same. During the steady-state free vibration phase, the values for the displacement and velocity obtained using the rate-independent model are about 20% smaller than the ones obtained using the rate-dependent model, denoting an overestimated damping associated with the rate-independent model.

Comparing the stress time-history obtained using the rate-independent and the rate-dependent models for both steady-state forced vibration and the free vibration phases, one can conclude that the models behave much alike. During this phases, SE_1 and SE_2 eventually reach a stress phase opposition, centered below the original pre-stress tension and then onwards the amplitudes of their stress cycles are the same.

The size and the shape of the hysteretic loops associated with the rate-independent and the rate-dependent models are very similar, as illustrated in Figure 5.13(d). The equivalent viscous damping, computed from these force-displacement diagrams, results 7% higher in the rate-independent model, confirming its overestimated damping.

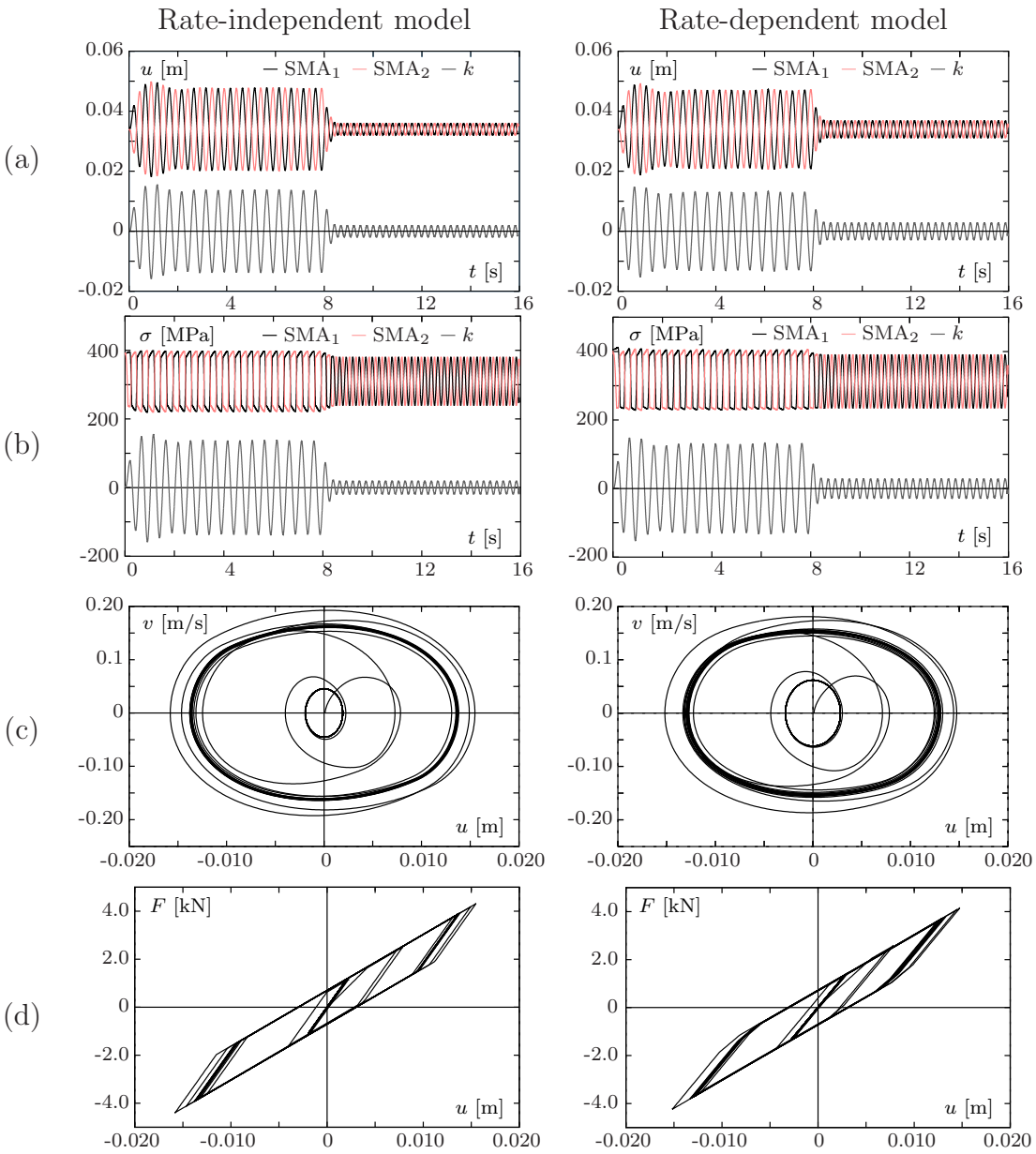

Figure 5.13: Two pre-tensioned SMA SE wires with re-centering element: (a) displacement time-history; (b) stress time-history; (c) phase-plane; (d) force-displacement.

5.6 Superelastic restrainer cables in a viaduct

During an earthquake event, bridges are susceptible to unseating and collapse due to excessive longitudinal support motion. The efficacy of using SE restrainer cables in bridges to reduce the hinge opening at the deck-abutment interfaces has been successfully demonstrated by Padgett *et al.* [127], during a series of experimental tests on a reduced scale concrete slab bridge.

In this section, the seismic simulation of SE restrainer cables in a viaduct is addressed, based on the numeric implementation used for the analysis of a SE vibration control system comprising two pre-strained wires and a re-centering element, as shown in Figure 5.14. The structure is considered to behave elastically.

Figure 5.14: Superelastic restrainer cables at bridge's supports.

5.6.1 Seismic analysis of the viaduct with SE restrainer cables

The structure used for the seismic simulation is the São Martinho railway viaduct [40]. This viaduct is a pre-stressed concrete railway viaduct with a total length, between abutments, of 852.0 m. It is built up of seven, 113.6 m length, independent segments and one segment of 56.8 m, adjacent to the south abutment. These segments are divided into 28.4 m spans and are structurally independent. The railway deck is a 13.0 m wide beam slab, comprising two 2.0×1.4 m main girders. The foundations are materialized by ϕ1.2 m piles with an average length of about 30.0 m. The concrete piers are tubular and have an average height of 12.0 m. Each pier is supported by five piles.

A simplified numerical model of one of these segments is combined with a SE based

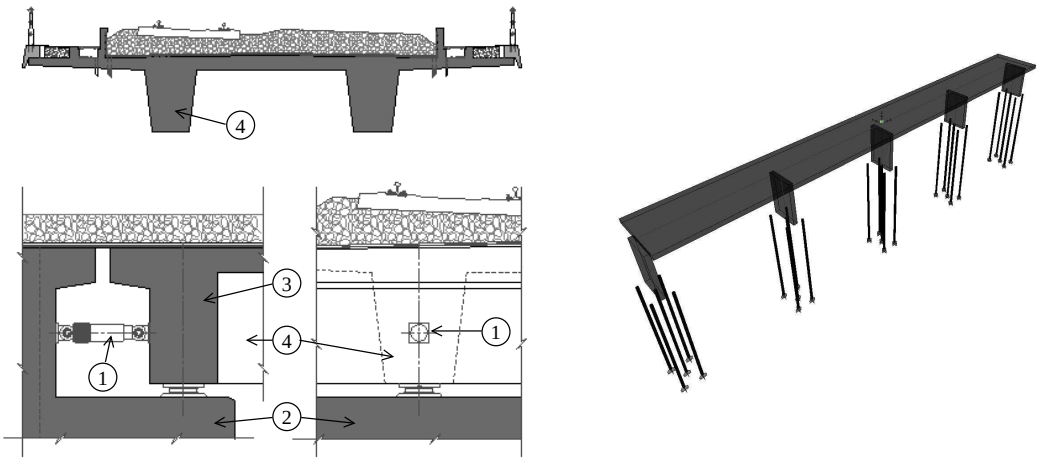

Legend: 1. SMA device, 2. Abutment, 3. Transverse girder, 4. Main girder

Figure 5.15: São Martinho railway viaduct: Mid-span cross section, SMA passive control device location and finite element model.

passive seismic control device. A longitudinal analysis of the segment is undertaken, assimilating it to a SDOF dynamic system with 4650 ton mass and stiffness of 355×10^3 kN/m. Pre-strained SE restraining elements are placed at the ends of the viaduct, one for each main girder. Each of them is composed of two sets of 1.0 m, with a total area of 3926 mm^2. This section could be built up from bars or from a set of smaller wires laid parallel, in strands, to form a cable. It is referred in the literature [103] that SE bars used in civil engineering applications, with diameters as large as 12.7 mm, can perform as good as the SE wires used in non civil engineering applications. However, the wire form of the shape-memory alloys shows higher strength and damping properties compared with the bars while the re-centering capabilities based on residual strains are not affected by section size [47]. The mechanical characteristics of the SMAs are the ones defined in Table 4.3.

During the seismic event, if the minimum stress to induce the martensitic transformation in the SE elements is not attained, they simply behave like additional linear elastic materials, increasing the system's stiffness. The displacement amplitude of the structure is hence decreased, but at the cost of increasing the system's natural frequency and leading to an undesirable increase in structural accelerations [148]. The introduction of pre-strain in the SE elements facilitates the beginning of the corresponding martensitic transformation, with the dissipation of energy by hysteresis.

The seismic action is introduced in the system by means of artificially generated accelerograms using the design acceleration power spectral density functions. Given the random nature of these generated accelerograms, the viaduct is submitted to six different series, represented in Figure 5.16.

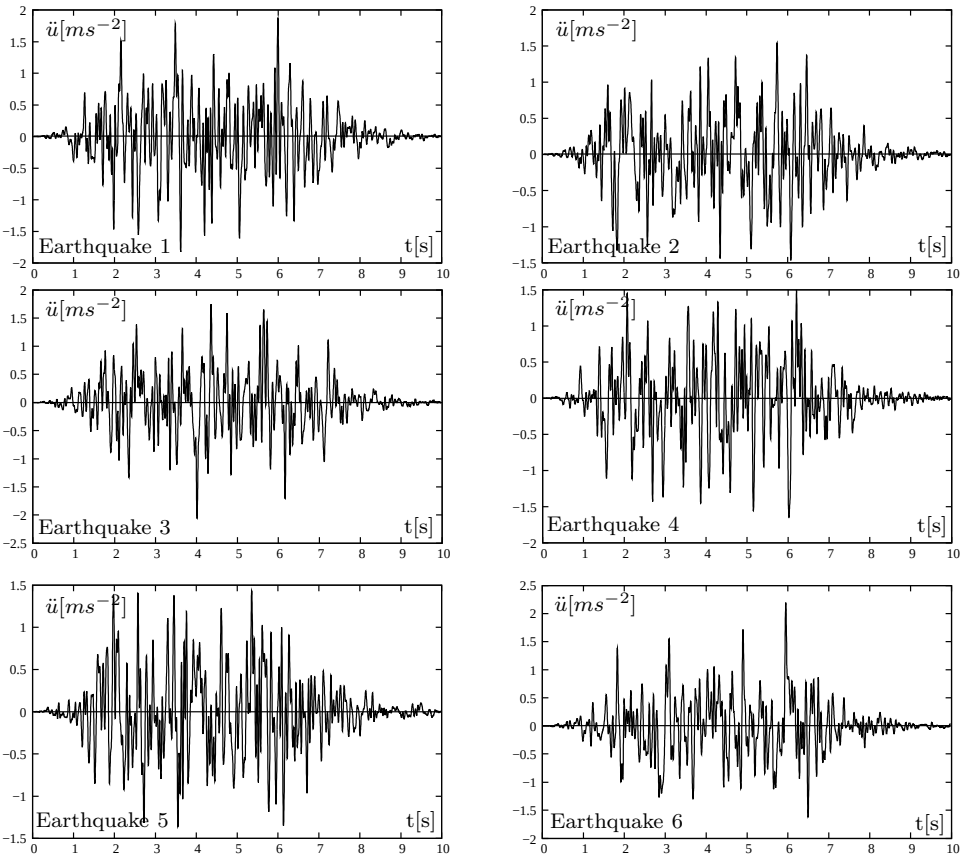

Figure 5.16: Generated accelerograms.

In Figure 5.17 is represented the longitudinal displacement time-history for the considered ground motions. One can see that the longitudinal displacement amplitude is considerably reduced with the passive control device, leading to a mean reduction of about 40% of the maximum longitudinal displacement. The vibration control device is also efficient in controlling the structural velocity and acceleration, as shown in the respective time-history, for the considered ground motions, in Figures 5.18 and 5.19.

Due the shape of the SE hysteresis, this device allows to control the value of the maximum force transmitted to the structure, as shown in the force time-history for

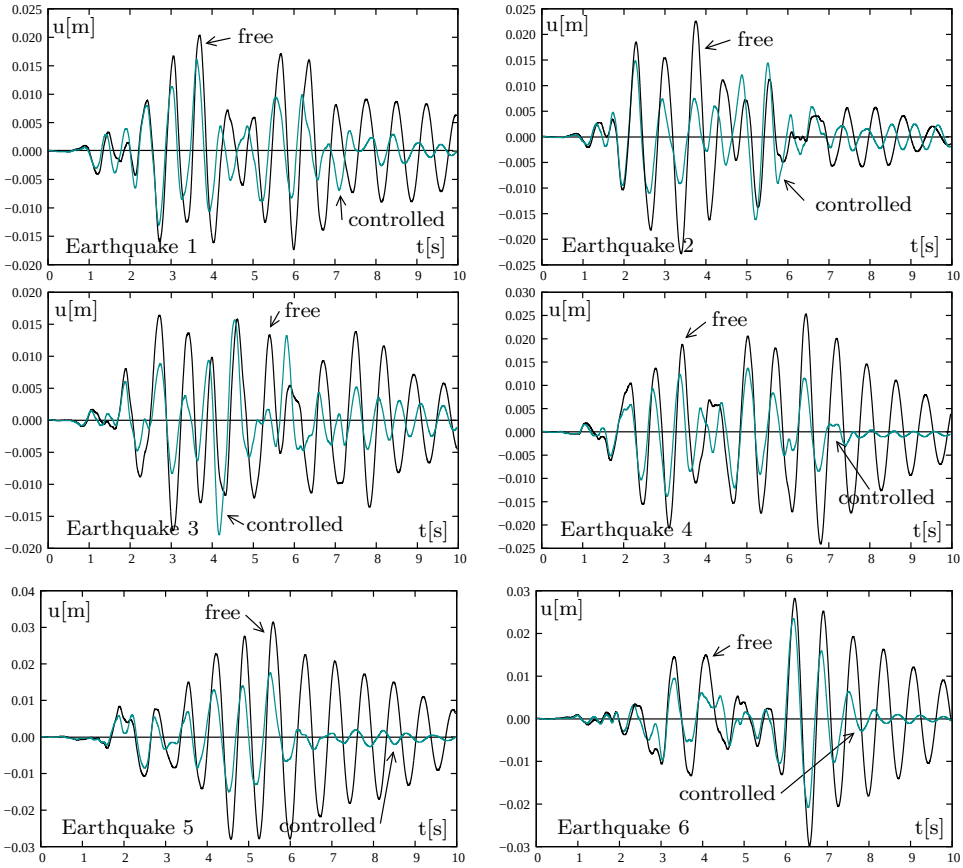

Figure 5.17: Longitudinal displacement time-history for free and controlled systems.

the considered ground motions, in Figure 5.20.

5.6.2 Influence of the model on the seismic analysis

The simplified numerical model of the São Martinho railway viaduct provided with an SMA based passive control device is used next to test the sensitivity of the dynamic response of the structure to the choice of the SMA constitutive model. The mechanical characteristics of the SMA wires are the ones defined in Table 5.1, for the rate-dependent and the rate-independent models. The viaduct is subjected to the same six artificial generated accelerograms. functions.

The time history of the longitudinal displacement of the viaduct deck is presented in Figure 5.21, for all six seismic actions and both constitutive models. The differences in the structural response of the controlled system, computed using the two models

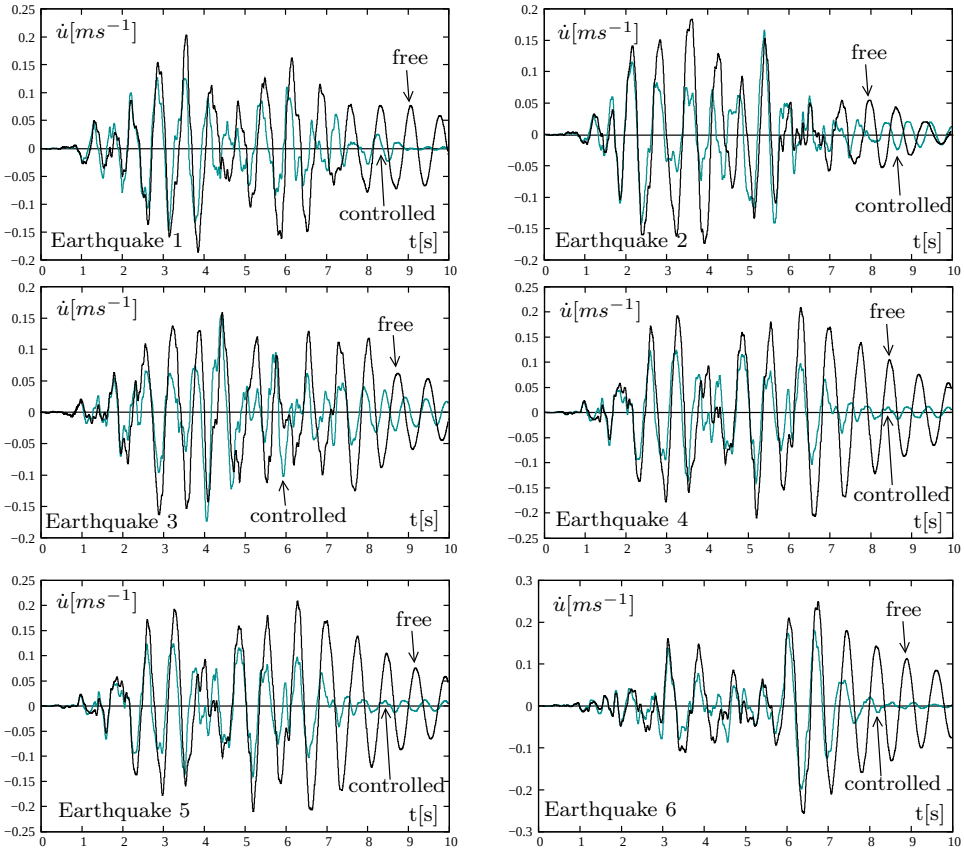

Figure 5.18: Longitudinal velocity time-history for free and controlled systems.

under analysis, are very small, as the mean average reduction in the displacements amplitude is 33% and 30% for the rate-independent and the rate-dependent models, respectively. This encourages one to use the rate-independent constitutive model, in the seismic simulation of SE based vibration control devices, due to its good accuracy and faster computational time.

5.6.3 Influence of the SE restraining area

The structural behavior of the viaduct deck during a seismic event is influenced by the area of the SE restraining elements. A parametric study regarding this influence is presented, assuming a SDOF system with frequencies of 0.5, 1.0, 1.5 and 2.0 Hz and considering a maximum total restraining area of 950 cm^2. The parametric study addresses the influence of the area of the SE restraining elements in the

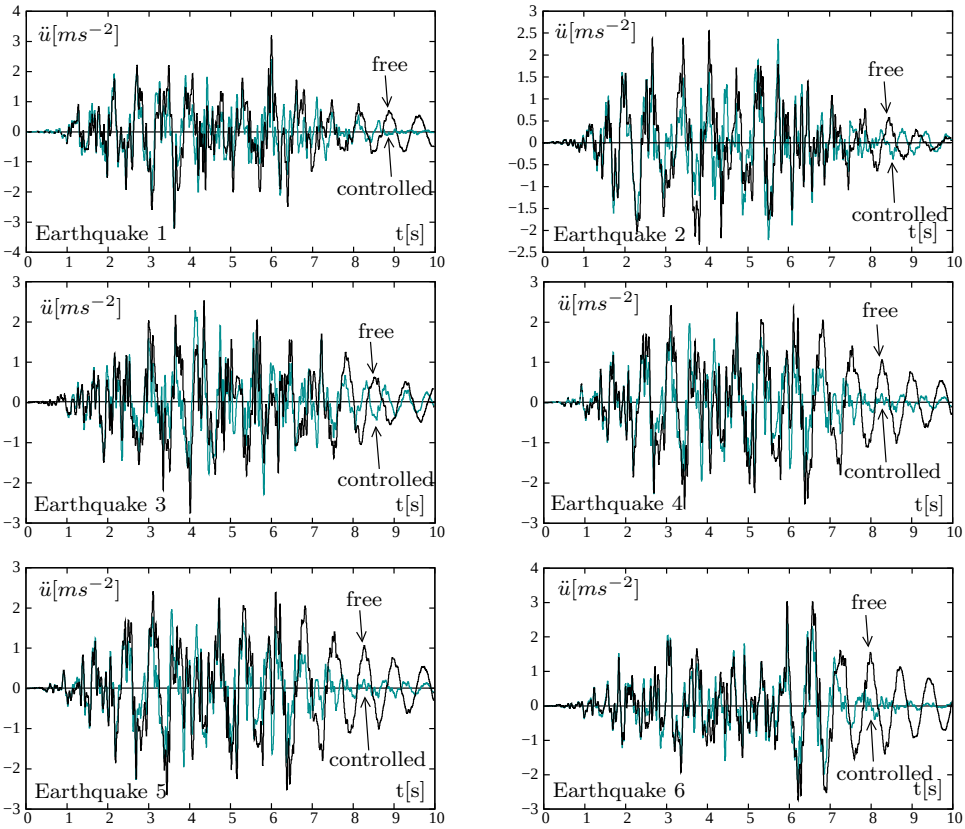

Figure 5.19: Longitudinal acceleration time-history for free and controlled systems.

longitudinal displacement, velocity and acceleration of the deck and corresponding SE force. This influence is translated by a set of curves, obtained using the average value of the maximum response resulting from the set of six artificially generated accelerograms. These curves are presented in Figure 5.22 and in Figure 5.23, for the four tested frequencies. The curves resulting from the parametric study are compiled in the following four graphs, shown in Figure 5.24. One can see that while for increasing areas of the SE restraining elements the mean longitudinal displacement and velocity of the deck decrease monotonously; see Figures 5.24(a) and (c), the mean longitudinal acceleration of the deck and the SE force decrease to a certain minimum value, before they start to increase again; see Figures 5.24(b) and (d). As the natural frequency of the structure increases, the displacement and velocity of the deck become smaller while the acceleration value increases. With the increase of the natural frequency the force transmitted to the SE restraining elements diminishes.

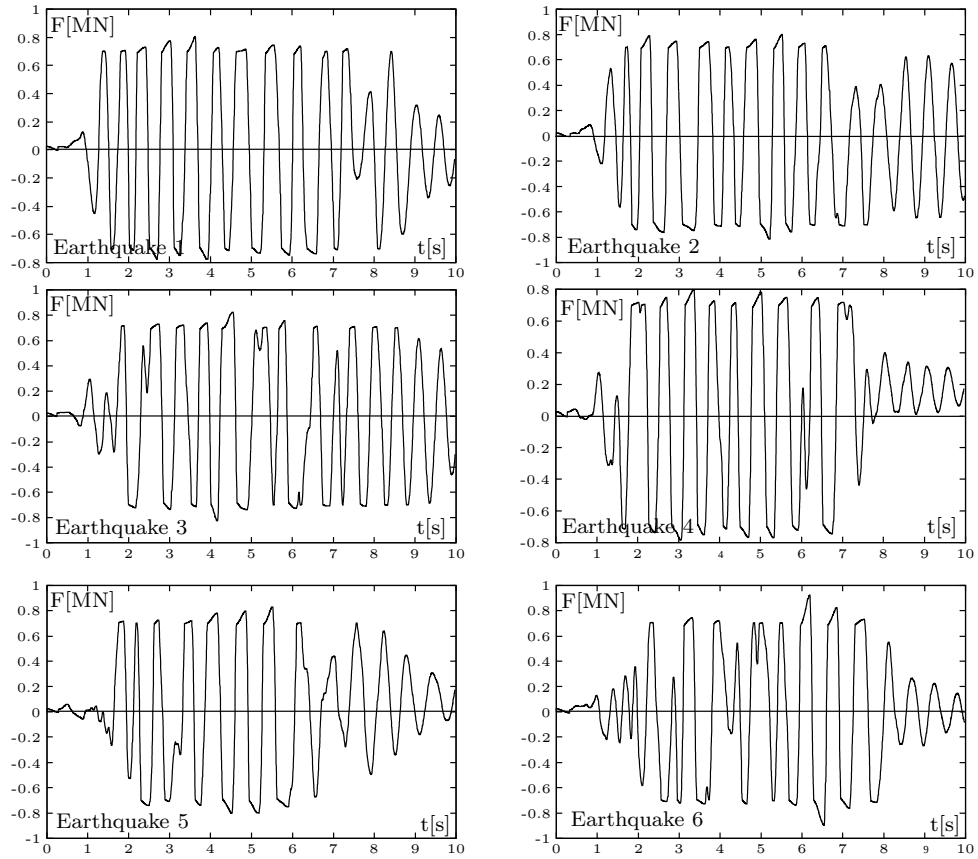

Figure 5.20: Force in the vibration control device time-history.

5.7 Closure

To illustrate the great potential of SE wires acting as restoring elements in passive seismic control devices, numerical models of three SE based passive vibration control devices are analyzed. Due to the nonlinear nature of these dynamic systems, the solution of the equation of motion is solved using the Newmark implicit algorithm.

The capability of these devices to mitigate vibrations and their self-centering abilities are demonstrated. The performances of these mechanisms are evaluated, including the influence of pre-strain in their damping capabilities, and their functioning principles are clearly identified. A study on the influence of the constitutive model on the damping provided by SE systems points to a damping overestimation by the R-I constitutive model.

The great versatility of SMA devices is confirmed, being able to describe a wide

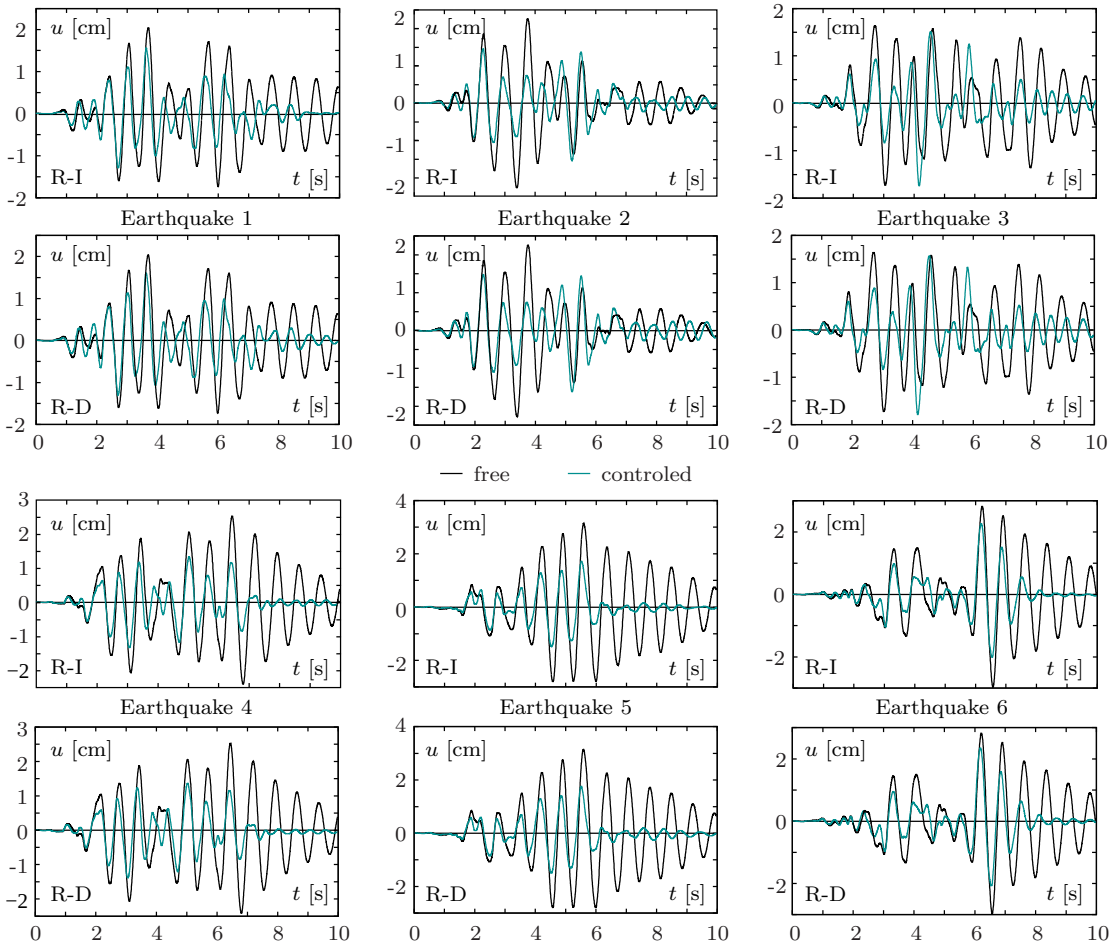

Figure 5.21: Time history of the longitudinal displacement of the viaduct deck.

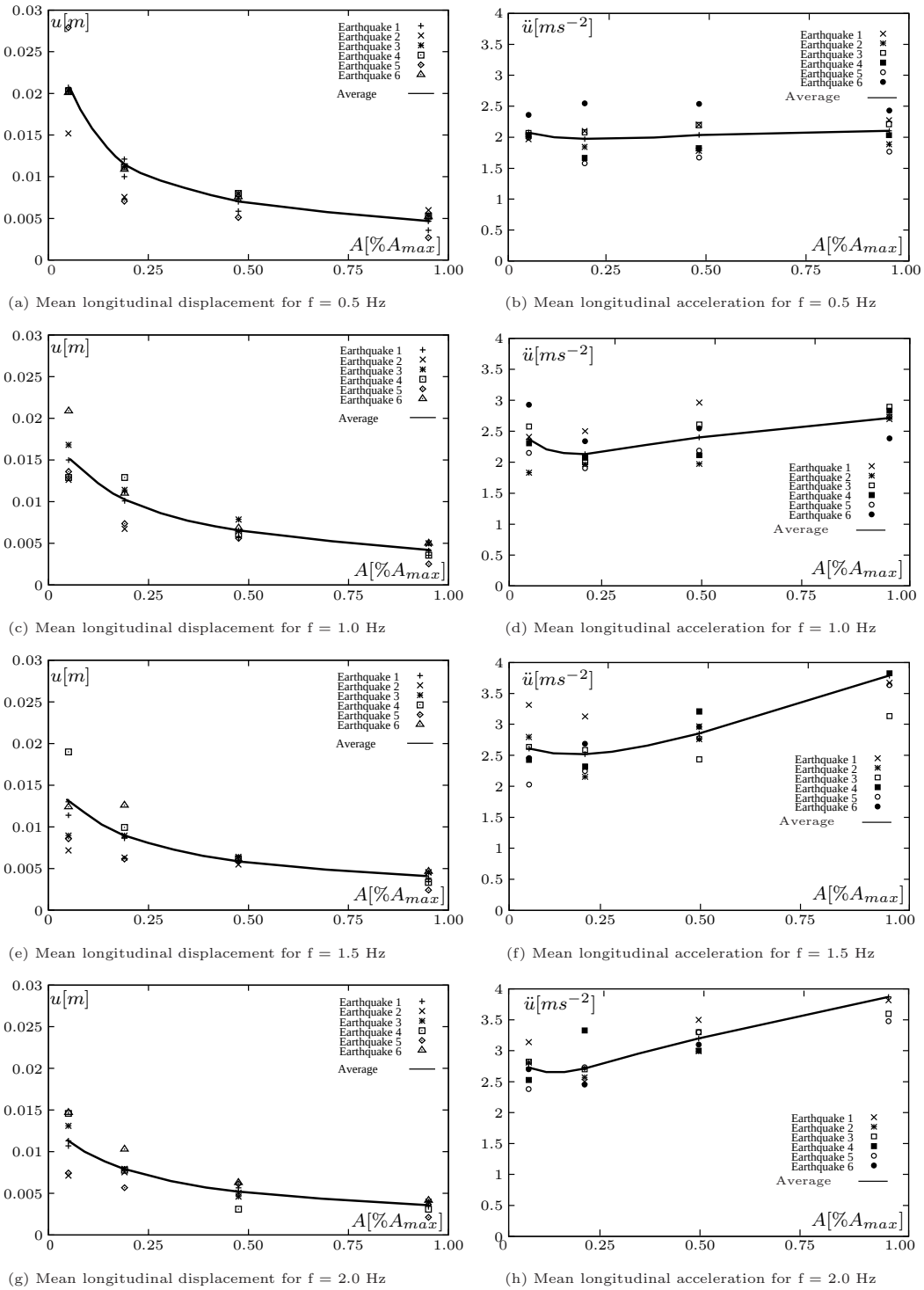

(a) Mean longitudinal displacement for f = 0.5 Hz

(b) Mean longitudinal acceleration for f = 0.5 Hz

(c) Mean longitudinal displacement for f = 1.0 Hz

(d) Mean longitudinal acceleration for f = 1.0 Hz

(e) Mean longitudinal displacement for f = 1.5 Hz

(f) Mean longitudinal acceleration for f = 1.5 Hz

(g) Mean longitudinal displacement for f = 2.0 Hz

(h) Mean longitudinal acceleration for f = 2.0 Hz

Figure 5.22: Longitudinal displacement and acceleration of the deck in function of the SE restraining area.

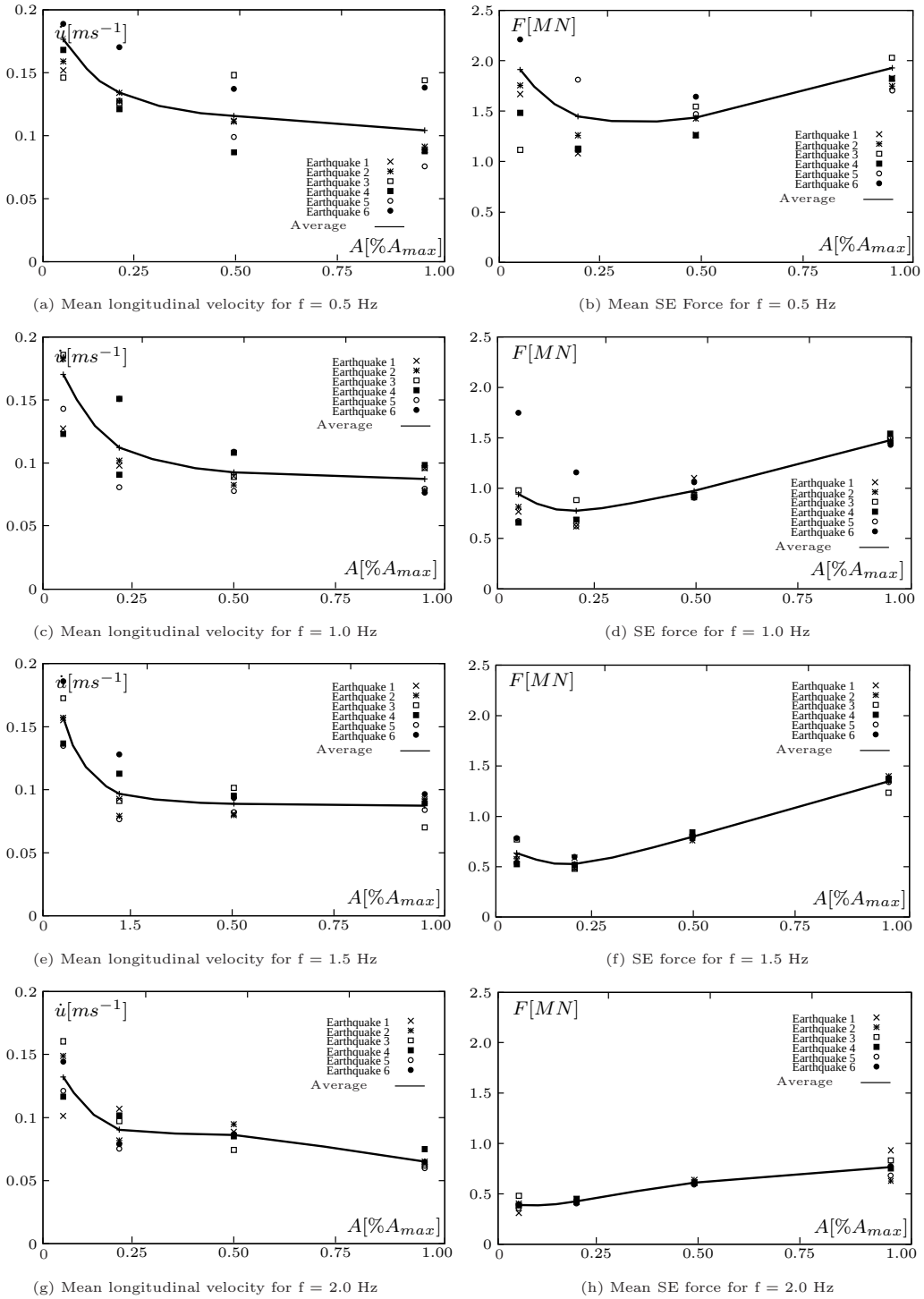

(a) Mean longitudinal velocity for f = 0.5 Hz

(b) Mean SE Force for f = 0.5 Hz

(c) Mean longitudinal velocity for f = 1.0 Hz

(d) SE force for f = 1.0 Hz

(e) Mean longitudinal velocity for f = 1.5 Hz

(f) SE force for f = 1.5 Hz

(g) Mean longitudinal velocity for f = 2.0 Hz

(h) Mean SE force for f = 2.0 Hz

Figure 5.23: Longitudinal velocity of the deck and SE force in function of the SE restraining area.

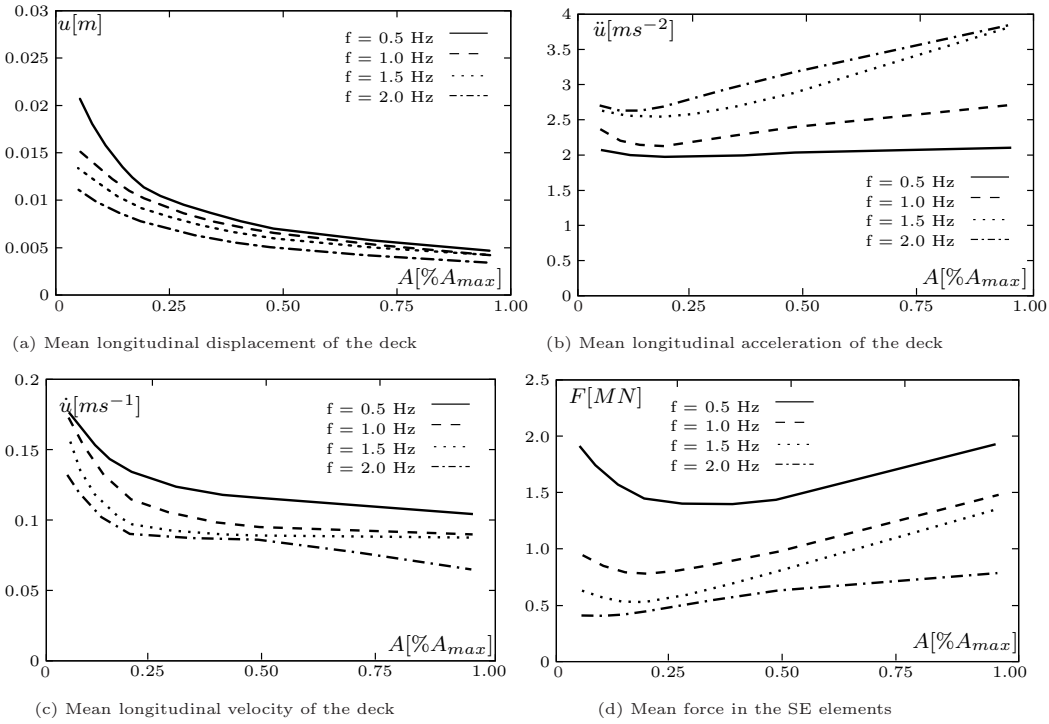

(a) Mean longitudinal displacement of the deck

(b) Mean longitudinal acceleration of the deck

(c) Mean longitudinal velocity of the deck

(d) Mean force in the SE elements

Figure 5.24: Parametric curves in function of the SE restraining area.

variety of cyclic behaviors, from fully re-centering to highly dissipating. This can be achieved by making simple functional variations of the SMA components and by acting on their mechanical properties. The shape of the hysteretic loops can be adjusted for a specific application, according to its particular dynamic requirements.

One of these devices is successfully tested as a seismic passive vibration control system in a simplified numerical model of a railway viaduct. This analysis confirmed the vast potential of SMAs in passive seismic control devices and encouraged future investigations in the field.

Chapter 6

Novel Superelastic Device

6.1 Introduction

The proposed vibration control device derives from the SE passive dissipation device proposed by Dolce *et al.* [52]. To increase its energy dissipation capabilities, the original device is based on a set of pre-strained SE wires working in phase opposition. However, a variety of stress-time effects observed in pre-strained SE wires [13] might have an adverse impact on the dynamic performances of the device. Mainly to avoid these problems, the proposed semi-active device uses a strategy that allows the continuous adapting of the accumulated strain in the wires, based on the response of the device to external excitations. As in an active control system, a controller monitors the feedback measurements and generates appropriate command signals for the device and, as in a passive control system, the control forces are developed as a result of the motion of the structure itself, with no need of external energy input. As the control forces act as to oppose the motion of the structural system, they promote the global stability of the structure [73, 151, 153, 154, 156]. According to presently accepted definitions the proposed device may be considered as a semi-active control system.

6.2 Semi-active device under harmonic excitation

In the following numerical simulations the rate-dependent constitutive model is used. The response of two passive vibration systems to harmonic ground accelerations is used to emphasis their dynamic characteristics. Their drawbacks are identified and then used as conditioning design parameters for the proposed semi-active system. In the numerical simulations that follow, the system, with zero initial conditions, is excited during 1 second by a 2Hz harmonic ground acceleration with an amplitude of $1.25\mathrm{m}s^{-2}$, followed by a phase of free oscillations.

6.2.1 Passive system with no pre-strain

The proposed semi-active control device is based on a passive system built up of two restoring SE elements working in phase opposition. Each of these elements is composed by 10 NiTi wires with a length of 1000 mm and 0.24 mm diameter. The mass of the system is 100 kg and the SE material parameters are the ones exhibited in Table 4.3. The response of this system to the prescribed harmonic excitation is given in Figure 6.1.

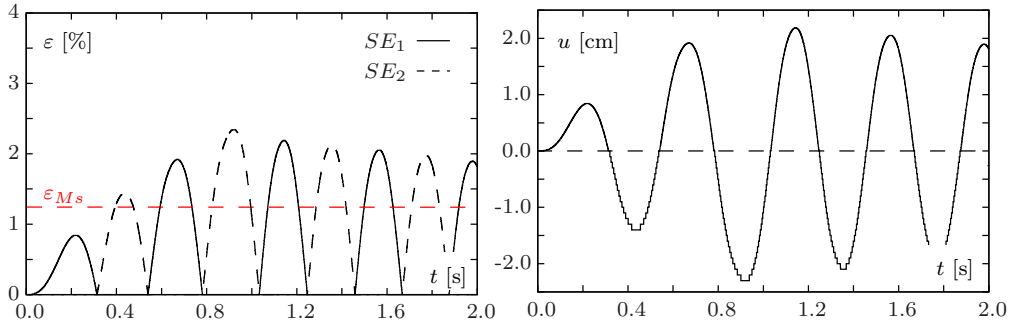

Figure 6.1: Passive system with no pre-strain subjected to an harmonic load. Strain and displacement time-histories.

When compressed, the wires exhibit zero stiffness and therefore SE_1 and SE_2 work alternately, as can be observed in Figure 6.1. In this particular case, the extent of the martensitic transformation caused by the dynamic displacements of the mass is quite small, corresponding to a martensite transformation ratio of about 15% and, hence, little damping occurs. The beginning of the martensitic transformation is

represented in the graph by the horizontal dotted line, $\varepsilon_{Ms} \simeq 1.25\%$.

6.2.2 Passive system with pre-strain

A common technique to enhance the damping capability of a SE system is to enforce a pre-strain in the SE elements [52]. For a given dynamic action, the pre-strain value can be computed as to guarantee that the SE elements are always tensioned during the dynamic process, contributing to the system's response. Moreover, the initial strain in the SE elements can be set to a level that can easily enable higher martensite transformation ratios and hence, higher damping [177].The effect of a 2.0% pre-strain in the wires of the previous passive system is illustrated in Figure 6.2, considering the same harmonic excitation.

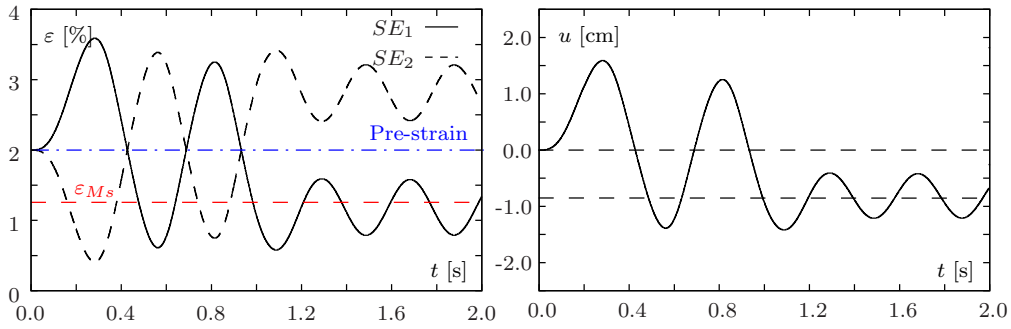

Figure 6.2: Passive system with pre-strain subjected to an harmonic load. Strain and displacement time histories.

In this case, both of the SE elements are always active, developing higher martensitic transformation ratios, up to values of about 40%. This means that the system is taking better advantage of the material's damping capabilities. However, two important drawbacks can be identified in this system. This particular wire arrangement, with two pre-strained SE wires working in phase opposition, leads to a system with no re-centering capability [52]. This can be confirmed in the displacements time-history, during the steady-state free vibration phase, when the oscillations are no longer centered in the original equilibrium position. The second drawback relates to a variety of stress-time effects that have been observed in various SMAs, that tend to adversely impact technological applications based on permanent pre-strained SE wires. According to the work presented by Auguet *et al.* [13], in the case of loading

under strain-controlled conditions, in the coexistence zone, stress seems to decrease under constant strain. The fact that stress induced by pre-strain gradually diminishes with time is a limitation for seismic vibration control devices.

Another phenomenon that might hinder the use of pre-strained SE wires in passive dissipation devices is the possible occurrence of permanent deformation due to cumulative SMA creep [165]. When this happens, the length of the SE wire increases continuously with cycling, meaning that, for a given oscillation amplitude, the strain is reduced, along with the amount of dissipated mechanical energy.

Cumulative creep in Nitinol is linked with the introduction of dislocations and other lattice defects generated at high stress, during the preceding loading cycle [107, 111]. Hence, this accumulated deformation may be controlled by keeping the SE wire inside certain recoverable limits in the SE window. These limits, which ensure an appropriate material behavior, are determined by the material composition and its thermo-mechanical treatment. In fact, the stability of the deformation behavior may be improved by raising the critical stress for slip. Thermo-mechanical heat treatments aimed to stabilize the SE behavior of Nitinol have been found effective [107], minimizing cumulative creep and avoiding the modification of the hysteretic cycle.

While a simple solution, involving a third elastic element, exists in order to recover the re-centering capability of the system [52, 53], the remaining problems related to aging under stress and cumulative creep do not have a simple solution in a passive device configuration. Aging under stress is difficult to avoid, as the use of permanent pre-strained SE wires is crucial in order to obtain competitive damping ratios in this type of systems. In what concerns the cumulative creep, keeping the strains inside the SE window is a very challenging task when dealing with arbitrary seismic excitation.

6.2.3 Semi-active system

The proposed semi-active control device minimizes the SMA rheological effects by controlling the strain in the SE wires. The strain is self-adjusting, allowing the wires to become strain/stress free, when not subjected to a dynamic excitation. The system is also able to keep the wires deformation inside a given SE window, while guaranteeing a minimal threshold to their strain level. The strain in the SE

wires is calibrated by controlling the displacements of the wire's supports. The two wire supports can independently assume two configurations, locked or unlocked. By default, the supports are locked, assuring the adequate restraining of the SE wires. If the system needs to compensate for an excessively low or high strain, in a given wire, it momentarily unlocks the wire through a controlled velocity process without introducing additional forces into the system. As the actuating elements have only two fixed positions, with no intermediate operating positions, this type of control system is usually referred to as a two-position or on-off controller [118]. In Figure 6.3 is presented the generic functional scheme of the original passive system together with the proposed semi-active system.

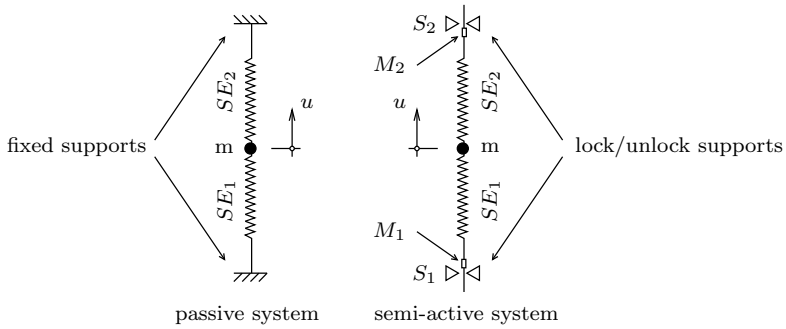

Figure 6.3: Generic functional scheme of the passive and the semi-active systems: SE wires (SE_1 and SE_2), supports (S_1 and S_2) and markers (M_1 and M_2).

Each one of the two SE wires is independently controlled. The output signal from the controller associated with the SE wire i is defined as $U_i(s)$. Each controller has two reference inputs, $R_i^u(s)$ and $R_i^l(s)$ corresponding to the strain upper-bound and lower-bound limits, which, in this case, are constants. Figure 6.4 shows the block diagram of this linear closed-loop control system; see Appendix A.3 for a brief introduction to automatic control systems. The controlled process is defined by the transfer function $G_{cp\,i}(s)$; see Appendix A.2 for the definition of a transfer function. The output $C_i(s)$ is fed back to the summing points, where it is compared with the reference inputs $R_i^u(s)$ and $R_i^l(s)$, yielding the actuating error signals $E_i^u(s) = R_i^u(s) - C_i(s)$ and $E_i^l(s) = R_i^l(s) - C_i(s)$. There is no need for feedback-path transfer functions, to modify the output in order to make it comparable with the reference input signals, since the output of the numerical simulation directly yields the updated strain value for each SE wire. The block diagram of the on-off control system for one SE wire is presented in Figure 6.4.

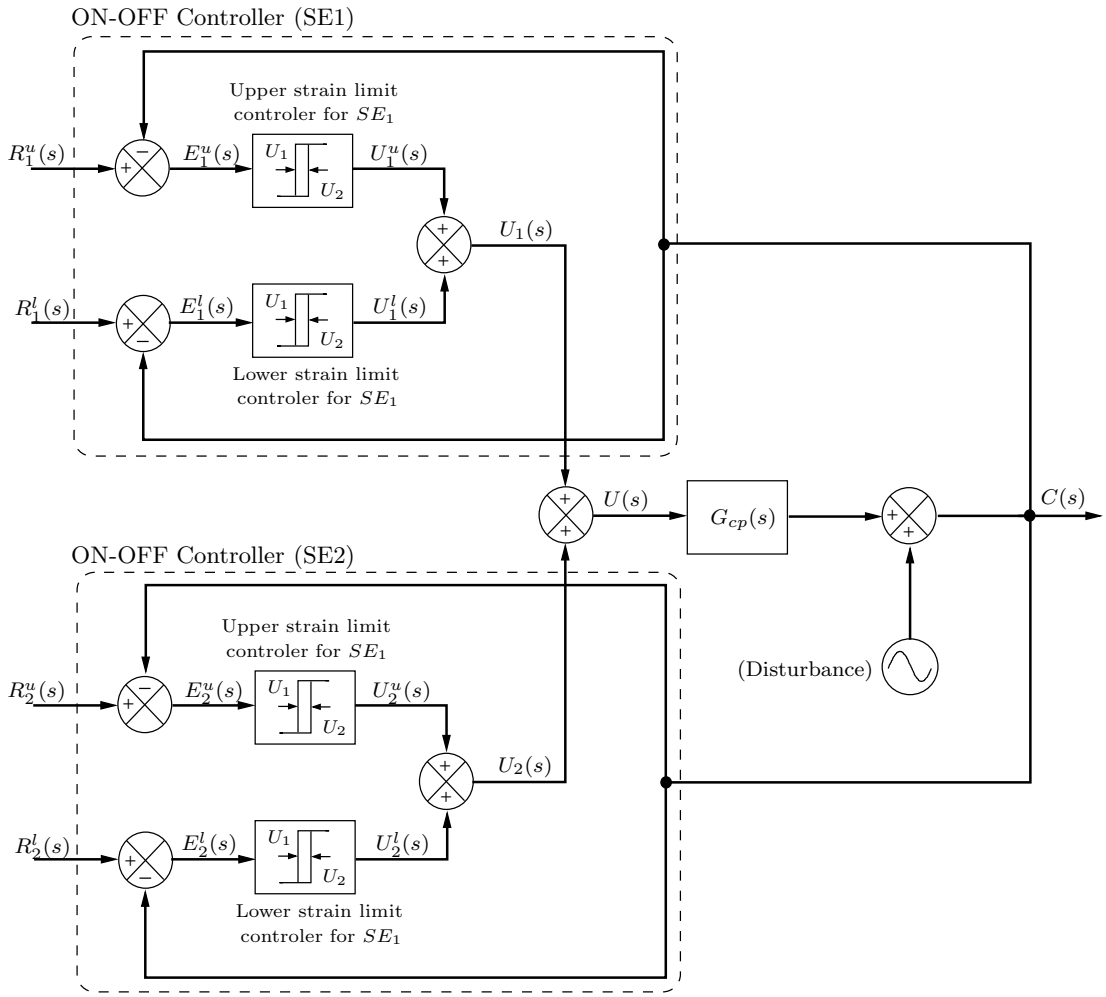

Figure 6.4: Block diagram of the on-off control system.

The signal $u_i(t)$ may assume the values $U_{1\,i}$ and $U_{2\,i}$, corresponding to the locked and unlocked configurations of the SE wire's supports, so that

$$u_i(t) = U_{1\,i}\,(\text{locked}), \quad \text{for} \quad e_i^u(t) > 0 \quad \text{or} \quad e_i^l(t) < 0$$
$$u_i(t) = U_{2\,i}\,(\text{unlocked}), \quad \text{for} \quad e_i^u(t) < 0 \quad \text{or} \quad e_i^l(t) > 0$$

The range through which the actuating error signal must move before the switching occurs is called a differential gap. The differential gap causes the controller output $u(t)$ to keep its current value until the actuating error signal has moved slightly beyond the zero value. In this numerical simulation, the differential gap is related to the size of the implemented time step. A generic strain level time-history for the

SE wire control system is shown in Figure 6.5.

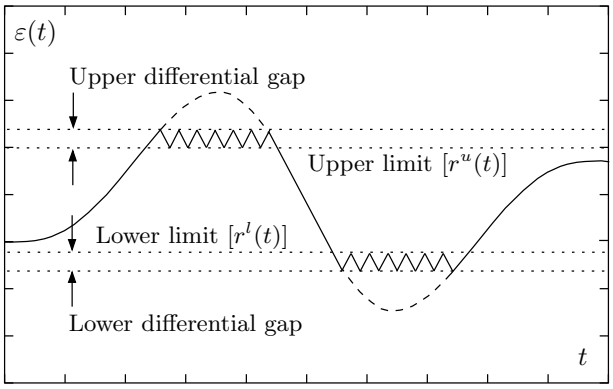

Figure 6.5: Strain level time-history for the SE wire control system.

Analyzing the plots in Figure 6.6, one can see that the proposed semi-active system is able to bound the strains in the SE wires between an upper and a lower strain limit, which, for this case study, are set to 3.0% and zero, respectively. When, during the dynamic oscillations, the strain in a given wire reaches one of these values, the corresponding support is unlocked until the displacement of the system's mass is reversed.

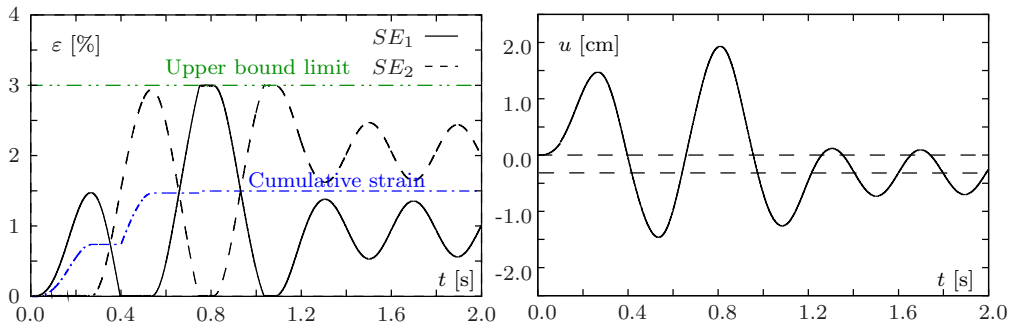

Figure 6.6: Semi-active system subjected to an harmonic load. Strain and displacement time-histories.

The process of unlocking and subsequent locking of SE wires allows the system either to increase their cumulative strain, when compensating for excessively low strains, or to decrease them, when compensating for excessively high strains. As the compensation for lower strains is larger and usually more frequent than the compensation for higher strains, the net accumulated strain in the SE wires is positive.

For the current case study the final accumulated strain in the system adds up to about 1.5%. Note that, there is no need for additional energy input to introduce the strain the SE wires, as the system uses the energy of the excitation itself. As the dynamic displacements develop, the system uses these displacements to gradually increase the strain in the SE wires, inside the established SE window.

When a SE element is unlocked, the system's stiffness decreases momentarily, leading to a slightly higher displacement amplitude, when compared with its pre-strained counterpart. By limiting the strains, the system also limits the martensite transformation ratio in the SE wires ($\xi_{max} = 30\%$ in the current test) and, consequently, the corresponding amount of energy dissipated per time. This means that the system takes longer to attain the steady-state free vibration phase. However, the amplitude of the oscillations in this phase is of the same order of magnitude as in the pre-strained system, see Figures 6.2 and 6.6.

The system is also excited with an harmonic ground acceleration with an amplitude of 2.5 ms^{-2}. To obtain a clearer picture of the steady-state forced vibration phase, the duration of the excitation is incremented from 1 to 3 seconds. The results presented in Figure 6.7 show that although the displacements exhibited by the system also increase, the strains in the SE wires continue to be bounded by the defined strain limits.

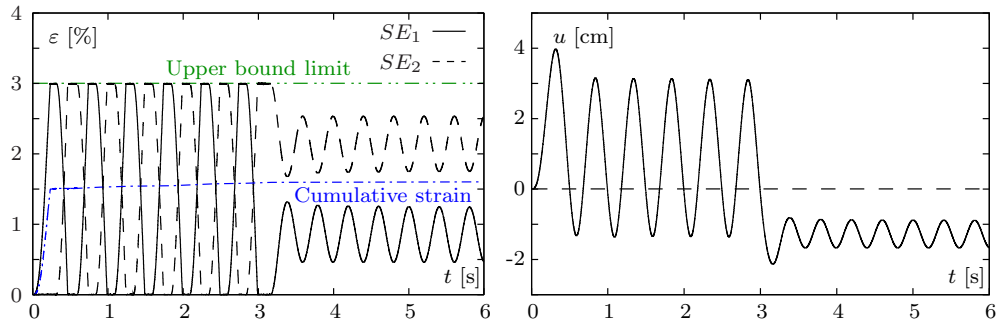

Figure 6.7: Semi-active system subjected to an harmonic load of higher amplitude. Strain and displacement time histories.

The strain-stress hysteretic cycles, presented in Figure 6.8 for the two SE elements show that, as a natural consequence of the applied strain constraints, the stresses in the corresponding SE wires are bounded as well.

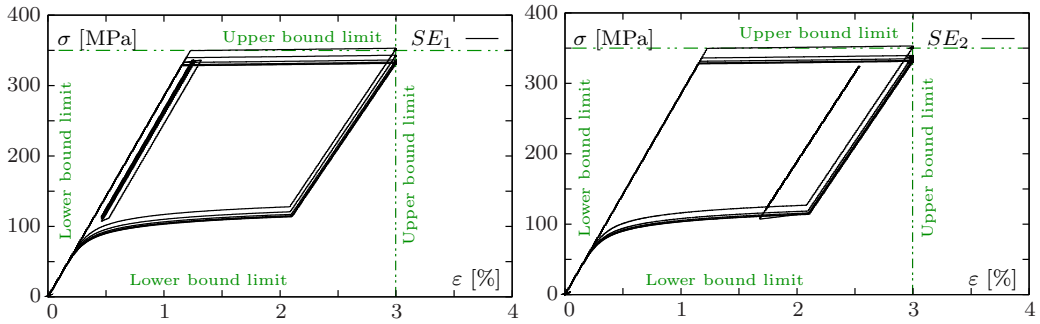

Figure 6.8: Semi-active system subjected to an harmonic load of higher amplitude. Strain-stress hysteretic response for SE_1 and SE_2.

It is known that the stress level related to the beginning and ending of the forward and inverse transformations are temperature dependent. For this particular loading frequency, during the initial mechanical loading cycles, the mean temperature of the SE wires decreases, until it stabilizes around a certain value. This phenomenon causes, during this transitional phase, a decrease of the stress upper-bound limit for both SE wires. This can be observed in Figures 6.9, in the force-displacement response curves.

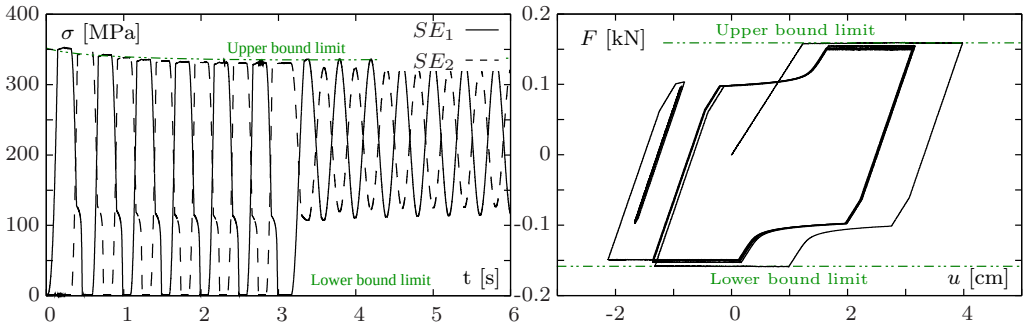

Figure 6.9: Semi-active system subjected to an harmonic load of higher amplitude. Stress time history and force-displacement hysteretic response.

The original passive system that served as a starting point for the present proposal of a semi-active system, has no re-centering capability, a mandatory feature for seismic applications. To accomplish this requirement, a third restoring element is usually introduced [52, 53]. This element enhances the re-centering capability of the system, driving it back towards its original equilibrium position. Assuming it has a pure elastic behavior, the force it delivers is proportional to the displacement of

the system. The final equilibrium position of the system depends on the balance between the force yielded by this re-centering element, and the net resisting force provided by the remaining SE elements.

In the proposed semi-active control device the re-centering capabilities can, under certain conditions, be assured by its ability to control the displacements of the wires at their supports. To emphasize this aspect, one considers again the 1 second, 2 Hz harmonic ground acceleration with an amplitude of 1.25 ms^{-2} and focus on the response of the proposed device, once it reaches its steady state free vibration phase. In Figure 6.10 are presented the corresponding strain and displacement time-histories.

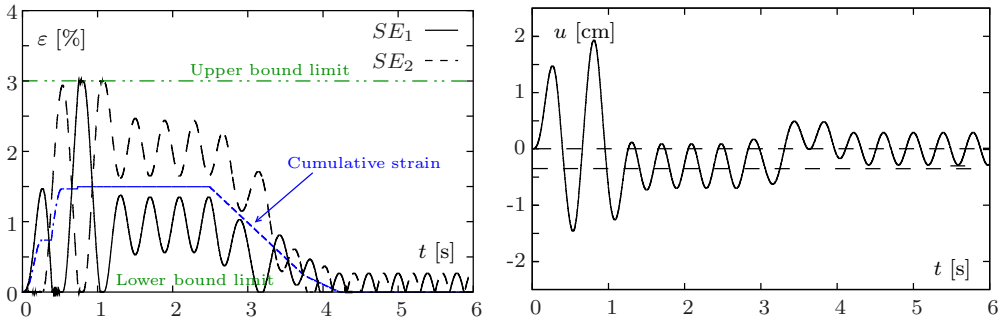

Figure 6.10: Re-centering of the semi-active system subjected to an harmonic load. Strain and displacement time-histories.

Analyzing the displacement time-history in Figure 6.10, one can see that, at the end of the loading period, the system oscillates around a new equilibrium position. To recover the initial equilibrium position, the strains/stresses in the SE wire elements are gradually set free, by unlocking the supports. During this process, the hysteretic loop is closed, giving the system an extra damping capability and enabling it to further decrease the amplitude of the free oscillations.

If during the loading period the displacement's amplitude exceeds a certain level, the releasing of the strain/stress in the SE wire elements may not result in the recovering of the initial equilibrium position. This is shown by analyzing the displacement's time-history of two markers, M_1 and M_2, placed adjacent to the SE elements supports (see Figure 6.3), for three different loading cases. The time-histories of the relative displacement of the markers in relation to their original position, for the different loading cases, are plotted in Figure 6.11.

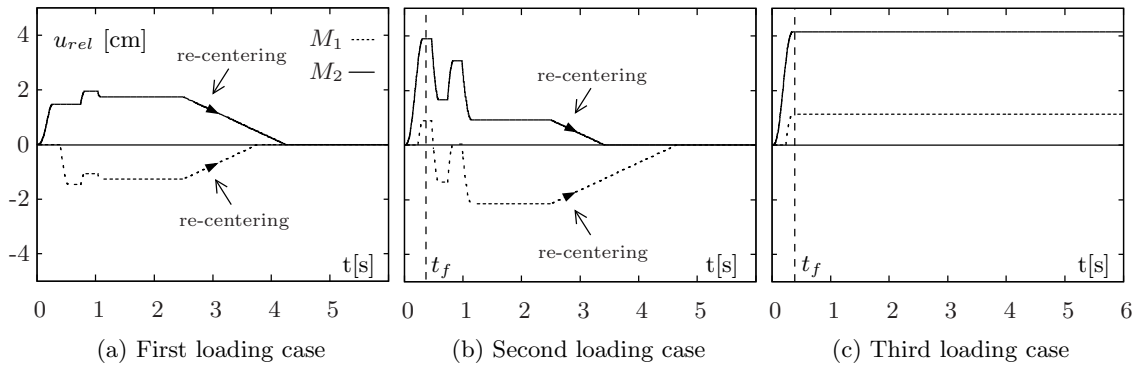

(a) First loading case (b) Second loading case (c) Third loading case

Figure 6.11: Relative displacements of the SE wires at the supports.

The first graph, Figure 6.11(a), corresponds to the loading case that produces the dynamic response represented in Figure 6.10. One can see that, throughout most of the dynamic test, M_1 moves downwards and M_2 moves upwards, as the wires are released to compensate for low strains. When compensating for high strains, M_1 and M_2 reverse their movement but remain on the positive and negative side of the displacements graph, respectively. During the steady-state free vibration phase, if the system releases the wires until M_1 and M_2 reach their initial position, the system is able to re-position itself in the original position.

In the second loading case, when the amplitude of the dynamic loading is doubled, while compensating for high strains, situations occur where M_1 becomes positive, as illustrated in Figure 6.11(b). However, when the system reaches its steady-state free vibration phase, as M_1 is negative and M_2 positive, it is still able to re-position itself in the original equilibrium position.

This is no longer the case if the dynamic load is interrupted at $t = t_f$. In this case the system reaches its steady-state free vibration phase in a situation where both M_1 and M_2 are positive, as it can be seen in Figure 6.11(c). From this configuration it is impossible to recover the system's original position just by releasing the SE elements. This action will only cause further displacements in the positive direction of marker M_1.

As the system may loose its re-centering capabilities for certain oscillation amplitudes, if one wants to guarantee the re-centering capabilities of the system a third elastic element should be used.

To clarify the sequence of actions taken by the proposed semi-active system during a dynamic loading, one considers the displacement time-history of a typical response to an harmonic excitation, as shown in Figure 6.12.

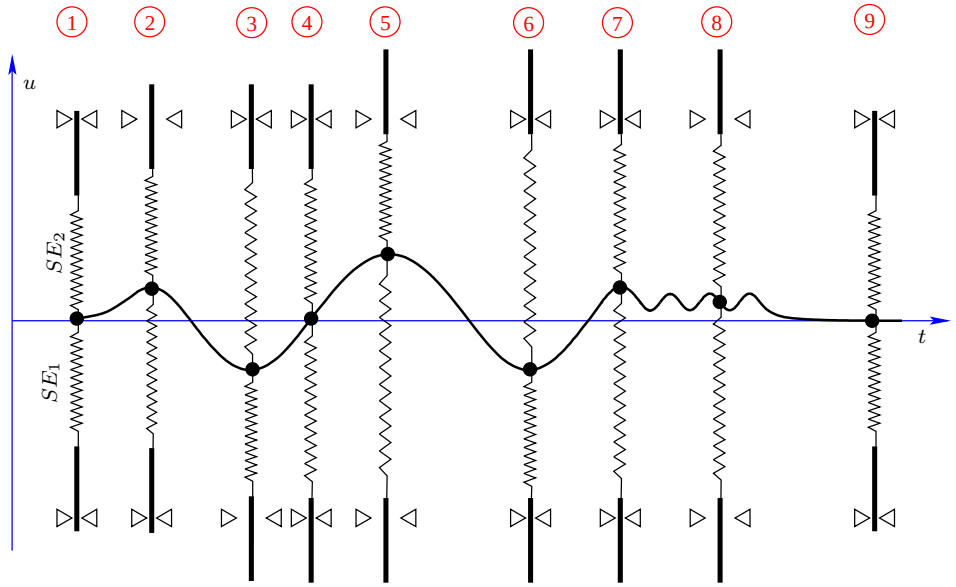

Figure 6.12: General behavior of the proposed semi-active control system.

The analysis starts with the system resting in its original equilibrium position, referred as position 1 in the graph. In this position both of the SE elements, SE_1 and SE_2, are strain/stress free and their supports, S_1 and S_2 locked.

Once the harmonic excitation is applied to the system, the mass starts to move (assume) upwards and the straining of SE_1 begins. During the first quarter cycle of the movement, between position 1 and 2 in the graph, S_2 is unlocked to prevent compression in the corresponding element, while the support of SE_1 is kept locked, to ensure the straining of the wire.

As the direction of the movement is reversed, S_2 is switch to locked, to preserve the accumulated strain in the wire. As the movement continues downwards, the support of SE_1 remains locked as well, until the mass reaches its original equilibrium position. With this configuration, displacements below this point would cause compression in the SE_1. For this reason, as soon as this happens, S_1 switches to unlocked, until position 3, when the mass reverses its direction once again.

At the end of the first loading cycle, position 4 in the graph, both SE wires have

already accumulated a certain level of strain. Note that this strain was introduced in the system by the external dynamic load itself, without any need of supplemental energy input.

Between positions 4 and 5, assuming that in the last one occurs the maximum displacement amplitude, both supports will switch from locked to unlocked: S_2, as the strain in SE_2 approaches zero to avoid compression, and S_1, as the strain in SE_1 goes beyond the defined value inside the SE window, preventing it from further straining. If, during an eventual steady-state forced vibration phase, positions 5 to 6, there is no need for adjustments in the SE wires to compensate low or high strains, both supports remain locked.

As soon as the dynamic excitation ceases, position 7, the amplitude of the free vibrations starts gradually to diminish because of the SE damping. The system reaches its steady-state free vibration phase, position 8, oscillating around an equilibrium position different from its original one. During this period, both supports remain locked. At this point, to recover the original equilibrium position, the system unlocks both of the cables, relinquishing the accumulated strain in the wires.

Note that, every time the system needs to unlock a support, the wire is released with a controlled velocity, which can be seen as a design parameter of the proposed semi-active device. In all the reported numeric tests, this velocity is set to 0.6 m/s.

Finally, position 9, the supports are locked again to prepare the device for the next dynamic excitation.

6.3 Semi-active device under seismic excitation

The efficiency of SE based passive control devices in the context of seismic loading was already analyzed, considering a simplified numerical model of the São Martinho railway viaduct. In this section, the same model is used to test the behavior of the proposed semi-active control device under seismic excitation. For the longitudinal analysis of the viaduct, it is assimilated to an elastic, SDOF dynamic system, with 4650 ton mass and a stiffness of 355×10^3 kN/m. An additional structural damping of 5% is provided to the system in order to make the analysis more realistic.

The records of two historic strong earthquakes are used in the numerical simulation: *El Centro*, with a magnitude of 7 M_W and *Kobe*, with a magnitude of 6.9 M_W. Their acceleration time-histories in units of gravity acceleration, G, as provided by the Pacific Earthquake Engineering Research Center and the University of California in the PEER Strong Motion Database [126], are given in Figure 6.13.

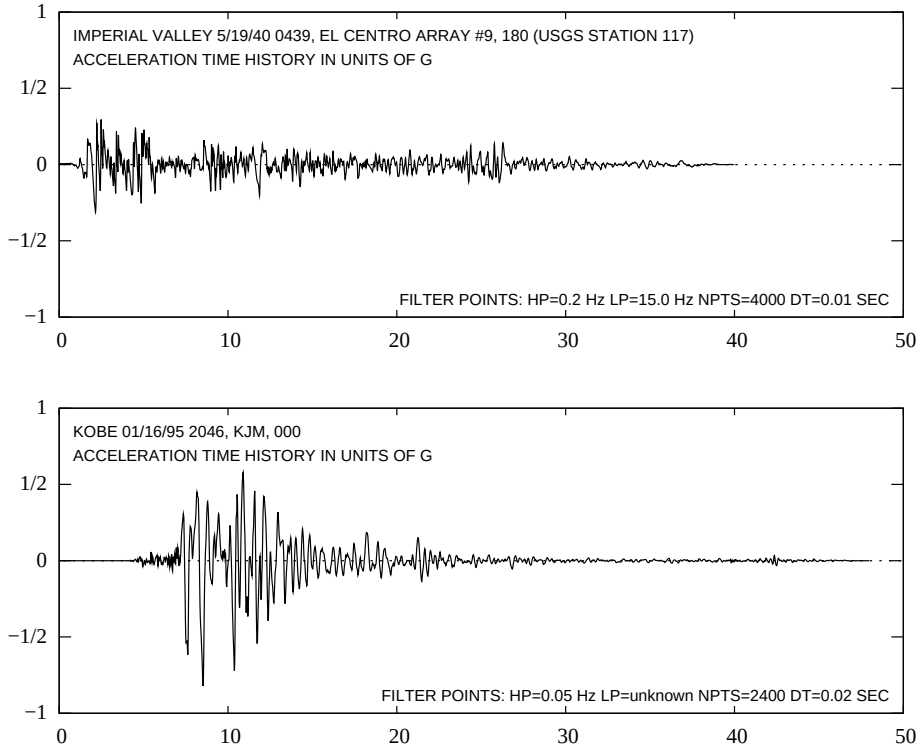

Figure 6.13: *El Centro* and *Kobe* earthquakes: PEER Strong Motion Database records [126].

To emphasize the benefits of the proposed semi-active control device on the structural response of the structure, three cases are considered: the uncontrolled structure, the structure controlled with a SE based passive device and the structure controlled with the proposed semi-active device. Note that, in order to get comparable sets of results, the strain level in the SE wires of the passive device was set equal with the maximum strain level attained in the semi-active device. To obtain an adequate response of the semi-active device to the higher frequency content of the seismic action, when the supports are unlocked, the wires are released with a velocity of 1 m/s.

Vibration control devices, both either passive or semi-active, are placed at the ends

of the tested viaduct, one for each main girder. Each device is composed by two sets of 1.0 m SE wires, each set with a total area of 100 cm^2. The mechanical characteristics of the SMAs are the ones defined in Table 4.3. A pre-strain of 2.25% is considered in the passive device, which equals the resulting cumulative strain in the semi-active device.

The displacement and acceleration time-histories of the viaduct's deck in the longitudinal direction, regarding the passive and semi-active control systems, for the *El Centro* earthquake, are presented in Figure 6.14.

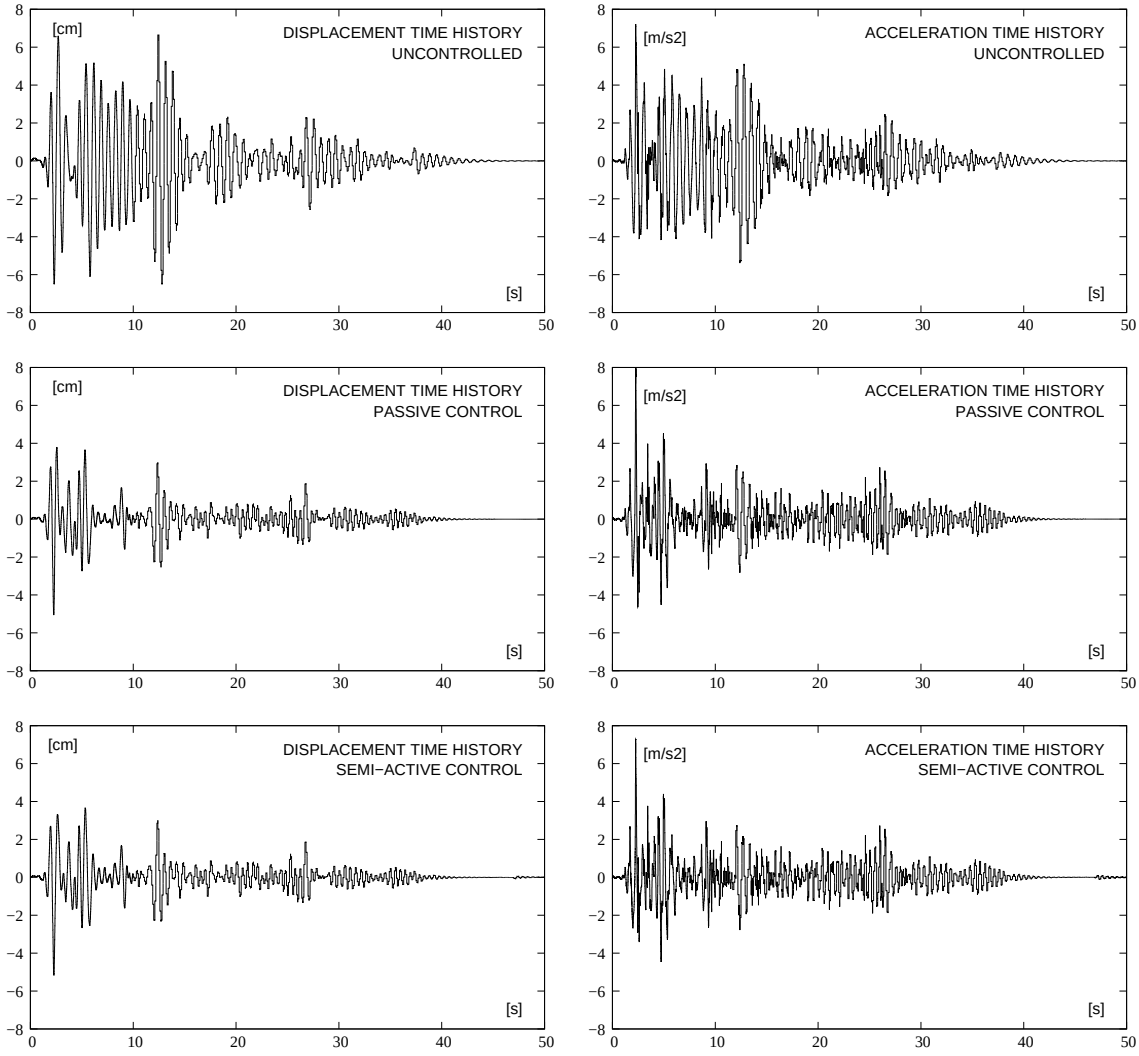

Figure 6.14: Response of the structure to *El Centro* earthquake: displacement and acceleration time history for the free and controlled structure.

The corresponding strain time-histories in the SE wires for the *El Centro* earthquake, are presented in Figure 6.15.

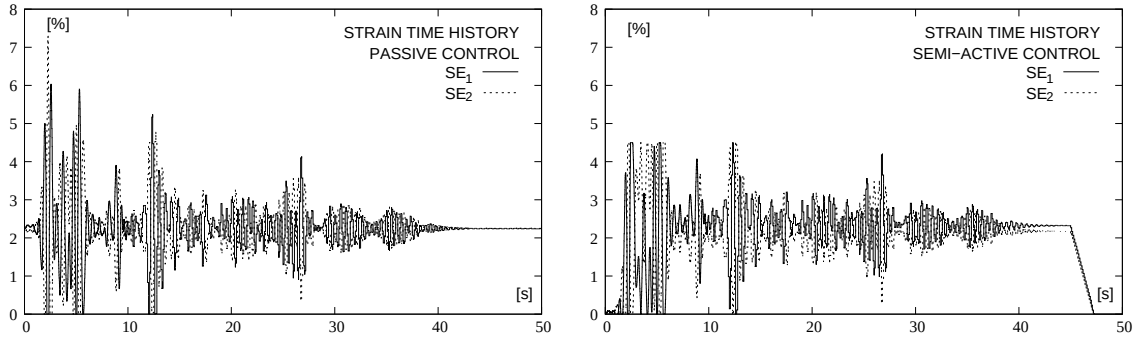

Figure 6.15: Response of the structure to *El Centro* earthquake: strain time history in the SE wires of the controlled structure.

Analyzing the plots in Figure 6.14, one can see that, during the seismic excitation, the two control devices exhibit similar damping characteristics, being able to considerably reduce the amplitude of the earthquake induced displacements and accelerations. The plots in Figure 6.15 however, illustrate that the strain time-history in the SE wires is quite different for the two adopted control solutions. Although the pre-strain in the passive device is equal to the cumulative strain in the semi-active device, one can see that the maximum strains developed in the passive device are considerably larger when compared with the ones developed in its semi-active counterpart. As their values are outside the SE window, the long term behavior of the passive device might be compromised. However, no failure occurs in the SE wires during the earthquake. One can observe that, when the seismic excitation stops, the SE wires return to their initial pre-strain, favoring the occurrence of stress-time effects. On the other hand, in the semi-active device, the wires return to their strain-free condition at the end of the loading.

To conclude, one may say that, for the given seismic excitation, except for the stress-time effect phenomena, the two control solution produce equivalent results. One must note, however, that the pre-strain level in the passive control device was calibrated according to the given seismic excitation, in order to avoid failure in the SE wires. If a different seismic action is applied to the same structure configuration, the results might be completely different. In order to illustrate this behavior, the structure is subjected to *Kobe* earthquake. The displacement and acceleration time-

histories of the viaduct deck in the longitudinal direction, regarding the passive and semi-active control systems, for the *Kobe* earthquake, are presented in Figure 6.16.

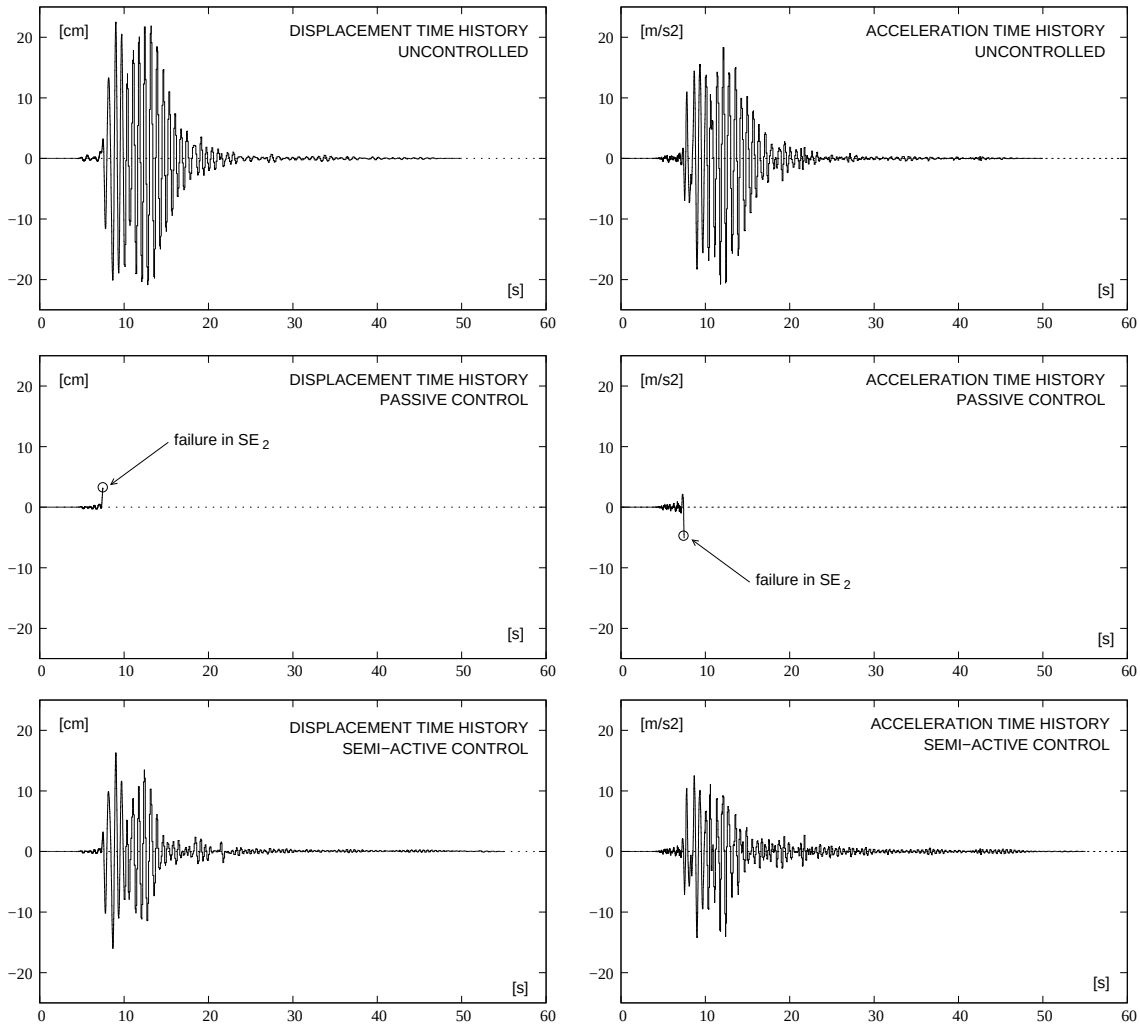

Figure 6.16: Response of the structure to *Kobe* earthquake: displacement and acceleration time history for the free and controlled structure.

The corresponding strain time-histories in the SE wires for the *Kobe* earthquake, are presented in Figure 6.17.

Analyzing the dynamical response of the structure presented in Figures 6.16 and 6.17, one can see that the passive control device fails, as its SE wire's recoverable strain capacity ($\simeq$ 10 to 12%) is exceeded. Besides stress-time effect and creep potential problems, the fact that this type of solutions need an *a priori* value for the level of pre-strain in the SE wires, represent an important drawback in the case of seismic

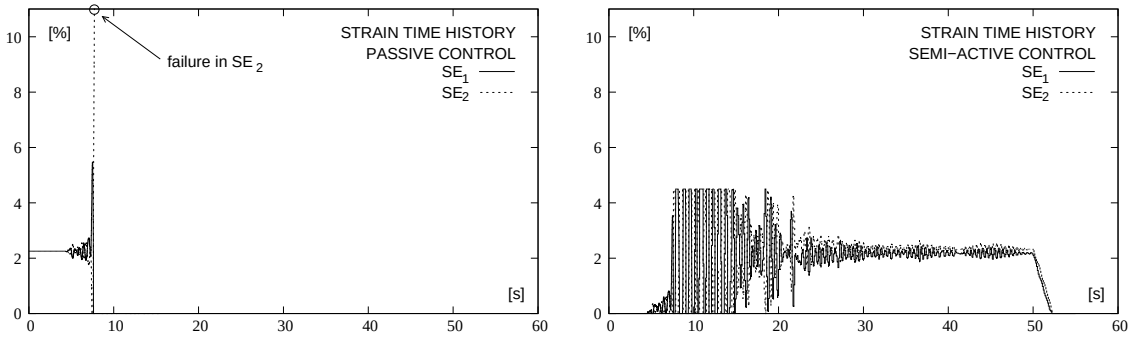

Figure 6.17: Response of the structure to *Kobe* earthquake: strain time history in the SE wires of the controlled structure.

applications. While estimates for the maximum strain in the SE wires are relatively easy to obtain in the case of service loads, and therefore a corresponding value for the necessary pre-strain can be computed, this is no longer the case for extraordinary dynamic loads.

With no need of initial pre-strain calibration, its semi-active counterpart responds well to virtually any level of dynamic excitation, as illustrated here in the case of *Kobe* earthquake. When the response of the structure is compared with the one obtained for the *El Centro* earthquake, one can see that the system exhibits similar characteristics. It presents important damping capabilities, it is able to confine the strains in the SE wires to predefined levels, inside the SE window, and finally, at the end of the action, it is able to recover the SE wires strain free condition.

Another benefit related to the semi-active control device is its ability to limit the force values throughout the entire duration of the seismic action. When implemented in a civil engineering structure the force that the semi-active device transmits to the structure can be easily controlled [39].

6.4 Closure

The proposed semi-active vibration control device originates from a passive control system, based on SE austenitic wires. The proposed semi-active device monitors the feedback strain measurements and based on this information, continuously adjusts the strain in the SE wires, in order to improve its behavior during dynamic loadings.

Permanent pre-strain in the SE wires is avoided since the strain accumulation results from the structural displacements during a dynamic action, with no need for external energy input. Stress-time effects in the SE wires are hence prevented. The SE wires are also set strain free at the end of the loading period.

The system is able to dissipate a considerable amount of energy while keeping the SE wires inside recoverable limits defined by a prescribed SE window, minimizing the effects related to cumulative creep. The system also guarantees a minimal threshold to the strain level in the SE wires and exhibits efficient re-centering capabilities.

The numerical simulations demonstrate the potential of the proposed semi-active control device in improving the seismic response of civil engineering structures.

Chapter 7

Prototype of the Novel SE Device

7.1 Introduction

In this chapter is presented a prototype of the novel vibration control device described in Chapter 6. The aim of this physical prototype is to further clarify and substantiate the results obtained during the numeric simulations. The main idea underlying the proposed semi-active control device is to improve the seismic behavior of a SE bridge restraining system, by limiting the corresponding strains/stresses inside a given SE window. Another important aspect of the proposed prototype is that the SE elements are strain/stress free up to the moment the dynamic excitation arises. With the beginning of the dynamic excitation the cumulative strain/stress process in the SE wires starts, enabling higher martensite transformations ratios and increased damping capacities in the system. The cumulative strain/stress in the SE wires is a direct result of the system's movement, which derives from the dynamic excitation.

7.2 Building the prototype

The prototype simulates the behavior of a bridge with SE restrainer cables in the deck-abutment interfaces, to limit the respective hinge opening during a dynamic event. In Figure 7.5 is shown a schematic drawing of a simple supported bridge with such a restraining system.

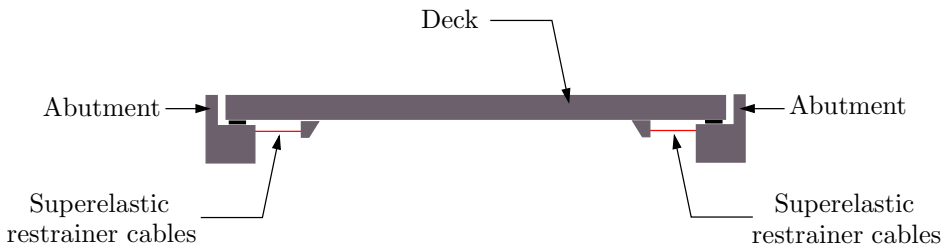

Figure 7.1: Simple supported bridge with a SE restraining system.

One of the main objectives of the control system is to confine the strain/stress values in the SE wires inside a prescribed SE window. In order to accomplish this goal, a stress control approach is used. This means that the system must be able to continuously read the stress values in the SE wires and adjust these values, if necessary, in order to guarantee that the prescribed SE window is respected. For the system to be able to read the stress values in the SE wires, it must be equipped with a set of two force-sensors, one sensor per wire. Each force-sensor is placed in series with the SE wire, at one of its supports. At the opposite ending of each wire, a linear actuator is placed, enabling the system to adjust the corresponding stress level. Although not strictly necessary to the control process itself, the prototype is equipped with a displacement-sensor and an accelerometer, in order to continuously monitor the position and acceleration of the system's mass. The design and manufacturing of the physical prototype is carried out using an educational version of SolidWorks. The main features of the control system prototype are shown in Figure 7.2.

The moving-mass-module (MMM) accommodates the SE wires force-sensors. The MMM is mounted on rails, enabling the displacements of the module in the direction of the dynamic loading. The displacement of the module is monitored by a displacement-sensor, which is placed underneath the module. The rails are fixed to a set of bars that also hold on both of the linear actuators, through thick end plates. The linear actuators comprise a clamping device that constrains the movement of the remaining extremity of the SE wires. The bars can be rigidly connected to a shake table, by means of four brackets.

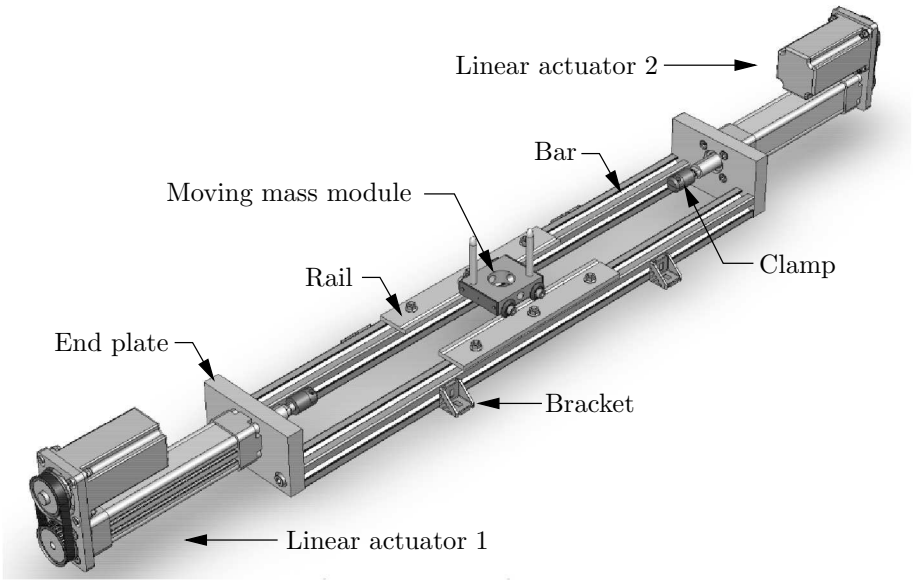

Figure 7.2: General design concept for the physical prototype.

7.2.1 Moving-mass-module

One of the kernel elements of the physical prototype is the MMM. The specifications for the design of this component mainly derive from these requisites:

1. As the physical prototype represents a SDOF dynamic system, the movement of the mass is limited to one direction. This movement has to be extremely smooth, involving the least possible friction;

2. The value of the mass should be able to vary, as to increase the system's experimental redundancy;

3. The moving mass system has to integrate two force-sensors for the SE wires, to continuously monitor their stress level;

4. The moving mass system has to comprehend a displacement-sensor in order to monitor its displacement with respect to the shake-table;

5. The moving mass system has to comprehend an accelerometer in order to monitor its acceleration.

In order to comply with these requisites, the MMM is built up as a modular system. The base of the module is made of a CK45 steel plate, with dimensions $a = 10$, $b = 20$ and $c = 30$ mm. This base presents five holes in order to make it lighter. The base module accommodates a series of additional steel plates, with different dimensions and weights, which are fixed to the base plate by two metallic pins. The mass of the moving mass base, as well as of the additional mass modules are presented in Table 7.2.

Element	*Mass (kg)*
Base	0.545
$M1$	0.497
$M2$	0.980
$M3$	2.035
$M4$	2.043

Table 7.1: Mass of the MMM elements.

These pins constitute two rounded head cylinders, with a total length of 100 mm and a diameter of 8 mm. The MMM is provided with a set of four steel beveled shape wheels, with RHP 618/8 bearings and is mounted on a set of two 40×10×300 mm AW-6063-T6 aluminum bars, with wedged shape rails. As the angle presented by the wedge shaped rails is wider than the one shown by beveled wheels, the contact area between the two pieces is minimized, reducing the mechanical friction developed in this interface. In Figure 7.3 is presented the result of the design phase of the MMM, including a general view of the module and a detail of the wheel-rail interface.

7.2.1.1 Force-sensors

In order to characterize the SE wires stress state, the MMM has to be provided with a set of two force-sensors. Given the limited dimensions of the module, the space available for the positioning of these sensors is quite reduced. Although one can easily find several types of miniature load cells on the market, their price is not compatible with the budget set for building the physical prototype. Hence, the alternative option is to design and built the force-sensors, taking into consideration the dimensional restrictions, the desired performance in terms of force readings and also the limited budget. The idea underlying the behavior of the force-sensor is

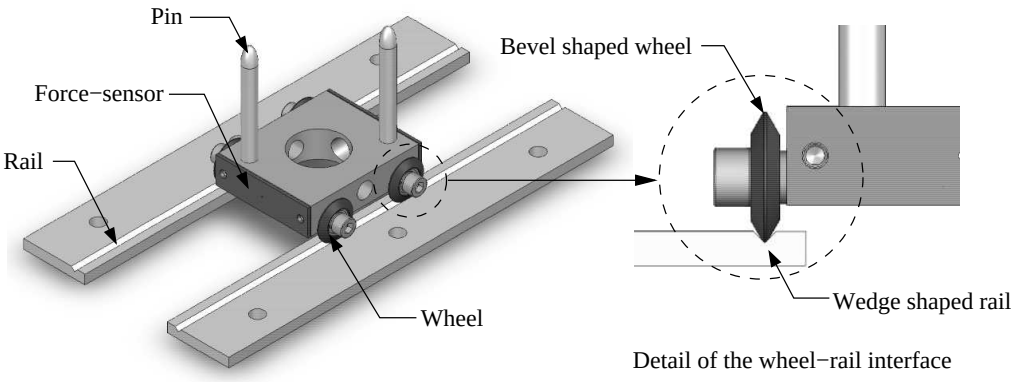

Figure 7.3: Moving-mass-module. Design phase.

to clamp the SE wire into a thin AW-6063-T6 aluminum plate, which is laterally fixed to the MMM. The SE wire is clamped to the aluminum plate using a special designed element; see Figure 7.4. This aluminum plate is equipped with a set of four strain-gauges disposed in a Wheatstone bridge configuration, to enable accurate force readings.

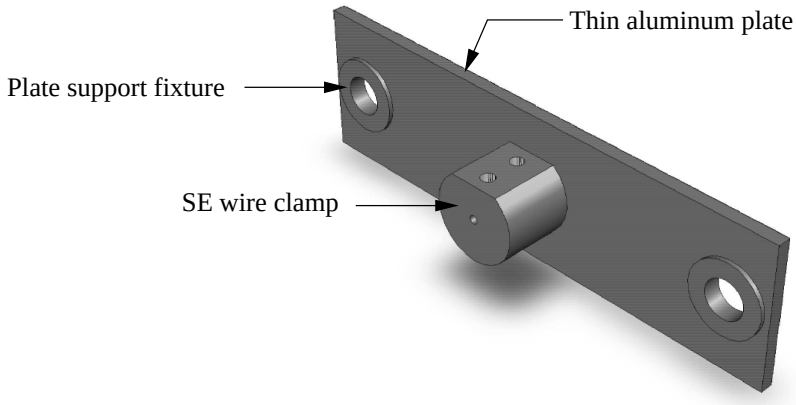

Figure 7.4: Concept design of the force-sensor.

The Wheatstone bridge is the electrical equivalent of two parallel voltage divider circuits [116]. One of the voltage divider circuits is composed by R_1 and R_2, and the second voltage divider circuit is composed by R_4 and R_3. The output of a Wheat-

stone bridge is measured between the middle nodes of the two voltage dividers. When a strain variation is applied to a specimen, the resistance of the strain-gauges, in the Wheatstone bridge, changes accordingly. The Wheatstone bridge configuration is used to help the measurement of small variations in the resistance that the four strain-gauges produce, corresponding to a change in the specimen's strain field. This bridge configuration is usually called a full-bridge, since it has four active strain-gauges [116]. In this particular case, two are mounted in the direction of the bending strain, with one on the maximum strain zone of the plate and the other on the minimum strain zone. The other two act as Poisson gauges and are mounted transversely to the principal axis of strain, adjacent to the other two strain-gauges. In order to built this bridge, two HBM T-rosettes with two measuring grids, model 1-XY13-1.5/350, are used. The dimensions of the T-rosettes are 9×5 mm with 1.5×1.5 mm measuring grids. The nominal resistance of these strain-gauges is 350 Ω, and their temperature response is matched to aluminum in order to minimize the system's sensitivity to temperature. In Figure 7.5 is represented a schematic drawing showing the position of the two T-rosettes on the force-sensor, together with the corresponding full-bridge circuit diagram. In this circuit diagram, V_{CH} is the measured voltage of the signal and V_{EX} the excitation voltage.

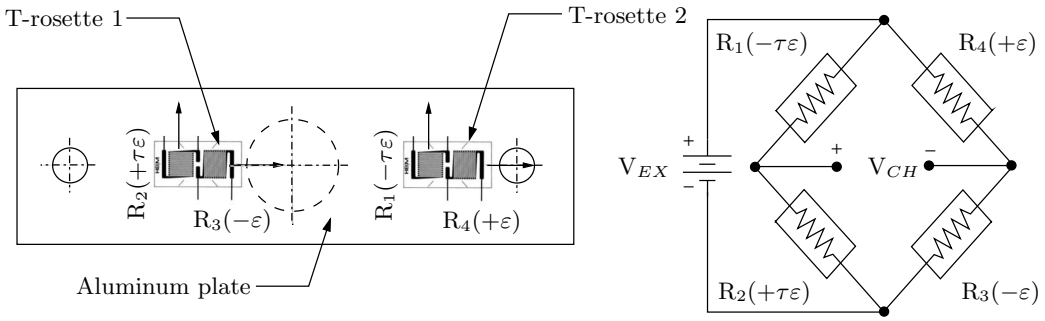

Figure 7.5: Schematics of the force-sensor. Full-bridge circuit diagram.

A FE model of the force-sensor is developed, using ANSYS 11.0, in order to obtain the strain field corresponding to the loading of the SE wire. This FE model enables not only to define the positioning of the T-rosettes on the force-sensor but also to calibrate the thickness of the aluminum plate in order to obtain an adequate signal from the bridge. The force used for the calibration of the FE model corresponds to a stress level of about 300 MPa in a Nitinol SE508 wire with 0.406 mm diameter, which

corresponds to half of the maximum stress associated with the loading plateau. In Figures 7.6 and 7.7 are represented two plots that resulted from the analysis of the FE model, namely the strain field in the longitudinal direction of the plate and the displacements along the direction of the SE wire. The dimensions considered for the plate are 60×17×2 mm. The maximum absolute strain in the plate yields 0.25 mε, corresponding to a stress of about 18 MPa. The maximum displacement in the plate along the z direction, which coincides with the wire's axis, yielded 0.013 mm.

The voltage ratio, V_r, is used in the voltage to strain conversion equation and is defined by the following equation [116]:

$$V_r = \frac{V_{CH}(strained) - V_{CH}(unstrained)}{V_{EX}} \tag{7.1}$$

To convert the strain units into voltage readings, for this type of full-bridge, the following equation may be used [116]:

$$V_r = -\frac{1}{2}\,\varepsilon\, GF\,(1+\nu) \tag{7.2}$$

The gauge-factor, GF, is a fundamental parameter of the strain-gauge, since it is a measure of its sensitivity to strain. The gauge-factor is defined as the ratio between the fractional change in electrical resistance and the fractional change in the length (strain) [115]:

$$GF = \frac{\Delta R/R_G}{\varepsilon} \tag{7.3}$$

where ΔR is the change in resistance caused by strain and R_G is the resistance of the undeformed gauge. As the value of the gauge-factor for the used strain-gauges is 1.96±1.5%, considering $\nu = 0.33$, V_r yields 0.33×10^{-3}. For the maximum stress level of the loading plateau this value is doubled, i.e. $V_r = 0.66\times10^{-3}$. For a bridge excitation voltage of 10V and considering $V_{CH}(\text{unstrained}) = 0$, the strained bridge output voltage yields approximately 6.6 mV. The necessary gain is then automatically applied to the readings, by the data acquisition system.

To guarantee that the strain-gauge is able to perform its task properly, the strain to be measured has to be transferred faultlessly and free of loss [72]. To achieve this purpose, an intimate connection is required between the strain-gauge and the aluminum plate. The surface of the metal is first cleaned, and a special cyanoacrilate

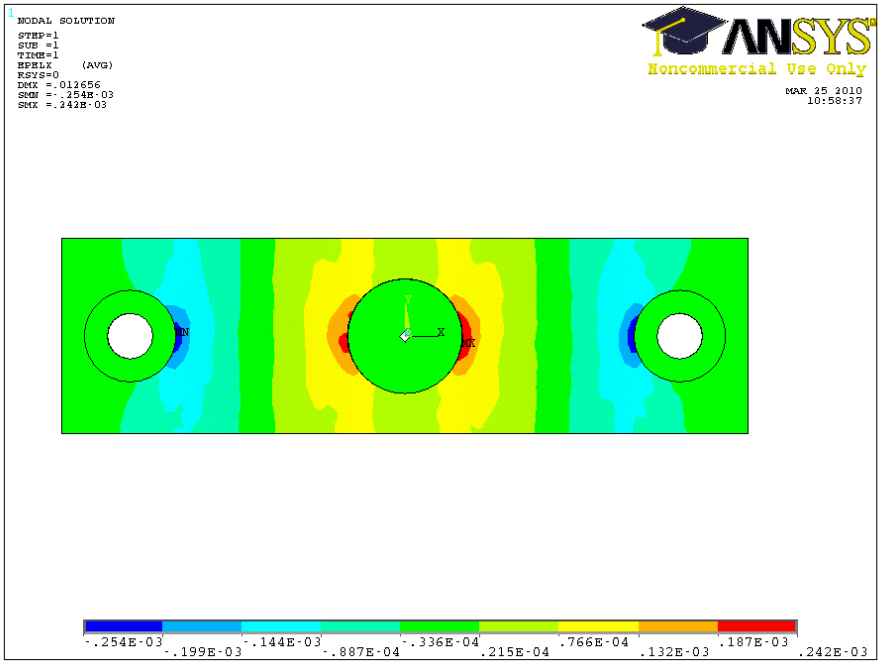

Figure 7.6: ANSYS results: plot of the strain field along the longitudinal direction of plate

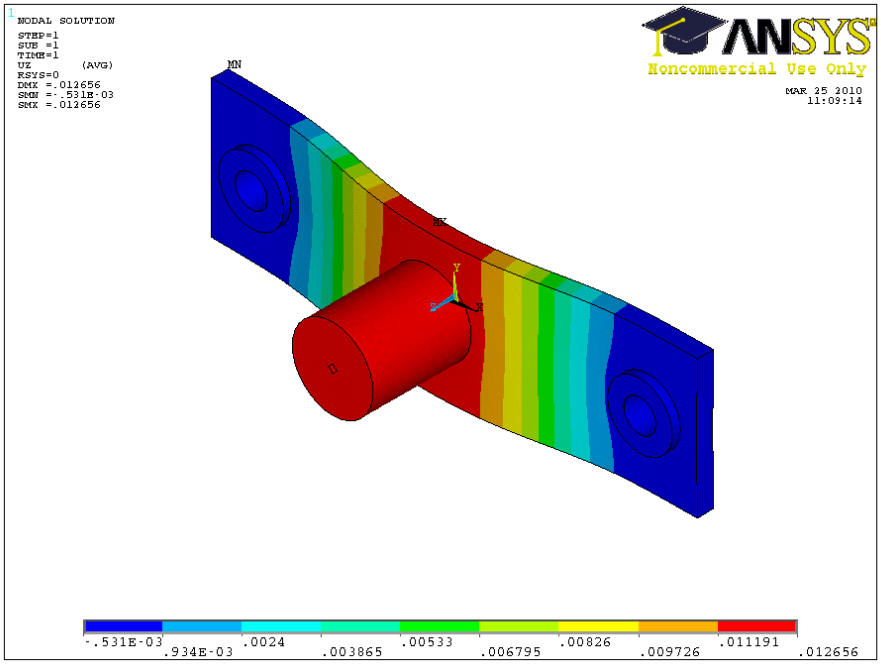

Figure 7.7: ANSYS results: plot of the displacement along the direction of the SE wire

cold curing adhesive (Z70) is used in order to guarantee the required bonding between the strain-gauge and the plate. Strain-gauges with integral solder terminals allow for the direct soldering of the measuring wiring cables. In this case, it is advisable to use separate solder terminals to facilitate faultless solder connections and protect the thin leads from tension forces of the cables [72]. Wiring within the bridge is executed with thin wires, in an approximately symmetric way, with identical wires presenting the same length. As the connection cables must not only transmit the measurement signal, but limit noise signals to an acceptable minimum, adequate electrical connection cables are used [72].

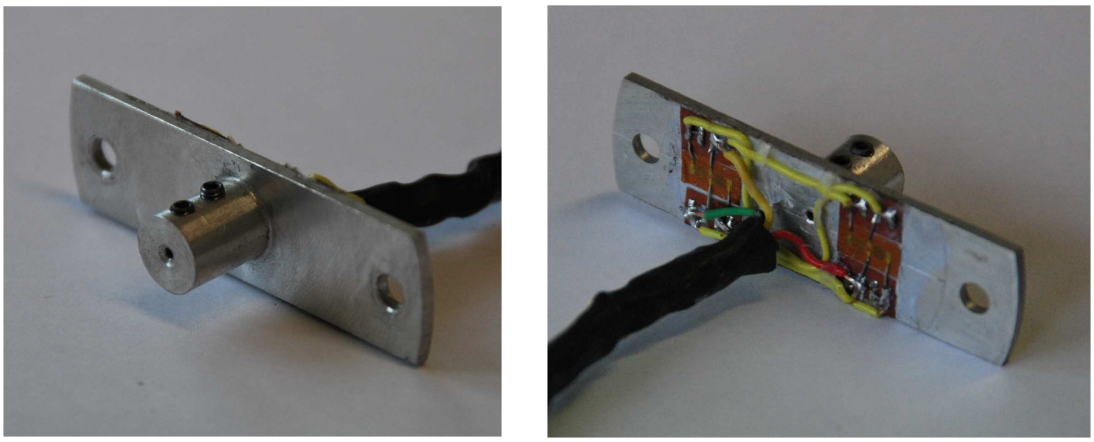

(a) Front view. (b) Rear view.

Figure 7.8: Force-sensor. General views.

In Figure 7.8 are shown two views of the force-sensor. Figure 7.8(a) depicts a front view of the force transducer with the clamping apparatus of the SE wire in evidence. In Figure 7.8(b) one can observe a rear view showing the strain-gauges, internal wiring connections and corresponding soldering terminals.

The strain-gauges are connected to the National Instruments (NI) SCXI-1520 8-Channel Universal Strain Gage Input Module, using the screw terminals from the Front-Mounting Terminal Block SCXI-1314. The calibration of the force-sensors is made using four reference weights. A Virtual Instrument (VI) is created, using a LabView 9.1 framework, that enables the signal acquisition from the force-sensor and, once calibrated, yields the desired force readings. Just for illustrative purposes, the block diagram of the force-sensor VI and its *front panel* are shown in

Figures 7.9 and 7.10.

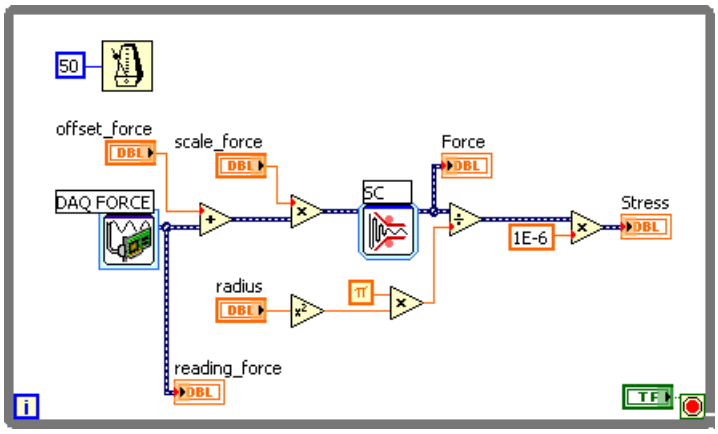

Figure 7.9: Force-sensor block diagram.

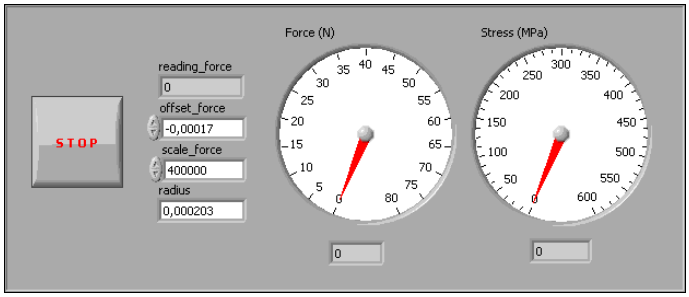

Figure 7.10: Force-sensor VI *front panel*.

A DAQ Assistant Express VI, using NI-DAQmx Software, is used to create, edit and run the analog input corresponding to the voltage measurement task. A sample compression of the data points is performed in order to attenuate the noise derived form the readings. The sample compression VI acquires a large number of data points (50 points) and compresses the data points into a smaller number of points, through an averaging process. To calibrate the force-sensor VI, the strain readings associated with the reference weights are then scaled and offset, in order to yield the corresponding force values ($F = m\,\varepsilon + b$).

The first step regarding the force-sensor VI calibration is to compensate for the initial offset of the strain readings. The m value is then calibrated, for all the

reference weights, in order for the VI to yield the precise value of the corresponding weight element. An average compensation is applied and the errors associated with the final readings are evaluated. The information regarding the calibration process of the force-sensor VI is presented in Table 7.2.

Element	*Weight* (N)	b	m	*Final reading* (N)	*Error* (%)
$W1$	4.87	-0.00017	40500	4.93	$+1.25$
$W2$	14.47	-0.00017	39500	9.48	-1.25
$W3$	34.41	-0.00017	39000	19.44	$+2.50$
$W4$	54.43	-0.00017	41000	20.52	-2.50

Table 7.2: Calibration of the force-sensor.

The calibration curve of the force-sensor VI, together with the final readings for the reference weights is presented in Figure 7.11.

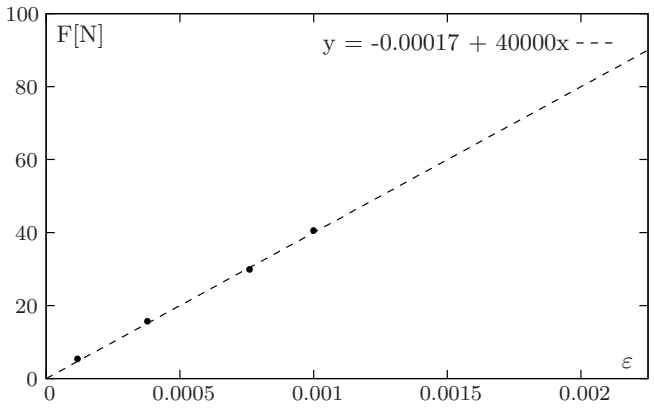

Figure 7.11: Calibration curve.

To finalize this section, two views of the complete MMM, as built, are shown in Figure 7.12. In Figure 7.12(a) is presented the base of the MMM, with the force-sensors already in place, together with the corresponding wiring. The cylindrical pins are also shown in the figure, positioned in one of the diagonals of the base module. In Figure 7.12(b) the loaded MMM is shown with two additional weights. These weights are secured to the base module by a set of two holes with a diameter of 9 mm, that accommodate the cylindrical pins.

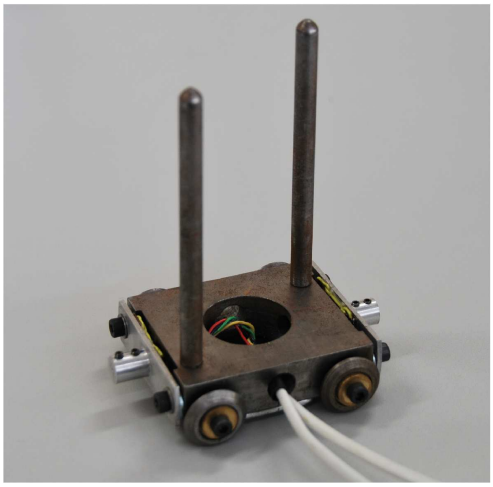

(a) Unloaded MMM.

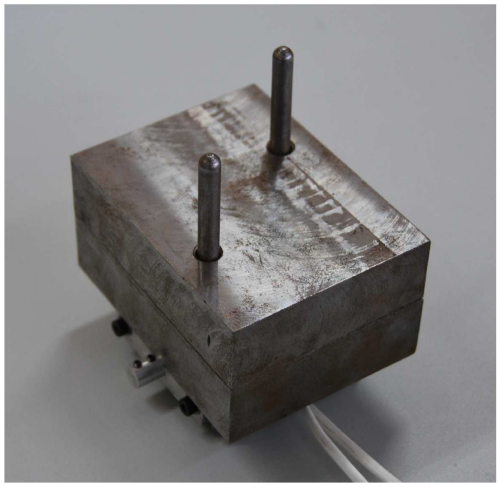

(b) Loaded MMM.

Figure 7.12: Moving-mass-module. General views.

7.2.1.2 Displacement-sensor

In order to monitor the displacements of the MMM with respect to the shake-table, a Solartron DC25 long-stroke LVDT (linear variable differential transformer) displacement transducer is used. The output of an LVDT is a linear function of displacement over its calibrated measurement range [7], which, in this equipment is ±25 mm. Measurement range is defined as ± distance from the transducer null position. Beyond this range the output becomes increasingly non-linear [7]. In Figure 7.13 is shown the dimensional drawing of the Solartron DC25 LVDT displacement transducer.

One end of the LVDT is fixed to the MMM while the other is fixed to the shake-table. The connection of the LVDT to the MMM is made at a lower level, underneath the base of the module, as shown in Figure 7.14.

The LVDT is connected to the NI SCXI-1520 8-Channel Universal Strain Gage Input Module, using the screw terminals from the Front-Mounting Terminal Block SCXI-1314. The calibration of the LVDT was made using a reference precision scale. A VI was created, using a LabView 9.1 framework, that enabled the signal acquisition from the LVDT and, once calibrated, yielded the desired linear displacement readings. A DAQ Assistant Express VI, using NI-DAQmx Software, was utilized to create, edit and run the analog input corresponding to the voltage measurement task.

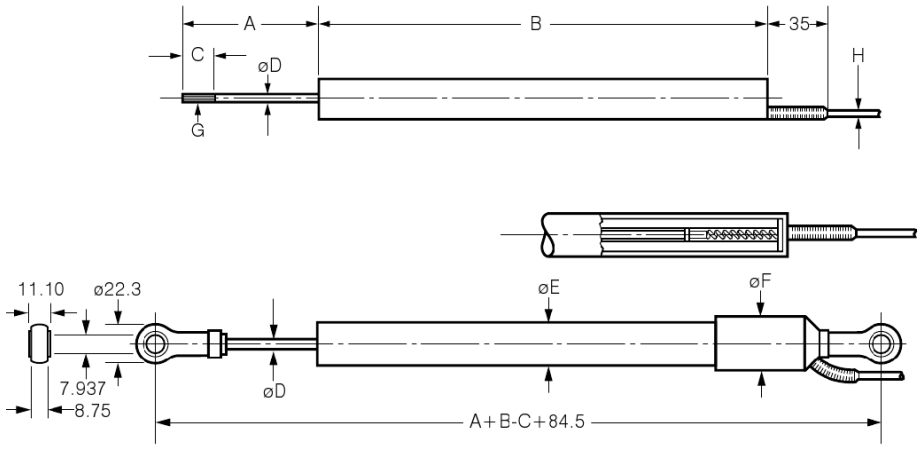

A	*B*	*C*	*D*	*E*	*F*	*G*	*H*
60	156	20	4.0	19	25	*M*4	3.5

Figure 7.13: Dimensional drawing of the Solartron DC25 LVDT displacement transducer (adapted from [7]).

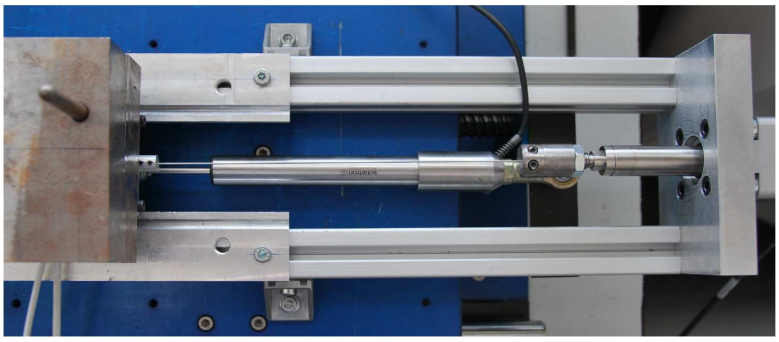

Figure 7.14: Position of the LVDT.

7.2.2 Linear actuators

The elements responsible for the adjustment of the stress level in the SE wires are analyzed in this section. This adjustment is achieved by controlling the position of the SE wires supports, using a set of linear actuators. The actuators, Bosh Rexroth EMC Electromechanical Cylinders, model EMC 32-12×5 L100 OF01 are

coupled with SIGMA II Omron-Yaskawa cylindrical servo-motors, model SGMAH-02AAA61D-OY. The mounting system for the electromechanical cylinders is described, as well as the clamping system that enables the connection of the SE wires to the linear actuators.

7.2.2.1 Electromechanical cylinder

The electromechanical cylinder (EMC) is a contained, stainless steel, precision rolled ball screw actuator designed to provide high thrust/speed capability with greater flexibility and control to applications traditionally using hydraulic and/or pneumatic cylinders [28]. It has a maximum stroke (H) of 100 mm, with high positioning accuracy and repeatability, reaching speeds up to 1.6 m/s, with a maximum axial force of 500 N [28]. In Figure 7.15 is presented a technical drawing of the EMC.

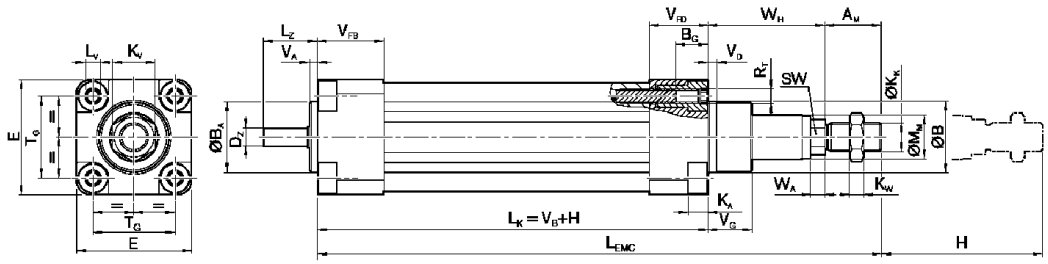

A_M	B	B_A	B_G	D_Z	E	K_K	K_A	K_V	L_V	L_Z	K_W
22	30	30	16	5	47	$M10 \times 1.25$	6.65	17	6	17	6

Figure 7.15: Dimensional drawing of the electromechanical cylinder (adapted from [28]).

7.2.2.2 Servo-motor and servo-drive

The 230 V servo-motor has a low-inertia design for extremely fast accelerations and short settling times. The highest allowable rotating speed for continuous operation (rated speed) is 3000 rpm with an output of 200 W. The rated torque amounts to

0.637 Nm, with a peak torque up to three times this value, during a period of 3 seconds. The servo-motor is provided with a 13 bits, 2048 pulse/rotation resolution, incremental encoder [120]. In Figure 7.16 is shown a dimensional drawing of the servo-motor, which weights about 1.1 kg.

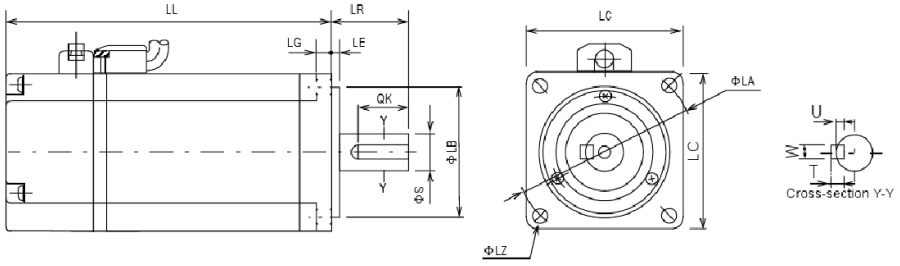

L	L_L	L_R	L_A	L_B	L_C	L_E	L_G	L_Z	S	Q_K	Tap × Depth
126.5	96.5	30	70	50^{h7}	60	3	6	5.5	14^{h6}	20	$M5 \times 8L$

Figure 7.16: Dimensional drawing of the Omron-Yaskawa servo-motor (adapted from [120]).

A SIGMA-II Omron-Yaskawa SGDH-02AE-OY servo-drive is used to control the servo-motor, allowing for analog and pulse inputs for speed, torque and position control.

7.2.2.3 Mounting system and clamps

The EMC presents two motor mounting options: direct, with a flange coupling and side-driven, with a belt side drive. This last configuration is chosen, since it results in the shortest possible installation length. The connection is secured by two 10 mm wide aluminum RS Timing pulleys, with 27 teeth and a 260×10 mm Syncroflex Timing belt. This belt is built up of two components, a polyurethane and a high grade steel cord tension member. The excellent bond between the two materials results in high power transmission capacity [41]. The obtained reduction gear ratio was of 1:1. To rigidly connect the electromechanical cylinder to the servo-motor, a special mounting plate was designed, measuring 125×64×10 mm and built in 7075-

T6 aluminum. In Figure 7.17 is presented the concept design of the mounting system and clamp.

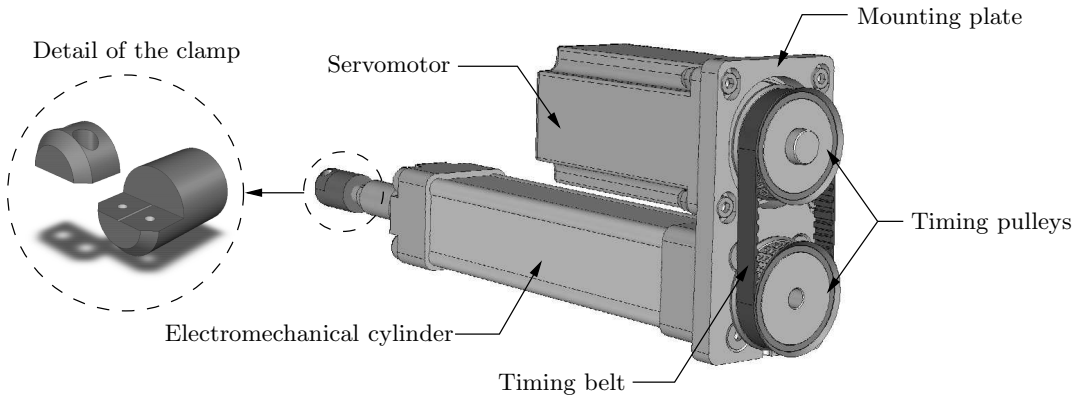

Figure 7.17: Design concept of the side-driven mounting system, with a belt side drive.

A special clamping system was designed, allowing the connection of SE the wires to the linear actuators. The clamps are cylindrical shaped elements made of steel, with 20 mm diameter. They are built up of two main components that when pressed together constrain the SE wire from moving. One of these pieces possesses a narrow, longitudinal indentation, that helps to fix the wire into place. The clamps can be screwed to the EMC electromechanical cylinders and are made from a 20 mm diameter, CK45 steel bar.

7.2.3 Prototype

The linear actuator modules are supported by two AW-5083-H111 aluminum plates, measuring 135×80×20 mm. The connection of the linear actuator groups to the end plates is assured by two sets of four M6 screws. These plates are rigidly fixed to a pair of 720 mm long, load bearing aluminum Bosch-Rexroth 30×30 strut profiles weighting 0.80 kg/m. These bars also accommodate the rails for the MMM. The Bosch-Rexroth profiles are fixed on the top stage of the shake table, as illustrated in Figure 7.18.

The Quanser Shake Table II, is an instructional shake table device that was originally

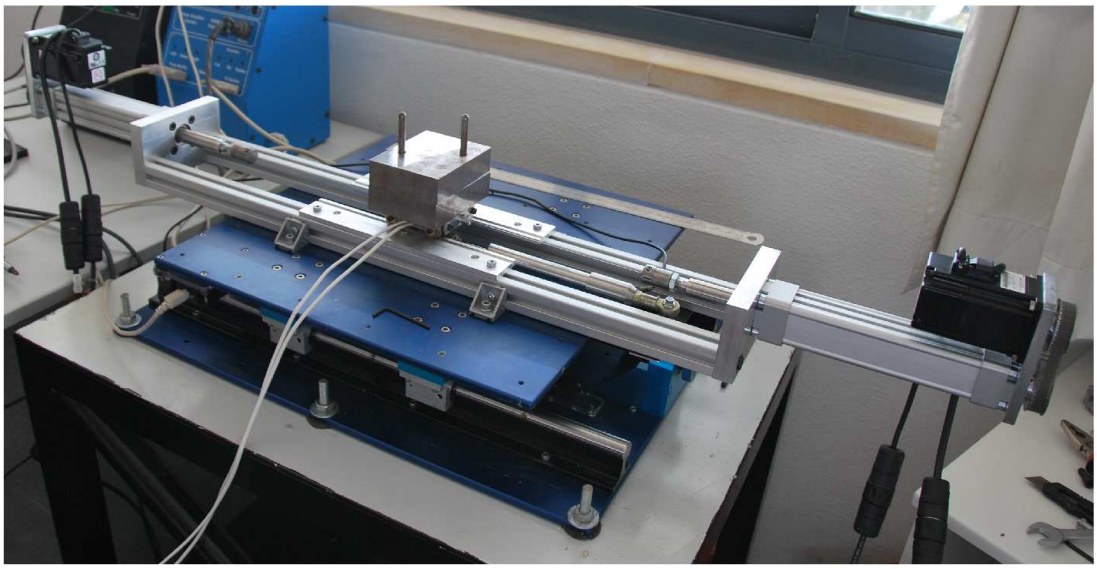

Figure 7.18: Shake-table system.

developed for the University Consortium on Instructional Shake Tables (UCIST) [140]. The motor driving the top stage of the shake table achieves an acceleration of 2.5 g with 15 kg payload. The top stage rides on two ground-hardened metal shafts using linear bearings, allowing for smooth linear motions with low path deflection. When centered, the stage is able to move 7.62 cm on each side, yielding a total travel of 15.24 cm. In order to move the top platform at a high acceleration, a robust ball-screw and motor assembly is used. The high-powered 400 W motor is a 3-phase brushless DC actuator, containing an embedded high-resolution encoder that allows the positioning of the stage with an effective linear resolution of 3.10 μm. An analog accelerometer is mounted on the Shake Table II platform in order to measure the acceleration of the stage directly. To be able to run the shake table, one has to additionally use the Universal Power Module (UPM180-25-B-PWM), a data-acquisition card, which in this case is the Quanser Q8 High-Performance H.I.L. (Hardware-in-the-Loop) Control Board and a PC running the WinCon control software.

In Figure 7.18 one can see the linear actuators, with the servo-motors already mounted on the electromechanical cylinders, and the connections for the SIGMA II encoder and power cables for the SGMAH servo-motor (R88A-CAWA003S-DE and R88A-CRWA003C-DE).

7.3 Experimenting the prototype

In this section, a thorough description of the experimental program regarding the testing of the physical prototype is presented. The main objective underlying the building of such prototype is to assess the practical feasibility of the proposed semi-active restraining control system, regarding its main conceptual features. The numerical analysis of the proposed system yields good indications on its general behavior. The experimental program starts with the implementation of several simple control VIs, aimed to control the servo-system in its various control modes encompassing the execution of increasingly complex VIs. The main steps regarding the implementation of the experimental program are:

1. General control of the servo-system;
2. Control of the stress level in a SE wire;
3. Control of the proposed semi-active restraining system.

7.3.1 General control of the servo-system

The experimental program starts with servo-motor trial operations without load, before connecting the servo-motor to the electromechanical cylinder. Control VIs are implemented for the three available control modes, i.e., speed, position and torque control modes, using a LabView 9.1 framework. These control modes require the configuration presented in Figure 7.19 to be implemented on the NI SCB-68 shielded I/O connector block.

The servo on signal (S-ON) determines whether the servo-motor power is on or off. The overtravel limit signals P-OT and N-OT, force the movable parts of the machine to stop if exceed the allowable range of motion. They are used to prevent damage to the devices during linear motion. The digital lines on the NI DAC device are able to generate these type of TTL (Transistor-Transistor Logic) compatible signals [120], which are defined in Appendix B.1.

From the three servo-drive control modes available, the speed-control mode is the one best fitted for the control system of the prototype. The variable which is manipulated

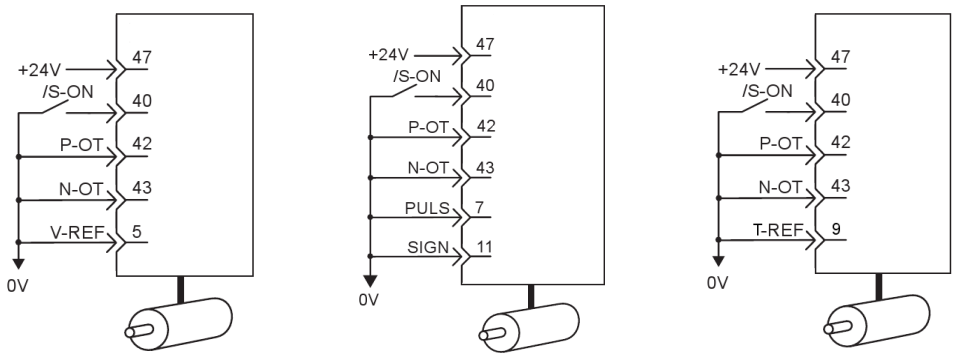

(a) Speed-control. (b) Position-control. (c) Torque-control.

Figure 7.19: Simplified external input signal circuits for the servosystem control modes, with corresponding connector pin (adapted from [120]).

by the controller is the analog voltage level for the servo-drive's speed reference (V-REF).

7.3.1.1 Speed-control mode

The maximum analog voltage level for the speed reference, is set to 6 V, which is equivalent to the rated speed of the servo-motor (3000 rpm). The analog voltage signal is a bipolar signal, with a range that includes both positive and negative values, in order to be able to change the travel direction of the shaft of the servo-motor. The internal voltage reference of the DAC is calibrated to the same range as the signal (-6 to +6 V), in order to maximize the DAC resolution. A VI that generates a variable voltage is built, which is able to continuously update the analog output channel. The block diagram of this VI is presented in Figure 7.20.

Both the analog output voltage channel, to control the speed of the servo-motor (V-REF), as well as the digital output channel, which controls all the digital channels (S-ON, P-OT and N-OT) can be seen in the block diagram of the speed-control VI. In appendix B.2 is also presented the implementation of a VI for the position-control mode. The specifications for the servo-drive are presented in appendix B.3.

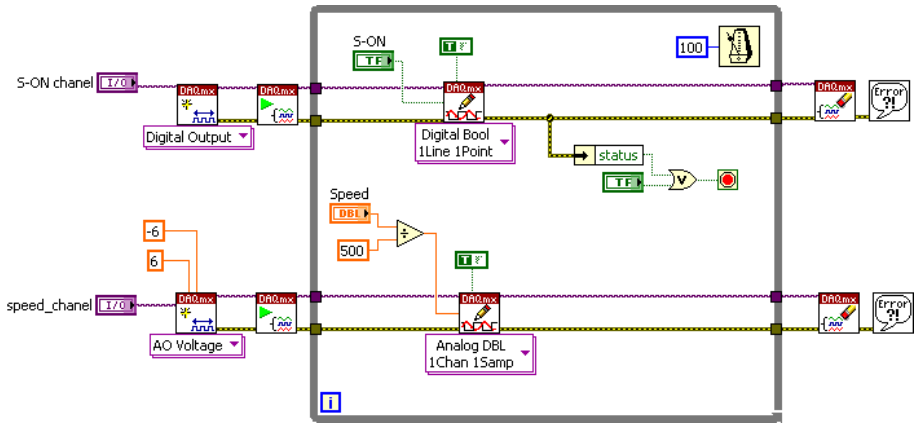

Figure 7.20: Block diagram of the speed-control VI.

7.3.2 Stress control in a SE wire

The main objective in this section is the implementation of an experimental setting allowing the stress control in a SE wire. In order to simplify this task, the displacements of the MMM are blocked by a 2 mm diameter steel bar. The general layout of the experiment is presented in Figure 7.21. The control strategy for the designated

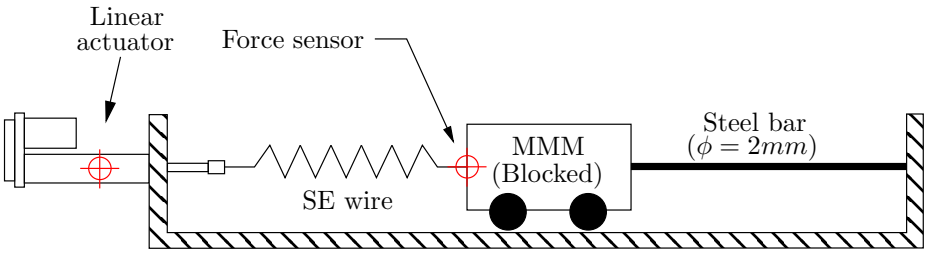

Figure 7.21: Experimental setup to control the stress level in a SE wire.

objective is implemented in LabView 9.1.

7.3.2.1 Proportional-plus-integral-plus-derivative (PID) controller

The control strategy is based on a PID controller, combining the proportional, integral and derivative control actions, defined in appendix A.4. The controller transfer

function $G_c(s)$ comprehends three terms, each one associated with the corresponding control action, yielding

$$G_c(s) = K_p + \frac{K_i}{s} + K_d\, s \tag{7.4}$$

where K_p, K_i and K_d are constants called gains. This transfer function may also be expressed in the following way

$$G_c(s) = K_p \left(1 + \frac{1}{T_i\, s} + T_d\, s\right) \tag{7.5}$$

where $T_i = K_p/K_i$ is the integral time and $T_d = K_d/K_p$ is the derivative time.

Being a closed-loop control system, the stress output signal $C(s)$ is fed back to the summing point, where it is compared with the reference stress input $R(s)$, yielding the actuating error signal $E(s)$. The output signal of the controller, $U(s)$ is the analog speed reference input for the servo-drive. The servo-drive is set to work in Speed Control mode. The feedback-path transfer function, $H(s)$ corresponds to the force-sensor, which measures the output variable in order to make it comparable with the reference input signal, resulting in the feedback stress signal, $B(s)$. Figure 7.22 shows the block diagram of the stress control system. The controlled process is defined by the transfer function $G_{cp}(s)$.

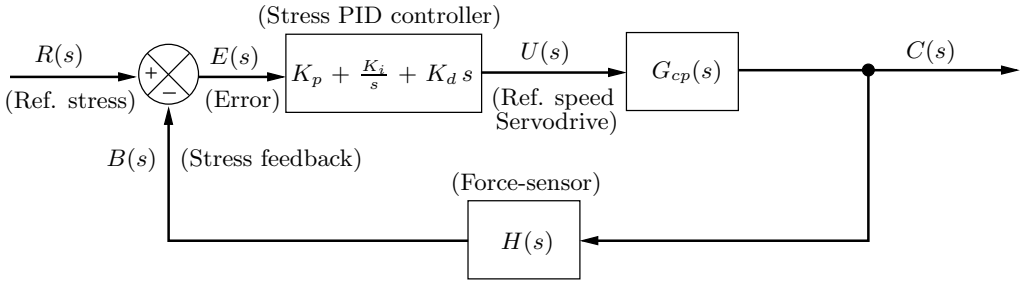

Figure 7.22: Block diagram of the stress control system.

The LabView PID Control Toolset Applications are used to implement the LabView control system. A basic PID algorithm is used, having as main inputs: the setpoint, which is the reference input stress, $R(s)$, the process variable (PV), $B(s)$, the PID gains, and the output range; see Figure 7.23. The PID gains consists of a cluster of three values, corresponding to K_p, T_i and T_d. The output range is used to specify

the range of the controller output. The default range of the controller output is -100 to 100, corresponding to values specified in terms of percentage of full scale.

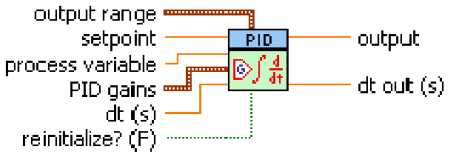

Figure 7.23: PID.vi [113].

The overtravel limit function is used to prevent the SE wire from failure, by limiting the maximum allowing stress to a prescribed value. The front panel of the stress control VI and corresponding block diagram are presented in Appendix C.1, in Figures C.1 and C.2, respectively. The block diagram contains several case structures which are ilustrated in Figures C.3, C.4 and C.5.

7.3.2.2 Transient-response analysis

In many control systems, the input excitations are of unpredictable nature and usually cannot be expressed deterministically by a mathematical expression. This constitutes a practical difficulty during the design and testing of a control system, since it is not feasible to implement a system that performs adequately for every input signal. Hence, for the evaluation of the performance of a control system, several test signals are commonly used, that are usually very simple functions of time. Some of the most common test signals are the step function and the ramp function, which are defined in appendix A.1.2. The design of a control system based on the analysis of these test signals usually leads to a system with a satisfactory behavior towards actual input signals.

The time response of a control system is characterized by the transient response and the steady-state response. Both of these responses are of great importance during the analysis of the dynamic behavior of a control system. The transient response usually denotes damped oscillations before reaching a steady-sate. The difference between the steady-state response and the input gives a good indication about the accuracy of the control system. If a system exhibits such a difference it is said to have a steady-state error. Using time-domain variables one can express the error

signal as

$$e(t) = r(t) - c(t) \tag{7.6}$$

where $r(t)$ is the reference input and $c(t)$ is the output. For these two quantities to be dimensionally the same, in order to be comparable, a feedback-path transfer function, $H(s)$, shown in Figure A.8, is usually incorporated in the control system, as already referred.

When a system is stable, showing a transient response that fades away as time grows, it is usual to characterize this part of the response with the use of a unit step input [85]. Typical performance criteria include delay time, rise time, peak time, overshoot and settling time. Figure 7.24 illustrates a typical response of a linear control system to a unit-step input.

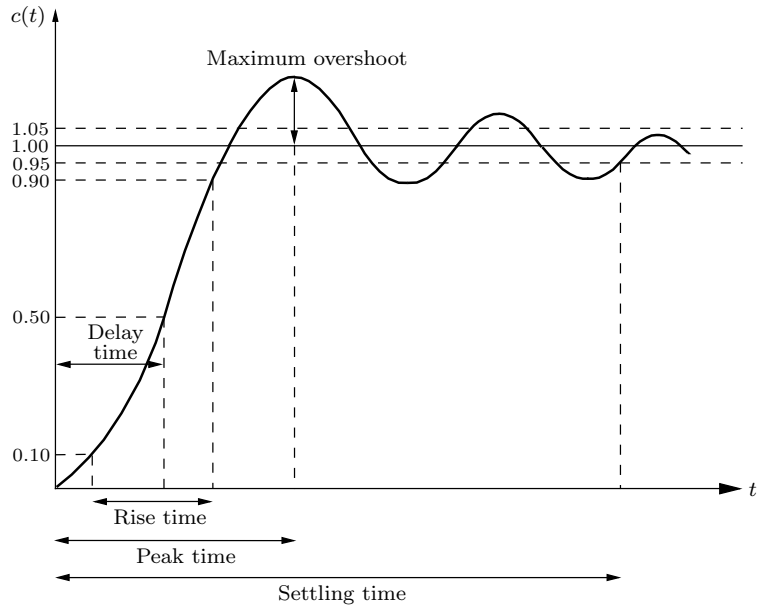

Figure 7.24: Typical unit-step reponse of a control system

The specifications for the performance criteria are given next:

1. Delay time. The delay time t_d represents the time required for the response to reach, for the first time, half of its final value.

2. Rise time. The rise time t_r represents the time required for the response to

rise from 10% to 90% of its final value.

3. Peak time. The peak time t_p represents the time required for the response to reach the first peak of the overshoot.

4. Maximum overshoot. The maximum overshoot is defined as the largest deviation of the response over the unit-step input. If the steady-state value of the response differs from unity, then it is common to use the maximum percent overshoot (M_p), defined by

$$M_p = \frac{c(t_p) - c(\infty)}{c(\infty)} \times 100\% \tag{7.7}$$

5. Settling time. The settling time t_s represents the time required for the response to decrease and stay within a specified percentage of its final value (usually 2% or 5%).

7.3.2.3 Tuning of the PID controller

In the design process of a control loop, in order to achieve an acceptable performance, the constants K_p, T_i and T_d, in equation (7.5) have to be adequately adjusted. This process of adjusting the controller parameters in order to meet given performance specifications is known as controller tuning. When the mathematical model of the process cannot be easily obtained, an analytical approach to this tuning is not possible and experimental approaches have to be used. To improve the performance of the controller, a tuning algorithm based on the Ziegler-Nichols [113] stability boundary rule is implemented. In this tuning method, the K_i and K_d gains are first set to zero and the K_p gain is increased until it reaches the *ultimate gain*, K_u, at which the output of the loop starts to oscillate. If the control system makes a change that is too large, when the error is small, it is equivalent to a high gain controller and it will lead to overshoot. If the controller makes changes that are too large and repeatedly overshoots the target, the output oscillates around the setpoint in either a constant, growing, or decaying sinusoid. If the oscillations increase with time then the system is said to be unstable, whereas if they decrease the system is stable. If the oscillations remain at a constant magnitude the system is marginally stable, as show in Figure 7.25. The corresponding period of oscillation, P_u is called the *ultimate period*. In appendix A.4.5 is presented an alternative tuning method

which is based on the experimental evaluation of the controlled process unit-step input response.

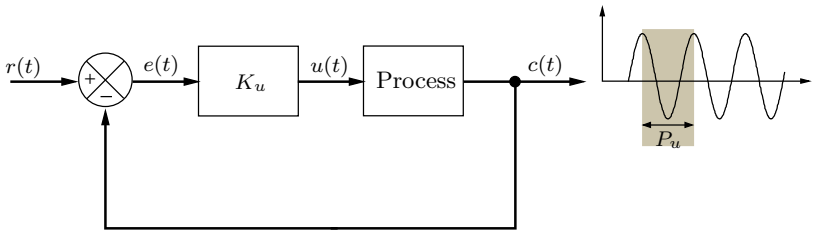

Figure 7.25: Closed loop tuning procedure: Ultimate gain.

The ultimate gain K_u and the corresponding oscillation period P_u are used to set the gains as shown in Table 7.3.

Controller	K_p	T_i	T_d
P	$0.5K_u$	–	–
PI	$0.4K_u$	$0.8P_u$	–
PID	$0.6K_u$	$0.5P_u$	$0.12P_u$

Table 7.3: Ziegler-Nichols tuning rule based on a stability boundary (Decay ratio of 0.25).

For the proposed prototype the *ultimate gain* yields an approximate value of $K_u = 0.30$ and the *ultimate period* $P_u = 0.7$ s. In order to obtain a *quarter decay ratio*[1] type response, K_p should be set to approximately half of that value, i.e., $K_p = 0.15$. The response of a proportional feedback system to a reference step-input is shown in Figure 7.26, together with some arbitrary parametric changes on the proportional gain defined by the proposed tuning rule ($K_p = 0.5K_u$). The reference signal is a force step-input, corresponding to a 50% variation of the maximum force allowed in the SE wire, with $F_{max} = 60$ N.

It is quite clear that the responsiveness of this proportional controller clearly increases with the increase of the corresponding gain, as the delay time (t_d), the rise time (t_r) and the peak time (t_p) decrease. The degree to which the controller overshoots the setpoint, as well as the degree of system oscillation also increase with the

[1] A quarter decay ratio corresponds to a decay of 25% in one period, on the transient response, yielding a good compromise between quick response and adequate stability margins [59].

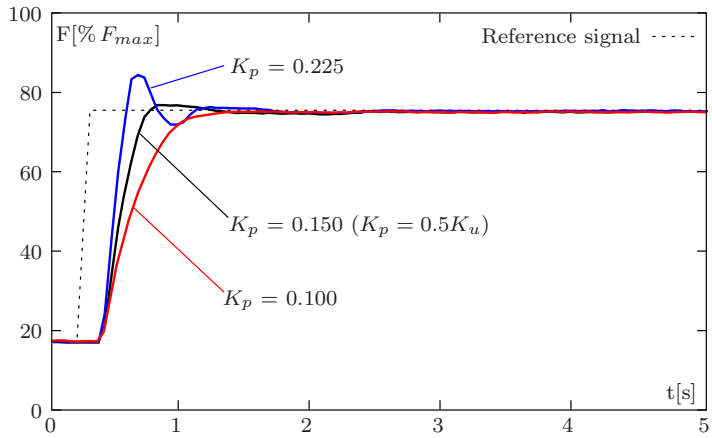

Figure 7.26: Plot of PV vs time, for three values of K_p ($T_i = \infty$, $T_d = 0$).

increase of K_p. The system shows a small steady-state error, for all the considered proportional gains.

The contribution of the integral term to the control system is proportional to the magnitude of the error as well as to its duration. When added to the proportional term, the integral term increases the responsiveness of the controller, causing the process to accelerate towards the defined setpoint. However, this may also introduce some undesirable overshoot to the system. The integral term also eliminates the steady-state error present in a proportional controller. The contribution of the integral term is determined by the integral time, T_i. Figure 7.27 illustrates the effect of adding the integral term in the control system, using the the gains associated with a PI control system for the Ziegler-Nichols tuning rule based on a stability boundary ($K_p = 0.4K_u, T_i = 0.8P_u$).

It can be seen in Figure 7.27 that as T_i decreases, increasing the magnitude of the contribution of the integral term in the controller, the responsiveness of the controller increases, with the decrease of the delay time (t_d), the rise time (t_r) and the peak time (t_p). The maximum overshoot clearly increases as the settling time (t_s) diminishes.

Regarding the contribution of the derivative term to the control system, due to its anticipatory nature, this term is able to slow down the rate of change of the controller output, reducing the magnitude of the overshoot and improving the stability of the system. However, the derivative term is highly sensitive to the noise in the

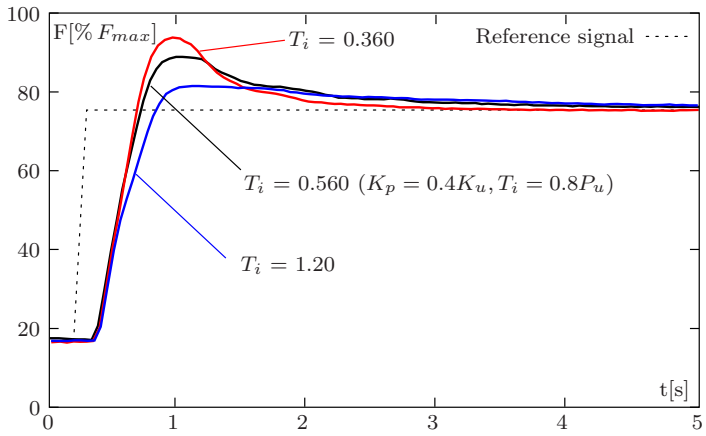

Figure 7.27: Plot of PV vs time, for three values of T_i(s) ($K_p = 0.12$, $T_d = 0$).

error signal, since the differentiation of a signal amplifies noise. This can cause instability in the process, if the error noise and the derivative time are sufficiently large. Figure 7.28 illustrates the effect of adding the derivative term in the control system, using the the gains associated with a PID control system for the Ziegler-Nichols tuning rule based on a stability boundary ($K_p = 0.6K_u, T_i = 0.5P_u, T_d = 0.12P_u$). It can be seen in Figure 7.28 that the responsiveness of the control system

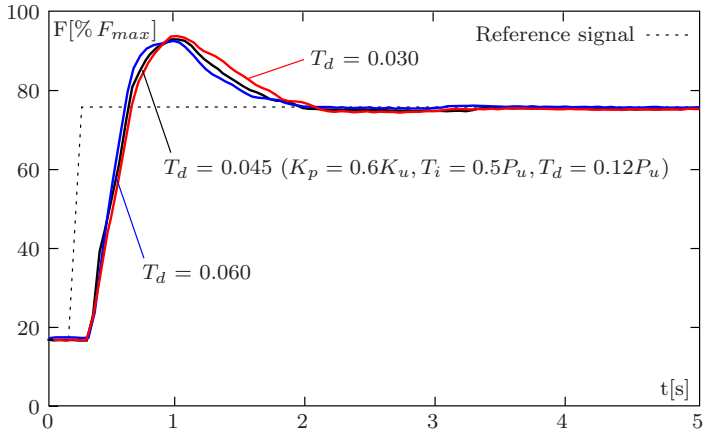

Figure 7.28: Plot of PV vs time, for three values of T_d(s) ($K_p = 0.18$, $T_i = 0.35$).

slightly decreases as the derivative time increases.

7.3.2.4 Sinusoidal stress input (reference signal)

To study the response of the control system to harmonic reference stress signals, a series of experimental tests are presented. These tests cover two different loading frequencies, namely 0.5 and 1.0 Hz for stress amplitudes ranging from 6.25 to 50% of the maximum force. The results presented in Figure 7.29 show that although the frequency and amplitude of the output stress signal are in good accordance with the corresponding input values, a time delay occurs. This time delay increases with both frequency and amplitude of the stress signal. In order to further evaluate the robustness of the proposed control system, random noise was added to the harmonic reference input stress signal, with noise amplitudes ranging from 3 to 12%. The base frequency and amplitude for the tested signals are 0.5 Hz and 12.5% of the maximum force, respectively. The results also show that the control system is able to adequately cope with the randomness of the reference signal, showing a good general responsiveness.

7.3.3 Displacement control for dynamic tensile testing

The following experimental tensile test aims to respond to the limited experimental evidence regarding SE behavior during dynamic loading, since the Zwick/Roell Z050 testing machine only yields a maximum strain-rate of 0.333%/s. The developed prototype shows a good responsiveness to higher loading frequencies, enabling the tensile testing of SE wires with strain-rates of 12%/s.

The tensile testing of the SE wire requires that the MMM is able to move in a controlled way. A strain-driven testing approach is developed for the experiment, using the same PID control strategy applied for the stress control of a SE wire. The PID algorithm yields the reference speed, $U_p(s)$, for servo-drive in it's speed control mode. The general layout of the dynamic tensile test experience is shown in Figure 7.30.

The steel bar is used to transmit the movement of the linear actuator to the MMM. The displacement of this module is monitored by a LVDT. The force-sensor yields the force readings in the SE wire, which is also equipped with a thermocouple.

The system is built of a position control loop linked to the SE wire and the cor-

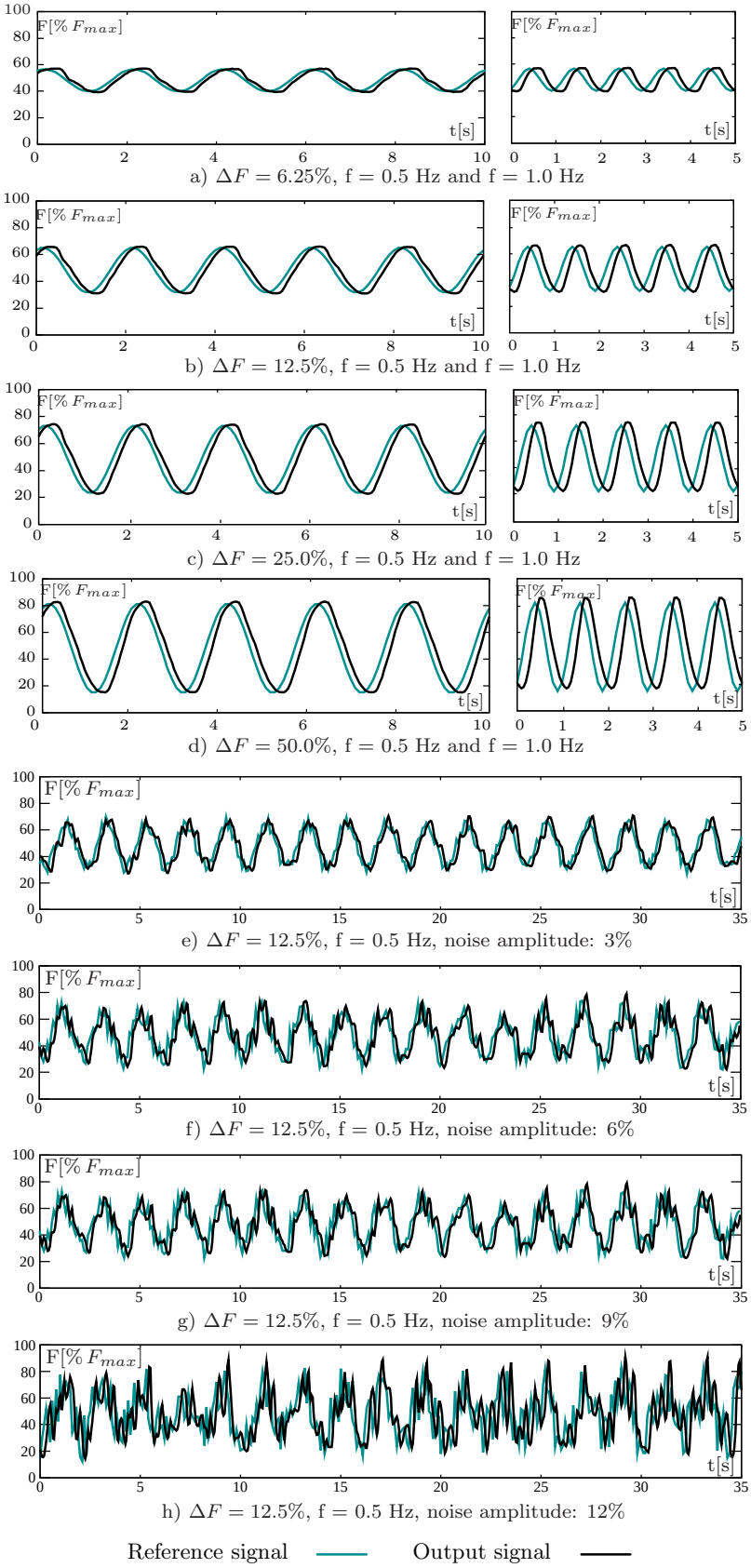

Figure 7.29: Harmonic reference stress signals: reference signal vs. output signal.

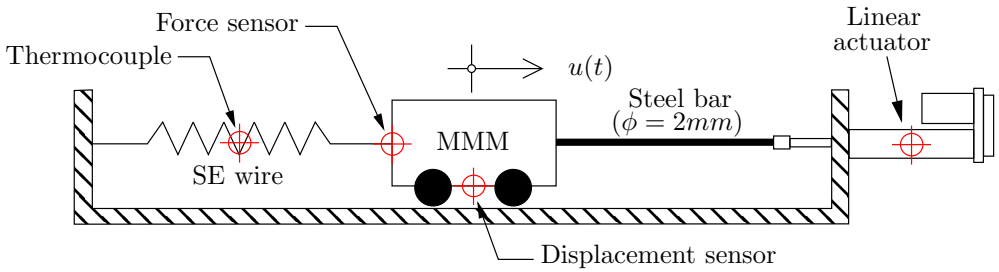

Figure 7.30: Experimental setup for the dynamic tensile test.

responding force-sensor. The reference position input, $R_p(s)$ is compared with the position output signal, $C_p(s)$ yielding the position error signal, $E_p(s)$. The feedback-path transfer function, $H_p(s)$ corresponds to the LVDT, which measures the output variable and yields the feedback position signal, $B_p(s)$. This system is presented in Figure 7.31.

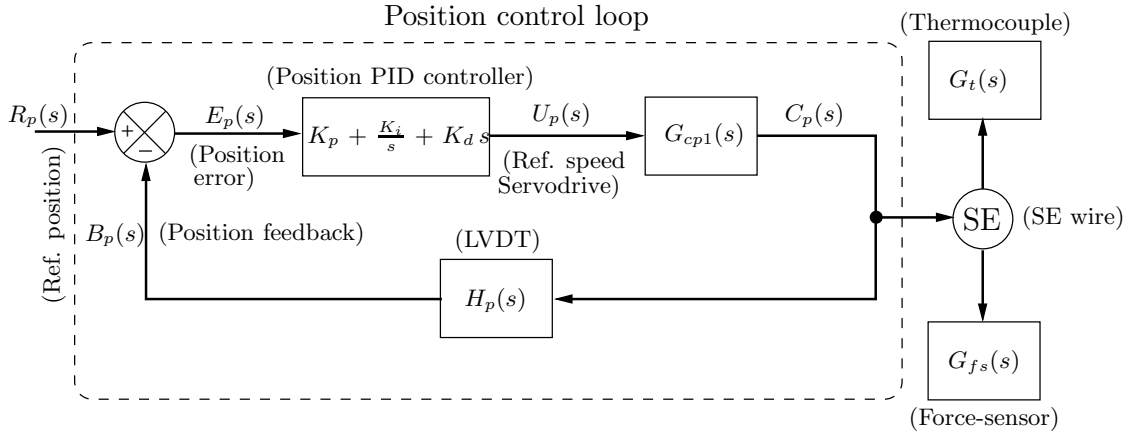

Figure 7.31: Displacement control loop for dynamic tensile testing.

The front panel of the displacement control VI, for dynamic tensile testing and its corresponding block diagram are presented in Appendix C.2, in Figures C.6 and C.7, respectively.

The results for six tensile tests, with strain-rates of 0.033, 0.120, 0.600, 1.20, 6.00 and 12.0%, are presented in Figure 7.32, featuring both the temperature time-histories and the corresponding stress-strain diagrams.

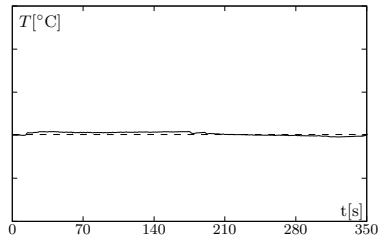

(a) Temperature time-history for $\dot{\varepsilon} = 0.033\%/s$

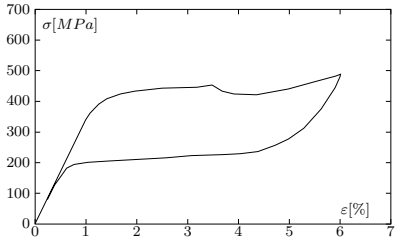

(b) Stress-strain diagram for $\dot{\varepsilon} = 0.033\%/s$

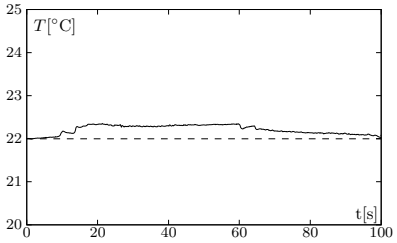

(c) Temperature time-history for $\dot{\varepsilon} = 0.120\%/s$

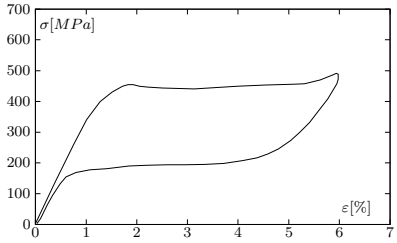

(d) Stress-strain diagram for $\dot{\varepsilon} = 0.120\%/s$

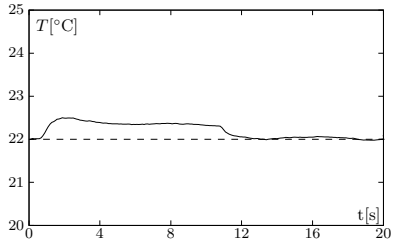

(e) Temperature time-history for $\dot{\varepsilon} = 0.600\%/s$

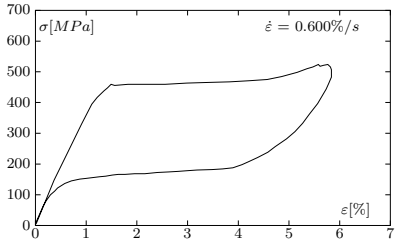

(f) Stress-strain diagram for $\dot{\varepsilon} = 0.600\%/s$

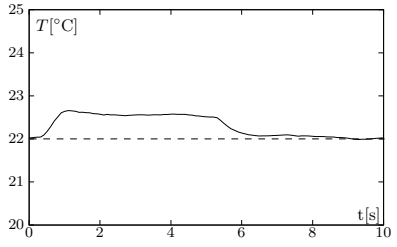

(g) Temperature time-history for $\dot{\varepsilon} = 1.20\%/s$

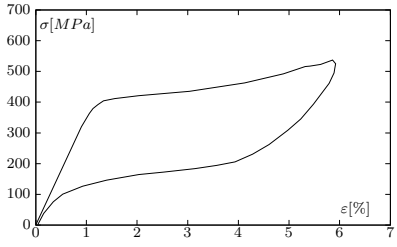

(h) Stress-strain diagram for $\dot{\varepsilon} = 1.20\%/s$

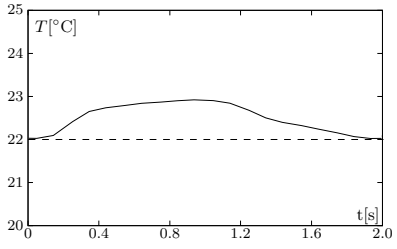

(g) Temperature time-history for $\dot{\varepsilon} = 6.00\%/s$

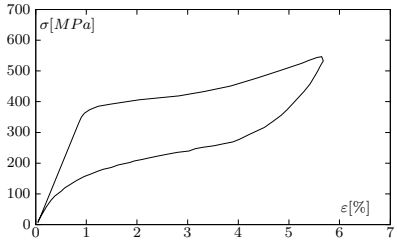

(h) Stress-strain diagram for $\dot{\varepsilon} = 6.00\%/s$

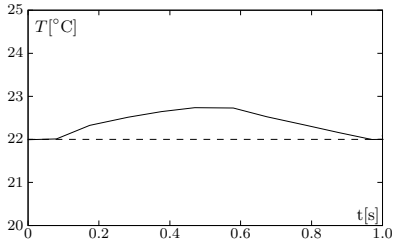

(g) Temperature time-history for $\dot{\varepsilon} = 12.0\%/s$

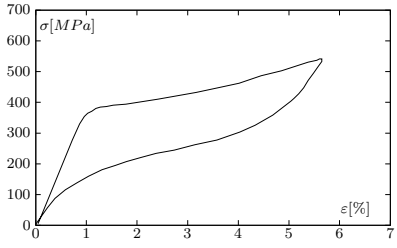

(h) Stress-strain diagram for $\dot{\varepsilon} = 12.0\%/s$

Figure 7.32: Dynamic tensile tests ($T_0 = 22°C$): Stress-strain diagrams and temperature time-histories.

Analyzing the experimental results obtained during tensile testing one can confirm that both the temperature time-histories as well as the stress-strain diagrams of the SE wire strongly depend on the loading strain-rate. Figure 7.33 shows the influence of strain-rate on the equivalent viscous damping. According to Figure 7.33, the

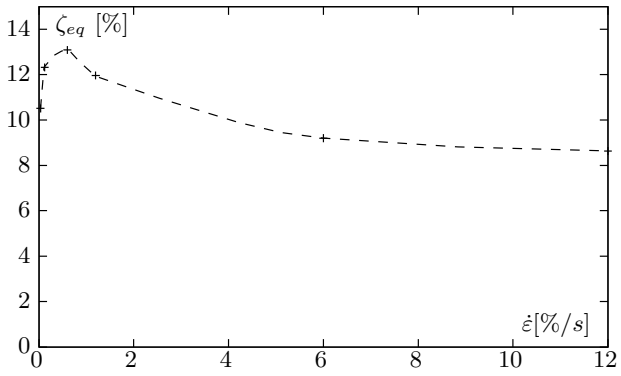

Figure 7.33: Influence of high strain-rates on the equivalent viscous damping.

influence of strain-rate on the SE behavior tends to diminish above a certain value, with the stabilization of the temperature time-history during the dynamic loading. Finally, one can also see that the maximum hysteresis is obtained for an intermediate value of the strain-rate, as already mentioned in Section 3.2.9.

7.3.4 SE control system with one restraining element

The objective of this section is to implement a vibration control prototype comprising a SE restraining element and to analyze its response to dynamic loadings. The experimental setup is illustrated in Figure 7.34.

In this experimental setup, linear actuator 1 enables the control of the stress level in the SE wire inside a prescribed SE window. The external disturbance is introduced in the system by the linear actuator 2, which is rigidly connected to the MMM by a 2 mm diameter steel bar. The control algorithm used to control the movement of the linear actuator 2 relies on the same PID displacement control strategy used in Section 7.3.3.

The control of the linear actuator 1 is based on the on-off controller presented in Section 6.2.3, assuming two possible states: PID-ON and PID-OFF. When the controller assumes the PID-ON state, it behaves like the PID stress controller presented

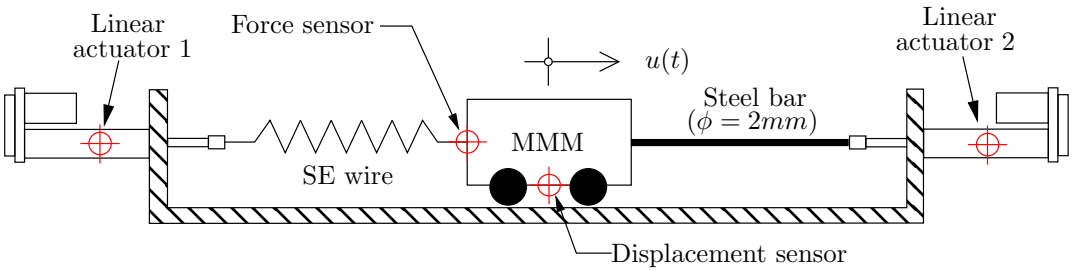

Figure 7.34: Experimental setup of the vibration control system with one restraining element.

in Section 7.3.2.1. In this situation, it may assume two different setpoints, corresponding to the upper and lower force limits defined for the SE wire. The controller chooses the setpoint depending on the force level in the SE wire at a given instant. The activation of the PID-ON state occurs when one of two prescribed force thresholds is surpassed, namely the high and low PID thresholds. The PID-ON state is active above the high force threshold and below the low force threshold. Between these two force delimiters the controller is set to be on the PID-OFF state. The differential gap between the force thresholds, to activate the PID controller, and the corresponding force setpoints works as an anticipatory feature of the system. It provides the controller with a reference force input while the force in the SE wire is still approaching this value. The block diagram of the SE vibration control system, with one restraining element, is presented in Figure 7.35.

The external disturbance consists of an harmonic excitation with an amplitude of 8.0 mm and frequency of 0.5 Hz. At the beginning of the dynamic loading, the SE wire is stress/strain free. For the first 8 seconds of the experiment the control system is switched off. During this period of time the restraining system only responds when the SE wire is strained, showing zero stiffness when facing compression. Therefore, the restraining system is only working in one direction of the movement, as it can be seen in the first four cycles of the force time-history, represented in Figure 7.36.

After the controller is switched on, the system rapidly starts to compensate for low stresses in the SE wire, and the corresponding force readings are shifted upwards. When the MMM moves left, in Figure 7.34, and the stress in the SE decreases below a given threshold, the linear actuator 1 also shifts left, as it tries to accommodate the displacement introduced by the external excitation. During the controlled phase,

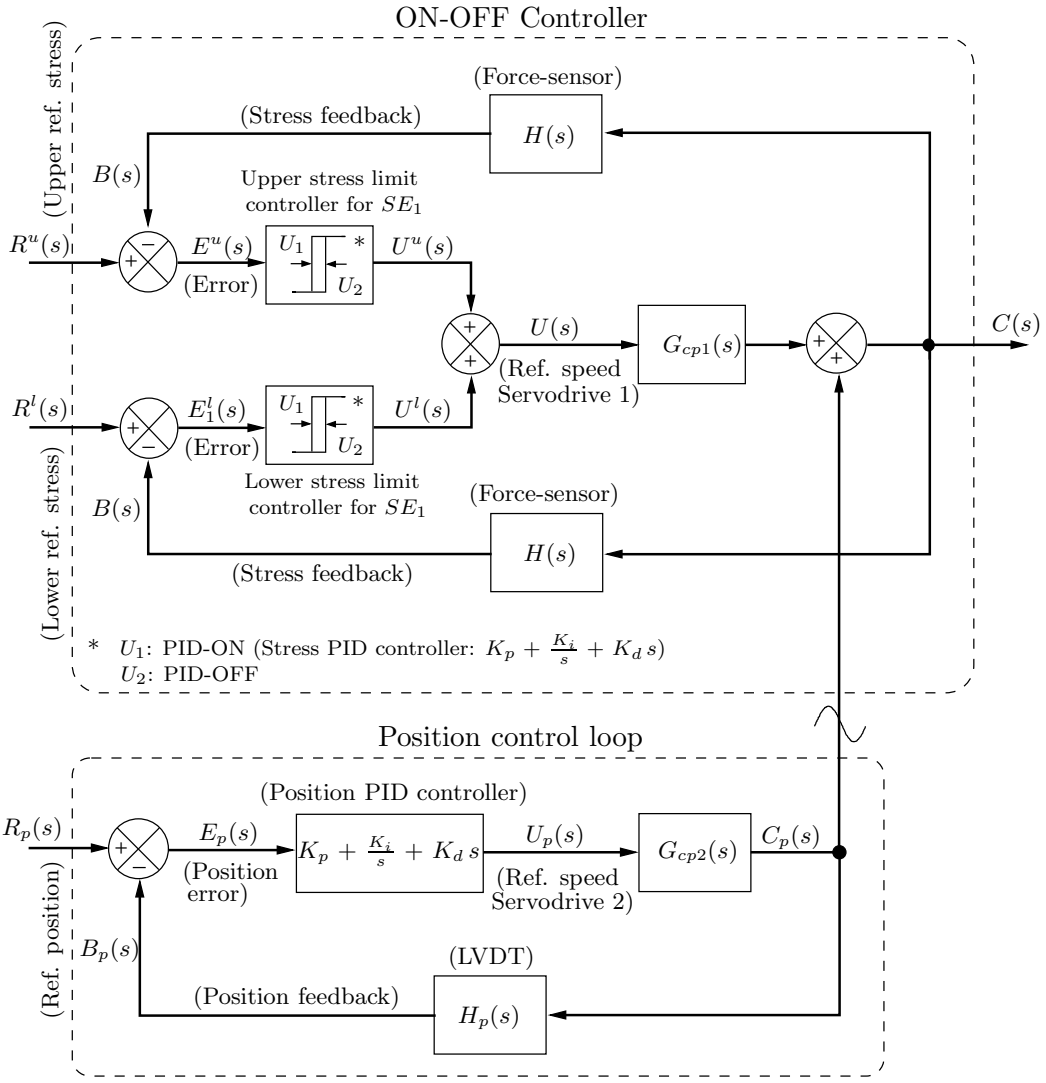

Figure 7.35: Block diagram of the SE vibration control system with one restraining element.

the force values in the SE wire are delimited by the two reference stress inputs. These reference stress inputs, which define the effective SE window, are set to 8 and 42% of the maximum force. These values correspond to the low and high setpoints of the PID controller, respectively. The PID threshold limits for the controller assume the values 12 and 38% of the maximum force, representing a differential of 4% in relation to the corresponding setpoints. In spite of this anticipatory feature of the controller, a small overshoot is present in both the upper and lower stress limits.

The force accumulation in the SE wire enhances its damping capability, since the

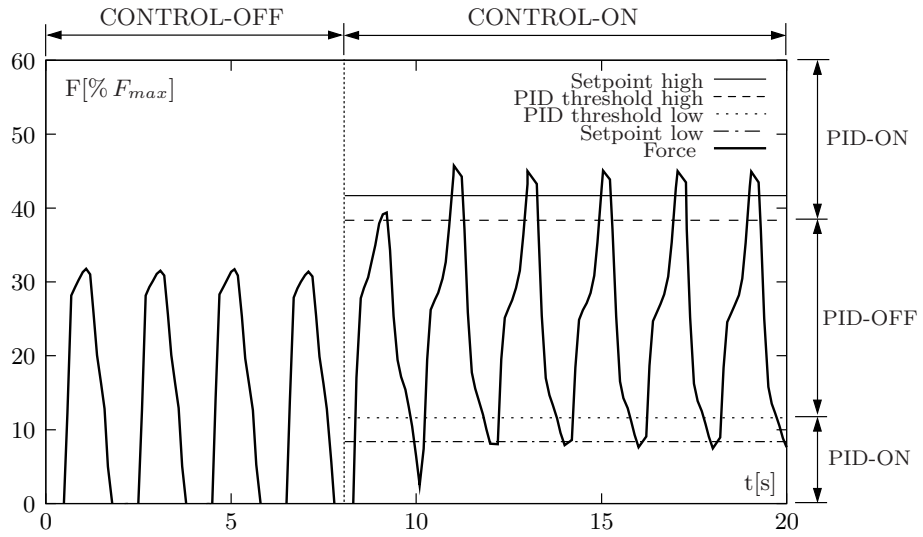

Figure 7.36: Force time-history.

extent of the martensitic transformation is increased. This can be seen in the force-displacement diagrams depicted in Figure 7.37, showing a comparison between the original SE hysteresis and the final hysteretic cycle. With the force accumulation process, the equivalent viscous damping changes from 14% to 16%. The front panel

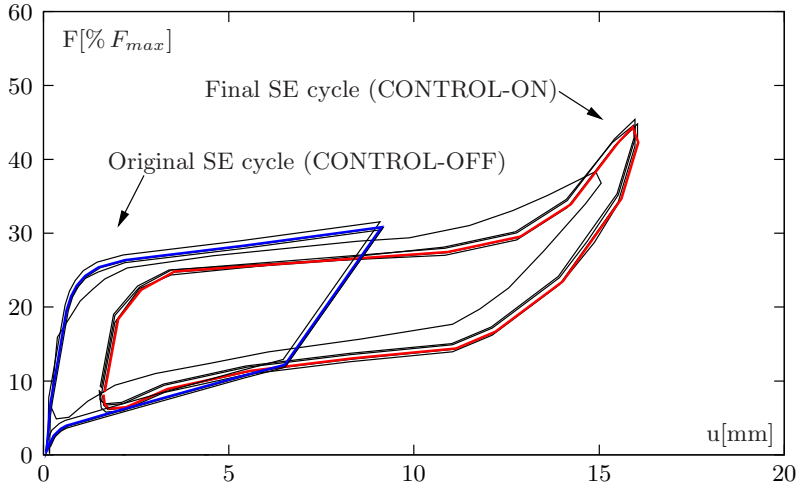

Figure 7.37: Comparison between the free and the controlled SE force-displacement diagrams.

of the SE vibration control system with one restraining element and corresponding block diagram are presented in Appendix C.3, in Figures C.12 and C.13, respectively.

7.3.5 SE control system with two restraining elements

In this last experimental test, the dynamic behavior of the proposed SE vibration control system with two restraining elements is analyzed. The layout of the experimental setup is shown in Figure 7.38.

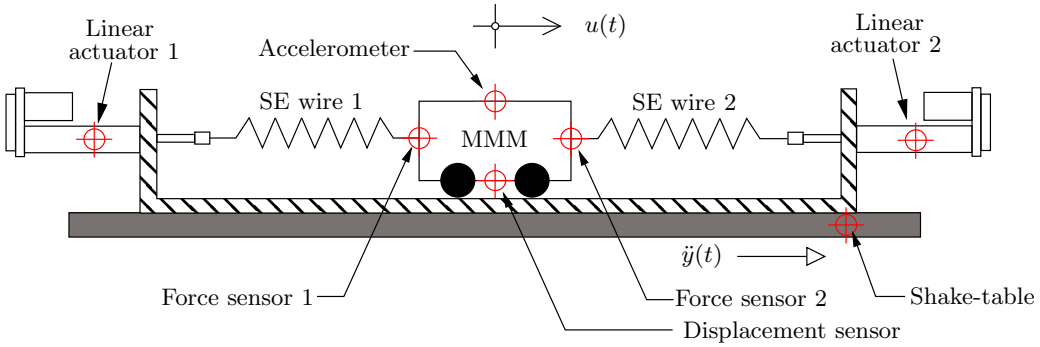

Figure 7.38: Experimental setup of the vibration control system with two restraining elements.

The main differences with respect to the experimental procedure analyzed in Section 7.3.4 are the additional SE wire provided to the system, the accelerometer, and the fact that the external disturbance is not introduced directly in the MMM by a linear actuator, but rather by the displacements induced by the shake-table. The controller is based on the same on-off scheme used for the single wire restraining system, considering an additional SE wire. An open-loop control system is used to monitor the displacements of the MMM, comprising a LVDT. In Figure 7.39 is represented the block diagram of the SE vibration control system with two restraining elements. The main controller can be divided into two independent controllers, each one responsible for the control of a single restraining SE wire. Each of these controllers has two reference stress inputs, delimiting the effective SE window, and yield a reference speed output for the corresponding servo-drive. The global output signal from the controller comprehends the reference speeds for both servo-drives, $U(s) = U_1(s) + U_2(s)$.

In order to analyze the influence of pre-strain on the shape of the force-displacement diagram associated with a SE control system with two restraining wires, an experimental parametric study is proposed. The SE wires are initially stressed up to a

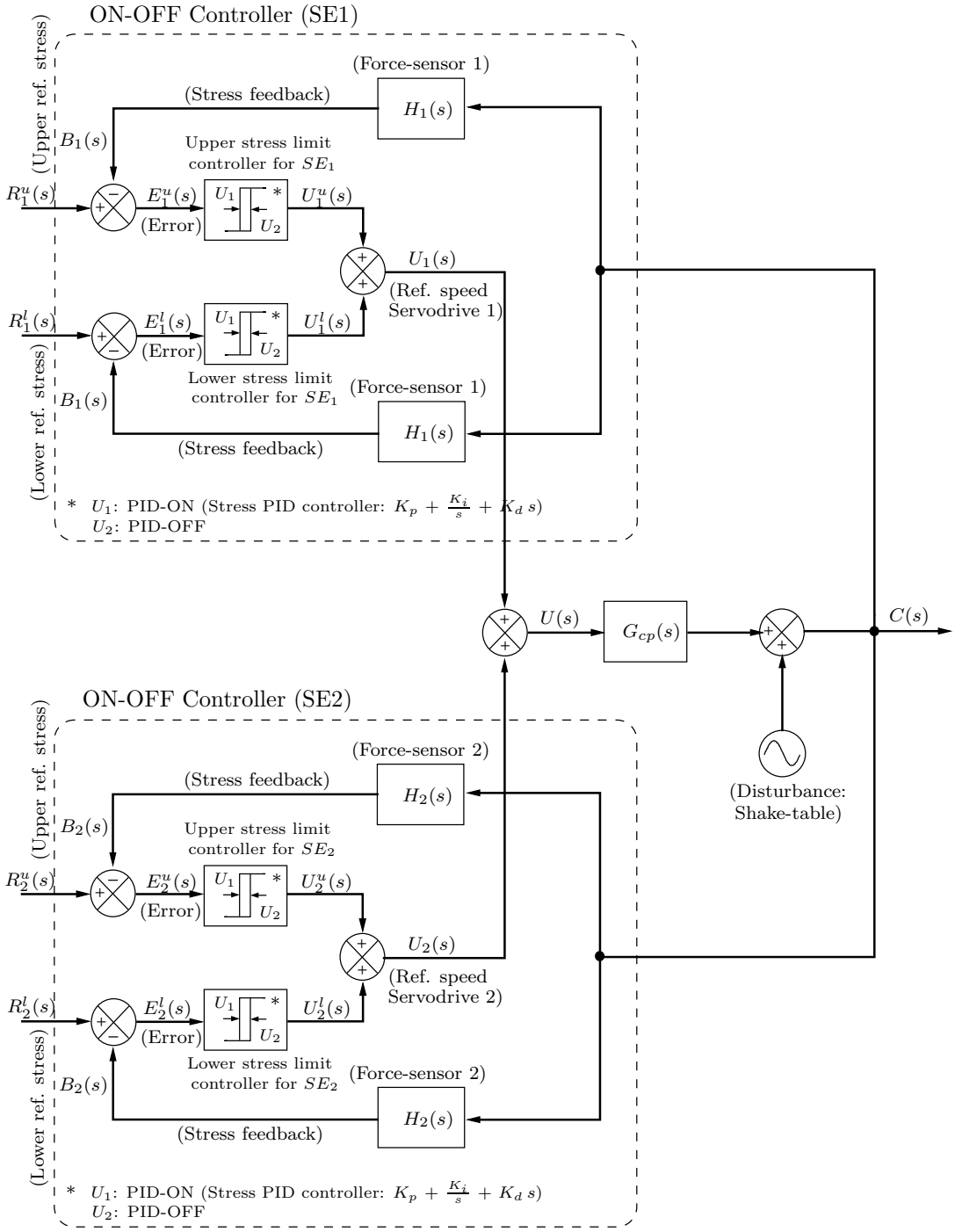

Figure 7.39: Block diagram of the SE vibration control system with two restraining elements.

certain level and then the system is subjected to a quasi-static harmonic displacement, yielding the full extent of the martensitic transformation in the wires. One can see the evolution of the SE hysteresis in Figure 7.40, as the pre-stress increases from 0 to 200 MPa.

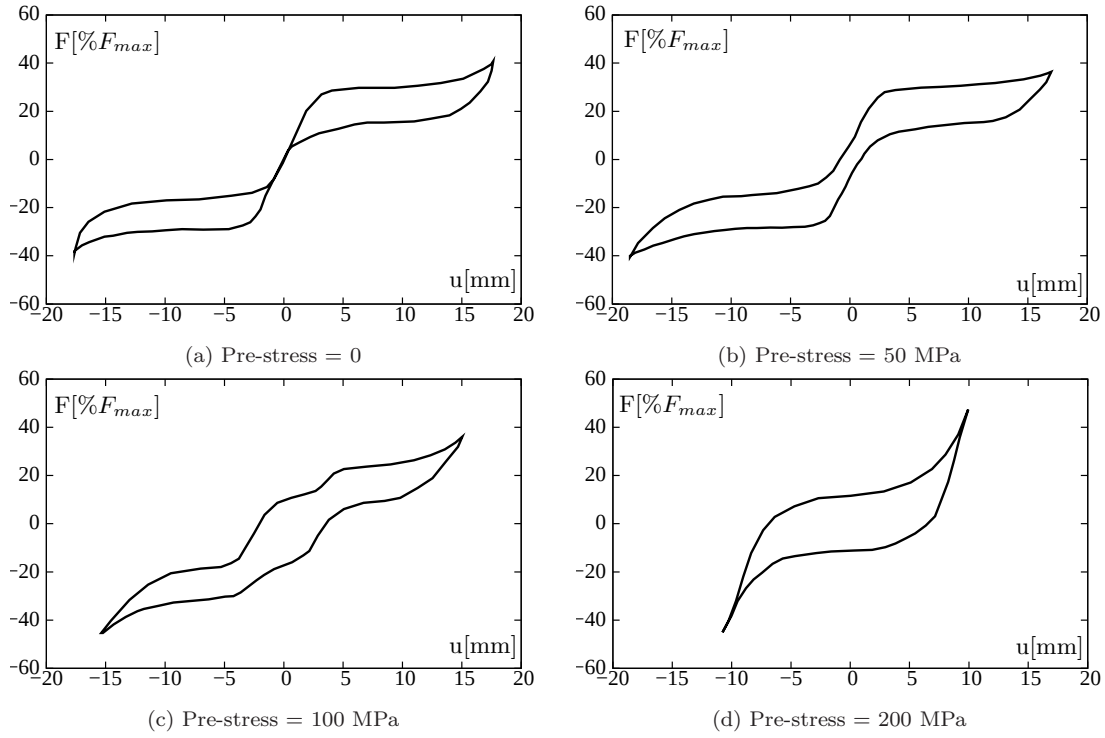

(a) Pre-stress = 0

(b) Pre-stress = 50 MPa

(c) Pre-stress = 100 MPa

(d) Pre-stress = 200 MPa

Figure 7.40: Force-displacement diagrams.

The behavior of the system with no pre-stress is represented in Figure 7.40(a), where the complementary SE wires enable the development of a full tension/compression SE hysteresis, with an equivalent viscous damping of about 10%. When the pre-stress is introduced in the SE wires, Figures 7.40(b) and (c), the equivalent viscous damping gradually increases as the hysteresis changes from two distinct SE areas to a single hysteretic curve, as illustrated in Figure 7.40(d). The equivalent viscous damping associated with this last SE hysteresis is 23%, meaning that with the introduction of pre-stress one has doubled the value of the SE damping available in the system.

An external disturbance is now introduced into the system, by the shake table, consisting of a harmonic excitation with an amplitude of 5 cm and a frequency

of 1 Hz. The SE wires are stress/strain free and the control system is switched off. When the MMM starts to move, as the stresses induced in the SE wires are in phase opposition, the wires are strained alternately. The force-displacement diagram resulting from this test is depicted on Figure 7.41(a). One can see that the amplitude of the displacements exhibited by the MMM is not high enough as to develop stress induced martensite in the SE specimens. The force-displacement diagram is confined to a single line, since the SE wires remain in their austenitic phase, showing no hysteretic damping. In a second phase of the experiment the SE wires are pre-stressed with 120 MPa and the system is subjected to the same external excitation. One can see that due to the presence of pre-stress, higher martensite transformation ratios are induced in the wires, allowing the system to develop a wide SE hysteresis, as shown in Figure 7.41(b).

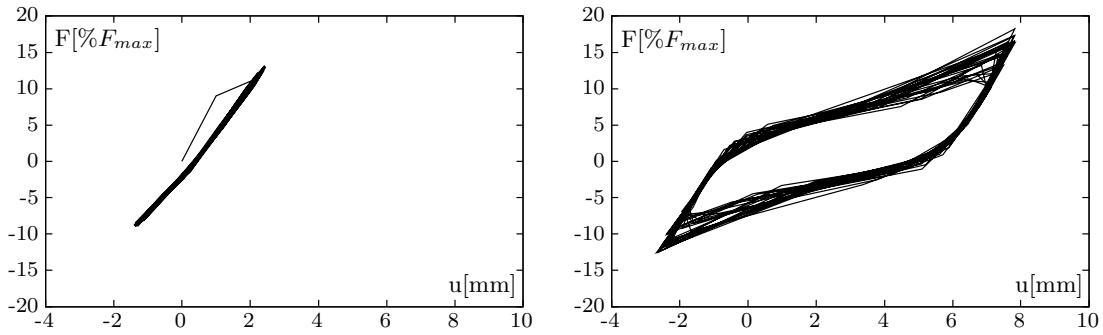

(a) Pre-stress = 0 (b) Pre-stress = 120MPa

Figure 7.41: Force-displacement diagrams.

The objective of the following experimental test is to assess the behavior of the proposed control system when submitted to an external harmonic excitation by the shake table. The external harmonic excitation is the same as previously described, with an amplitude of 5 cm and a frequency of 1 Hz. The low and high setpoints of the PID controller are set to 11 and 22% of the maximum force and the PID threshold limits for the controller assume the values 13 and 24% of the maximum force. The response of the system to the external excitation regarding the force time-history in SE_1 and the force-displacement diagram is represented in Figures 7.42 and 7.43. During approximately the first ten seconds of the test, the controller is switched off. For this period of time, the SE wires work alternately while remaining in their austenitic form. This is translated by a linear relation between the total

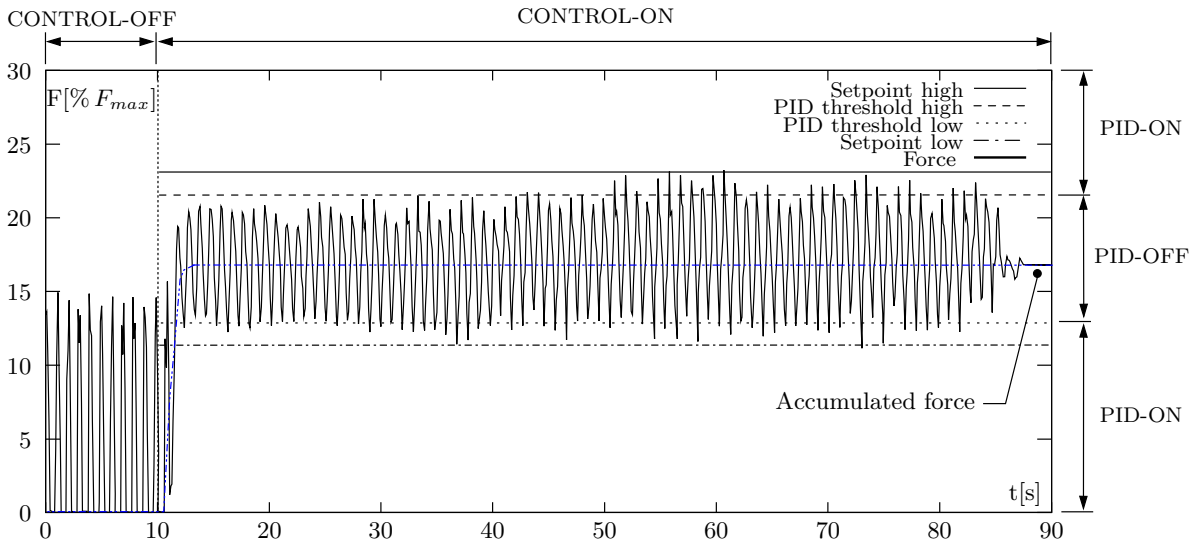

Figure 7.42: Force time-history (SE_1).

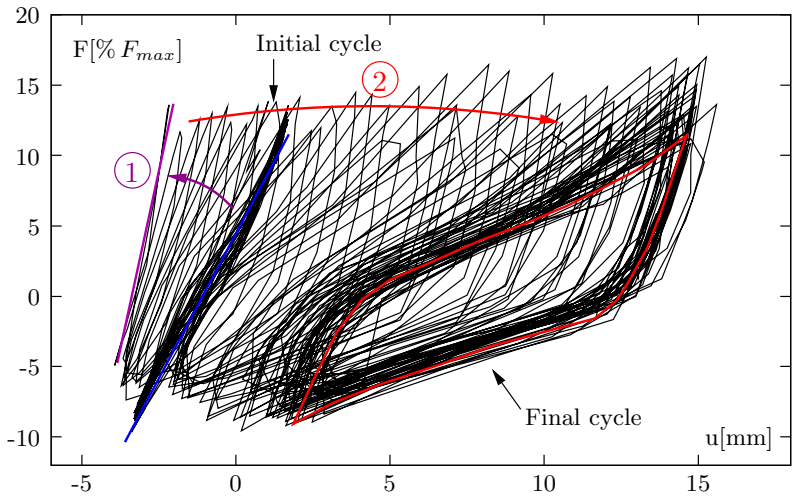

Figure 7.43: Force-displacement diagram evolution.

force yielded by the system and the corresponding displacements of the MMM, represented by the blue line in Figure 7.43. When the control system is switched on and the SE wires start working simultaneously, as they begin to accumulate force, the overall stiffness of the system is increased. This increase is represented in Figure 7.43 by step 1, during which the slope of the line representing the force-displacement relation becomes steeper, since both of the austenitic SE wires start contributing to the system's stiffness. After this initial stiffening, as the SE wires continue to accumulate force, stress induced martensite starts to develop and the

system becomes gradually more flexible. This process is described by step 2, and leads to the appearance of a stabilized SE hysteretic loop.

During the experimental test, the accelerations in the MMM are monitored, enabling to plot the corresponding acceleration time-history, which is shown in Figure 7.44. According to this register, the acceleration levels in the MMM are decreased when

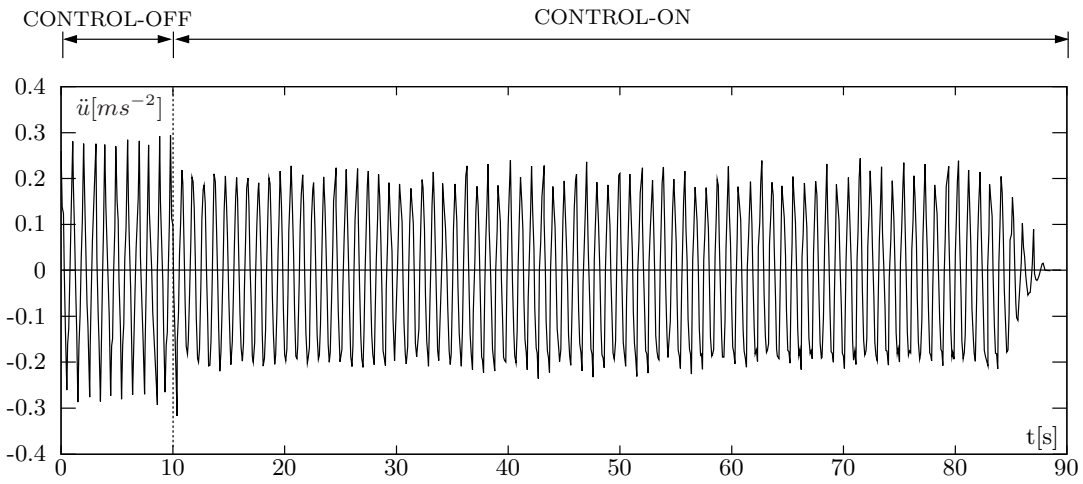

Figure 7.44: Acceleration time-history.

the control system is switched on, which is consistent with the additional damping provided to the system by the SE wires. When the external excitation ceases to exist, the acceleration rapidly converges to zero.

The front panel of the SE vibration control system with two restraining elements and corresponding block diagram are presented in Appendix C.4, in Figures C.16 and C.17, respectively. Some of the case structures contained in the block diagram are illustrated in Figures C.18, C.19, C.20 and C.21.

7.4 Closure

A detailed analysis of the proposed SE restraining prototype and subsequent experimental testing allow to demonstrate the potential of this device as a restraining system for structural vibration control.

The main guideline for the actuation principles of the prototype consist in the control

of the stress level in the SE wires during the dynamic excitation, with the possibility to accumulate stress, enabling higher martensite ratios, and to relieve stress, preventing the wires from yielding. A thorough description of the kernel parts of the prototype provide an extended insight into the developed approach to meet these guidelines. The integration of the control algorithms into the prototype is also addressed. The control algorithms are implemented using a LabView platform, and are based in a PID control approach. Several considerations regarding this type of control systems are made, including relevant aspects related to the tuning of the controller.

To accomplish the proposed objective, several experimental setups are tested. The last experimental procedure features a fully operational version of the proposed SE vibration control system with two restraining SE elements. The response of the system to an external harmonic excitation, induced by a shake table, proves to be rather adequate. The system promotes the force accumulation in the SE wires, enabling the development of a wide SE hysteretic loop, while also controling their maximum force and decreasing the acceleration of the MMM.

Chapter 8

Summary, Conclusions and Future Work

8.1 Summary and conclusions

Shape-memory alloys are a class of peculiar metallic alloys presenting a unique property regarding applications in structural vibration control: superelasticity. It derives from a diffusionless phase transformation in solids called martensitic transformation. This crystallographic phase transformation depends on stress and temperature and enables the material to change from the parent phase, a high energy phase called austenite to a low energy phase called martensite. Superelasticity is associated with the formation of stress induced martensite, which is developed above a certain critical stress threshold. It translates into the ability of the material to totally recover from large, nonlinear, deformations while developing a hysteretic loop. This superelastic hysteretic behavior confers to SMAs a vast potential for technological applications in the field of seismic structural hazard mitigation.

One of the main objectives of this study has been the characterization of the behavior of superelastic Nitinol, identifying ways to optimize its properties for seismic applications. An extensive experimental program is conducted, including temperature-controlled cyclic tensile tests, differential scanning calorimetry and infrared thermoimaging. These experimental tests are complemented by an exhaustive analysis of the corresponding phase-diagram paths and superelastic hysteresis, providing a valu-

able insight into the identification of the main variables influencing the superelastic damping in Nitinol.

After discussing the theoretical background concerning constitutive models for SMAs, a rate-independent model and a rate-dependent model are implemented. These strain-driven, time-discrete numerical models couple the mechanical laws with the kinetic transformation laws, and also with a heat balance equation describing the convective heat problem, in the case of the rate-dependent model. The good performance of these numerical models is confirmed by comparing the numerical simulations with experimental data and literature results from a series of strain-rate analysis with frequency ranging from 0.2 to 4 Hz.

To illustrate the performance of superelastic wires when acting as restoring elements in passive seismic control devices, numerical models of a couple of dynamic systems are analyzed, including a simplified numerical model of a railway viaduct equipped with a superelastic restraining system. This analysis confirms the benefits of using SMAs in passive seismic control devices and encourages future investigations in the field.

The most important contribution of this work consists on the development of an original semi-active vibration control device, which is able to dissipate a considerable amount of energy during a dynamic event, while keeping the superelastic wires inside recoverable limits defined by a prescribed superelastic window. This limits the degradation effects due to cyclic loading in SE Nitinol, also reducing the influence of cycling on damping. With this device, strain accumulation in the SE Nitinol wires derives from the the structural displacements during the dynamic action, avoiding permanent pre-strain in the material with the associated stress-relaxation.

A small-scale prototype of this device is built, simulating the proposed SE vibration control system, comprising two restraining superelastic elements.

The main findings resulting from this study include the following:

- The superelastic damping capacity of Nitinol is influenced by temperature. An increase on ambient temperature, in strain-controlled situations, causes the damping capacity of the Nitinol wires to marginally decrease. It is also showed that an annual temperature variation of 20°C, yields an increment on the critical stress to induce martensite of about 130 MPa, compromising the

SIM development. Hence, an adequate temperature isolation system would highly benefit a vibration mitigation device based on superelastic SMAs.

- The superelastic damping capacity of a Nitinol wire is influenced by strain-amplitude. As the strain-amplitude increases, the damping capacity of SE Nitinol also increases.

- The superelastic damping capacity of a Nitinol wire is influenced by strain-rate. In fact, when passing from quasi-static loading conditions to dynamic ones, important changes occur in the temperature time-history and in the corresponding stress-strain diagram, affecting its dissipation capacity. The evaluation of the equivalent viscous damping for a wide range of strain-rates demonstrated that, as the strain-rate increased from quasi-static conditions, the dissipation capacity of the Nitinol wire first suffers a slight increase and then decreases until it stabilizes. The development of a rate-dependent numerical model, coupling mechanical and kinetic transformations laws with a thermal balance equation, allowed to apprehend the dynamic behavior of SE Nitinol at higher strain-rates. This model confirmed that for a cyclic strain-amplitude of 6.5%, the behavior of SE Nitinol wires is mainly insensitive to strain-rate for frequencies in the range of 0.2 to 4 Hz.

- The superelastic damping capacity of a Nitinol wire is influenced by cyclic loading. In fact, cyclic loading causes cumulative creep deformation in SE Nitinol, increasing the elongation of the wire. For a given oscillation amplitude this is translated in a decrease of the wire's net strain, along with the amount of dissipated energy. Cyclic loading also causes the decrease in both the critical stress to induce martensite and in the width of the hysteretic loop. According to the experimental tests, these effects can be rather important, amounting up to 1.1% of accumulated strain, a maximum decrease of about 160 MPa in the critical stress for SIM and an average strain decrease of 1.5% on the SE hysteretic width. These effects gradually stabilize with cycling, although this stabilization process can endure for about 100 cycles. During this process the damping capacity of the SE Nitinol wire continuously decreases. It was also shown that the degradation increases with both temperature and strain-rate.

- The superelastic damping capacity of a Nitinol wire is influenced by aging at constant strain in the coexistence zone. It is shown that if the material ages at

constant strain in the coexistence domain, a stress step occurs, leading to the stress relaxation of the material. As pre-strain is very important in superelastic based vibration control devices, because it enhances their damping capacity, the stress relaxation of the material has to be conveniently controlled.

- The performance of several SDOF mechanisms based on SE restoring elements is analyzed under dynamic loading, emphasizing their capability to mitigate vibrations and self-centering abilities. The great versatility of SMA devices is confirmed, being able to describe a wide variety of cyclic behaviors, from fully re-centering to highly dissipating. This can be achieved by making simple functional variations of the SMA components and by acting on their mechanical properties. The shape of the hysteretic loops can be adjusted for a specific application, according to its particular dynamic requirements. One of these devices is successfully tested as a seismic passive vibration control system in a simplified numerical model of a railway viaduct. This analysis confirmed the potential of SMAs in passive seismic control devices and encourages future investigations in the field.

- A detailed analysis of the proposed superelastic restraining prototype allows to demonstrate the potential of this device as a restraining system for structural vibration control. The guidelines for the actuation principles of the prototype mainly consist in the control of the stress level in the superelastic wires, during the dynamic excitation, with the possibility to accumulate stress and enable higher martensite ratios. A thorough description of the kernel parts of the prototype enables an extended insight into the developed approach to meet these guidelines. The integration of the control algorithms into the prototype is also addressed. The control algorithms are implemented using a LabView platform, and are based in a PID control approach. Several considerations regarding this type of control systems are made, including relevant aspects related to the tuning of the controller. To accomplish the proposed objective several experimental setups are considered. The last experimental procedure features a full operational prototype of the proposed SE vibration control system with two restraining superelastic elements.

8.2 Future Work

This work has presented a full operational prototype of a SE vibration control device, being able to adequately fulfill a series of prescribed stress control guidelines. However, even though the implementation of these guidelines yielded a successful vibration control mechanism, mainly for academic pursuits, there are several aspects in which this mechanism can be further improved through additional research.

The main drawback of the presented mechanism consists in the fact that the stress control in the SE Nitinol wires is achieved through the use of electromechanical actuators. The compensation either for high or low stresses in the SE wires is achieved by the movement of these actuators, which are placed in series with the wires, in the force flow path. This means that the actuators have to be able to sustain the forces developed in the SE wires during the dynamic loading, which, in the case of civil engineering structures, are considerable high. In order to comply with these forces it would be necessary to use high bearing capacity electromechanical actuators, with high costs and high energy demands, undesirable to a restraining mechanism. In order to meet the requirements of fast response and low power consumption, promising alternatives are being currently studied.

In what follows, a general description of these alternative stress control mechanisms is presented:

- To compensate for low stresses the SE Nitinol wire is connected to a retractor by a webbing. This retractor uses a spool as its central element, which is attached to the other end of the webbing. Inside the retractor an angular spring applies a force to the spool, so it winds up any loose wire. When the wire is pulled out due to slow structural deformations associated with ambient temperature variations or rheological effects, the spool rotates counter-clockwise, turning the attached spring in the same direction. In fact, the rotating spool works to untwist the spring. As the spring wants to return to its original shape, it resists this twisting motion. If the SE Nitinol wire is released, the spring tightens up, rotating the spool clockwise until there is no more slack in the wire. The retractor also has a locking mechanism that stops the spool from rotating when the structure undergoes a fast dynamic action. This may be implemented by a weighted pendulum or a ball bearing that are deflected

by acceleration locking into pawls on the reel [67], as illustrated in Figure 8.1.

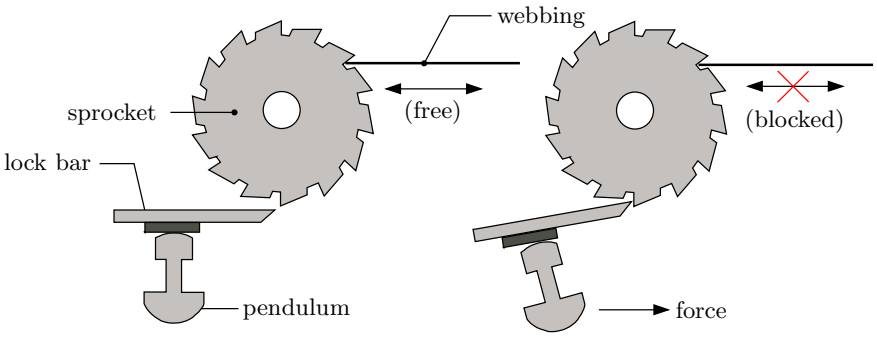

Figure 8.1: Retractor locking mechanism.

- To compensate for high stresses in the SE Nitinol wires a load limiter is used, that absorbs the load during a fast dynamic action, while keeping the SE Nitinol wire force at a controlled and pre-defined level. This is accomplished by a mechanism in the retractor that allows the webbing to be pulled out slightly, in a controlled way, if the force on the SE Nitinol wire exceeds a certain threshold. The load limiter is integrated with the retractor, where a torsion bar is integrated with the spool. When a force exceeding a certain level acts on the SE Nitinol wire, the torsion bar twists, allowing the spool to turn. This produces a controlled reduction in the locking effect of the inertia reel, limiting the stress on the wire [67]. In a typical load limiter for a seat-belt system, which is aimed to reduced torso injuries in car occupants during a collision, the torsion metal bar yields plastically when a certain critical load is reached, so as to allow the previously locked seat-belt to be slightly released, at a constant force level; see Figure 8.2. Based on this mechanism an approximately constant force restraint can be obtained [67]. As the torsion bar yields plastically, the load limiter is not reusable. Due to the continuous oscillatory nature of the seismic restraining problem, it is necessary to adapt the force limiter so that is can be reusable. To accomplish this goal two ideas are to be explored. The first one consists on the replacement of the torsion metal bar with a SE austenitic torsion bar, featuring the same type of hysteretic damping associated with tension stress fields [50, 58, 146, 147, 170]. The behavior of a SE bar subjected to torsion is represented in Figure 8.3(a).

(a) Straight bar during normal service. (b) Twisted bar to limit force in the belt.

Figure 8.2: Load limiter (adapted from [19]).

The second idea consists on using a load limiter with magnetorheological fluid. A MR fluid consists of a suspension of magnetic polarizable micro-particles in a carrier fluid. When subjected to a magnetic field, the fluid greatly increases its viscosity developing a yield stress which monotonically increases with the strength of the applied magnetic field, as shown in Figure 8.3(b).

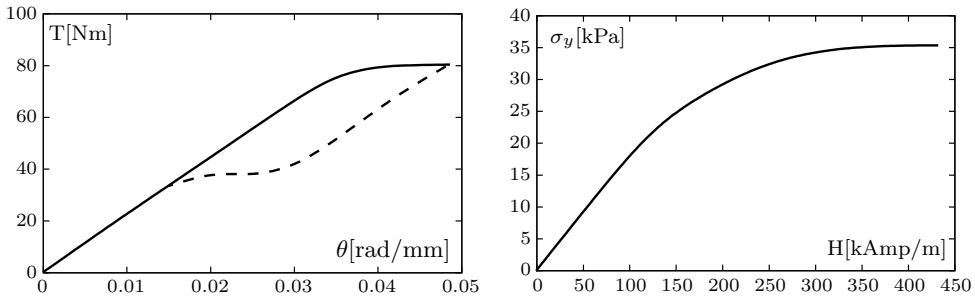

(a) Torsion vs. angle per unit lenght [170] (b) Yield stress vs. magnetic field strength [98]

Figure 8.3: Force-displacement diagrams.

MR dampers are very reliable, relatively inexpensive to manufacture and have small power requirements (20-50 watts). The need for a large power generator can therefore be eliminated since they can operate with a battery. The transmission is fully reversible and almost instantaneous and since the device forces are adjusted by varying the strength of the magnetic field, no mechanical valves are required [80]. This rheological character is very favorable for developing simple, quiet, fast-response interfaces between electronic controls and mechanical systems [83]. The MR fluid can be used either in valve mode,

with the fluid flowing through an orifice, or in shear mode, with the fluid shearing between two surfaces. In the absence of a magnetic field, the MR fluid flows freely or allows free movement. Upon application of a magnetic field, the fluid's particles align with the direction of the field in chain-like fashion, thereby restricting the fluid's movement within the gap, in proportion to the strength of the magnetic field [98]. Based on the shear mode, a MR rotary disk brake can be linked to the retractor spool. By adjusting the strength of the magnetic field in the cavity of the MR brake, the viscosity of the MR fluid can be controlled in order to vary the torque of the brake. MR devices have demonstrated promise in civil engineering applications [151, 153, 154, **?**].

The schematics of the restraining systems comprising the SE torsion bar and the MR brake are illustrated in Figures 8.4 and 8.5.

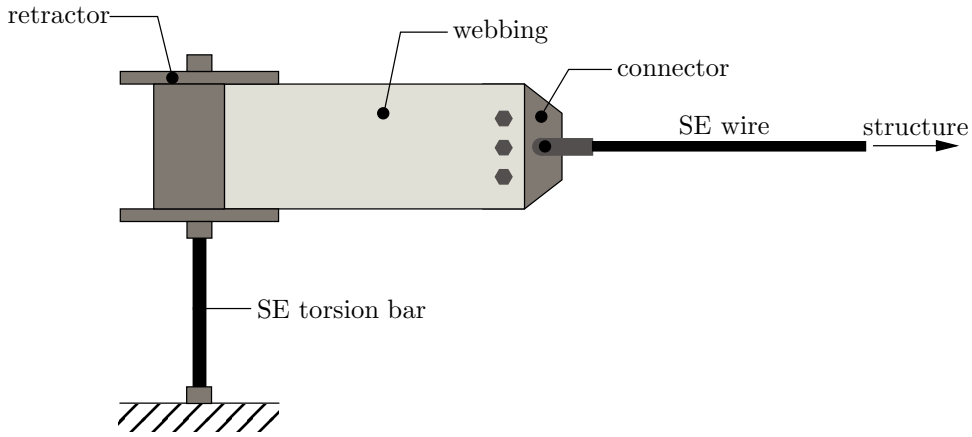

Figure 8.4: Schematics of a retractor with SE torsion bar.

There are also other areas in which this work can also be extended through additional research, which include the following:

- Integration of the degradation curves associated with cumulative creep deformation, the critical stress needed to induce martensite and the width of the hysteretic loop in the numerical models.
- Further experimental characterization of the aging effects in SE wires, regarding strain-creep and stress-relaxation, in the coexistence zone, would certainly give a valuable insight to pursuit the investigation.

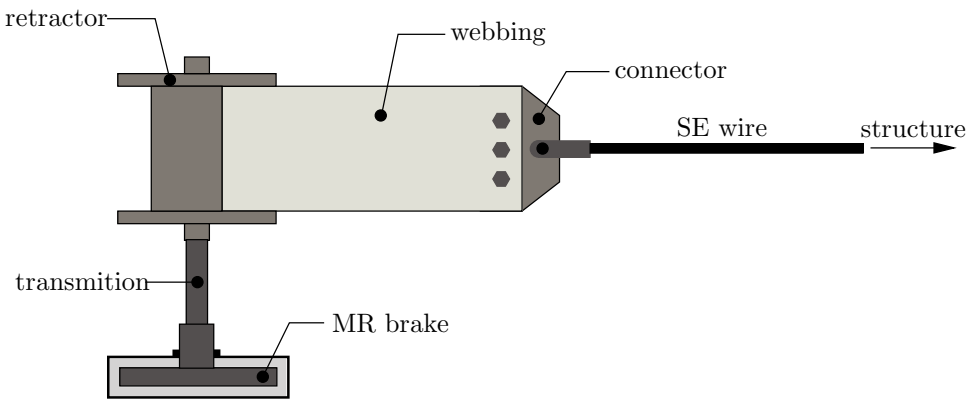

Figure 8.5: Schematics of a retractor with MR brake.

Appendix A

Modeling of control systems

In this appendix are presented some introductory concepts regarding the modeling of control systems.

A.1 Laplace Transformation

A.1.1 Definition of the Laplace transformation

The Laplace transform of a function $f(t)$, defined for all real numbers $t \geq 0$, is the function $F(s)$, defined by [92]:

$$F(s) = \mathscr{L}[(f(t)] = \int_0^\infty e^{-st} dt[f(t)] = \int_0^\infty f(t)\, e^{-st} dt \tag{A.1}$$

where s is a complex variable and $\mathscr{L}$ is an operator indicating that the quantity that it prefixes is to be transformed by the Laplace integral $\int_0^\infty e^{-st} dt$.

For the Laplace transform of a function $f(t)$ to exist, the Laplace integral has to converge. The integral will converge if $f(t)$ is piecewise continue in every finite interval for $t > 0$ and if it is of exponential order as t approaches infinity. The function $f(t)$ has an exponential order at infinity if, and only if, there exist α and M such that

$$|f(t)| \leq M e^{-\alpha\, t}$$

Then, the Laplace transform $\mathscr{L}[(f(t)]$ is defined for $s > \alpha$.

A.1.2 Laplace transforms of several common functions

A.1.2.1 Step function

Consider the step function represented in Figure A.1, in which

$$f(t) = \begin{cases} 0, & \text{for} \quad t < 0 \\ \\ A, & \text{for} \quad t > 0 \end{cases}$$

where A is a constant.

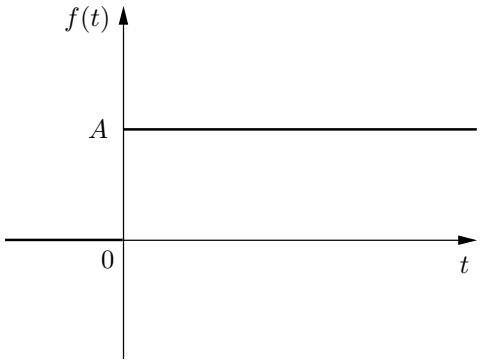

Figure A.1: Step function

The step function is not defined at $t = 0$. The Laplace transform of this step function is calculated using the definition expressed in equation (A.1), yielding

$$\begin{aligned} F(s) &= \mathscr{L}[(f(t)] = \int_0^\infty f(t)\, e^{-st} dt = \int_0^\infty A\, e^{-st} dt = \\ &= -\frac{Ae^{-st}}{s}\Big|_0^\infty = \frac{A}{s} \end{aligned} \tag{A.2}$$

The step function in which $A = 1$ is called unit-step function or Heaviside step function. The Laplace transform of the unit-step function is $1/s$.

A.1.2.2 Ramp function

Consider the ramp function represented in Figure A.2, in which

$$f(t) = \begin{cases} 0, & \text{for} \quad t < 0 \\ \\ A\,t, & \text{for} \quad t \geq 0 \end{cases}$$

where A is a constant.

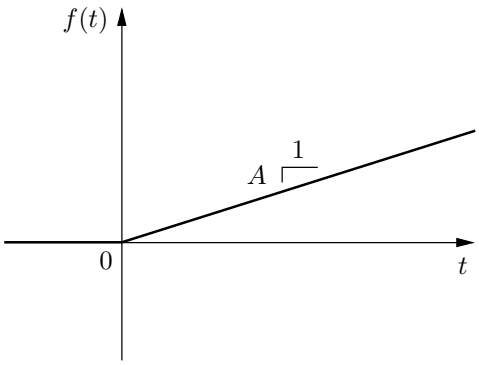

Figure A.2: Ramp function

The Laplace transform of this ramp function is obtained as

$$\begin{aligned} F(s) &= \mathscr{L}[(f(t)] = \int_0^\infty f(t)\, e^{-st} dt = \int_0^\infty At\, e^{-st} dt = \\ &= \frac{Ate^{-st}}{-s}\Big|_0^\infty - \int_0^\infty \frac{Ae^{-st}}{-s}\, e^{-st} dt = \frac{A}{s^2} \end{aligned} \tag{A.3}$$

As in the case of the step function, the ramp function in which $A = 1$ is called unit-ramp function.

A.1.2.3 Pulse function

Consider the pulse function represented in Figure A.3, in which

$$f(t) = \begin{cases} \dfrac{A}{t_0}, & \text{for} \quad t < 0 < t_0 \\ \\ 0 \quad \text{for} \quad t < 0,\, t_0 < t \end{cases}$$

where A and t_0 are constants.

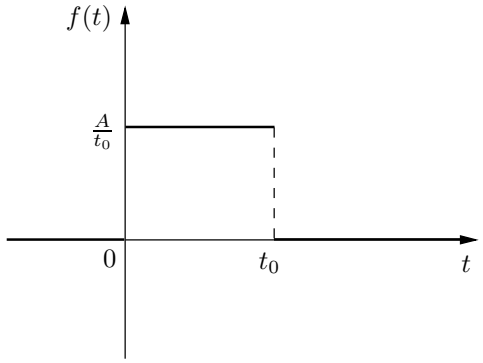

Figure A.3: Pulse function

The Laplace transform of this pulse function is obtained as

$$\begin{aligned} F(s) &= \mathscr{L}[(f(t)] = \int_0^{t_0} f(t)\, e^{-st} dt = \int_0^{t_0} \frac{A}{t_0}\, e^{-st} dt = \\ &= -\frac{Ae^{-st}}{t_0 s}\Big|_0^{t_0} = \frac{A}{t_0 s}(1 - e^{-st_0}) \end{aligned} \tag{A.4}$$

A.1.2.4 Impulse function

The impulse function is a special limiting case of the pulse function in which t_0 tends to zero. It represents an infinitely sharp peak that bounds an area A, since the height of the impulse is A/t_0 and its duration is t_0. This function has the value zero everywhere except at $x = 0$ where its value is infinitely large, in such a way that its total integral yields A. The schematic representation of the impulse function is usually a line surmounted by an arrow, with the the value of the area A next to the arrowhead, as shown in Figure A.4.

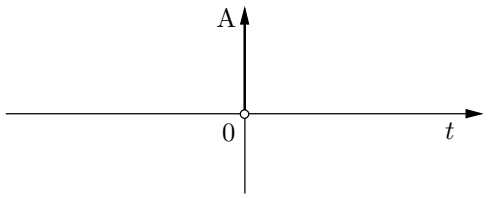

Figure A.4: Impulse function

Consider the impulse function

$$f(t) = \begin{cases} \lim\limits_{t_0 \to 0} \dfrac{A}{t_0} \\ \\ 0 \quad \text{for} \quad t < 0,\, t_0 < t \end{cases}$$

The magnitude of the impulse is measured by its area. When $A = 1$ this function is also known as Dirac delta function $\delta(x)$ or the unit impulse function. Referring to Equation (A.5), the Laplace function of this impulse function is obtained as

$$G(s) \quad = \quad \mathscr{L}[(g(t)] = \lim_{t_0 \to 0} \left[\frac{A}{t_0 s}(1 - e^{-st_0}) \right]$$

since

$$\lim_{t_0 \to 0} t_0 s = \lim_{t_0 \to 0} A(1 - e^{-st_0}) = 0 \quad \text{and}$$

$$\lim_{t_0 \to 0} \frac{\frac{d}{dt_0}(t_0 s)}{\frac{d}{dt_0}[A(1 - e^{-st_0}]} = \frac{As}{s} = A$$

l'Hôpital's rule states that

$$\lim_{t_0 \to 0} \left[\frac{A}{t_0 s}(1 - e^{-st_0}) \right] = \lim_{t_0 \to 0} \frac{\frac{d}{dt_0}(t_0 s)}{\frac{d}{dt_0}[A(1 - e^{-st_0}]} = A \tag{A.5}$$

And thus, the Laplace transform of the impulse function is equal to the area under the impulse.

A.1.3 Laplace transforms properties

A.1.3.1 Linearity

A linear function $f(x)$ is a function that satisfies both the adaptivity and homogeneity properties. Additivity is also referred to as the superposition property and it states that, the net response caused by two or more different forcing functions is the sum of the responses which would have been caused by each forcing function individually. This property can be mathematically expressed as $f(x+y) = f(x)+f(y)$. Homogeneity of degree 1 is when $f(\alpha x) = \alpha f(x)$, for all α.

The Laplace transform is a linear function, and hence, the Laplace transform of a sum is the sum of Laplace transforms of each term. Consider two Laplace transformable functions $f(t)$ and $g(t)$ with Laplace transforms $F(s)$ and $G(s)$, respectively.

$$\mathscr{L}[f(t)+g(t)] = \mathscr{L}[f(t)] + \mathscr{L}[g(t)] = F(s) + G(s) \tag{A.6}$$

This can be easily proved using basic rules of integration, as shown next

$$\begin{aligned}\mathscr{L}[(f(t)+g(t)] &= \int_0^\infty [f(t)+g(t)]\, e^{-st} dt = \\ &= \int_0^\infty f(t)\, e^{-st} dt + \int_0^\infty g(t)\, e^{-st} dt = F(s) + G(s)\end{aligned}$$

The homogeneity of the Laplace transform can be proved in the following way

$$\mathscr{L}[af(t)] = a\,\mathscr{L}[f(t)] = a\,F(s) \tag{A.7}$$

$$\begin{aligned}\mathscr{L}[a(f(t)] &= \int_0^\infty af(t)\, e^{-st} dt = \\ &= a\int_0^\infty f(t)\, e^{-st} dt = a\,F(s)\end{aligned}$$

A.1.3.2 Differentiation and integration

Consider the Laplace integral expressed in Equation A.1. Integrating this integral by parts yields

$$F(s) = \int_0^\infty f(t)e^{-st}\,dt = f(t)\frac{e^{-st}}{-s}\Big|_0^\infty - \int_0^\infty \left[\frac{d}{dt}f(t)\right]\frac{e^{-st}}{-s} =$$
$$= \frac{f(0)}{s} + \frac{1}{s}\int_0^\infty \left[\frac{d}{dt}f(t)\right]e^{-st}\,dt = \frac{f(0)}{s} + \frac{1}{s}\mathscr{L}\left[\frac{d}{dt}f(t)\right]$$

this means that

$$\mathscr{L}\left[\frac{d}{dt}f(t)\right] = sF(s) - f(0) \tag{A.8}$$

where $f(0)$ represents the value of $f(t)$ evaluated at $t = 0$. This procedure may be equally applied to the second derivative of $f(t)$, yielding

$$\mathscr{L}\left[\frac{d^2}{dt^2}f(t)\right] = s^2F(s) - sf(0) - \dot{f(0)} \tag{A.9}$$

where $\dot{f(0)}$ represents the value of $df(t)/dt$ evaluated at $t = 0$. In the case of the n^{th} derivative, one obtains

$$\mathscr{L}\left[\frac{d^n}{dt^n}f(t)\right] = s^nF(s) - s^{n-1}f(0) - s^{n-2}\dot{f(0)} - \cdots - sf^{(n-2)}(0) - f^{(n-1)}(0)$$

where $f(0), \dot{f(0)}, \ldots, f^{(n-1)}(0)$ represent the values of $f(t), df(t)/dt, \ldots, d^{(n-1)}/dt^{(n-1)}$, respectively evaluated at $t = 0$. If all the initial values of $f(t)$ and its derivatives are equal to zero, then the Laplace transform of the n^{th} derivative of $f(t)$ is given by $s^nF(s)$.

In order to obtain the Laplace transform of integrals one has to refer to Equation (A.1) and expand it using the integration by parts rules. This means that

$$\mathscr{L}\left[\int f(t)\,dt\right] = \int_0^\infty \left[\int f(t)\,dt\right]e^{-st}dt =$$
$$= \int f(t)\,dt\,\frac{e^{-st}}{-s}\Big|_0^\infty - \int_0^\infty f(t)\frac{e^{-st}}{-s}dt = \frac{f^{-1}(0)}{s} + \frac{F(s)}{s} \tag{A.10}$$

where $f^{-1}(0)$ represents $\int f(t)dt$ at $t = 0$.

In the case of a definite integral, $\int_0^t f(t)\,dt$, as

$$\int_0^t f(t)\,dt = \int f(t)\,dt - f^{-1}(0)$$

and

$$\mathscr{L}\left[\int_0^t f(t)\,dt\right] = \mathscr{L}\left[\int f(t)\,dt\right] - \mathscr{L}\left[f^{-1}(0)\right]$$

since

$$\mathscr{L}\left[f^{-1}(0)\right] = \frac{f^{-1}(0)}{s}$$

one obtains that

$$\mathscr{L}\left[\int_0^t f(t)\,dt\right] = \frac{F(s)}{s} \tag{A.11}$$

A.2 Transfer function

A transfer function is a mathematical representation of the relation between the input and output of a linear, time-invariant (LTI) system. A system is called linear if the relation between the input and the output of the system is a linear function. Time invariance means that if an input is applied to a system, at any given time instant, or τ seconds apart from that instant, the output will be identical, except for the corresponding time delay. That is, if the output due to input $x(t)$ is $y(t)$, then the output due to input $x(t-\tau)$ is $y(t-\tau)$. Hence, the system is time invariant because the output does not depend on the particular time the input is applied.

Consider the LTI system defined by the following differential equation:

$$\begin{aligned} &a_0 y^n(t) + a_1 y^{(n-1)}(t) + \cdots + a_{(n-1)}\dot{y}(t) + a_n y(t) = \\ &b_0 u^m(t) + b_1 u^{(m-1)}(t) + \cdots + b_{(m-1)}\dot{x}(t) + b_m x(t) \quad (n \geq m) \end{aligned} \tag{A.12}$$

where $y(t)$ is the output variable of the system and $x(t)$ is the input. Taking the Laplace transforms of both sides of Equation A.12, and assuming that all initial

conditions are zero, one obtains

$$(a_0 s^n + a_1 s^{(n-1)} + \cdots + a_{(n-1)} s + a_n) Y(s) =$$
$$= (b_0 s^m + b_1 s^{(m-1)} + \cdots + b_{(m-1)} s + b_m) U(s)$$

The transfer function $G(s)$, relating the input and output of a LTI system, yields

$$G(s) = \frac{Y(s)}{U(s)} = \frac{b_0 s^m + b_1 s^{(m-1)} + \cdots + b_{(m-1)} s + b_m}{a_0 s^n + a_1 s^{(n-1)} + \cdots + a_{(n-1)} s + a_n}$$

The order of the system is given by the highest power of s in the denominator of the transfer function.

A.3 Control systems

The main objective of a automatic control system is to control a system variable, causing it to comply with a desired reference value. This variable is measured and controlled and it is called the controlled variable. Normally, the controlled variable constitutes the output of the system. The manipulation of the controlled variable is achieved by the system components through the variation, in a prescribed manner, of the actuating signal, also called the input signal.

The basic control system concept may be graphically described by the simple block diagram presented in Figure A.5, in which a system G, with a Laplace transfer function $G(s)$, relates the input and the output signals. Block diagrams illustrate the functions performed by each component of the control system, as well the correspondent signal flows. Block diagrams are built up of functional blocks, which represent the mathematical operation performed on the input signal, producing an output. Transfer functions of the components are placed is the corresponding blocks, which are connected by arrows to indicate the direction of the signals flow.

In this case, the output of the block $O(s)$ is obtained by multiplying the input signal $I(s)$ by the transfer function $G(s)$, i.e. $O(s) = G(s)I(s)$, with $G(s) = O(s)/I(s)$. A summing operation can also be translated into a block diagram, by the use of a circle where the various input signals converge, and an output signal emerges. To

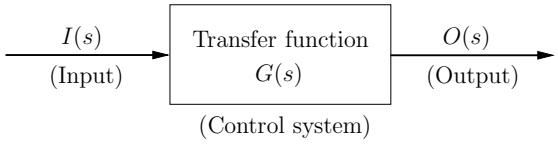

Figure A.5: Basic control system

perform this operation, the signs of the input signals have to be considered, i.e. if a signal is to be added, a plus sign is used, and if a signal is to be subtracted, a minus sign is used. All the signals converging in a summing point have to show the same dimensions and units. A branch point is a ramification point where a given signal goes concurrently to other blocks or summing points.

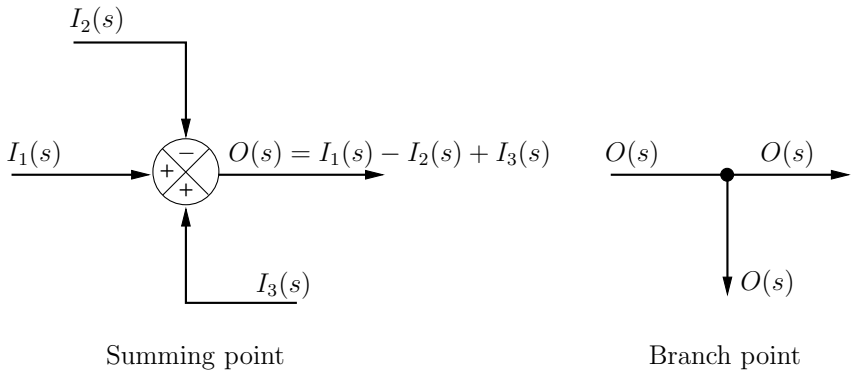

Figure A.6: Summing and branch points

A control system that is able to feed the output variable back and compare it with the reference input, using the difference as a means of control is called a closed-loop control system or feedback control system. When a system does not have the feedback structure, it is called an open-loop system. Figure A.7 shows the block diagram of a linear closed-loop control system. The controlled process is defined by the transfer function $G_{cp}(s)$ and the controller by the transfer function $G_c(s)$. The output $C(s)$ is fed back to the summing point, where it is compared with the reference input $R(s)$, yielding the actuating error signal $E(s)$. To modify the output in order to make it comparable with the reference input signal, a feedback-path transfer function, $H(s)$, is used. In this example, the resulting feedback signal is $B(s)$.

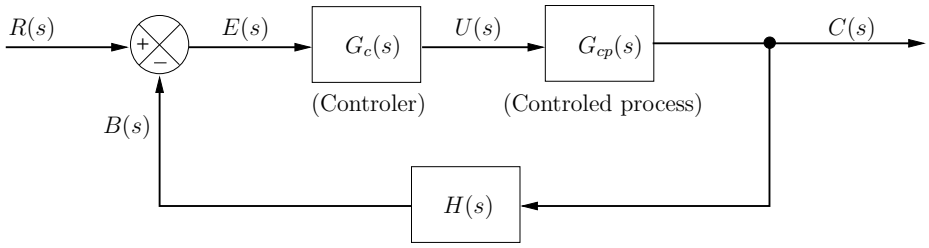

Figure A.7: Block diagram of a closed-loop system

This diagram can be simplified since

$$U(s) = G_c(s)\, E(s) \quad \text{and} \quad C(s) = G_{cp}(s)\, C_c(s)$$

yielding

$$C(s) = G_{cp}(s)\, G_c(s)\, E(s) = G(s)\, E(s) \quad \text{with} \quad G(s) = G_{cp}(s)\, G_c(s) \tag{A.13}$$

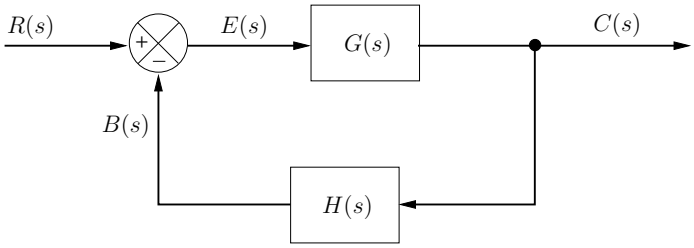

Figure A.8: Simplified block diagram of a closed-loop system

The output of the block, $C(s)$, is hence obtained by multiplying the forward-path transfer function $G(s)$ (feed-forward transfer function) by $E(s)$. The closed-loop transfer function $M(s)$, relating the output $C(s)$ and the input $R(s)$ signals, may be calculated in the following way

$$B(s) = H(s)\, C(s) \tag{A.14}$$

$$E(s) = R(s) - B(s) \tag{A.15}$$

substituting Equation (A.13) in Equation (A.15) gives

$$C(s) = G(s)\,[R(s) - B(s)] = G(s)\,R(s) - G(s)\,B(s) \tag{A.16}$$

substituting Equation (A.14) in Equation (A.16) yields

$$C(s) = G(s)\,R(s) - G(s)\,H(s)\,C(s) \tag{A.17}$$

with some algebraic manipulation, the closed-loop transfer function of the system may be obtained, reading

$$M(s) = \frac{C(s)}{R(s)} = \frac{G(s)}{1 + G(s)\,H(s)} \tag{A.18}$$

A.4 Basic control actions

A.4.1 Proportional control

When the output of the controller $u(t)$ is made to be linearly proportional to the actuating error signal ($e(t)$, the controller is said to have a proportional control action [118]. The general form of proportional control is

$$u(t) = K_p\,e(t) \tag{A.19}$$

where K_p is a constant, usually named the proportional gain. The controller transfer function yields

$$G_c(s) = \frac{U(s)}{E(s)} = K_p \tag{A.20}$$

A.4.2 Derivative control

In derivative control the controller output signal is proportional to the rate of change of the actuating error signal $e(t)$ [118]. The general form of derivative control is

$$u(t) = K_d\,\frac{d\,e(t)}{d\,t} \tag{A.21}$$

where K_d is a constant. The transfer function of the derivative controller is

$$G_c(s) = \frac{U(s)}{E(s)} = K_d\, s \tag{A.22}$$

Since $d\,e(t)/d\,t$ represents the slope of $e(t)$, the derivative control is mainly an anticipatory type of control. As the controller measures the instantaneous slope of $e(t)$, it is able to predict the system's overshoot and produce an adequate correcting effort, before the overshoot actually occurs.

A.4.3 Integral control

Integral control may be considered the counterpart of derivative control, producing an output that is proportional to the integral of the error signal [118]. It's general form is

$$u(t) = K_i \int_0^t e(t)\, dt \tag{A.23}$$

where K_i is a constant. The transfer function of the integral controller yields

$$G_c(s) = \frac{U(s)}{E(s)} = \frac{K_i}{s} \tag{A.24}$$

Integral control is very useful for the reduction or elimination of constant steady-state errors, typically at the cost of a worse transient response.

A.4.4 Proportional-plus-integral-plus-derivative control

The proportional-plus-integral-plus-derivative (PID) controller combines the proportional, integral and derivative control actions. The control signal is a linear combination of the error, the integral of the error, and the time-rate of the change of the error. The equation of a controller with this combined action is given by

$$u(t) = K_p\, e(t) + K_i \int_0^t e(t)\, dt + K_d \frac{d\, e(t)}{d\, t} \tag{A.25}$$

and the corresponing transfer function

$$G_c(s) = \frac{U(s)}{E(s)} = K_p + \frac{K_i}{s} + K_d\, s \tag{A.26}$$

This transfer function may also be expressed in the following way

$$G_c(s) = K_p \left(1 + \frac{1}{T_i\, s} + T_d\, s\right) \tag{A.27}$$

where K_p is the proportional gain, $T_i = K_p/K_i$, the integral time and $T_d = K_d/K_p$ is the derivative time.

A.4.5 Ziegler-Nichols tuning of PID controlers

In the design process of a control loop, in order to achieve an acceptable performance, the constants K_p, T_i and T_d, in Equation (A.27) have to be adequately adjusted. This process of adjusting the controller parameters in order to meet given performance specifications is known as controller tuning. When the mathematical model of the process cannot be easily obtained, an analytical approach to this tuning is not possible and experimental approaches have to be used. Callender *et al.* [33] first tried to establish the specification of satisfactory control parameters, for PID controllers, based on the transient response characteristics of the process itself. Ziegler and Nichols realized that the step responses of a large number of control systems show a S-shaped process response curve. For this type of systems, they proposed a tuning method which is based on the experimental evaluation of the controlled process unit-step input response, as shown in Figures A.9 and A.10 [59].

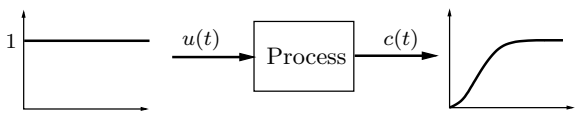

Figure A.9: Open loop tuning procedure: Step test.

The S-shaped curve may be approximated by a first order system plus a time delay

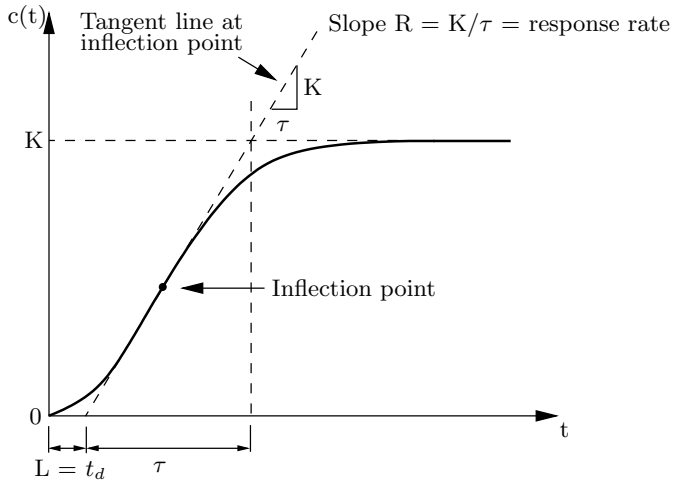

Figure A.10: S-shaped response curve.

of t_d, with a transfer function expressed by

$$\frac{C(s)}{U(s)} = \frac{K\, e^{-t_d\, s}}{\tau\, s + 1} \tag{A.28}$$

The constants in Equation (A.28) can be derived from the inspection of the unit step response of the process. The delay time (t_d) and time constant (τ) may be determined by drawing a tangent line at the inflection point of the S-shaped curve and determining the intersections of this tangent line with the time axis and line $c(t) = K$. In this method, the controller parameters are chosen to yield 25% maximum overshoot in step response. The values suggested by Ziegler and Nichols are shown in Table A.1.

Controller	K_p	T_i	T_d
P	$1/(RL)$	–	–
PI	$0.9/(RL)$	$L/0.3$	–
PID	$1.2/(RL)$	$2L$	$0.5L$

Table A.1: Ziegler-Nichols tuning rule based on step response (Decay ratio of 0.25).

Appendix B

Implementation of control systems

In this appendix is presented some additional information regarding the practical implementation of automatic control systems.

B.1 TTL signal

A TTL signal is a type of binary electrical signaling based on the TTL (transistor-transistor logic) standard [114]. It must meet both voltage and time specifications, as shown in Figure B.1. Regarding the voltage specification, a TTL signal has two

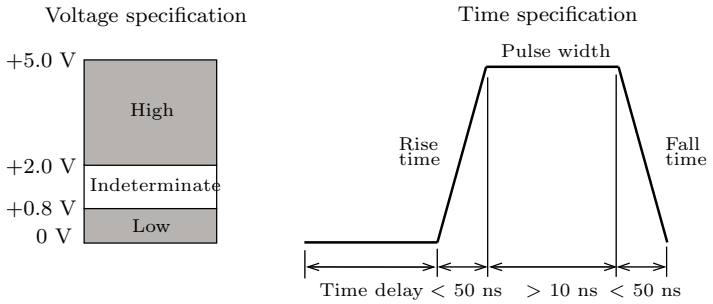

Figure B.1: Specifications of a TTL compatible signal (adapted from [114]).

states: logic low and logic high. Logic low signals are signals between 0 to +0.8 V. Logic high signals are signals between +2 to +5 V. Signals between +0.8 and +2 V are indeterminate and should be avoided, in order for the digital signal lines to read

the signal correctly [120]. A pulse comprises two parts: the delay, which is the first part of the pulse (t_D), and the pulse width (t_W), which is the remaining part. These two phases are always in opposite logic levels. In positive logic, the pulse width is logic high and the delay is logic low. In negative logic, the pulse width is logic low and the delay is logic high. The time specifications comprise the signal's maximum rise and fall times (50 ns) and its minimum pulse with (10 ns) [120]. The rise/fall time is a measure of how quickly the signal transitions from low to high or from high to low. For a counter device to be able to detect the rising and falling edges of a given signal, the transition period must occur within 50 ns or less [114]. In addition to this time restrain, there must be a minimum time delay between the instant the counter detects a rising or falling edge until it can detect another rising or falling edge. This delay is known as the minimum pulse width [114]. The pulse period is the time it takes for a pulse to complete one cycle ($T_p = t_D + t_W$) while the pulse frequency is the inverse of the period ($f_p = 1/T_p$). The duty cycle translates the relation between the pulse width and its corresponding period (duty cycle $= t_W/T_p$).

Regarding the S-ON signal, the logic low level corresponds to the on position of the servomotor. In this position the servomotor can be operated. Concerning the signals P-OT and N-OT, the low logic level corresponds to the normal operation status, meaning that the forward and reverse rotations are allowed. The high level corresponds to an over-travel situation and hence the forward or/and reverse rotation is/are prohibited, for the P-OT and N-OT signals respectively. These digital signals are common to all the external input signal circuits regarding the various control modes of the servo-system.

B.2 Position-control

When in the position-control mode, the servo-drive controls the servomotor position by means of a pulse train position reference. When a counter device is used to generate TTL signals, this is usually called pulse generation. The generated signal can be a single pulse or a continuous set of pulses, known as a pulse train [114], as shown in Figure B.2.

In Figure B.3 is shown the block diagram of the position-control VI.

The position-control VI contains a counter and two additional digital output chan-

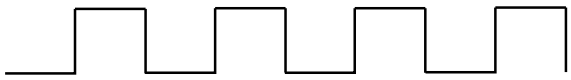

Figure B.2: Pulse train.

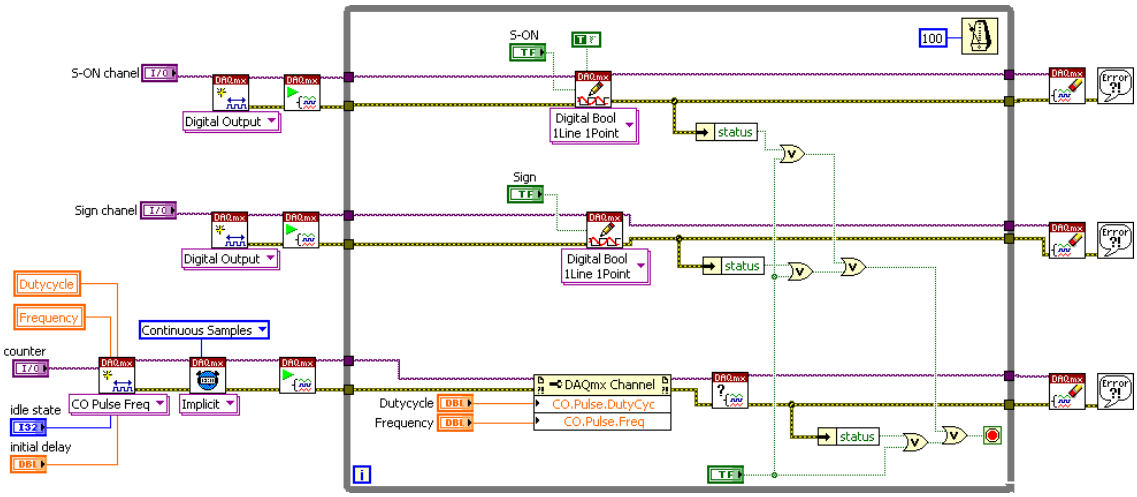

Figure B.3: Block diagram of the position-control VI.

nels. The counter generates the pulse signals, once specified the corresponding duty-cycle and frequency (PULS). One of the digital channels controls the travel direction of the shaft of the servomotor (SIGN) and the remaining digital channel S-ON, P-OT and N-OT.

B.3 Servo-drive specifications

The servodrive has three available control modes, i.e., speed, position and torque control modes. In the speed-control mode the servo-drive controls the speed of the servomotor by means of an analog voltage speed reference. In the position-control mode the servo-drive controls the servomotor position by means of a pulse train position reference. It controls the position with the number of input pulses, and speed with the corresponding input pulse frequency. In the torque-control mode the servo-drive controls the servomotor's output torque by means of an analog voltage

torque reference. The torque-control mode is used to output a required amount of torque for specific operations. In Figure B.4, the dimensional drawing of the servo-drive is presented.

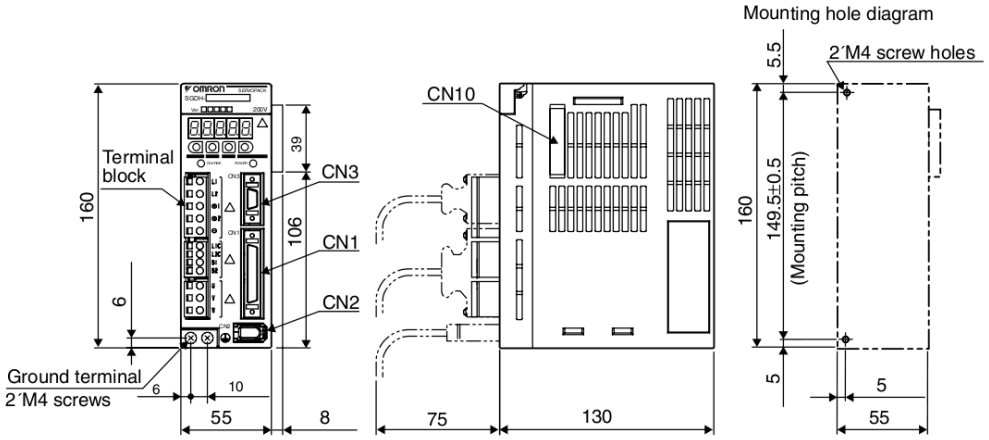

Figure B.4: Dimensional drawing of the Omron-Yaskawa servo-drive (mm) [119].

The servo-drive system is a closed-loop control system with a feedback structure. It consists of three feedback loops, i.e., position loop, speed loop, and current loop [121], as illustrated in the block diagram presented in Figure B.5.

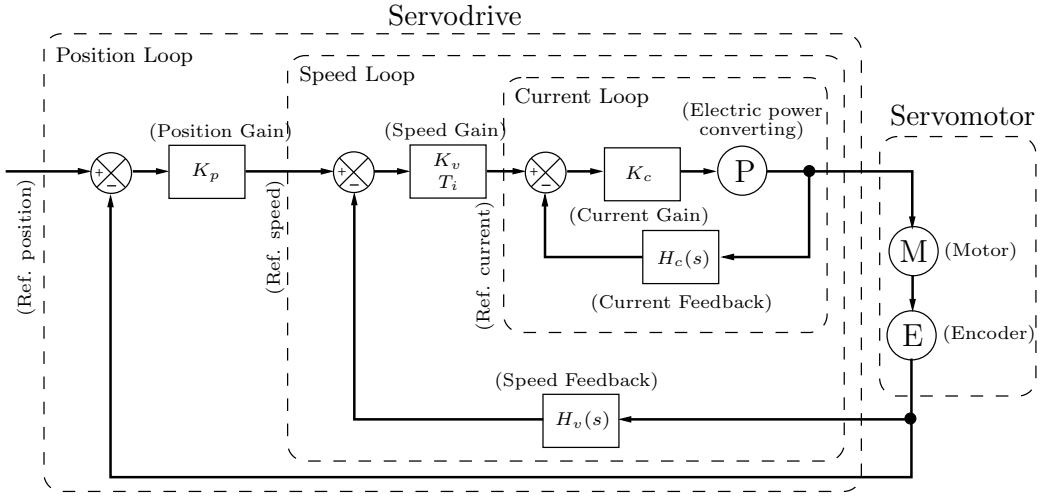

Figure B.5: General block diagram of the servo system (adapted from [121]).

The position loop is used to let the rotation angle of the motor reach the reference position (i.e., the desired rotation angle), that was externally designated. The output

of the position loop is the reference speed input of the speed loop. The position loop feeds back the position data, i.e., the information on the rotation angle provided by the encoder. The speed loop is used to let the motor rotate at the speed designated by the external analog speed reference input, when the system is in Speed Control mode, or the speed command that is the output from the position loop. The output from the speed loop is the reference current input of the current (torque) loop. The speed loop feeds back the speed data, computed from the output data provided by the encoder. The current loop provides the motor with the current designated by the current reference input that is the output from the speed loop, feeding back the motor current value. The response characteristics of the servo system can be changed by adjusting the gain values in the feedback loops, which can be particularly useful to mitigate possible overshooting or undershooting problems.

The servo-drives are connected to the NI PXI-6221 multifunction M Series data acquisition (DAQ) board, using the NI SCB-68 shielded I/O connector block, combined with the NI SHC68-68-EPM shielded cable.

Appendix C

Virtual instruments

In this appendix are displayed the block diagrams of a series of virtual instruments described in the body of the dissertation, as well as the corresponding front panels. The case structures featured in the block diagrams are also presented in this appendix.

C.1 Control of the stress level in a SE wire VI

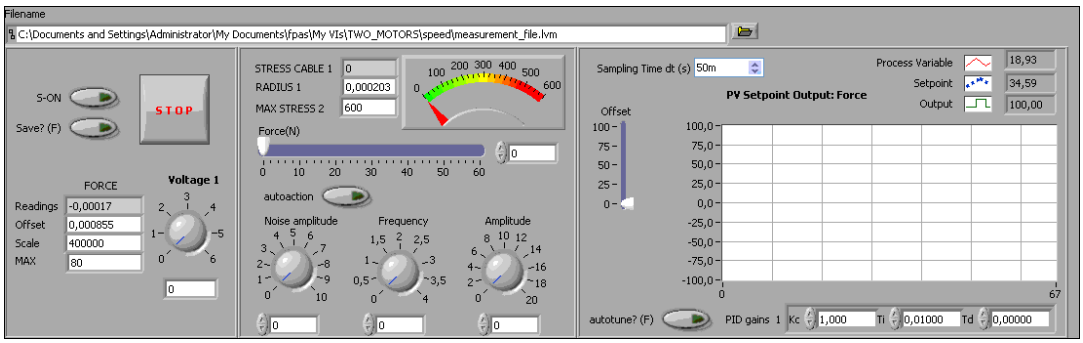

Figure C.1: Front panel of the stress control VI.

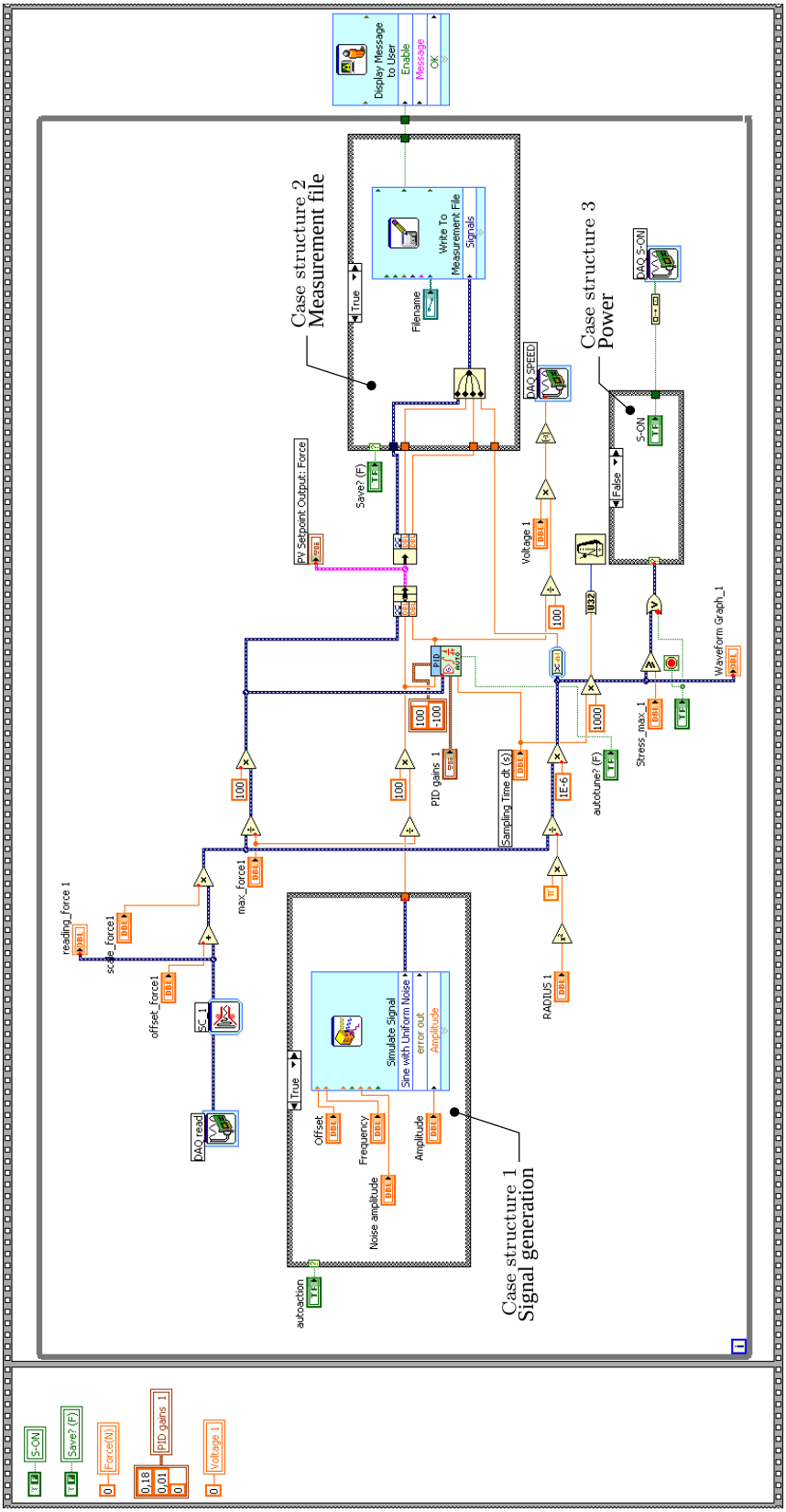

Figure C.2: Block diagram of the stress control VI.

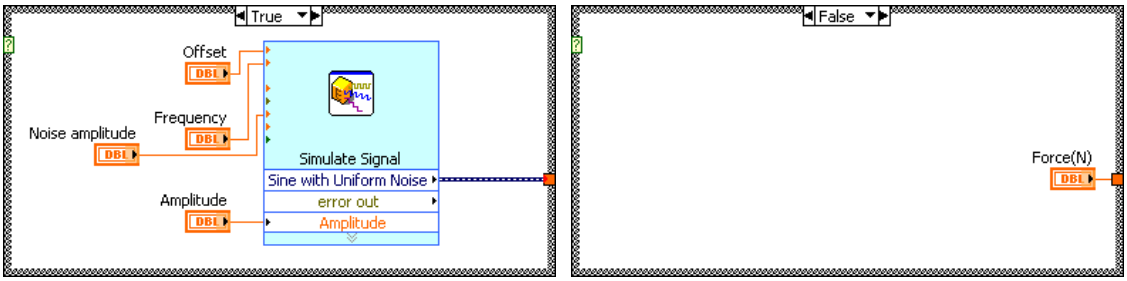

Figure C.3: Case structure 1: signal generation (true-false).

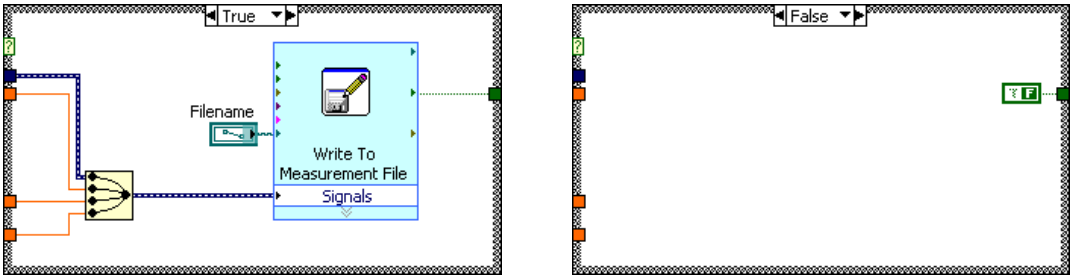

Figure C.4: Case structure 2: measurement file (true-false).

Figure C.5: Case structure 3: power (true-false).

C.2 Displacement control for dynamic tensile testing

The case structures contained in the block diagram are ilustrated in Figures C.8, C.9, C.10 and C.11.

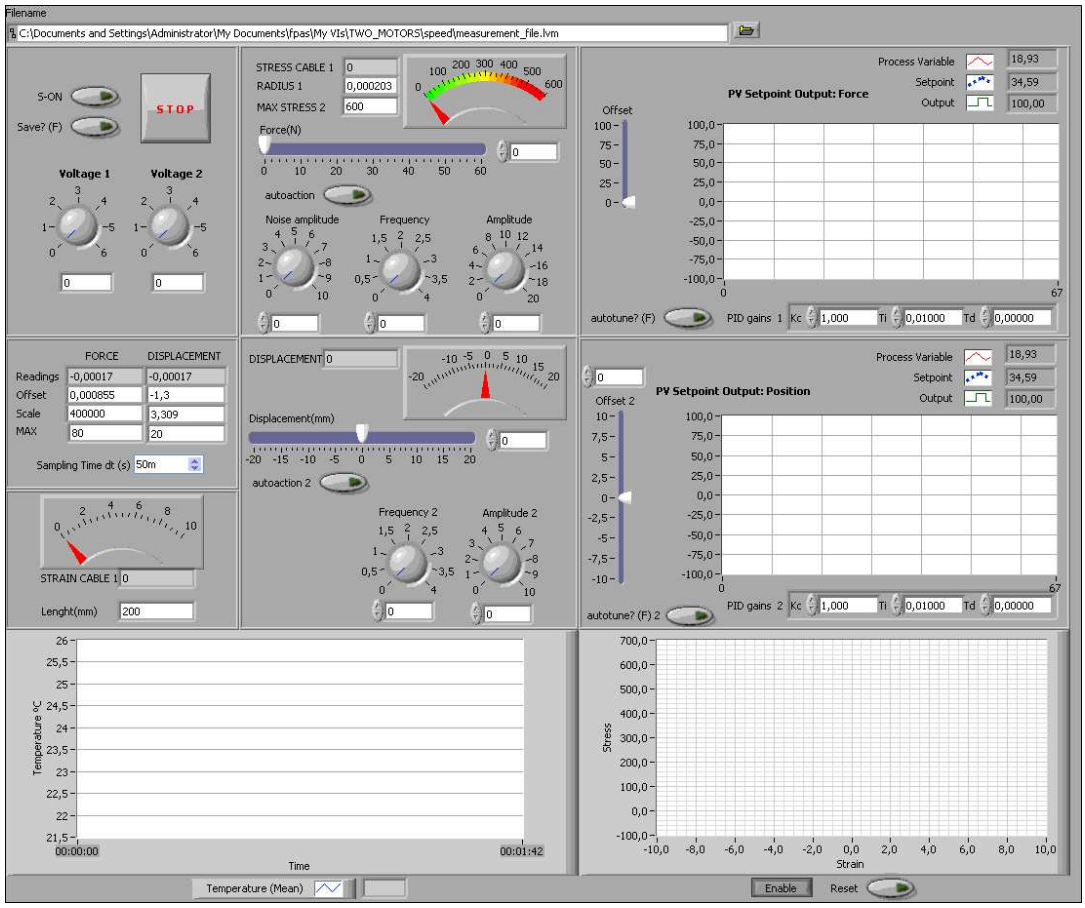

Figure C.6: Front panel of the displacement control VI for dynamic tensile testing.

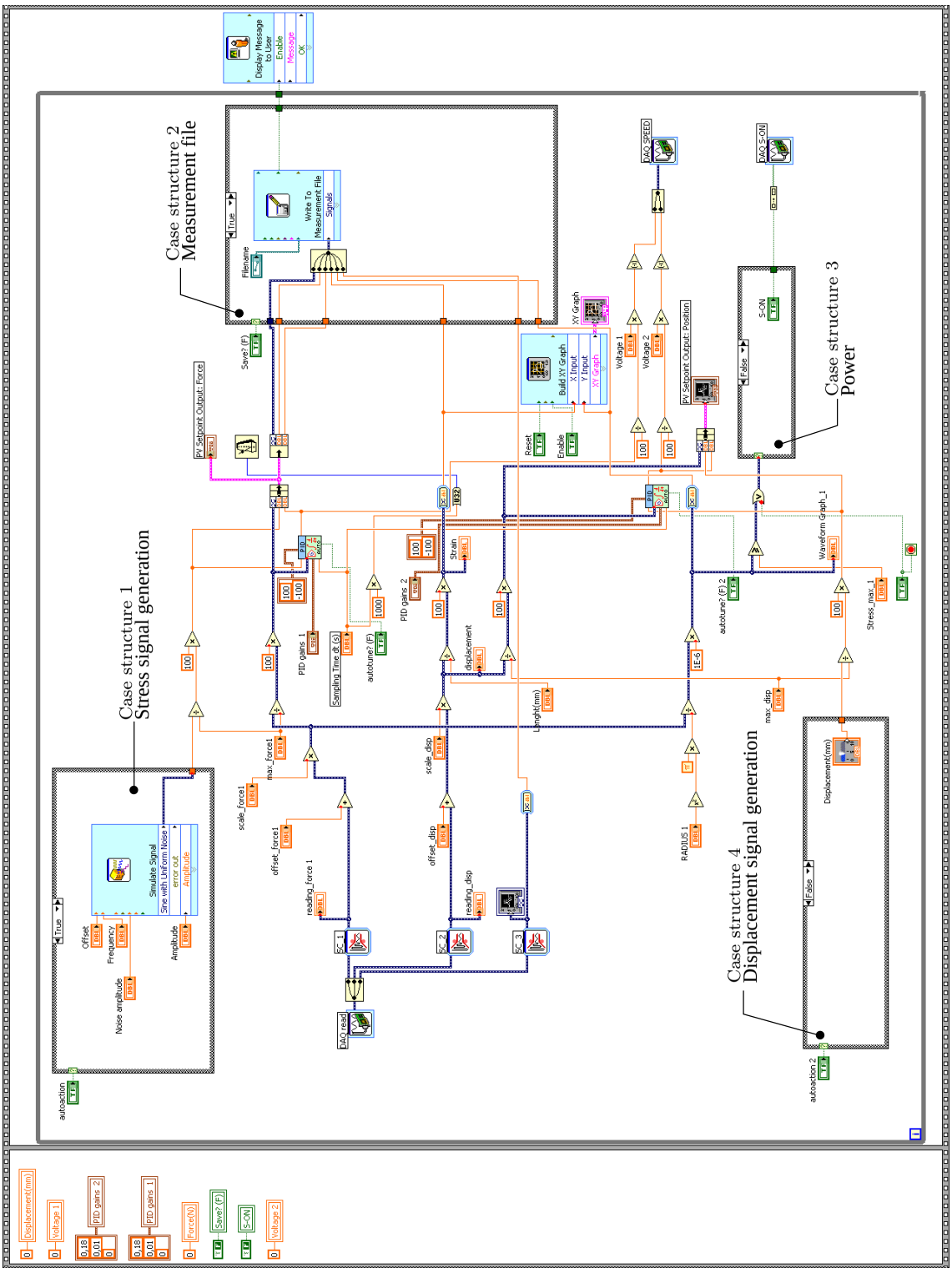

Figure C.7: Block diagram of the displacement control VI for dynamic tensile testing.

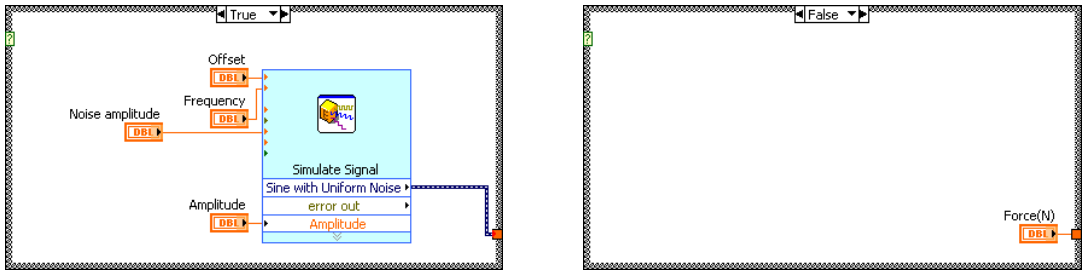

Figure C.8: Case structure 1: stress signal generation (true-false).

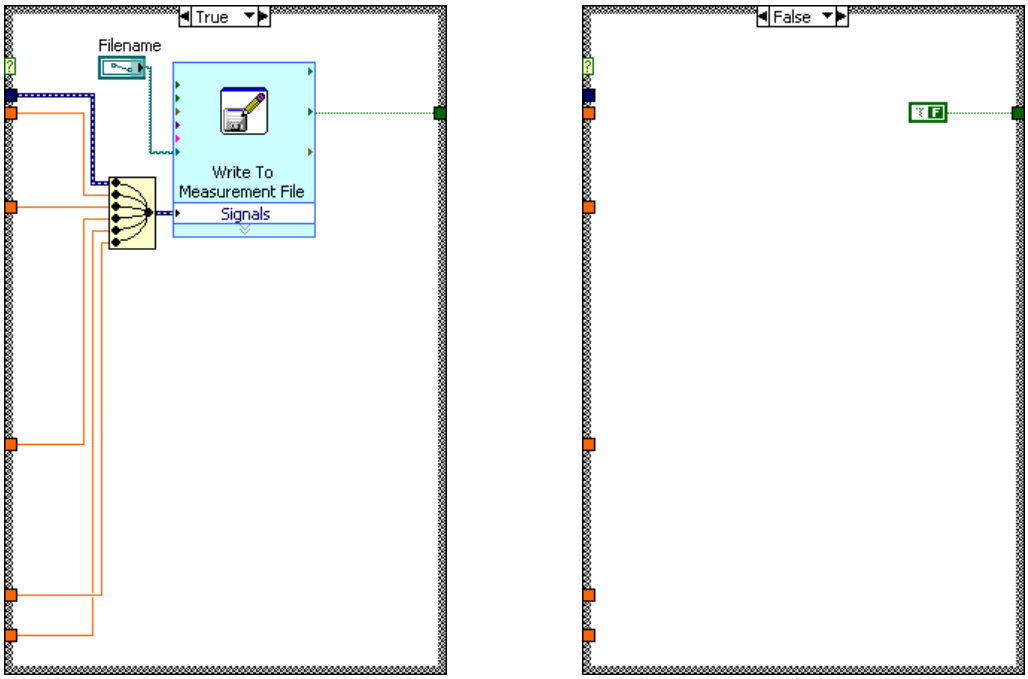

Figure C.9: Case structure 2: measurement file (true-false).

Figure C.10: Case structure 3: power (true-false).

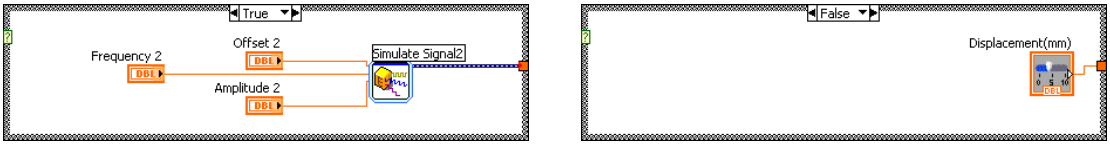

Figure C.11: Case structure 4: displacement signal generation (true-false).

C.3 Superelastic vibration control system with one restraining element

Some of the case structures contained in the block diagram are ilustrated in Figures C.14 and C.15.

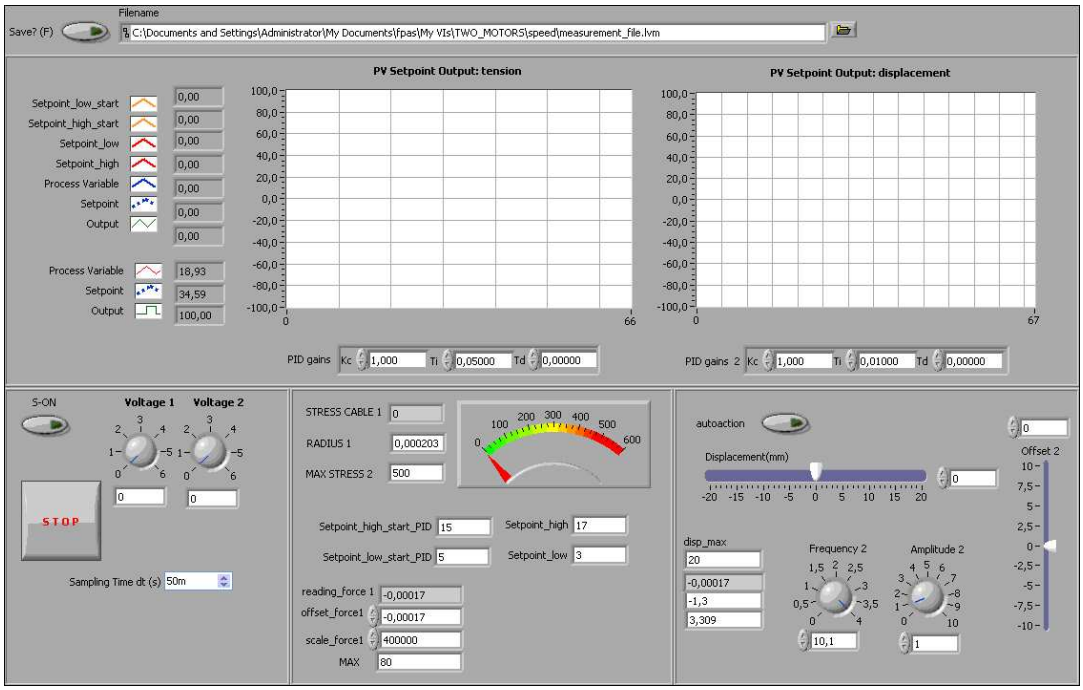

Figure C.12: Front panel of SE vibration control system with one restraining element.

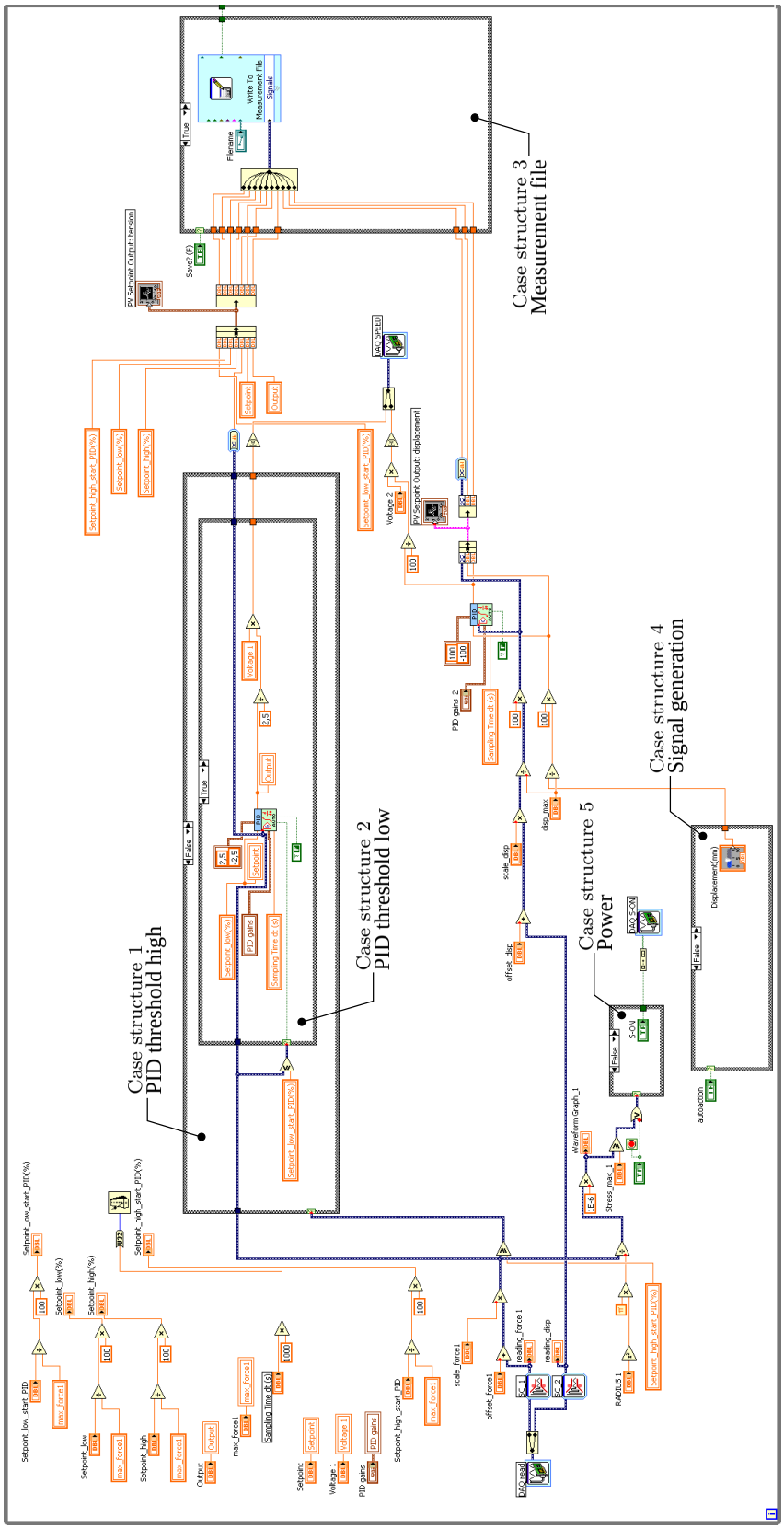

Figure C.13: Block diagram of the SE vibration control system with one restraining element (partial).

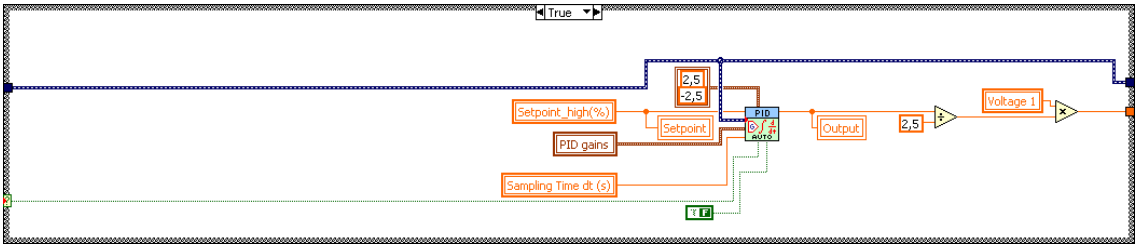

Figure C.14: Case structure 1: PID threshold high (true).

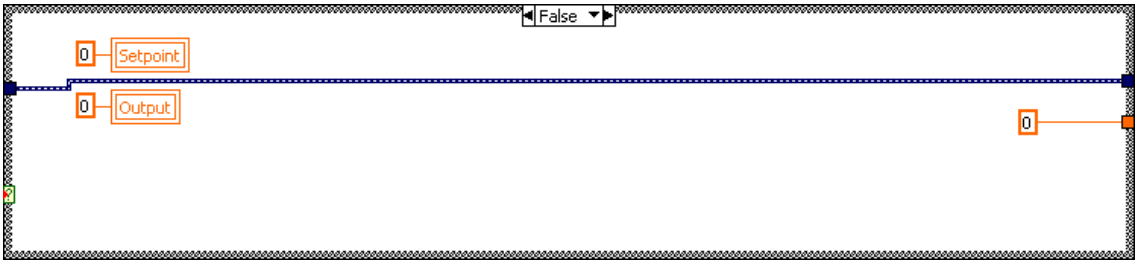

Figure C.15: Case structure 2: PID threshold low (false).

C.4 Superelastic vibration control system with two restraining elements

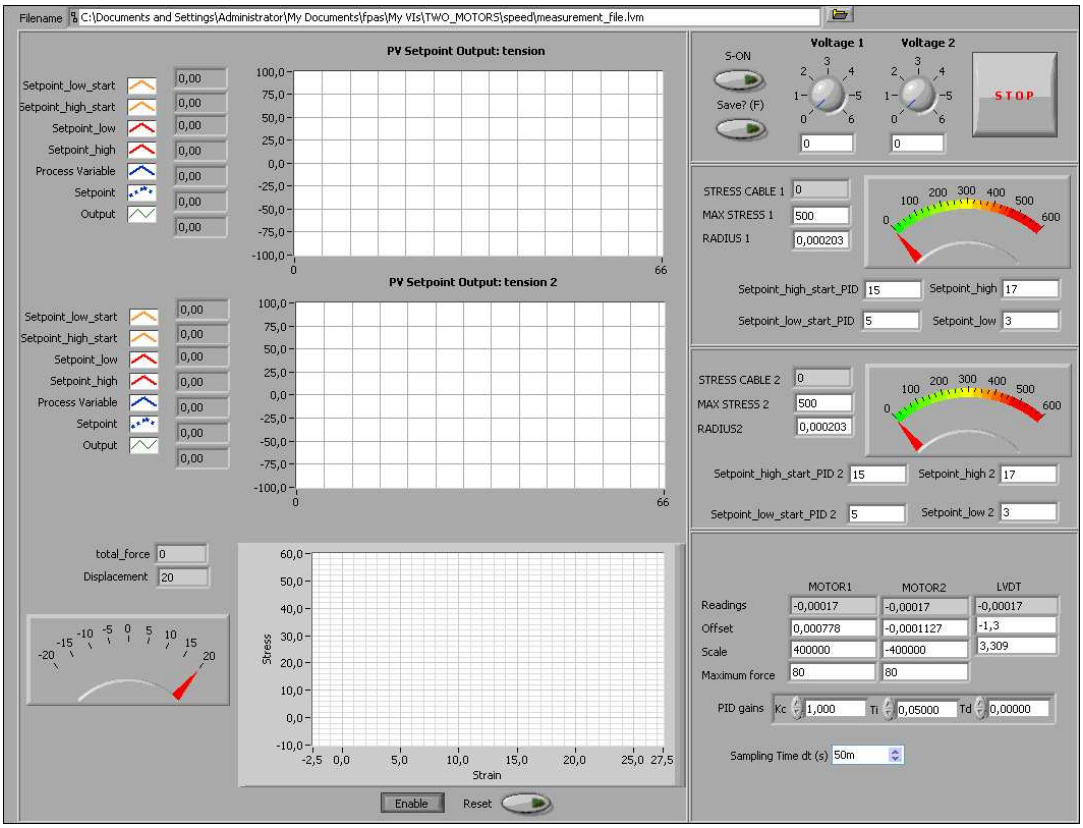

Figure C.16: Front panel of the SE control system with two restraining elements.

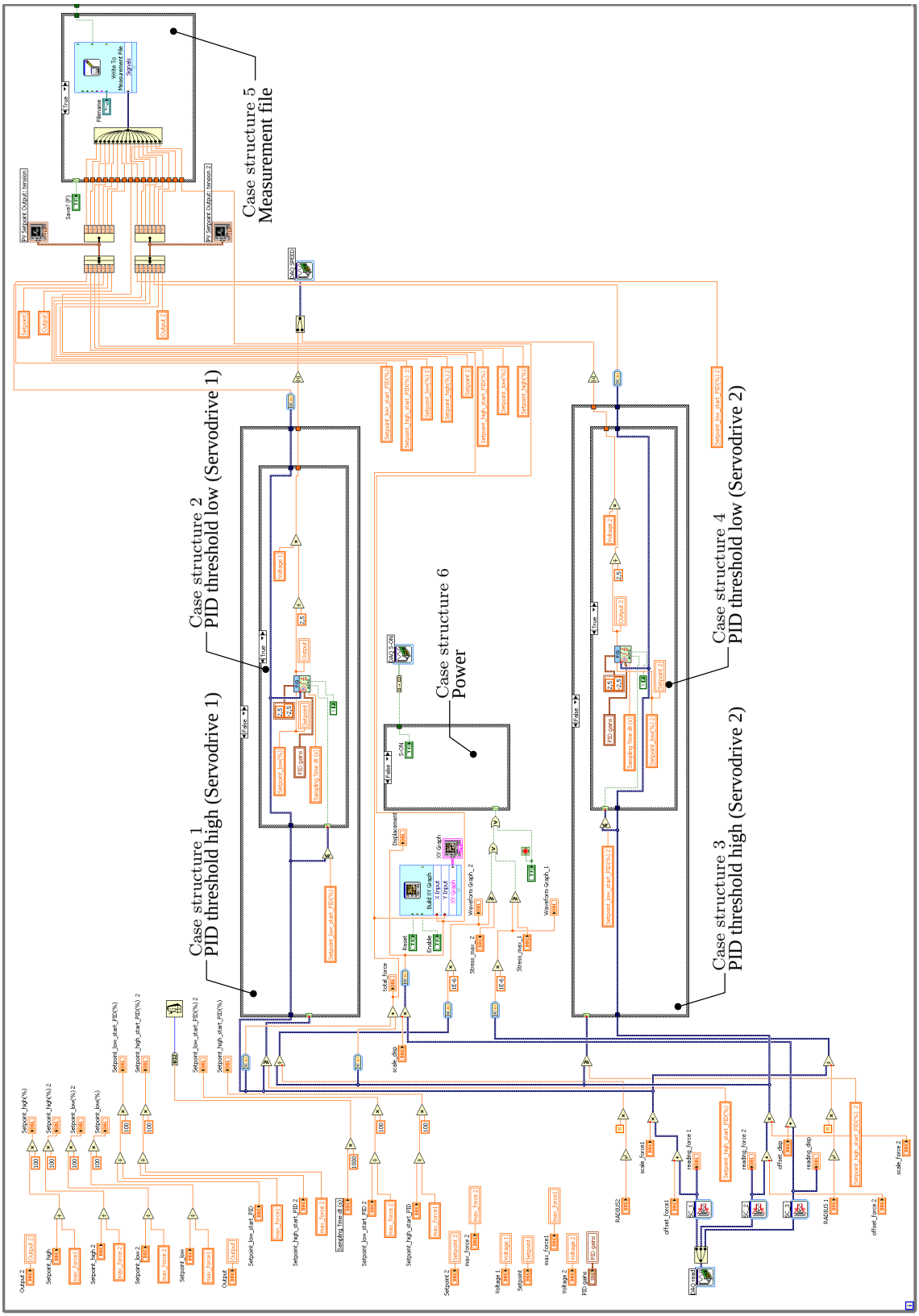

Figure C.17: Block diagram of the SE vibration control system with two restraining elements (partial).

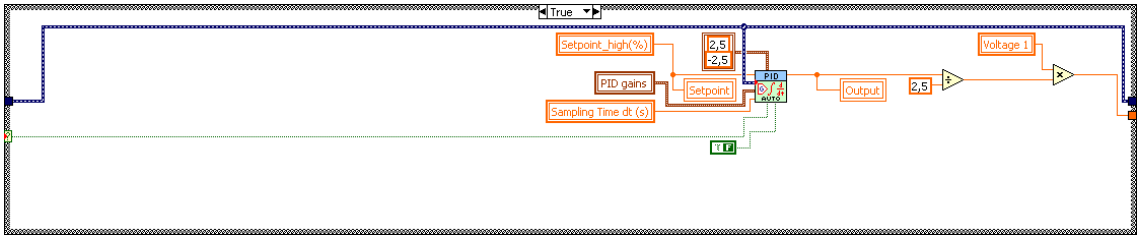

Figure C.18: Case structure 1: PID threshold high (Servodrive 1) (true).

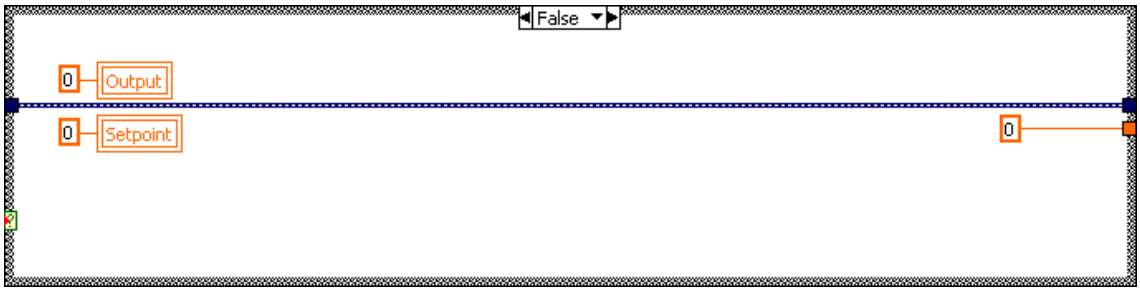

Figure C.19: Case structure 2: PID threshold low (Servodrive 1) (false).

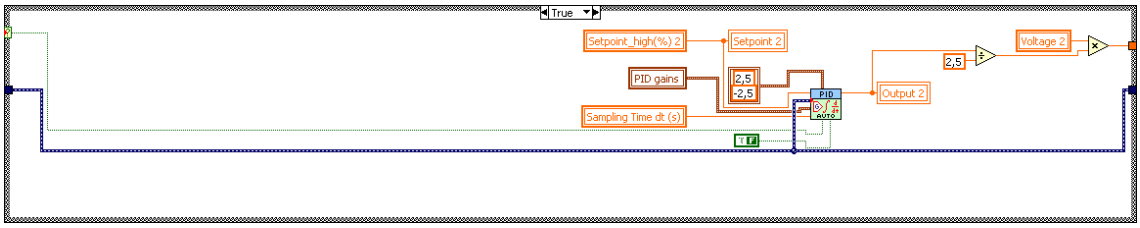

Figure C.20: Case structure 3: PID threshold high (Servodrive 2) (true).

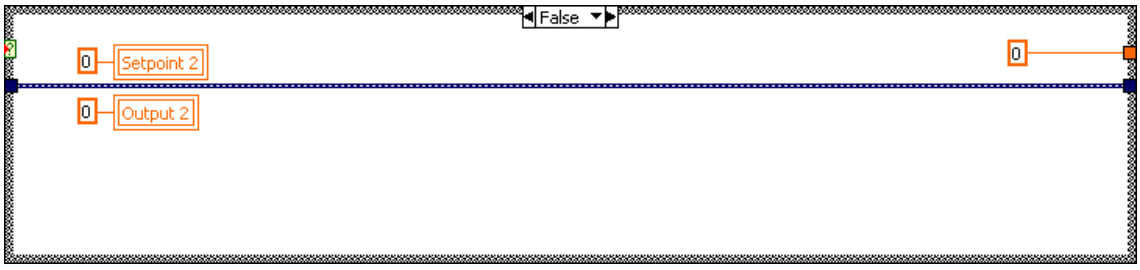

Figure C.21: Case structure 4: PID threshold low (Servodrive 2) (false).

Bibliography

[1] Addington, M., and Schodek, D. *Smart Materials and Technologies for the architecture and design professions.* Architectural Press, 2005.

[2] Aiken, I. D., Nims, D. K., Whittaker, A. S., and Kelly, J. M. Testing of Passive Energy Dissipation Systems. *Earthquake Spectra 9*, 3 (1993), 335–369.

[3] Aizawa, S., Kakizawa, T., and Higasino, M. Case studies of smart materials for civil structures. *Smart Materials and Structures 7* (1998), 617–626.

[4] Alam, M. S., Youssef, M. A., and Nehdi, M. Utilizing shape memory alloys to enhance the performance and safety of civil infrastructure: a review. *Canadian Journal of Civil Engineering 34* (2007), 1075–1086.

[5] Alam, M. S., Youssef, M. A., and Nehdi, M. Analytical prediction of the seismic behaviour of superelastic shape memory alloy reinforced concrete elements. *Engineering Structures 30* (2008), 3399–3411.

[6] Amarante dos Santos, F. P., and Cismaşiu, C. Comparison Between Two SMA Constitutive Models for Seismic Applications. *Journal of Vibration and Control 16*, 6 (2010), 897–914.

[7] AMETEK Inc. *Solartron Metrology Catalogue*, 2006.

[8] Andrawes, B., and DesRoches, R. Comparison Between Shape Memory Alloy Restrainers and and Other Bridge Retrofit Devices. *ASCE Journal of Bridge Engineering 12*, 6 (2007), 700–709.

[9] Ascher, U., and Petzold, L. R. *Computer methods for ordinary differential equations and differential-algebraic equations.* SIAM, 1998.

[10] Ashby, M. F., and Jones, D. R. H. *Engineering Materials 2: An Introduction to Microstructures, Processing and Design*, 3rd ed. Butterworth-Heinemann, 1986.

[11] Auguet, C., Isalgue, A., Lovey, Martorell, F., and Torra, V. Metastable effects on martensitic transformation in SMA Part 4. Thermomechanical properties of CuAlBe and NiTi observations for dampers in family houses. *Journal of Thermal Analysis and Calorimetry 88*, 2 (2007), 537–548.

[12] Auguet, C., Isalgue, A., Lovey, F. C., Ruiz, S., and Torra, V. Metastable effects on martensitic transformation in SMA Part III. Tentative temperature effects in a NiTi alloy. *Journal of Thermal Analysis and Calorimetry 89*, 2 (2007), 537–542.

[13] Auguet, C., Isalgue, A., Torra, V., Lovey, F. C., and Pelegrina, J. L. Metastable effects on martensitic transformation in SMA Part VII. aging problems in NiTi. *Journal of Thermal Analysis and Calorimetry 92*, 1 (2008), 63–71.

[14] Auricchio, F., Fugazza, D., and Desroches, R. Earthquake Performance of Steel Frames with Nitinol Braces. *Journal of Earthquake Engineering 10*, 4 (2006), 45–66.

[15] Auricchio, F., Fugazza, D., and DesRoches, R. Numerical and Experimental Evaluation of the Damping Properties of Shape-Memory Alloys. *Journal of Engineering Materials and Technology 128*, 3 (2006), 312–319.

[16] Auricchio, F., and Sacco, E. A one-dimensional model for superelastic shape-memory alloys with different elastic properties between austenite and martensite. *International Journal of Non-Linear Mechanics 32*, 6 (1997), 1101–1114.

[17] Auricchio, F., and Sacco, E. A temperature-dependent beam for shape-memory alloys: constitutive modelling, finite-element implementation and numerical simulations. *Computer Methods in Applied Mechanics and Engineering 174* (1997), 171–190.

[18] Auricchio, F., Taylor, R. L., and Lubliner, J. Shape-Memory Alloys: macromodelling and numerical simulations of the superelastic behaviour.

Computer Methods in Applied Mechanics and Engineering 146 (1997), 281–312.

[19] Autoliv, Inc. *Load limiter*. http://www.autoliv.com.

[20] Azadi, B., Rajapakse, R. K. N. D., and Maijer, D. M. One-dimensional thermomechanical model for dynamic pseudoelastic response of shape memory alloys. *Smart Materials and Structures 15* (2006), 996–1008.

[21] Balandraud, X., Ernst, E., and Soós. Relaxation and creep phenomena in shape memory alloys. Part II: Stress relaxation and strain creep during phase transformation. *Zeitschrift für angewandte Mathematik und Physik 51* (2000), 419–448.

[22] Balandraud, X., Ernst, E., and Soós. Monotone strain-stress models for shape memory alloys hysteresis loop and pseudoelastic behavior. *Zeitschrift für angewandte Mathematik und Physik 56* (2005), 304–256.

[23] Bekker, A., and Brinson, L. C. Phase Diagram based description of the hysteresis behavior of shape memory alloys. *Acta Metallurgica et Materialia 46*, 10 (1997), 3649–3655.

[24] Bhattacharyya, A., Sweeney, L., and G., F. M. Experimental characterization of free convection during thermal phase transformations in shape memory alloy wires. *Smart Materials and Structures 11* (2002), 411–422.

[25] Birman, V. Shape memory elastic foundation and supports for passive vibration control of composite plates. *International Journal of Solids and Structures 45* (2008), 320–335.

[26] Bondaryev, E. N., and Wayman, C. M. Some Stress-Strain-Temperature Relationships for Shape Memory Alloys. *Metallurgical Transactions A 19A* (1988), 2407–2413.

[27] Boroschek, R. L., Farias, G., Moroni, O., and Sarrazin, M. Effect of SMA braces in a Steel Frame Building. *Journal of Earthquake Engineering 11* (2007), 326–342.

[28] Bosch Rexroth AG. *Electromechanical Cylinder EMC*, 2009. R310EN 3306.

[29] Brinson, L. C. One-Dimensional Constitutive Behavior of Shape Memory Alloys: Thermomechanical Derivation with Non-Constant Material Functions and Redefined Martensite Internal Variable. *Journal of Intelligent Material Systems and Structures 4* (1993), 229–242.

[30] Brinson, L. C., and Huang, M. S. Simplifications and Comparisons of Shape Memory Alloy Constitutive Models. *Journal of Intelligent Material Systems and Structures 7* (1996), 108–114.

[31] Brocca, M., Brinson, L. C., and Bazant, P. Three Dimensional Constitutive Model for Shape Memory Alloys Based on Microplane Model. *Journal of the Mechanics and Physics of Solids 50* (2002), 1051–1077.

[32] Bruno, S., and Valente, C. Comparative response analysis of conventional and innovative seismic protection strategies. *Earthquake Engineering and Structural Dynamics 31* (2007), 1067–1092.

[33] Callender, A., Hartree, D. R., and Porter, A. *Time Lag in a Control System*. Phil. Trans. R. Soc. A. London: Cambridge University Press, 1936.

[34] Casciati, S., and Faravelli, L. Structural components in shape memory alloy for localized energy dissipation. *Computers and Structures 86* (2008), 330–339.

[35] Castellano, M. G., Indirli, M., and Martelli, A. Progress of application, research and development and design guidelines for shape memory alloy devices for cultural heritage structures in italy. *SPIE Proceedings 4330* (2000), 250–261.

[36] Chang, B. C., Shaw, J. A., and Iadicola, M. A. Thermodynamics of shape memory alloy wire: modeling, experiments, and application. *Continuum Mechanics and Thermodynamics 18*, 1-2 (2006), 83–118.

[37] Chang, L. C., and Read, T. A. Plastic deformation and diffusionless phase changes in metals - The gold-cadmium beta phase. *Trans AIME 189* (1951), 47–52.

[38] Chopra, A. K. *Dynamics of Structures: theory and applications to earthquake engineering*, 2nd ed. Prentice-Hall, Inc., 2001.

[39] Cismasiu, C., and Amarante dos Santos, F. P. *Shape Memory Alloys*. Sciyo, 2010.

[40] Cismasiu, C., and Santos, F. P. A. Numerical simulation of superelastic shape memory alloys subjected to dynamic loads. *Smart Materials and Structures 17*, 2 (2008), 25–36.

[41] Continental Contitech. *Product Range SYNCHROFLEX Timing Belts - Power Transmission Group*. WT6220E 09.06(BL).

[42] Corbi, O. Shape memory alloys and their application in structural oscillations attenuation. *Simulation Modelling Practice and Theory 11* (2003), 387–402.

[43] Croci, G. Strengthening the Basilica of St. Francis of Assisi after the September 1997 Earthquake. *Structural Engineering International 11*, 3 (2001), 207–210.

[44] De la Flor, S., and Urbina, F. F. Constitutive model of shape memory alloys: Theoretical formulation and experimental validation. *Materials Science and Engineering*, A 427 (2006), 112–122.

[45] DeGarmo, . E., Black, J. T., and Kohser, R. *Degarmo's Materials and Processes in Manufaturing*. Wiley, 2007.

[46] DesRoches, R., and Delemont, M. Seismic retrofit of simply supported bridges using shape memory alloys. *Engineering Structures 24* (2002), 325–332.

[47] DesRoches, R., McCormick, J., and Delemont, M. Cyclic Properties of Superelastic Shape Memory Alloy Wires and Bars. *Journal of Structural Engineering 130*, 1 (2004), 1–38.

[48] DesRoches, R., Pfeifer, T., Leon, R. T., and Lam, T. Full-Scale Tests of Seismic Cable Restrainer Retrots for Simply Supported Bridges. *Journal of Bridge Engineering 8*, 4 (2003), 191–198.

[49] DesRoches, R., and Smith, B. Shape memory alloys in seismic resistant design and retrofit: a critical review of their potential applications. *ournal of Earthquake Engineering 7*, 3 (2003), 1–15.

[50] Dolce, M., and Cardone, D. Mechanical behaviour of shape memory alloys for seismic applications 1. Martensite and austenite NiTi bars subjected to torsion. *International Journal of Mechanical Sciences*, 43 (2001), 2631–2656.

[51] Dolce, M., and Cardone, D. Mechanical behaviour of shape memory alloys for seismic applications 2. Austenite NiTi wires subjected to tension. *International Journal of Mechanical Sciences*, 43 (2001), 2657–2677.

[52] Dolce, M., Cardone, D., and Marnetto, R. Implementation and testing of passive control devices based on shape memory alloys. *Earthquake Engineering and Structural Dynamics*, 29 (2000), 945–968.

[53] Dolce, M., Cardone, D., Ponzo, F. C., and Valente, C. Shaking table tests on reinforced concrete frames without and with passive control systems. *Earthquake Engineering and Structural Dynamics 34* (2005), 1687–1717.

[54] Dolce, M., Donatello, C., and Ponzo, F. C. Shaking-table tests on reinforced concrete frames with different isolation systems. *Earthquake Engineering and Structural Dynamics 36* (2007), 573–596.

[55] Duerig, T. W., and Pelton, A. R. *Materials Propreties Handbook: Titanium Alloys*. ASM International, 1994.

[56] Entemeyer, D., Patoor, E., Eberhardt, A., and Berveiller, M. Strain rate sensitivity in superelasticity. *International Journal of Plasticity 16* (2000), 1269–1288.

[57] Faulkner, M. G., Amalraj, J. J., and Bhattacharyya, A. Experimental determination of thermal and electrical properties of Ni-Ti shape memory wires. *Smart Materials and Structures*, 9 (2000), 632–639.

[58] Filleul, M. P., and Jordan, L. Torsional properties of Ni-Ti and Copper Ni-Ti wires: the effect of temperature on physical properties. *European Journal of Orthodontics*, 19 (1997), 637–646.

[59] Franklin, G. F., Powell, J. D., and Emami-Naeini, A. *Feedback Control of Dynamic Systems*, 3rd ed. Addison-Wesley, 1994.

[60] Fugazza, D. Shape-memory alloy device in earthquake engineering: Mechanical propreties, constitutive modelling and numerical simulations. Master's thesis, Rose School. Europeean School of Advanced Studies in Reduction of Seismic Risk, Pavia, Italy, 2003.

[61] Gadaj, S. P., Nowacki, W. K., and Pieczyska, E. A. Temperature evolution in deformed shape memory alloy. *Journal of Engineering Mechanics 43* (2002), 151–155.

[62] Gandhi, F., and Wolons, D. Characterization of the pseudoelastic damping behavior of shape memory alloy wires using complex modulus. *Smart Materials and Structures 8* (1999), 49–56.

[63] Govindjee, S., and Garrett, J. H. A computational model for shape memory alloys. *International Journal of Solids and Structures 37* (2000), 735–760.

[64] Graesser, E. J., and Cozzarelli, F. A. Shape-Memory Alloys as New Materials for Aseismic Isolation. *Journal of Engineering Mechanics 117*, 11 (1991), 2590–2608.

[65] Graesser, E. J., and Cozzarelli, F. A. A proposed three-dimensional constitutive model for shape memory alloys. *Journal of Intelligent Material Systems and Structures 5* (1994), 78–89.

[66] Greninger, A. B., and Mooradian, V. G. Strain transformation in metastable bete copper-zinc and beta copper-tin alloys. *Trans AIME 128* (1938), 337–368.

[67] Haland, Y. Evolution of the Three Point Seat Belt - from Yesterday to Tomorrow. Tech. rep., Autoliv, 2006.

[68] Hamburger, R. O., Foutch, D. A., and Cornell, C. A. Translating research to practice: FEMA/SAC performance-based design procedures. *Earthquake Spectra 19*, 2 (2003), 255–267.

[69] Han, Y. L., Li, Q. S., Li, A. Q., Leung, A. Y. T., and Lin, P. H. Structural vibration control by shape memory alloy damper. *Earthquake Engineering & Structural Dynamics 32*, 3 (2003), 483–494.

[70] Heinonen, J., Vessonen, I., Klinge, P., and Jarvinen, E. Controlling stiffness of a frame spring by changing the boundary condition with an SMA actuator. *Computers and Structures 86* (2007), 398–406.

[71] Hodgson, D. E., and Brown, J. W. *Using Nitinol Alloys*. Shape Memory Applications, Inc., 2000.

[72] Hoffmann, K. *Practical hints for the apllication of strain gages*. Hottinger Baldwin Messtechnik, 1984.

[73] Housner, G. W., Bergman, L. A., Caughey, T. K., Chassiakos, A. G., Claus, R. O., Masri, S. F., Skelton, R. E., Soong, T. T., Spencer, B. F., and Yao, J. T. P. Structural control. past, present, and future. *Journal of Engineering Mechanics 123*, 9 (1997), 897–971.

[74] Hsieh, S. F., and Wu, S. K. Lattice parameters of martensite in TiNiZrHf quaternary shape memory alloys. *Journal of Alloys and Compounds 312* (2000), 288–294.

[75] Hwang, J. S., and Ku, S. W. Analytical Modeling of High Damping Rubber Bearings. *Journal of Structural Engineering 123*, 8 (1997), 1029–1036.

[76] Incropera, F. P., and DeWitt, D. P. *Fundamentals of heat and mass transfer*, 6th ed. John Wiley and Sons, Inc., 2006.

[77] Indirli, M., Castellano, M. G., Clemente, P., and Martelli, A. Demo-application of shape memory alloy devices: The rehabilitation of the S. Giorgio Church bell-tower. *SPIE Proceedings 4330* (2001), 262–272.

[78] Isalgue, A., Torra, V., Yawny, A., and Lovey, F. Metastable effects on martensitic transformation in SMA Part VI. the ClausiusClapeyron relationship. *Journal of Thermal Analysis and Calorimetry 91*, 3 (2008), 991–998.

[79] Ivshin, Y., and Pence, T. J. A Thermomechanical Model for a One Variant Shape Memory Material. *Journal of Intelligent Material Systems and Structures 5*, 4 (1994), 455–473.

[80] Jansen, L. M., and Dyke, S. J. Semi-Active Control Strategies for MR Dampers: A Comparative Study. *Journal of Engineering Mechanics 126*, 8 (2000), 795–803.

[81] Jean, R. D., and Hu, C. T. Shape memory effect by constant-stress ageing in Ti-50.5 at % Ni alloy. *Journal of Materials Science 29* (1994), 449–455.

[82] Johnson, R., Padgett, J. E., Maragakis, M. E., DesRoches, R., and Saiidi, M. S. Large scale testing of Nitinol shape-memory alloy devices for retrofitting of bridges. *Smart Materials and Structures 17*, 3 (2008).

[83] Jolly, M., Bender, J., and Carlson, J. Properties and applications of commercial magnetorheological fluids. *Journal of Intelligent Material Systems and Structures 10*, 1 (1999), 5–13.

[84] Juntunen, D. Study of Michigan's Continuous Span Variable Depth T-beam Bridges. Tech. Rep. R-1374, Michigan Department of Transportation, Testing and Research Section, 2000.

[85] Kuo, B. C. *Automatic Control Systems*, 3rd ed. Prentice-Hall, Inc., 1975.

[86] Kurdjumov, G. V., and Khandros, L. G. *Doklady Akademii Nauk SSSR 66* (1949), 211–213.

[87] Lacarbonara, W., Bernardini, D., and Vestroni, F. Nonlinear thermomechanical oscillations of shape-memory devices. *International Journal of Solids and Structures 41*, 5-6 (2004), 1209–1234.

[88] Lagoudas, D. C., Entchev, P. B., and Kumar, P. K. Thermomechanical characterization of SMA actuators under cyclic loading. *Proceedings of 2003 ASME International Mechanical Engineering Congress*, IMECE2003-42933 (2003), 211–217.

[89] Lagoudas, D. C., Ravi-Chandar, K., Sarh, K., and Popov, P. Dynamic Loading of Polycrystalline Shape Memory Alloy Rods. *Mechanics of materials 35*, 7 (2003), 689–716.

[90] Lakes, R. S. Viscoelastic measurement techniques. *Review Scientific Instruments 75*, 4 (2004), 797–810.

[91] Lammering, R., and Schmidt, I. Experimental investigations on the damping capacity of NiTi components. *Smart Materials and Structures 10* (2001), 853–859.

[92] Laplace, P. S. *Théorie analytique des probabilités*. Paris, 1812.

[93] Leo, P. H., Shild, T. W., and Bruno, O. P. Transient heat transfer effects on the pseudoelastic behavior of shape memory wires. *Acta Metallurgica et Materialia 41* (1993), 2477–2485.

[94] Lexcellent, C., and Rejzner, J. Modeling of the strain rate effect, creep and relaxation of a NiTi shape memory alloy under tension (compression)-torsional proportional loading in the pseudoelastic range. *Smart Materials and Structures 9* (2000), 613–621.

[95] Li, H., Liu, M., and Ou, J. Vibration mitigation of a stay cable with one shape memory alloy damper. *Structural Control and Health Monitoring 11* (2000), 21–36.

[96] Liang, C., and Rogers, C. A. One-Dimensional Thermomechanical Constitutive Relations for Shape-Memory Materials. *Journal of Intelligent Systems and Structures 1* (1990), 207–234.

[97] Liang, C., and Rogers, C. A. Design of Shape Memory Alloy Springs With Applications in Vibration Control. *Journal of Vibration and Acoustics 115* (1993), 129–135.

[98] Lord Corporation. *Lord technical data, MRF-122EG Magneto-Rheological Fluid*, 2008.

[99] Ma, N., Song, G., and Tarefder, R. A. Vibration control of a frame structure using shape memory alloy braces. *Proceedings of the Third International Conference on Earthquake Engineering* (2004).

[100] Magee, C. L. Nucleation of martensite. In *Phase Transformations*, ASM, Ed. 1970, pp. 115–156.

[101] Matsui, R., Tobushi, H., and Ikawa, T. Transformation-induced creep and stress relaxation of TiNi shape memory alloy. *Proceedings of the Institution of Mechanical Engineers, Part L: Journal of Materials: Design and Applications 218*, 4 (2004), 343–353.

[102] McCormick, J. *Cyclic behavior of shape-memory alloys: material characterization and optimization.* PhD thesis, School of Civil and Environmental Engineering of the Georgia Institute of Technology, 2006.

[103] McCormick, J., DesRoches, R., Fugazza, D., and Auricchio, F. Seismic Vibration Control Using Superelastic Shape Memory Alloys. *Journal of Engineering Materials and Technology 128*, 3 (2006), 294–301.

[104] McCormick, J., Tyber, J., DesRoches, R., Gall, K., and Maier, H. J. Structural Engineering with NiTi. II: Mechanical Behavior and Scaling. *Journal of Engineering Mechanics 133*, 9 (2007), 1019–1029.

[105] Messner, C., and Werner, E. Temperature distribution due to localised martensitic transformation in SMA tensile test specimens. *Computational Materials Science 26* (2003), 95–101.

[106] Michaud, V. Can shape memory alloy composites be smart? *Scripta Materialia 50* (2004), 249–253.

[107] Miyazaki, S., Imai, T., and Otsuka, K. Effect of Cyclic Deformation on the Pseudoelasticity Characteristics of Ti-Ni Alloys. *Metallurgical and Materials Transactions A 17*, 1 (1986), 115–120.

[108] Modena, C., and Lourenco, P. B. *Structural Analysis of Historical Constructions*. Taylor and Francis Group, 2004.

[109] Montecinos, S., Moroni, M., and Sepulveda, A. Superelastic behavior and damping capacity of CuAlBe alloys. *Materials Science and Engineering A 419* (2005), 91–97.

[110] Motahari, S. A., Ghassemieh, M., and A., A. S. Implementation of shape memory alloy dampers for passive control of structures subjected to seismic excitations. *Journal of Constructional Steel Research 63* (2007), 1570–1579.

[111] Moumni, Z., Van Herpen, A., and Riberty, P. Fatigue analysis of shape memory alloys: energy approach. *Smart Materials and Structures 14* (2005), S287–S292.

[112] Nae, F. A., Tadashige, I., and Matsuzaki, Y. The active tuning of a shape memory alloy pseudoelastic property. *Smart Materials and Structures 13* (2004), 503–511.

[113] National Instruments Corporation. *PID Control Toolset User Manual*, 2001.

[114] National Instruments Corporation. *Data Acquisition and Signal Conditioning Course Manual*, 2003.

[115] National Instruments Corporation. *Choosing the Right Strain-Gauge for Your Application*, 2006.

[116] National Instruments Corporation. *Strain Gauge Configuration Types*, 2006.

[117] Ocel, J., DesRoches, R., Leon, R. T., Hess, W. G., Krumme, R., Hayes, J., and Sweeney, S. Steel Beam-Column Connections Using Shape Memory Alloys. *Journal of Structural Engineering 130*, 5 (2004), 732–740.

[118] Ogata, K. *Modern Control Engineering*, 3rd ed. Prentice-Hall International, Inc., 1997.

[119] Omron-Yaskawa Electric Corporation. *Sigma-II Series Servodrive SGDH-* Datasheet.* Cat. No. I48E-EN-01.

[120] Omron-Yaskawa Electric Corporation. *Sigma-II Series SGM*H/SGDH user's Manual.* SIEPS80000005C.

[121] Omron-Yaskawa Electric Corporation. *Technical Guide: Servo System Startup.* Cat. No. I801-E1-1.

[122] Ortín, J., and Delaey, L. Hysteresis in shape-memory alloys. *International Journal of Non-Linear Mechanics 37* (2002), 1275–1281.

[123] Ostowari, K., and Souroushian, P. Field Trial of Shape-Memory Based Rehabilitation System. Tech. Rep. NCHRP-48, IDEA Program, Transportation Research Board, National Research Council, 2000.

[124] Otsuka, K., and Wayman, C. M., Eds. *Shape memory materials* (1998), Cambridge University Press.

[125] Ozbulut, O. E., Mir, C., Moroni, M. O., Sarrazin, M., and Roschke, P. N. A fuzzy model of superelastic shape memory alloys for vibration control in civil engineering applications. *Smart Materials and Structures 16* (2007), 818–829.

[126] Pacific Earthquake Engineering Research Center. *PEER Strong Motion Database.* http://peer.berkeley.edu/smcat.

[127] Padgett, J. E., DesRoches, R., and Ehlinger, R. Experimental response modication of a four-span bridge retrofit with shape memory alloys. *Structural Control and Health Monitoring* (2009).

[128] Paiva, A., Savi, M. A., Braga, A. M. B., and Pacheco, P. M. C. L. A constitutive model for shape memory alloys considering tensile-compressive asymmetry and plasticity. *International Journal of Solids and Structures 42* (2005), 3439–3457.

[129] Panoskaltsis, V. P., and Bahuguna, S. and, S. D. On the thermomechanical modeling of shape memory alloys. *International Journal of Non-Linear Mechanics 39* (2004), 709–722.

[130] Pappas, P., Bollas, D., Parthenios, J., Dracopoulos, V., and Galiotis, C. Transformation fatigue and stress relaxation of shape memory alloy wires. *Smart Materials and Structures 16* (2007), 2560–2570.

[131] Patoor, E., Lagoudas, D. C., Entchev, P., Brinson, C., and Gao, X. Shape memory alloys, Part I: General properties and modeling of single crystals. *Mechanics of Materials 38* (2006), 391–429.

[132] Pieczyska, E. A., Gadaj, S. P., Nowacki, W. K., Makino, Y., and Tobushi, H. Characteristics of energy storage and dissipation in TiNi shape memory alloy. *Science and Technology of Advanced Materials 6* (2005), 889–894.

[133] Pieczyska, E. A., Gadaj, S. P., Nowacki, W. K., and Tobushi, H. Phase-Transformation Fronts Evolution for Stress and Strain Controlled Tension Tests in TiNi Shape Memory Alloy. *Experimental Mechanics 46* (2006), 531–542.

[134] Pieczyska, E. A., Gadaj, S. P., Nowacki, W. K., and Tobushi, H. Stress relaxation during superelastic behavior of TiNi shape memory alloy. *International Journal of Applied Electromagnetics and Mechanics 23* (2006), 3–8.

[135] Piedboeuf, M. C., and Gauvin, R. Damping behaviour of shape memory alloys: strain amplitude, frequency and temperature effects. *Journal of Sound and Vibration 214*, 5 (1998), 885–901.

[136] Potapov, P. L., Shelyakov, A. V., and Schryvers, D. On the crystal structure of tini-cu martensite. *Scripta Materialia 44* (2001), 1–7.

[137] Potapov, P. L., Shelyakov, A. V., and Schryvers, D. A one-dimensional strain-rate-dependent constitutive model for superelastic shape memory alloys. *Smart Materials and Structures 16* (2007), 191–197.

[138] Pungor, E. *A Practical Guide to Instrumental Analysis*. CRC Press LLC, 1995.

[139] Qiang, P., and Cho, C. The Investigation of a Shape Memory Alloy Micro-Damper for MEMS Applications. *Sensors 7* (2007), 1887–1900.

[140] Quanser Inc. *Quanser Shake Table II User Manual*, 2007. Document Number 632/Revision 3.10.

[141] Reynolds, D. R. *A Nonlinear Thermodynamic Model for Phase Transitions in Shape Memory Alloy Wires*. PhD thesis, Rice University, Houston, Texas, 2003.

[142] Saadat, S., Noori, M., Davoodi, H., Suzuki, Y., and Masuda, A. Using NiTi SMA tendons for vibration control of coastal structures. *Smart Materials and Structures 10* (2001), 695–704.

[143] Saadat, S., Salichs, J., Noori, M., Hou, Z., Davoodi, H., Bar-on, I. Suzuki, Y., and Masuda, A. An overview of vibration and seismic applications of NiTi shape memory alloy. *Smart Materials and Structures 11* (2002), 218–229.

[144] Saint-Sulpice, L., Chirani, S. A., and Calloch, S. Super-elastic behavior of shape memory alloys under proportional cyclic loadings. *Materials Science and Engineering A 481-482* (2008), 174–177.

[145] Saint-Sulpice, L., Chirani, S. A., and Calloch, S. A 3D super-elastic model for shape memory alloys taking into account progressive strain under cyclic loadings. *Mechanics of Materials 41* (2009), 12–26.

[146] Seelecke, S. Torsional vibration of a shape memory wire. *Continuum Mechanics and Thermodynamics 9* (1997), 165–173.

[147] Seelecke, S. Modeling the dynamic behavior of shape memory alloys. *International Journal of Non-Linear Mechanics 37* (2002), 1363–1374.

[148] Seelecke, S., Heintze, O., and Masuda, A. Simulation of earthquake-induced structural vibrations in systems with SMA damping elements. *SPIE Smart Structures and Materials 4697* (2002).

[149] Shook, D. A., Roschke, P. N., and Ozbulut, O. E. Superelastic semi-active damping of a base-isolated structure. *Structural Control and Health Monitoring 15* (2008), 746–768.

[150] Song, G., Ma, N., and Li, H. N. Applications of shape memory alloys in civil structures. *Engineering Structures 28* (2006), 1266–1274.

[151] Soong, T. T., and Spencer, B. F. Supplemental energy dissipation: state-of-the-art and state-of-the-practice. *Engineering Structures 24* (2002), 243–259.

[152] Soroushian, P., Ostowari, K., and Nossoni, A.and Chowdhury, B. Repair and strengthening of concrete structures through applications of corrective posttensioning forces with shape memory alloys. *Transportation Research Record 1770* (2001), 2026.

[153] Spencer, B. F., and Nagarajaiah, S. State of the Art of Structural Control. *Journal of Structural Engineering 129*, 7 (2009), 845–856.

[154] Spencer, B. F., and Sain, M. K. Controlling Buildings: A New Frontier in Feedback. *Special Issue of the IEEE Control Systems Magazine on Emerging Technology 17*, 6 (1997), 1935.

[155] Sun, S., and Rajapakse, R. K. N. D. Simulation of pseudoelastic behaviour of sma under cyclic loading. *Computational Materials Science 28* (2003), 663–674.

[156] Symans, M. D., and Constantinou, M. C. Semi-active control systems for seismic protection of structures: a state-of-the-art review. *Engineering Structures 21* (1999), 469–487.

[157] Tamai, H., and Kitagawa, Y.and Fukuta, T. Application of sma rods to exposed-type column bases in smart structural systems. In *Proc., 13th World Conf. on Earthquake Engineering*, no. 1884.

[158] Tamai, H., and Kitagawa, Y. Pseudoelastic behavior of shape memory alloy wire and its application to seismic resistance member for building. *Computational Materials Science 25*, 1-2 (2002), 218–227.

[159] Tanaka, K., Kobayashi, S., and Sato, Y. Thermomechanics of transformation pseudoelasticity and shape memory effect in alloys. *International Journal of Plasticity 2* (1986), 59–72.

[160] Tanaka, K., Nishimura, F., Hayashi, T., Tobushi, H., and Lexcellent, C. Phenomenological analysis on subloops and cyclic behavior in shape memory alloys under mechanical and/or thermal loads. *Mechanics of Materials 19* (1995), 281–292.

[161] Thomas, L. C. *Heat Transfer*. Prentice-Hall, Inc., 1992.

[162] Tobushi, H., Iwanaga, H., Tanaka, K., Hori, T., and Sawada, T. Deformation behaviour of TiNi shape memory alloy subjected to variable stress and temperature. *Continuum Mechanics and Thermodynamics 3* (1991), 79–93.

[163] Tobushi, H., Iwanaga, H., Tanaka, K., Hori, T., and Sawada, T. Stress-strain-temperature relations of TiNi shape memory alloy suitable for thermomechanical cycling. *JSME International Journal. Series A, Solid Mechanics and Material Engineering 35*, 3 (1992), 271–277.

[164] Tobushi, H., Shimeno, Y., Hachisuka, T., and Tanaka, K. Influence of strain rate on superelastic properties of TiNi shape memory alloy. *Mechanics of Materials 30* (1998), 141–150.

[165] Torra, V., Isalgue, A., Martorell, F., Terriault, P., and Lovey, F. Built in dampers for family homes via SMA: An ANSYS computation scheme based on mesoscopic and microscopic experimental analyses. *Engineering Structures 29* (2007), 1889–1902.

[166] Torra, V., Pelegrina, J., Isalgue, A., and Lovey, F. Metastable effects on martensitic transformation in SMA (I): Recoverable effects by the action of thermodynamic forces in parent phase. *Journal of Thermal Analysis and Calorimetry 81* (2005), 131–135.

[167] van der Wijst, M. W. M. Shape Memory Alloys featuring Nitinol. Tech. Rep. 256199, Technische Universiteit Eindhoven, 1992.

[168] Van Humbeeck, J., and Liu, Y. Shape memory alloys as damping materials. *Materials Science Forum* (2000), 327–338.

[169] Vitiello, A., Giorleo, G., and Morace, R. E. Analysis of thermomechanical behaviour of Nitinol wires with high strain rates. *Smart Materials and Structures 14* (2005), 215–221.

[170] Vitiello, A., Squillace, A., and U., P. Characterization of Nitinol under torsional loads through a numerical implementation of the Boyd-Lagoudas constitutive model and comparison of the results with experimental data. *Smart Materials and Structures 16* (2007), 76–82.

[171] Šittner, P., and Novák, V. L. Load Partitioning in Shape Memory Alloy Polycrystals Studied by In-situ Neutron Diffraction and Modeling. *Presented at IUTAM2001 Symposium on Mechanics of Martensitic Phase Transformation in Solids* (2001), 179–188.

[172] Wang, X., Xu, B., and Yue, Z. Phase transformation behavior of pseudoelastic NiTi shape memory alloys under large strain. *Journal of Alloys and Compounds 463* (2008), 417–422.

[173] Weisstein, E. W. Polygon Area. From MathWorld–A Wolfram Web Resource.http://mathworld.wolfram.com/PolygonArea.html.

[174] Wilde, K., Gardoni, P., and Fujino, Y. Base isolation system with shape memory alloy device for elevated highway bridges. *Engineering Structures 22* (2000), 222–229.

[175] Yoshida, I., Ono, T., and Asai, M. Internal friction of Ti-Ni alloys. *Journal of Alloys and Compounds 310* (2000), 339–343.

[176] Zhang, Y., and Zu, S. Seismic Response Control of Building Structures with Superelastic Shape Memory Alloy Wire Dampers. *Journal of Engineering Mechanics 134*, 3 (2007), 240–251.

[177] Zhang, Y., and Zu, S. A shape memory alloy-based reusable hysteretic damper for seismic hazard mitigation. *Smart Materials and Structures 16* (2007), 1603–1623.

[178] Zuo, X. B., Chang, W., Li, A. Q., and Chen, Q. F. Design and experimental investigation of a superelastic SMA damper. *Materials Science and Engineering A 438-440* (2006), 1150–1153.

Index